

On Superficial Interneurons of Dorsal Hippocampal CA1

Demi Brizee

Doctor of Philosophy (D.Phil.) Thesis

2024

St Peter's College

MRC Brain Network Dynamics Unit

Nuffield Department of Clinical Neurosciences

University of Oxford

Oxford, United Kingdom

Abstract

On Superficial Interneurons of Dorsal Hippocampal CA1

Demi Brizee, St Peter's College
Thesis submitted for the degree of Doctor of Philosophy, Trinity Term 2024

Inhibition plays a pivotal role in information processing in the brain. Cortical areas have developed a plethora of distinct inhibitory interneuron types, with over 20 distinct types described in dorsal CA1 of the hippocampus. In contrast to CA1 pyramidal neurons, interneurons are found scattered across all layers and display distinct morphological, molecular, and electrophysiological characteristics. However, the function of superficial layer interneurons (the strata radiatum, lacunosum, and moleculare) remains poorly understood, compared to their counterparts in strata oriens and pyramidale, due to the scarcity of studies in the intact brain. Here, I validated a cross platform-based tetrode depth estimation approach to navigate the superficial layers of dorsal hippocampal CA1, which allowed me to map simultaneously recorded superficial interneurons, pyramidal neurons, and network activity across different mice into a common spatial framework. I found that superficial interneurons exhibit layer-specific spike waveform characteristics, which do not follow commonly used interneuron classification rules. Additionally, superficial interneuron spike-timing characteristics and engagement in theta oscillations, sharp-wave ripples, and behavioural states, appeared to be spatially structured along the radial axis of dorsal CA1. Anatomical and functional connectivity mapping showed that superficial interneurons are differentially recruited by CA3 and entorhinal cortex in a network state-dependent manner. Furthermore, superficial interneurons' interaction with their peers and pyramidal neurons appeared to be layer and state-dependent. Finally, these data combined showed that stratum lacunosum features a set of unique characteristics compared to the neighbouring strata radiatum and moleculare, indicating this layer may form a separate submodule in the local network. Together, these findings reveal the spatial and temporal structure of inhibitory activity across layers of dorsal CA1 and provide a strong foundation to unravel the role of superficial interneurons in both health and disease.

Acknowledgments

It has been an honour to go through this Thesis writing process, following a path paved by the greatest minds in a city that has been immersed in science for centuries. My younger self would never have dared to dream of writing my contribution to one of the largest and oldest libraries in the world. Yet here I am, editing the final paragraphs and sharing these last words surrounded by millions of books under watchful eye of the statue of Dr. John Radcliffe.

This work would not have existed without the support of the wonderful people around me. I thank my supervisors Prof. David Dupret, Dr. Vítor Lopes-dos-Santos, and Prof. Peter J. Magill for their support and guidance on a journey I have not always made easy. I would like to thank David for making this project possible, allowing me to be part of an amazing team, and for his confidence in me and my skills employed within and beyond the boundaries of my own project. I thank Vítor for the support to seize every opportunity that came by (in and outside Oxford), his unlimited patience during the hours spent on my training in coding and complex analysis, the enjoyable discussions, and the confidence in me and my skills as a scientist. Lastly, I would like to thank Peter for his support and guidance in this DPhil project and beyond.

Many thanks to the past and current members of the Dupret lab. Over the past few years, I have had the privilege to work with the most wonderful people who have gifted me their time and effort to get to know me, lift me up, and inspire me, while keeping me grounded and honest. I am grateful for the friendship they offered, the lessons they have taught me, and their continued support. Also, I would like to thank the amazing supporting staff, and the wider BNDU community for their wonderful support and discussions.

On a personal note, thanks to my partner for his support during the highs and lows, and for keeping me on course even when my compass broke. Lastly, I thank my family and, in particular, my parents who always encouraged me to explore the world, follow my heart, and live a life they may not have dared to dream of.

This DPhil project has been supported by the Biotechnology and Biological Sciences Research Council Interdisciplinary Biosciences DTP, the Scatcherd European Scholarships, and St Peter's College.

Contents

Abstract **3**
Acknowledgments **5**
Abbreviations **15**
Chapter 1. General Introduction **17**
1.1 Introduction 17
1.2 Organisation of the hippocampus 18
1.3 Rhythms in the hippocampus 20
1.4 The interneurons in the hippocampus 22
1.5 The function of inhibition 24
1.5.1 Inhibitory recruitment motifs 25
1.5.2 Results of inhibition on post-synaptic neurons 27
1.6 Studying the superficial interneurons of the hippocampus 29
1.7 In this Thesis 32
Chapter 2. Distinct CA1 layers feature unique LFP signatures suitable for tetrode depth estimation **35**
2.1 Introduction 35
2.2 Methods 36
2.2.1 Animals 36
2.2.2 Custom microdrives 37
2.2.3 Surgical procedure 37
2.2.4 Recording procedure 38
2.2.5 Silicon probe data 39
2.2.6 Tetrode data acquisition 39
2.2.7 Signal processing and analysis 39
2.2.8 Tetrode depth estimation 41
2.2.9 Histology 43
2.3 Results 44
2.3.1 Layer-specific network patterns allow recording depth estimation 44
2.3.2 LFP-guided recording depth estimation is transferable across different recording platforms 46
2.3.3 Cross-validation shows reliable LFP-guided tetrode recording depth estimation 48
2.4 Discussion 49
Chapter 3. Spike waveform characteristics of superficial interneurons **55**
3.1 Introduction 55

3.2 Method 58
3.2.1 Mice 58
3.2.2 Data acquisition and recording procedures 58
3.2.3 Data analysis 59
3.3 Results 65
3.3.1 Spike waveform validation and stability across different layers in dorsal CA1 65
3.3.2 Spike waveform characteristics differ across the radial axis of dorsal CA1 70
3.3.3 Spike waveform clustering reveals heterogeneous spike waveform population 75
3.4 Discussion 78
Chapter 4. Spike characteristics of superficial interneurons in dorsal CA1 are spatially organised 85
4.1 Introduction 85
4.2 Methods 87
4.2.1 Mice, surgical procedure, and data acquisition 87
4.2.2 Data analysis 87
4.2.3 Statistical testing 92
4.3 Results 92
4.3.1 Superficial interneurons display distinct temporal spike structures 92
4.3.2 Superficial interneurons show distinct spike timing characteristics in distinct brain states 96
4.3.3 Superficial interneurons display differential spiking behaviour in theta oscillations 98
4.3.4 Superficial interneurons display differential spiking patterns in theta-nested gamma oscillations 100
4.3.5 Superficial interneurons correlate differentially to speed 103
4.3.6 Superficial interneurons display differential spiking behaviour in sharp-wave ripples 107
4.3.7 Superficial interneurons cluster based on spike characteristics 109
4.4 Discussion 113
Chapter 5. Superficial interneurons are differently targeted by CA3 and EC 119
5.1 Introduction 119
5.2 Methods 121
5.2.1 Animals 121
5.2.2 Viruses 122
5.2.3 Surgical procedures 123
5.2.4 Histology 124
5.2.5 Imaging 126
5.2.6 Data analysis 126
5.2.7 Statistics 129
5.3 Results 129
5.3.1 Cell type-specific, anterograde, transsynaptic tracing reveals differential targeting of dorsal CA1 GABAergic neurons by CA3 and entorhinal cortex 129
5.3.2 Functional connectivity mapping 140
5.3.3 Discussion 153

Chapter 6. Interactions between superficial interneurons, pyramidal neurons, and the local network 159
6.1 Introduction 159
6.2 Methods 161
6.2.1 Mice, surgical procedure, and data acquisition 161
6.2.2 Data analysis 162
6.2.3 Statistical testing 163
6.3 Results 164
6.3.1 Pyramidale interneurons but not superficial interneurons generate short-latency spike reduction in the pyramidal neuron population 164
6.3.2 Pyramidal neuron spiking patterns are influenced by superficial interneurons 166
6.3.3 Co-activation between superficial interneurons and the neural local network is state-dependent 168
Chapter 7. Stratum Lacunosum is a distinct layer in dorsal CA1 177
7.1 Introduction 177
7.2 Methods 180
7.2.1 Literature review 180
7.2.2 Data collection 180
7.2.3 Data analysis 180
7.2.4 Statistical testing 181
7.3 Results 181
7.3.1 The majority of studies mention stratum lacunosum as a joined layer with moleculare 181
7.3.2 Lacunosum exhibits a unique gamma profile 183
7.3.3 Lacunosum houses unique interneurons based on spike-waveform and firing patterns 185
7.3.4 Lacunosum neurons are differentially targeted by CA3 and EC inputs compared to radiatum and moleculare neurons 187
7.4 Discussion 187
Chapter 8. General Discussion 191
8.1 Overview 191
8.2 Spatial structure of inhibition along the radial axis of dorsal CA1 192
8.3 Temporal structure of inhibition along the radial axis of dorsal CA1 194
8.4 Functional implications of laminarly organised and state-dependent inhibitory activity 198
8.5 Future directions 200
8.6 Concluding remarks 205
References 207

Figures

Figure 2.3.1 – Electrophysiological landmarks of distinct anatomical layers of dorsal CA1 45
Figure 2.3.2 – LFP-guided tetrode depth estimation 47
Figure 2.3.3 – Cross-validation shows valid LFP-guided layer assignment 49
Figure 3.2.1 – Behavioural paradigms 59
Figure 3.2.2 – Spike waveform measurements 61
Figure 3.2.3 – Optimizing spike waveform clustering parameter space 64
Figure 3.3.1 – Number of recorded units as a function of depth 66
Figure 3.3.2 – Spike waveform stability and quality control 67
Figure 3.3.3 – Spike waveform sources across subdomains and major neuron classes 69
Figure 3.3.4 – Distinct waveform shapes in different layers of dorsal CA1 71
Figure 3.3.5 – Spike waveform shapes cluster along the radial axis of dorsal CA1 74
Figure 3.3.6 – Spike waveform shape clusters distribute differently across distinct layers of dorsal CA1 76
Figure 4.3.1 – Superficial interneurons display varying spike characteristics 94
Figure 4.3.2 – Superficial interneuron spike characteristics differ across brain states 97
Figure 4.3.3 – Superficial interneurons display varying spiking behaviour in theta cycles ... 99
Figure 4.3.4 – Superficial interneurons display differential coupling to theta-nested gamma oscillations in CA1 101
Figure 4.3.5 – Superficial interneurons correlate differently to speed 104
Figure 4.3.6 – Superficial interneurons display varying spiking behaviour in sharp-wave ripples 106
Figure 4.3.7 – Superficial interneurons can be clustered in electrophysiologically distinct groups 110
Figure 5.2.1 – Behavioural paradigm 124
Figure 5.2.2 – Mapping individual hippocampal images into a common anatomical space 125
Figure 5.3.1 – CA3 and EC target different numbers of interneurons across distinct layers of dorsal CA1 130
Figure 5.3.2 – Differential targeting pattern of interneurons by EC and CA3 in ipsi- and contralateral hemisphere 132
Figure 5.3.3 – Soma characteristics suggest targeting of distinct interneuron populations by CA3 and EC in stratum lacunosum 134
Figure 5.3.4 – EC and CA3-targeted interneurons show different axonal projection patterns within dCA1 137
Figure 5.3.5 – Different neurite distribution in ipsi- vs contralaterally targeted interneurons 139

Figure 5.3.6 – Recorded interneuron populations are comparable between CA3 and EC stimulation groups and are not affected by repeated laser stimulation 141
Figure 5.3.7 – Input-specific optical recruitment of superficial interneurons by CA3 and EC 143
Figure 5.3.8 – CA3 and EC recruit superficial interneurons differently along the radial axis of dorsal CA1 145
Figure 5.3.9 – Comparison of baseline spike characteristics shows no difference between interneurons recruited by CA3 or EC terminal stimulation 148
Figure 5.3.10 – Information transfer from CA3 and EC depends on brain state 149
Figure 5.3.11 – Interneuron recruitment by CA3 and EC as a function of stimulation phase 151
Figure 5.4.1 – CA3 and EC may have asymmetric inhibitory control over local CA1 network inputs 155
Figure 6.3.1 – Superficial interneurons do not induce detectible spike reduction in pyramidal neuron population 165
Figure 6.3.2 – Cycle-by-cycle superficial interneuron activity is associated with pyramidal neuron spike timing changes 167
Figure 6.3.3 – Superficial interneurons display layer- and state-specific coactivity structures 169
Figure 7.3.1 – The vast majority of papers published between 1960 and present group the strata lacunosum and moleculare 182
Figure 7.3.2 – Distinct theta-nested gamma profile in stratum lacunosum 184
Figure 7.3.3 – Distinct spike characteristics in stratum lacunosum compared to strata radiatum and moleculare 186

Tables

Table 1.4.1 – Characteristics of canonical hippocampal interneuron types 23
Table 2.2.1 – List of mice used for tetrode depth validation 37
Table 3.2.1 – Overview of mice used for the superficial interneuron dataset 58
Table 4.3.1 – Spike timing characteristics in awake and sleep 94
Table 4.3.2 – Spike characteristics in sharp-wave ripples 104
Table 4.3.3 – Spike characteristics of electrophysiological clusters 107
Table 4.3.4 – Comparative statistics of electrophysiological cluster spike characteristics 108
Table 4.3.4 – Comparative statistics of electrophysiological cluster spike characteristics - continued 109
Table 5.2.1 – Mice used for anatomical and functional mapping experiments 118
Table 5.2.2 – Viruses used for anatomical and functional mapping experiments 118
Table 5.2.3 – Overview of the mice and sections used for anterograde tracing experiment 122
Table 5.3.1 – Comparative statistics of soma shapes between CA1 layers 131
Table 6.3.1 – Pyramidal neuron spike rate change in pre- and post-spike windows 162
Table 6.3.2 – Pyramidal neurons spike timing changes in response to interneuron activity 165
Table 6.3.3 – Correlation coefficients between neuron groups in theta oscillations 168
Table 6.3.4 – Correlation coefficients between neuron groups in sharp-wave ripples 168
Table 6.3.5 – Differences in correlation coefficients between network states across layers 169
Table 7.2.1 – Terms used for PubMed search 178
Table 7.2.2 – Chapters from which data originates 178
Table 7.3.1 – Means and differences between Lacunosum and Raditam+Moleculare interneurons across spike characteristics 184

Abbreviations

AAV	Adeno-Associated Virus
AIS	Axon Initial Segment
AP	Anterior-Posterior
CA	Cornu Ammonis
CB	Calbindin
CCK	Cholecystokinin
ChR2	Channelrhodopsin-2
CI	Confidence Interval
cNOR	continuous Novel Object Recognition
Contra	Contralateral
CSD	Current Source Density
CV	Coefficient of Variation
CV2	Coefficient of Variation 2
DBSCAN	Density-Based Spatial Clustering of Applications with Noise
DG	Dentate Gyrus
DV	Dorsal-Ventral
EC	Entorhinal Cortex
EMD	Empirical Mode Decomposition
eYFP	enhanced Yellow Fluorescent Protein
GABA	Gamma-Aminobutyric Acid
gDG	Granular Layer of the Dentate Gyrus
Grik-4	Glutamate Receptor Ionotropic Kainate 4
IMFs	Intrinsic Mode Functions (related to EMD)
Ipsi	Ipsilateral
ISI	Interspike Interval
ISIn	Interneuron-Specific Interneuron
kNN	k-Nearest Neighbors
Lac	Stratum Lacunosum
LEDs	Light-Emitting Diodes
LFP	Local Field Potential
mDG	Molecular Layer of the Dentate Gyrus
MI	Mutual Information
mid-descen	mid-descending
ML	Medial-Lateral
Mol	Stratum Moleculare
M2R	Muscarinic Acetylcholine Receptor M2
NB	Naive Bayesian
NDNF	Neuron-Derived Neurotrophic Factor
nNOS	Neuronal Nitric Oxide Synthase

NPY	Neuropeptide Y
Or	Stratum Oriens
PB	Phosphate Buffer
PFA	Paraformaldehyde
PIn	Pyramidal Layer Interneuron
PSD	Power Spectral Density
PV	Parvalbumin
Pyr	Stratum Pyramidale
Rad	Stratum Radiatum
SATB1	Special AT-rich Sequence-Binding Protein 1
SST	Somatostatin
STA	Spike-Triggered Average
SWR	Sharp-Wave Ripple
UMAP	Uniform Manifold Approximation and Projection
Vgat	Vesicular GABA Transporter
VIP	Vasoactive Intestinal Peptide
vGlut3	Vesicular Glutamate Transporter 3
YFP	Yellow Fluorescent Protein

Chapter 1. General Introduction

1.1 Introduction

Only when the early microscopists started to investigate nerve tissue and learned how to visualise individual neurons did the unparalleled heterogeneity of brain cells become apparent (Schaffer, 1892; Ramón y Cajal, 1904). Over a century later, our understanding of cells making up the most fascinating organ of the body has dramatically improved (Altimus et al., 2020). We have learned that the brain is made up of neuronal and non-neuronal (glia) cells, and while glia should not be underestimated, it is the neurons that have fed the imagination of scientists, artists, philosophers, and engineers for decades. Neurons, unlike any other cell type, store our experiences, intelligence, and personality; and are likely the key to what makes us human (Konopka et al., 2012; Campagnola et al., 2022; Loomba et al., 2022; Pinson et al., 2022). However, despite a century of study, many questions remain unanswered.

One of the most impactful discoveries was the existence of the counterbalancing neurotransmitters Glutamate and Gamma-Aminobutyric acid (GABA) (Roberts and Frankel, 1950; Florey, 1954), which were initially referred to as Factor E and I. Glutamate and GABA were shown to exert an excitatory and inhibitory effect, respectively, on neural signalling in the peripheral and central nervous system. Although it took almost two decades after its discovery to be accepted as a neurotransmitter rather than merely a metabolite, GABA is now known as one of the most important signalling molecules (Bowery and Smart, 2006; Smart and Stephenson, 2019). The importance of inhibition is evidenced by the wide implications of GABAergic neuron dysfunction in disease aetiology (Marín, 2012; Magloire et al., 2019; Ruden et al., 2021; Hijazi et al., 2023). In less than a century, the field went from visualizing and describing the shape of ‘short axon’ neurons to discovering the pivotal role of GABAergic neurons in health and disease.

In subsequent studies, it became clear that GABA and glutamate were present in morphologically distinct neurons (Freund and Buzsáki, 1996). Most brain regions feature GABAergic neurons, but the cortical structures of the brain have developed the broadest library of types (Freund and Buzsáki, 1996; Jonas and Buzsáki, 2007; Ascoli et al., 2008; Pelkey et al., 2017; Booker and Vida, 2018; Fishell and Kepecs, 2020). The hippocampus, a brain region critically involved in learning, memory, and spatial navigation, houses a wide variety of interneurons (Freund and Buzsáki, 1996; Klausberger and Somogyi, 2008; Booker and Vida, 2018). This large variety of neurons is thought to exponentially increase the computational power of neuronal circuits by modulating neuronal activity level, timing, and gain (Ferrante et al., 2009; Roux and Buzsáki, 2015; Fishell and Kepecs, 2020), and it is not unthinkable that the encoding, storage, and retrieval of information is dependent on precisely timed, well-orchestrated neuronal activity conducted by inhibition (Tzilivaki et al., 2023). That GABAergic neurons are vital to hippocampal functioning is evidenced by their implication in a wide range of neurological and psychiatric disorders, such as epilepsy, dementia, and schizophrenia (Marín, 2012; Magloire et al., 2019; Ruden et al., 2021; Hijazi et al., 2023). Although our knowledge is rapidly evolving, we still have a lot of ground to cover in our understanding of interneurons and their function in the hippocampal circuitry.

1.2 Organisation of the hippocampus

When examining interneuron functioning in dorsal CA1, it is important to understand the anatomical environment in which these neurons live. The hippocampus consists of four subregions the dentate gyrus and cornis ammonis (CA) 1, 2, and 3 (Freund and Buzsáki, 1996; David and Pierre, 2006; van Strien et al., 2009). Here, I briefly summarize the anatomical organisation of the hippocampus, focussing on CA1 as the centre of the anatomical framework.

CA1 is considered the hippocampus's output region. The entorhinal cortex is a major afferent source and forms a strong information loop with the hippocampus. Entorhinal cortex information can reach CA1 through two different routes (van Strien et al., 2009): First, following the trisynaptic (or indirect) pathway, information is transferred from layer 2 entorhinal cortex principal neurons to the granule cells in the dentate gyrus and, from there, passed on to CA3, which in turn projects

to CA1. Second, in the direct pathway, layer 3 principal neurons of the entorhinal cortex directly project to CA1 pyramidale neurons (Kajiwara et al., 2008; van Strien et al., 2009). Then, CA1 neurons feedback to the entorhinal cortex through direct projections and via the subiculum (Roy et al., 2017), which closes the hippocampal-cortical loop. Together, these pathways form two major inputs to CA1, one through CA3 and the other one directly from the entorhinal cortex.

The CA1 consists of multiple layers, discriminated based on differences in cell densities, cell-body shapes, and the presence of fibres or substances such as myelin (Schaffer, 1892; Ramón y Cajal, 1904; Kajiwara et al., 2008). Following modern nomenclature, CA1 comprises the following layers, listed from the corpus callosum towards the dentate gyrus: the strata alveus, oriens, pyramidale, radiatum, lacunosum-moleculare (David and Pierre, 2006; Kajiwara et al., 2008; van Strien et al., 2009) (but see **Chapter 7**). Notably, in the rodent brain, the strata radiatum, lacunosum, and moleculare are paradoxically referred to as superficial, despite being most ventral to the pyramidale on the coronal axis, due to inversion of CA1 during development (Schaffer, 1892; Ramón y Cajal, 1904; Takács et al., 2012; Urbán and Guillemot, 2014). Furthermore, different CA1 layers house different subdomains of pyramidal neurons, the principal cells of CA1, as well as distinct afferents. While interneurons are scattered across the layers, pyramidal neuron somata form a densely packed sheet restricted to the stratum pyramidale (Freund and Buzsáki, 1996). Pyramidal neuron neurites cover the remaining layers, with their basal dendrites and axons stretching into the stratum oriens, the apical dendrite reaching into the stratum radiatum, and the apical tuft fanning out in the strata lacunosum and moleculare. Besides these layers harbouring different pyramidal neuron subdomains, they also house distinct afferents (Kajiwara et al., 2008; van Strien et al., 2009). CA3 projections arrive in CA1 in the strata oriens and radiatum, while the inputs originating from the entorhinal cortex are confined to the strata lacunosum and moleculare. Together, the layers of CA1 reflect a well-structured architecture, organising the arrival of distinct inputs on separate pyramidal neuron dendritic domains.

Overall, the hippocampus is a highly organized structure, characterized by a segregated, largely unidirectional afferent system, distinct layers, and a spatially organized neuron population. This

well-organised architecture is important to understand CA1 superficial interneurons as part of a larger network.

1.3 Rhythms in the hippocampus

Electrical and chemical currents form the foundation of neuronal communication (Buzsáki et al., 2012). Summation of these currents across the neuronal population can generate potentials large enough to be recorded in the extracellular space, and such electrical fluctuations are referred to as local field potentials (LFPs) (Buzsáki et al., 2012). Due to the alignment of hippocampal pyramidal neurons and their major inputs, similarly timed network activity is concentrated in space and leads to well-discernible LFP patterns (Buzsáki et al., 2012). These LFP patterns can reflect discrete events or form rhythmic patterns that occur in chains or bursts (van de Ven et al., 2016; Lopes-dos-Santos et al., 2018; McHugh et al., 2024), which are thought to reflect different neuronal operations (Colgin, 2016). The hippocampus features several oscillations which operate within different frequency bands, such as theta (4-12 Hz), gamma (25-150 Hz), and ripples (100-250 Hz). These oscillations have been extensively reviewed (Buzsáki, 2002, 2015; Buzsáki and Wang, 2012; Colgin, 2016), and I will only give a brief overview here.

In rodents, theta is one of the slower yet powerful oscillations, which dominates the hippocampal LFP during locomotion (Buzsáki, 2002). While theta oscillations can be recorded across all layers of dorsal CA1, its phase changes as a function of depth, with a nearly complete phase reversal at the hippocampal fissure compared to the stratum pyramidale (Buzsáki, 2002). Gamma oscillations occupy a faster frequency band than theta and can be divided further into slow (25-40), mid (50-90), and fast (100-150) gamma (Lopes-dos-Santos et al., 2018). During locomotion, gamma oscillations occur as theta-nested bursts, which prefer different theta phases depending on the gamma type (Lopes-dos-Santos et al., 2023). Slow and fast-gamma oscillations occur in different subspaces along the radial axis of dorsal CA1, while a mid-gamma oscillation is found along the full axis (Lopes-dos-Santos et al., 2023). Lastly, sharp-wave ripples comprise two components (Buzsáki, 2015). The ripples are fast oscillations that ride on top of slower prominent LFP events called sharp-waves. Sharp-wave ripples occur during sleep and immobility (Buzsáki,

1986). Despite changing their shape as a function of depth, the sharp-wave can be identified across all layers of CA1, while the ripples only occur in the stratum pyramidale (Lopes-dos-Santos et al., 2023). Together, distinct oscillations are characterised by specific frequencies and are differentially distributed across the radial axis of dorsal CA1.

Based on the variations in frequency and location, it has been suggested that distinct oscillations reflect activation of specific network motifs and underly different brain functions (Colgin, 2015, 2016). Although some suggest theta frequency activity is supported by local (inter)neurons (Chapman and Lacaille, 1999a; Capogna, 2011), CA1 theta rhythms are paced by oscillators in the medial septum (Buzsáki, 2002; Nuñez and Buño, 2021). These external pacers are thought to support interregional communication by aligning neuron activity across different intra and extrahippocampal regions (Colgin, 2016). The origin of slow and mid-gamma in CA1 is not fully understood, but several reports suggest that these rhythms are generated outside CA1 (Bragin et al., 1995; Colgin, 2016; Fernandez-Ruiz et al., 2023). The spatial segregation of these oscillations and their links with distinct input regions have led to the idea that these oscillations may facilitate input-specific communication with CA1, and possibly distinct network operations such as learning and memory (Carr and Frank, 2012; Colgin, 2015, 2016). Conversely, fast-gamma and ripples, the fastest oscillations, are thought to arise from recurrent connections between local excitatory and/or inhibitory neurons (Bartos et al., 2007; Buzsáki and Wang, 2012; Gan et al., 2017). Despite these circuits not being completely unravelled, the extracellular registration of oscillations provides an opportunity for circuit interrogation without needing access to its components. Thus, oscillations with different frequencies likely have distinct underlying local or interregional networks and provide network access without needing to obtain single-cell information.

Overall, distinct oscillations can be recorded in the brain's extracellular space, with a broad variety of oscillatory patterns particularly prominent in the hippocampus. These oscillations, characterized by specific frequency bands, occur in different subspaces along CA1's radial axis, suggesting they are driven by distinct local or interregional networks that likely support unique network functions. Together, these oscillations are informative on ongoing network activity and permit network interrogation without recording single cells.

1.4 The interneurons in the hippocampus

The hippocampus houses a plethora of interneurons and, in contrast to pyramidale neurons, interneurons are found across all layers. Despite the lack of a consensus on how to classify interneurons, in the hippocampus, distinct types are mostly distinguished based on axonal morphology, combined with molecular expression patterns, and electrophysiological characteristics (see **Table 1.4.1**). The classification and descriptions of hippocampal interneuron types have been extensively reviewed over the past decades (Freund and Buzsáki, 1996; Somogyi and Klausberger, 2005; Klausberger and Somogyi, 2008; Klausberger, 2009; Pelkey et al., 2017; Booker and Vida, 2018; Tzilivaki et al., 2023). Therefore, I will only briefly recapitulate the major classes and the interneuron types they comprise.

In general, three major groups of interneurons are identified based on their post-synaptic targets: the pyramidal neuron peri-somatic region, pyramidal neuron dendrites, and other interneurons (Somogyi and Klausberger, 2005; Chamberland and Topolnik, 2012). These interneuron groups are often further divided based on molecular expression patterns (see **Table 1.4.1**) (Somogyi and Klausberger, 2005; Pelkey et al., 2017; Booker and Vida, 2018). First, peri-somatic targeting interneurons comprise three interneuron types. Two of these types are referred to as basket cells and comprise Parvalbumin (PV) and Cholecystokinin (CCK) positive neurons. Both these types tightly wrap their axons around the pyramidal cell somata, hence their name 'basket' cells. The third type are axo-axonic cells (also known as chandelier cells), a highly specialized interneuron type specifically targeting pyramidal neuron AIS – the action potential initiation zone of neurons (Somogyi and Klausberger, 2005; Jiang et al., 2015). By strategically targeting pyramidal neurons at the major integration and action potential initiation sites, these neurons can directly control pyramidal neurons output.

Secondly, most interneuron types in the hippocampus target pyramidal neuron dendrites (Klausberger, 2009). Interneurons within the dendrite targeting group are distinguished based on the dendritic domain they target and the expression of molecular markers (see **Table 1.4.1**), comprising of Oriens-Lacunosum-Moleculare interneurons, Bistratified interneurons, Ivy cells, Schaffer

Morphology															Main Molecular Markers	Electrophysiology						References
Type	Soma Location	Soma Location				Dendrites				Axon					Soma Shape	Postsynaptic Target		FR in Theta	Mean Theta Phase	Mean Theta Phase (degrees; trough=0)	SWR Engagement	FR in SWR	Spike Pattern	
		O	P	R	LM	O	P	R	LM	O	P	R	LM	DG									
AAC	Pyr	+	++	+		+	++	+	+	++	++					axon initial segment pyramidal neurons	PV+, SATB1-	17	Peak	185	biphasic (on-off)		fast-spiking	Somogyi et al., 1983; Viney et al., 2013; Dudok et al., 2021; Pelkey et al., 2017; Booker and Vida, 2018
Basket Cell PV	Or, Pyr, Rad	+	++	+		++	++	++			++					peri-somatic region, local interneurons	PV+, SATB1+	21	Late descending	271/289	active	122	fast-spiking	Pawelzik et al., 2002; Klausberger et al., 2003; Lapray et al., 2012; Tukker et al., 2013
Basket Cell CCK	Pyr, Rad		++	+		+		++	+	+	++	+				peri-somatic region	CCK+, vGlut3+	12	Late ascending	163	non-modulating	4	regular spiking, accomodating	Acsády et al., 1996; Pawelzik et al., 2002; Somogyi et al., 2004; Pelkey et al., 2017; Booker and Vida, 2018
Basket Cell CCK	Pyr, Rad	+	+	++		+		++	+	+	++	+				peri-somatic region	CCK+, VIP+	7	Late ascending	186	non-modulating	1.5	regular spiking, accomodating	Mátyás et al., 2004; Booker et al., 2016)
OLM	Or	++	+			++				+			++		horizontally oriented	pyramidal neuron dendritic tuft, and local interneurons	SST+	4.9/19	early ascending	341/15	inactive	0.2/12	Regular spiking, adapting	Klausberger et al., 2003; Maccaferri and Lacaille, 2003; Katona et al., 2014; Pelkey et al., 2017; Booker and Vida, 2018
PPA	Rad, LM border			++	++			++	++				++	+		Pyramidal neuron trunk	CCK+	5.8	Ascending	100	non-modulating	1.5	regular spiking, adapting, accomodating	Vida et al., 1998; Pawelzik et al., 2002; Klausberger, 2005; Booker et al., 2016; Pelkey et al., 2017; Booker and Vida, 2018
SCA	Rad, LM border	+	+	++	++	+		++	+	++	+	++				Oblique dendrites	CCK+, CB+, CB1R+	8.6	Late ascending	156	non-modulating	0.3	regular, accomodating	Hájos and Mody, 1997; Vida et al., 1998; Booker et al., 2016; Pelkey et al., 2017; Booker and Vida, 2018
Neurogliaform	LM			+	++			+	++			+	++	+	small round	shaft and spines	nNOS or/and NPY	6/7.4	Peak/Early descending	200	non-modulating	2.3/3.4	delayed weakly accomodating, barrage firing	Vida et al., 1998; Price, 2005; Fuentealba et al., 2010; Pelkey et al., 2017; Booker and Vida, 2018; Sakala et al., 2022;
Ivy	Pyr, Rad	+	++				+			++	++	++	+				nNos and NPY	2.8	Early ascending	46	non-modulating	5.2	delayed, stuttering, accomodating	Fuentealba et al., 2008; Lapray et al., 2012; Pelkey et al., 2017; Booker and Vida, 2018
Bistratified	Or, Pyr, Rad	+	++	+		+	+	+		++	+	++				Pyramidal neuron oblique and basal dendrites, PV- interneurons	PV+, SST+	36	Trough	16	active	107	Regular spiking, adapting	Klausberger et al., 2004; Katona et al., 2014; Pelkey et al., 2017; Booker and Vida, 2018; Chamberland et al., 2023
ISIn-I		+	+	+		+	+	+				++			small round	CB+, CR+ interneuron, but not PV+ interneurons	CR+, VIP-	higher then immobility						Acsády et al., 1996; Chamberland and Topolnik, 2012; Pelkey et al., 2017; Booker and Vida, 2018; Geiller et al., 2020;
ISIn-II				+	++				++			++			vertically oriented	CR+, CCK+, CB+, with preference for VIP+/CCK+ co-expressing interneurons	VIP+, CR-, CCK-, M2R-	higher then immobility						Acsády et al., 1996; Chamberland and Topolnik, 2012; Pelkey et al., 2017; Booker and Vida, 2018; Geiller et al., 2020;
ISIn-III			+	+		+	+	+	+	++					vertically oriented	OLM and CB+ neurons in OR, (PPA, SCA)	nNos+, CR+, VIP+	higher then immobility	Peak (estimation)		inactive (estimation)		irregular and regularly spiking adapting phenotypes	Acsády et al., 1996; Chamberland and Topolnik, 2012; Tyan et al., 2014; Pelkey et al., 2017; Booker and Vida, 2018; Geiller et al., 2020; Luo et al., 2020; Bilash et al., 2023

Table 1.4.1 – Characteristics of canonical hippocampal interneuron types

collateral associated, Perforant path associated neurons, and Neurogliaform cells (Klausberger, 2009). In most cases, these interneurons, restrict their axon to one or multiple hippocampal layers, and the domains they target often coincide with distinct input sources (Klausberger, 2009; Booker and Vida, 2018). By targeting distinct pyramidal dendrite subdomains and input termination sites, these interneurons can control input-specific dendritic integration (Leão et al., 2012; Lovett-Barron et al., 2012; Bilash et al., 2023). Additionally, differential targeting pattern allows these interneurons to bias pyramidal neurons to specific inputs and are well-positioned to regulate plasticity (Price, 2005; Royer et al., 2012; Palacios-Filardo et al., 2021). Thus, dendrite targeting interneurons are best positioned to control pyramidal neuron inputs.

Lastly, interneuron-specific interneurons target primarily other interneurons. This group comprises interneuron-specific interneuron (ISIn) types 1, 2, and 3, which are distinguished based on anatomical appearance and molecular expression patterns (Chamberland and Topolnik, 2012; Booker and Vida, 2018). Besides specifically targeting interneurons, ISIn seem to prefer dendrite-targeting interneuron types (Chamberland and Topolnik, 2012; Pelkey et al., 2017), as ISIn types 1 and 2 have been suggested to avoid PV-positive interneurons (Gulyás et al., 1996; Pelkey et al., 2017). However, compared to the peri-somatic and dendrite targeting groups, ISIn are less-well studied, particularly in the functional domain. Nevertheless, by directly targeting other interneurons, these neurons are ideally situated to reduce domain-specific inhibition and disinhibit pyramidal neurons.

Together, interneuron classification in the hippocampus is mostly focused on the axonal targeting pattern. By targeting differential pyramidal neuron subdomains, distinct interneuron types can regulate integration and action potential generation separately. Furthermore, overlap between the interneuron type axonal plexus and different afferents onto pyramidal neuron dendrites could support input selection or inhibit domain- and input-specific plasticity, while interneurons specifically targeting interneurons can create windows in which these input-shifts and plasticity are permitted. Overall, these strategically positioned axon terminals of varying interneuron types allow tight regulation of information processing in the hippocampus.

1.5 The function of inhibition

Interneurons play a key role in brain functioning (Markram et al., 2004; Bartos et al., 2007; Klausberger and Somogyi, 2008; Fishell and Kepecs, 2020). Upon the discovery of inhibition, it was interpreted as just a counteracting mechanism to excitation (Bowery and Smart, 2006). However, decades of interneuron research revealed that inhibition, particularly in the central nervous system, is much more. Recent comparative studies have shown that particularly inhibitory neurons differentiate humans and primates from lower-order species such as mice (Krienen et al., 2020; Loomba et al., 2022), suggesting that inhibition may play a key role in the expansion of the brain's computational power. In addition, brain regions executing complex computations, such as the neocortex and the hippocampus, have developed a wide library of different interneuron types (Somogyi and Klausberger, 2005; Ascoli et al., 2008; Jiang et al., 2015). Such increased interneuron repertoire, with different types performing distinct roles, provides flexibility to structurally fixed neuronal networks (McKenzie, 2018; Cardin, 2019). However, how interneurons support network functioning is still under investigation. Assessment of interneuron function can focus on two things: understanding in what context interneurons get recruited or how their activity affects their targets (Kepecs and Fishell, 2014). The first will be dictated by afferents and brain states, while the second is constrained by the efferent connectivity of the neuron. In this section, I will discuss three common interneuron recruitment motifs found across the brain and explore how interneurons can affect their post-synaptic partners.

1.5.1 Inhibitory recruitment motifs

Interneuron function is dependent on afferent connectivity, and different interneuron recruitment motifs have been described (Roux and Buzsáki, 2015). The first motif is feed-forward inhibition, which is characterised by a shared excitatory input projecting to the interneuron and principal neurons (pyramidal neurons in the hippocampus), and the interneuron projecting onto the pyramidal neuron. The classical model of signal transduction within this motif states that the interneuron and pyramidal neuron get both excited by their shared input and that, due to the synaptic delay, the inhibitory signal arrives at the pyramidal neuron shortly after the excitatory signal (Buzsáki, 1984). Therefore, this motif would restrain the pyramidal neuron's response window in time.

However, due to specialised features of the interneurons, such as simple dendrites and unique ion channel expression, signal conduction and thus synapic delays could be reduced to a minimum, which in some cases results in inhibitory signalling arriving on the pyramidal neurons before the excitatory input (Roux and Buzsáki, 2015). These observations have led to the idea that feed-forward inhibition can restrain pyramidal neuron response windows in both immediate past and future, sharpening of pyramidal neuron response curves. Thus, feedforward inhibition may be an important motif to improve the signal-to-noise ratio in neuronal networks.

Secondly, inhibition can follow a feedback motif. This motif relies on local pyramidal neurons driving interneuron activity and, in turn, interneurons inhibiting the local pyramidal neurons (Bartos et al., 2007; Buzsáki and Wang, 2012; Roux and Buzsáki, 2015). Strictly, feedback inhibition refers to a recurrent type of inhibition, in which the active pyramidal neuron and the activated interneuron are interconnected, exciting and inhibiting each other, respectively (Csicsvari et al., 1998). However, another type of feedback inhibition has been recognised, in which the activated interneuron does not target the activating pyramidal neuron but neighbouring neurons instead. This form of feedback inhibition is referred to as lateral inhibition (McKenzie, 2018; McKenzie et al., 2021). The direct feedback through interneurons driven by local excitatory neurons has been thought to function as rate stabilising motif (Roux and Buzsáki, 2015). Thus, feedback inhibition may play a vital role in rate control in neuronal networks.

The last motif seen throughout the brain is disinhibition (Roux and Buzsáki, 2015). In contrast to the two motifs described above, disinhibition does not involve specific recruitment but is characterised by the blockage of it (Chamberland and Topolnik, 2012). The disinhibitory motive involves a chain of two interneurons and a pyramidal neuron. The first interneuron is activated and inhibits the second interneuron, which leads to a reduction of inhibitory inputs on the pyramidal neuron. In other words, the pyramidal neurons are released from its inhibition through the inhibition of interneurons. The flexible recruitment of interneurons targeting interneurons involved in other motifs allows neuronal networks to temporarily change information flow (Guet-McCreight et al., 2020). Thus, disinhibition could temporarily lift stabilizing motifs such as feed-forward and feed-back inhibition to support flexibility in neuronal networks.

Most of these motifs are attributed to specific interneuron types. However, they are not mutually exclusive, and the same interneuron could provide multiple forms of inhibition depending on their presynaptic partners. Fast-spiking neurons (mostly PV-positive basket cells) have been shown to provide feedforward and feedback inhibition (Hu et al., 2014). Additionally, the dendrite targeting SST-positive interneurons mostly receive inputs from local pyramidal interneurons leading to feedback inhibition, but facilitating responses to repetitive Schaffer collateral stimulation suggests they can provide feedforward inhibition as well (Chamberland et al., 2024). Both these example interneuron types reside in the deep layers of CA1. Conversely, most superficial interneurons are less likely to provide feedback inhibition, especially those not extending their dendrites into the stratum oriens, as pyramidal neuron axons travel through this layer and do not ascend towards the superficial layers (Amaral et al., 1991). Together, depending on the efferent and afferent connectivity of interneurons, they can be involved in multiple network motifs.

1.5.2 Results of inhibition on post-synaptic neurons

Besides connectivity motifs, the function of interneurons is dependent on the effect they have on their postsynaptic target (Kepecs and Fishell, 2014). In contrast to excitatory transmission, where the postsynaptic response often heavily depends on the postsynaptic expression of receptors, inhibitory postsynaptic potential dynamics are often dependent on the presynaptic interneurons (Campagnola et al., 2022). Due to the large variety of interneurons, the specific post-synaptic targets, and the differential activation timing, interneurons can have various effects on the postsynaptic neuron and the larger network (Bartos et al., 2007; Roux and Buzsáki, 2015; Fishell and Kepecs, 2020). Inhibitory effect on the postsynaptic neurons can directly involve neuronal output, such as a spike reduction or a change in spike timing, interfere with inputs through shunting of excitatory inputs, compartmentalisation within the postsynaptic dendrite, or changes in input summations (Jadi et al., 2012; Lovett-Barron et al., 2012; Palmer et al., 2012a; Royer et al., 2012). Together, due to the large variety of interneurons, the effect of inhibition can take many forms and shapes.

The most tangible and intuitive results of inhibition are the change in spike number or timing of the postsynaptic neurons. In particular, peri-somatic targeting neurons have been shown to robustly

reduce spike output of postsynaptic neurons. Large-scale electrophysiology recording studies have shown that, at a single cell level, such strong inhibitory connections can be visualised between cell pairs (Csicsvari et al., 1998; English et al., 2017; Petersen et al., 2021). At the network level, the removal of peri-somatic inhibition, often through the silencing of PV-positive interneurons, leads to a global increase of pyramidal neuron activity (Royer et al., 2012). Conversely, optogenetic interneuron activation effectively reduces pyramidal neuron spiking, which is so powerful that this approach has been used as a tool to silence specific brain regions (Zutshi et al., 2022). Additionally, directional connectivity between interneurons and pyramidal neurons leads to 'lateral' inhibition, which is thought to play an important role in assembly selection and size (Lee et al., 2014; Morrison et al., 2016). Furthermore, inhibition plays an important role in spike timing. For example, in the hippocampus silencing of PV- and CCK-positive interneurons, and pan-neuronal silencing have been shown to shift the preferred spike phase of pyramidal neurons and disrupt place cell phase-precession in theta oscillations, respectively (Royer et al., 2012; Valero et al., 2022; Rangel Guerrero et al., 2024). Lastly, interneurons have been implicated in the generation of oscillatory activity. By rhythmically inhibiting their postsynaptic targets, interneurons are proposed to underly oscillatory patterns within and between cortical and subcortical regions (Bartos et al., 2007; Cardin et al., 2009; Sohal et al., 2009; Viney et al., 2013; Gan et al., 2017; Noguchi et al., 2022). Together, interneuron activity is a key regulator of population activity levels, assembly selection and size, and spike timing through direct inhibitory control.

A second important but more subtle mechanism through which interneurons regulate network activity often involves regulations of the input-output transformation of the postsynaptic neuron (Milstein et al., 2015; Bilash et al., 2023). In pyramidal neurons, the complex dendritic tree allows for complex and compartmentalised computations (Spruston, 2008; Palmer et al., 2012a). In particular, dendrite-targeting interneurons, strategically positioning inhibitory synapses on their postsynaptic targets have been shown to switch dendritic states, which either permit or block generation of dendritic spikes (Lovett-Barron et al., 2012; Royer et al., 2012; Bilash et al., 2023). These states are strongly correlated with synaptic plasticity and learning. In addition, interneuron engagement constraints supralinear input summation in pyramidal neuron dendrites

(Lovett-Barron et al., 2012; Milstein et al., 2015). Furthermore, inhibition can compartmentalise excitatory inputs to specific locations on the dendrite and decouple apical dendrite and somatic activity (Lovett-Barron et al., 2012; Aime et al., 2022). Such soma-dendritic decoupling is suggested to allow dendritic computations without disrupting or changing the neuron's output. Lastly, dendritic inhibition can selectively bias their postsynaptic partner to particular inputs. In the hippocampus, layer-specific inhibition has been shown to shunt entorhinal cortex-specific excitatory activity and bias pyramidal neurons to CA3 inputs or decouple pyramidal neurons from entorhinal cortex-imposed rhythms (Leão et al., 2012; Sakalar et al., 2022). Together, inhibition, and in particular dendritically targeted inhibition, plays a key role in input-output transformation, input selection, dendritic integration, and plasticity.

In summary, interneurons play a crucial and multifaceted role in shaping hippocampal network dynamics through both direct modulation of postsynaptic spiking and more subtle regulation of dendritic processing. By controlling spike timing, assembly selection, and the input/output function, peri-somatic and dendritic targeting interneurons not only regulate immediate neuronal responses but also influence processes such as synaptic plasticity and learning. Overall, interneurons are pivotal in maintaining neural and network function, making them key players in both normal brain function and potential targets in neurological disorders.

1.6 Studying the superficial interneurons of the hippocampus

As described above, many different types of interneurons reside in the hippocampus. Over one-third of these interneurons are found in the superficial layers: strata radiatum, lacunosum, and moleculare. When focussing on interneuron types, nearly 70% are housed by the strata radiatum, lacunosum/moleculare, and 20% are exclusively found in these superficial layers (Bezaire and Soltesz, 2013). Despite their abundance, these superficial interneurons are less well-studied compared to their deep counterparts, such as parvalbumin- and somatostatin-positive interneurons which are elaborately investigated (Hu et al., 2014; Urban-Ciecko and Barth, 2016). These differences mostly originate from the identifiability and accessibility of these deep interneurons compared to the superficial interneurons. Electrophysiologically, fast-spiking interneurons are

relatively easy to discriminate from pyramidal neurons, and expression of distinct ion channels resulting in differential spike waveform shapes facilitates classification even further, especially for PV-positive interneurons (Földy et al., 2016). Additionally, due to the development of highly specific molecular targeting strategies for PV and SST-positive types, which are lacking for superficial neurons, studies have been directed mostly to the deep interneuron types (Hippenmeyer et al., 2005; Taniguchi et al., 2011). Furthermore, due to the inversion of CA1 and the lack of easily identifiable layer-specific electrophysiological landmarks beyond the stratum pyramidale, superficial interneurons are harder to access than deep interneurons (see **Chapter 2**). Together, these limitations have led to a gap between the study of superficial compared to deep interneurons in the intact hippocampal CA1.

Superficial interneurons have mostly been studied using *ex vivo* techniques or single-cell approaches such as juxta-cellular recordings with *post hoc* morphological and chemical examination (Somogyi and Klausberger, 2005). Morphological interrogation has shown that superficial interneurons comprise a diverse population and mostly target pyramidal neuron dendrites and interneurons, but peri-somatic targeting superficial interneurons have also been described (Somogyi and Klausberger, 2005; Pelkey et al., 2017; Booker and Vida, 2018). Additionally, *ex vivo* whole-cell recordings suggest that superficial interneurons have distinct spike characteristics, and activation of these interneurons results in inhibitory currents in the postsynaptic pyramidal neurons as well as interneurons (Vida et al., 1998; Bertrand and Lacaille, 2001; Price, 2005). Since superficial interneurons are embedded in the input layers of CA1 and activation of distinct afferent fibre bundles results in the recruitment of these neurons, combined with the paucity of recurrent connections from local pyramidale neurons, superficial interneurons are hypothesised to provide feed-forward inhibition (Capogna, 2011). Indeed such motives have been identified and have been shown to operate at distinct temporal scales (Basu et al., 2016; Bilash et al., 2023). Furthermore, *in vivo* juxta cellular recordings have revealed that distinct morphologically defined types display differential coupling to network events such as theta oscillations and sharp-wave ripples (Klausberger and Somogyi, 2008). Together, *ex vivo* and single-cell approaches have been important tools in the identification and description of superficial interneurons.

To advance our understanding of hippocampal functioning and the role of superficial interneurons,

they should be studied under behaviourally relevant circumstances in conjunction with their intact network, rather than in isolation. However, technical limitations interfere with such studies. Although juxta cellular recording can be performed in awake freely-moving animals (Lapray et al., 2012; Katona et al., 2014), most studies involving superficial interneurons published to date were conducted in anaesthetised head-fixed rodents (Klausberger et al., 2003, 2004; Klausberger, 2005; Jinno et al., 2007), constraining our understanding of superficial interneuron function in behaviour. Additionally, in most juxta-cellular recording studies only one cell is registered at the time, leading to only a handful of reported neurons and prohibiting studying the relationship between interneurons and other neurons. Due to the low sample size and reported inter-neuron variability it remains unclear whether these reports are truly representative of the population (Katona et al., 2014). Recent calcium studies have attempted to overcome these limitations and successfully combined pan-interneuron calcium imaging, while mice perform a behavioural task, with *post hoc* molecular identification (Geiller et al., 2020). Although these recording were performed in head-fixed mice, they allowed examination of simultaneously recorded neurons in different behavioural conditions. However, the interneuron-specific expression of calcium indicators does not permit coregistration of pyramidal neurons, and these indicators' temporal dynamics are not fast enough to resolve neuronal activity at the short timescales of most hippocampal oscillations (Zhang et al., 2023). Thus, simultaneously recording from multiple superficial interneurons at high temporal resolution in conjunction with CA1 pyramidal neurons is challenging due to technical limitations, but necessary to gain a better understanding of their role in hippocampal functioning.

Overall, superficial interneurons have been suggested to play an important role in the CA1 network through feed-forward inhibition and input selection. However, these hypotheses are often driven by *ex vivo* experiments. *In vivo* experiments, on the other hand, have mostly been focused on the description of individual interneurons due to the limited accessibility and identifiability of superficial interneurons. Thus, to advance our understanding of superficial interneurons it is essential to employ recording techniques that can register multiple neurons simultaneously, during ongoing behaviour, at temporal resolutions fine enough to relate interneuron activity to local network events.

1.7 In this Thesis

From its first discovery in simple circuits, such as those in the spinal cord, to the most complex computations performed by the human brain, inhibition has proved to be vital to a well-functioning brain. Despite rapid expansion of our knowledge on how inhibitory neurons are involved in network functioning in health and disease, a full grasp of the function of individual interneuron types remains out of reach. Interneuron types that are harder to access based on the regions or layers they reside in or the lack of precise molecular targeting strategies, remain poorly studied *in vivo*. In dorsal CA1 of the hippocampus, these 'understudied' neurons comprise a group mostly located in the superficial layers: strata radiatum and lacunosum/moleculare. However, given their positioning, superficial interneurons are likely candidates to regulate incoming information to dorsal CA1, making them key players in the hippocampal network functioning, but only a very few papers have attempted to understand the activity patterns and function of superficial interneurons in relation to their local network and behaviour. Together, due to the lack of bespoke targeting strategies for superficial interneurons and the limited number of reports on their function – beyond merely being thought of as CA1 gatekeepers – their exact role in the hippocampal network remains unclear.

In this Thesis, I aimed to examine the spiking characteristics of superficial interneurons in relation local network events as well as neuron-to-neuron interactions. To do so, I validated a layer-specific tetrode targeting method to estimate the recording depth of individual neurons (**Chapter 2**). Additionally, this method revealed that the stratum lacunosum can be electrophysiologically discriminated from the stratum radiatum and moleculare. In **Chapter 3**, I examined spike characteristics along the radial axis of dorsal CA1 and implemented quality control measures applicable to all layers. Furthermore, I showed that distinct spike waveforms occupy different spaces along the radial axis. To gain insights in the function of superficial interneurons, I examined spiking patterns and engagement in local network events, which revealed that superficial interneurons display distinctive spiking behaviour across different CA1 layers (**Chapter 4**). Such distinctive, spatially distributed behaviour prompted the question of whether differential recruitment by CA1's major input sources could underly these differences. In **Chapter 5**, I

examine the anatomical and functional connectivity between CA3 and entorhinal cortex to CA1 interneurons, which revealed input-specific interneuron engagement across different CA1 layers. Furthermore, I examined the relationships between superficial interneurons and pyramidal neurons, the output neurons of CA1, by capturing the coactivity between pyramidal neurons and superficial interneurons as well as interneurons amongst each other in **Chapter 6**. These analyses revealed that superficial interneurons do not provide direct, detectible inhibition onto pyramidal neurons population but affect their spike timing. Finally, throughout these Chapters, the image emerged that stratum lacunosum displays distinct characteristics at a neuronal as well as network level. In **Chapter 7**, I re-examined the data presented in previous Chapters and found evidence supporting the idea that stratum lacunosum is a unique superficial layer. In **Chapter 8**, I conclude by discussing my findings in a broader context, aiming to extend our current understanding of CA1 superficial interneurons, and suggesting directions for future research.

Chapter 2. Distinct CA1 layers feature unique LFP signatures suitable for tetrode depth estimation

2.1 Introduction

Determining recording electrode depth is crucial to record from distinct hippocampal layers and has been traditionally estimated using LFP-based information. The laminar organisation of CA1 and its distinct inputs generate a unique network activity across the dorsoventral axis (Buzsáki et al., 1986; Buzsáki, 2002). The spatial separation and distinct timing of CA1 inputs onto the pyramidal neuron dendrites generate discernible LFP profiles, which can be employed as electrophysiological landmarks along CA1's radial axis often revealed by current source density (CSD) analysis (Buzsáki et al., 1986; Buzsáki, 2002; Lopes-dos-Santos et al., 2018, 2023; Zutshi et al., 2022). During sleep and immobility, CA1 displays distinct network events referred to as sharp-wave ripples. The sharp-waves are discrete LFP events characterised by a large amplitude negative deflection in the stratum radiatum and a positive deflection in the adjacent strata pyramidale and lacunosum/moleculare (Buzsáki, 1986, 2015). The ripple is a fast (100-250 Hz) oscillation riding on top of the sharp-wave and only detectible in the pyramidal layer. When taken together, the shape of the sharp-wave and presence of a ripple can inform the recording depth of the electrode. In addition, relative changes seen in theta (4-12 Hz) oscillation, most prominent during awake exploration, can be informative to infer recording depth (Buzsáki et al., 1986; Buzsáki, 2002). Theta oscillation power and phase change gradually along the radial axis, with the maximum theta power and a near complete phase reversal at the hippocampal fissure compared to the stratum pyramidale (Buzsáki et al., 1986). Together, cross-referencing these LFP-based, state-dependent 'landmarks' could inform recording depth estimation *in vivo*.

Recording depth in the hippocampus is often estimated using linear probes, leveraging the fixed electrode spacing combined with known relative LFP changes along the radial axis of dorsal CA1 (Buzsáki et al., 1986). However, the perpendicular orientation relative to the horizontally aligned hippocampal layers and the thin probe design limits the simultaneous recording of large numbers of hippocampal neurons (Steinmetz et al., 2018; Guardamagna et al., 2022). Multi-tetrode microdrives allow independent positioning of multiple tetrodes on a horizontal plane, maximizing sampling long the layers' plane. However, the lack of multiple vertically aligned recording sites makes precise and reliable recording depth estimation challenging. Therefore, combining tetrode recordings with a depth estimation approach would provide a powerful tool to access superficial interneurons while retaining the ability to record multiple neurons simultaneously across layers.

In this Chapter, I explore whether depth estimation can be combined with tetrode recordings through LFP-guided tetrode positioning in dorsal CA1 using a previously developed linear probe-based LFP template (Lopes-dos-Santos et al., 2023). Utilizing raw LFP signals rather than CSD analysis, combined with the highly reproducible landmarks between mice, makes this approach highly suitable for tetrode recordings in freely behaving mice (Buzsáki et al., 1986; Lopes-dos-Santos et al., 2023). By mapping LFP profiles obtained through tetrode recordings onto the linear probe-based template, I predicted the recording depth of individual tetrodes and was able to reconstruct LFP changes across depths similar to those seen in linear probes. I confirmed correct depth estimation by assessing both layer-specific gamma oscillations as well as *post hoc* histological examination of the tetrode tips. Lastly, I show that this technique permits the precise targeting of the stratum lacunosum. Together, the precise depth estimation of individual tetrodes shows the cross-platform potential of LFP-based depth estimation and permits access to nearly all layers of dorsal CA1 at a high temporal and spatial resolution.

2.2 Methods

2.2.1 Animals

These experiments were conducted across 8 4-7 months old male mice in a C57BL/6 background (**Table 2.2.1**). Implanted mice were group-housed until the surgical procedure. All mice had access

to food and water ad libitum, chew sticks, and nesting material and were held in individually ventilated cages on a 12/12h light/dark cycle (lights on at 07:00), 19–23°C ambient temperature and 40–70% humidity. All experimental procedures performed in this study followed the Animals (Scientific Procedures) Act, 1986 (United Kingdom) and underwent ethical review by the Animals in Science Regulation Unit of the UK Home Office.

Mouse line	RRID	Number of mice	Genotype
C57BL/6	IMSR_JAX:000664	1	
Vglut2-Cre	IMSR_JAX:028863	3	Heterozygote
Vglut2-Cre;DAT-Flp	IMSR_JAX:028863; IMSR_JAX:035436	1	Heterozygote for both constructs
PV-cre	IMSR_JAX:017320	2	Heterozygote
VIP-cre	IMSR_JAX:010908	1	Heterozygote

Table 2.2.1 – List of mice used for tetrode depth validation

2.2.2 Custom microdrives

All tetrode recordings were performed with custom-made microdrives as described by van de Ven et al., 2016. In short, the plastic casing was custom-designed. The casing holds 28 pins that carry one plastic shuttle per pair. All shuttles are attached to a screw allowing its independent movement along the pins. Tetrodes were made by twisting four insulated tungsten wires (12 µm diameter, California Fine Wire) together and briefly heating them to generate a single bundle. Each tetrode was loaded in one of the metal cannulas attached to the shuttles. If optic fibres were used, they were loaded into the drive and glued to the casing, fixing the position of the optic fibres. The ground was made from a 50 μm tungsten wire and fed through the casing along with the tetrodes. Tetrodes wires as well as the ground wires were secured using gold pins. Finally, the adaptors are inserted into the gold pins and glued.

2.2.3 Surgical procedure

For micro-drive implantation, mice were anaesthetised using isoflurane (induction at 4% and maintained at 0.5–2%) in O_2 (2L/min) and received peri-surgical analgesia using Vetergesic (0.1 mg/kg s.c.) systemically and Marcaine (<8 mg/kg) locally. The scalp was opened and the skull was thoroughly cleaned, after which four anchoring screws (M1) were implanted, one on each side halfway between the eye and coronal suture and two over the cerebellum, the latter two also served as ground. Then, the screws were covered in bone cement (Refobacin® Bone Cement R,

Zimmer Biomet) forming the foundation of the implant. In addition, multiple small craniotomies were made over dorsal CA1 to accommodate the tetrodes (microdrives: spanning -1.9 to -2.5mm posterior and ±0.9 to ±1.66 mm lateral from Bregma, respectively. Some mice included in the depth estimation experiment had tetrodes implanted across multiple brain regions, which were not used for this specific experiment. The 14-tetrode micro-drive or silicon probe was implanted utilising a stereotactic frame. After tetrodes entered the brain, the probe/drive was lowered with a speed of ~100-200 μm per minute. The exposed tetrodes parts were covered in wax to ensure independent movement during the recordings. The wax and bottom of the drive were covered in dental cement to fix the drive to the skull and screws. If optic fibres were implanted along the tetrodes, the dental cement was covered in black nail polish. Daily post-surgical monitoring was performed for 4-7 subsequent days after the surgery. Animals were allowed to recover for at least 7 days before undergoing cable habituation. Correct tetrode positioning was confirmed by the electrophysiological profile of the local field potentials (see tetrode profiling) and *post hoc* histology visualizing probe/tetrode tracks.

2.2.4 Recording procedure

After a one-week recovery, mice were daily habituated to the experimenter and a microfibre 'handling cloth' of which one was specifically assigned to one mouse. The mice were gradually habituated to manual fixation of the drive while being held in the cloth to give the experimenter access to the drive for safe (un)tethering of the mice later during the experiment. Furthermore, mice were familiarized with the experimental setup and recording environments such as the open field (either a square box ~48x48 cm or a circular environment ~46 cm diameter) and the sleep box (a 15x15 cm box filled with the mouse's home cage bedding used to record sleep sessions). For the recordings in this Chapter, mice were placed in the sleep box and recording was started after sleep initiation, then a 5 to 10-minute recording was made during slow-wave sleep, after which 5-10 additional minutes were recorded while the mouse explored the open field. This was repeated interleaved with tetrode depth assessment (see **section 2.2.6**).

2.2.5 Silicon probe data

Silicon probe data used in this Chapter was obtained from a published dataset available in the Dupret laboratory (Lopes-dos-Santos et al., 2023). In short, probes were implanted at (AP -2.0 mm posterior and +1.7mm lateral from Bregma). After a one-week recovery period mice were similarly habituated to the setup manual fixation, and the recording environments as described for the tetrode recordings (see **section 2.2.4**). After appropriate habituation, the probe was gradually lowered along the dorsoventral axis till the most dorsal probe was positioned in the pyramidal layer, which was identified by the presence of sharp-wave ripple events. Then, unlike the tetrode recordings, the probe remained in position across multiple recording days. Recordings were performed during awake exploration sessions and sleep sessions similar to those described in recording procedure (see s**ection 2.2.4**).

2.2.6 Tetrode data acquisition

2.2.6.1 Multichannel data acquisition and position tracking

The extracellular signals from the electrodes were amplified, multiplexed, and digitized using a single integrated circuit (RHD2164, Intan Technologies; http://intantech.com/products_RHD2000.html) in the head stage connected to the implanted microdrive during recording. The amplified and filtered (pass band 0.09 Hz to 7.60 kHz) electrophysiological signals were digitized at 20 kHz and saved to a disk along with the synchronization signals (transistor-transistor logic digital pulses) from the position tracking. The location of the animal was tracked using three differently coloured LEDs attached to the head stage and captured at 39 Hz by an overhead colour camera (https://github.com/kevin-allen/positrack/wiki).

2.2.7 Signal processing and analysis

All electrophysiological signal processing and depth estimation were performed using custom code available in the Dupret laboratory and described in (Lopes-dos-Santos et al., 2023), of which a brief description can be found below:

2.2.7.1 Software

Data were analysed in Python 3.10 using the following packages: Numpy v1.24.3, Pandas v1.5.3, Scipy v1.11.2, Matplotlib v3.7.1, and Seaborn v0.21.2. Images were analysed using ImageJ v2.1.0/1.53f51.

2.2.7.2 Signal preprocessing

For all LFP analyses, the initial 20 kHz signal was pre-processed by applying an anti-aliasing filter (8th-order Chebyshev type I filter) and then down-sampled to 1,250Hz using the decimate function from the signal submodule of Scipy.

2.2.7.3 SWR detection

The down-sampled LFP signal was filtered for the ripple band (80-250 Hz) alongside a high-frequency control (200-500 Hz) for sharp-wave ripple detection. Hilbert transform was used to compute the instantaneous envelope and phases. Candidate ripples were selected when the signal surpassed a 5-times median value. Each candidate event underwent a series of checks: (1) The ripple band power (derived from squaring the mean ripple amplitude) in the detection channel should exceed twice the magnitude obtained for the reference channel. This confirms that the detected events in the differential signal had a stronger presence in the detection channel; (2) The mean frequency of the event should surpass 100 Hz; (3) The event must comprise a minimum of 4 complete ripple cycles; (4) The power in the ripple band should be at least double compared to the control high-frequency band.

2.2.7.4 Theta detection

For theta oscillations detection to guide tetrode placement in the recording room, the data was filtered using a 4th-order Butterworth filter between 4 and 18 Hz, with zero-phase filtering via the scipy.singal.filtfilt function to prevent phase distortion. Individual theta cycles were then detected as described by Lopes dos Santos et al. (Lopes-dos-Santos et al., 2018). To delineate individual theta cycles, we identified the local maxima (peaks) and minima (troughs) of the theta-filtered signal that surpassed the amplitude of a delta component extracted from the same raw LFP using a

similar filter with a 0.5 to 4 Hz band. Each peak-trough-peak sequence was considered a candidate theta cycle. Valid cycles had peak-trough and trough-peak intervals of 31-100 ms (corresponding to 16-4 Hz) and peak-to-peak intervals of 71-200 ms (14-5 Hz).

To detect theta for the depth estimation manifold, masked Empirical Mode Decomposition (EMD) was employed to isolate theta oscillations from the filtered LFP (Lopes-dos-Santos et al., 2018). Six Intrinsic Mode Functions (IMFs) and a residue were computed, with IMF-6 capturing theta oscillations. The residual LFP, not captured by the first six IMFs, served as the lower frequency component, with its envelope setting the amplitude threshold for peaks and troughs. Individual theta cycles were then identified as previously described. Six control points were determined for each cycle, allowing for the computation of the instantaneous theta phase through linear interpolation.

2.2.7.5 Supra-theta phase-frequency spectrograms

To identify theta-nested oscillations, spectrograms of supra-theta range frequencies were computed and triggered averages aligned to the mid-descending phase of pyramidale theta generated for all tetrodes. Spectrograms were produced utilizing the complex Morlet Wavelet Transform method. This analysis involved choosing 24 logarithmically spaced frequencies ranging from 18 Hz to 310 Hz unless otherwise specified. Each wavelet kernel underwent L1 normalization, which adjusts the sum of the absolute values of the elements in a vector to equal 1. This normalization ensures that the wavelet maintains consistent amplitude levels across individual frequency components, preventing any amplification or attenuation.

2.2.8 Tetrode depth estimation

2.2.8.1 Online tetrode positioning along the radial axis of dorsal CA1

In this validation dataset, tetrodes were positioned based on averaged LFP signals aligned to a putative pyramidal layer channel. After the recordings had concluded, these signals were mapped onto a 2D depth estimation embedding (see **section 2.2.8.2**). At the start of the experiment, the tetrodes reach into the pyramidal layer and are lowered in ~30-60 μm steps interleaved with

short recordings to estimate the tetrode depth till they have reached the intended layer. First, 5-10 minutes of sleep was recorded in the sleep box after which mice were transferred to an open field to record 5-10 minutes of awake exploration. Then, SWR and theta were detected for an 'alignment reference' tetrode in the pyramidal layer (see **section 2.2.7**). If multiple tetrodes were positioned in the pyramidal layer, the tetrode with the largest mean ripple envelope amplitude was selected as the alignment reference. After detecting these LFP-based events for the alignment tetrode, two complementary profiles were computed for all available tetrodes in dorsal CA1 using the down-sampled LFP traces: (1) the sharp-wave ripple-triggered profile, which was constructed by averaging the raw LFP aligned to ripple amplitude peak; (2) the theta profile, which was constructed by averaging the raw LFP aligned by the mid-descending theta phase of stratum pyramidale theta of pyramidal layer theta. These LFP event-based triggered averages were used to infer the recording layer based on LFP landmarks described for linear probe recordings (Lopes-dos-Santos et al., 2023). Pyramidale tetrodes were targeted to a profile containing a sharp-wave with a clear ripple riding on it. Radiatum tetrodes were targeted to a profile comprising a negative sharp-wave without a ripple, and a ~25-ms theta-phase advancement in relation to the pyramidal layer. Lacunosum-Moleculare tetrodes were targeted to a positive sharp-wave during ripples and near-complete phase reversal (~55 ms) of theta relative to the pyramidal layer.

2.2.8.2 Offline tetrode depth estimation

The LFP feature manifold (LFP-guided depth estimation) presented in Lopes-dos-Santos et al. 2023 was used to estimate tetrode recording depth. In short, this manifold was built utilising LFP-triggered averages of SWR and theta waveforms obtained from linear probe recordings across the full extent of the radial axis of dorsal CA1 (Pyramidal layer to granular layer of the dentate gyrus). These waveforms represent the average raw LFP signals for each of these individual channels, centred around either the ripple power peaks or the mid-descending phase of theta (see also 2.2.8.1). The length of these triggered averages was 500 ms for sharp-waves and 150 ms for theta. To focus on waveform shape rather than amplitude, every waveform was z-scored individually. Then, the first four principal components were extracted for both the theta as well as the SWR waveforms. Using these principal component projections, the manifold was then

computed employing the Isomap method from the manifold submodule of sklearn (version 1.3; with parameters n_neighbors = 15 and n_components = 2). Subsequently, to employ the manifold as a depth estimation tool, the 2D manifold was linearized to represent every position along the manifold by a single depth estimation value. The anatomical layer centre coordinates of different linear probe recordings (n=6 mice) were projected into the manifold by selecting electrodes representing putative layers (incl. pyramidale, radiatum, lacunosum-moleculare, and hippocampal fissure) based on LFP-derived landmarks. Lastly, layer borders were defined as those values corresponding to the 2.5th – 97.5th percentile of a Gaussian fit to the data points corresponding to a particular layer (Pyramidale: -20, 30; Radiatum: 30, 55; Lacunosum-Moleculare: 75, 105).

2.2.9 Histology

2.2.9.1 Tissue processing and imaging

After completion of the electrophysiological recordings, mice were anaesthetized with pentobarbital and transcardially perfused with 4% PFA (150 ml, 8 – 10 ml/min). Subsequently, the heads with implanted tetrode microdrives were post-fixed overnight at 4 ˚C. The next day, the implanted microdrives were removed and the brains were resected followed by post-fixation in 4% PFA for 2 hours. Then brains were either sectioned at 50 micrometres on a vibratome (VT1000S; Leica Microsystems, Wetzlar, Germany) or embedded in gelatine and cryoprotected to be sectioned on a freezing microtome (Epredia HM 450 with a Physitemp BFS-40MPA freezing stage). For embedding, brains were first incubated overnight in 10% sucrose 0.1M Phosphate Buffer solution at 4 ˚C. Then embedded in gelatine (12% gelatine / 10% sucrose), stored in 30% sucrose 0.1M PB overnight at 4 ˚C for cryoprotection, and sectioned the following day utilizing the freezing sliding microtome (Stedehouder et al., 2018). Sections were stained with 4',6-diamidino-2-phenylindole (DAPI; 0.5 µg/ml, Sigma-Aldrich, cat# D8417) diluted 1:1000 in PB to label cell nuclei, mounted, and cover-slipped with Vectashield mounting medium. Images were acquired using a Zeiss LSM 880 confocal microscope equipped with Plan-Apochromat 10x/0.45, 20x/0.8 objectives. DAPI and an empty channel were imaged using excitation wavelengths of 405, and either 458 or 633 nm.

2.2.9.2 Image analysis

Tetrode tracks were identified in the tissue and the section with the deepest part of the track was used to measure the tetrode recording depth to the anatomical layers. In case two tetrodes were lowered to the superficial layers, I matched the tetrodes to the electrophysiological profiles based on the anatomical tetrode layout and the physical location of the tetrode in the tissue. For these experiments, maximally two tetrodes were lowered per hemisphere to guarantee correct tetrode identification. Hippocampal layers were defined based on DAPI signal density and tetrode depth was measured using the measurement tool in ImageJ.

2.3 Results

2.3.1 Layer-specific network patterns allow recording depth estimation

To record from superficial interneurons using tetrodes, we developed a strategy to navigate the stratum radiatum and lacunosum-moleculare of CA1. Distinct CA1 layers can be distinguished using two specific network patterns: theta (5-12 Hz) oscillations during exploration and sharp-wave ripples (SWRs; 100 – 250 Hz) during sleep (Buzsáki, 1986, 2002). First, I assessed whether the described electrophysiological landmarks for distinct CA1 layers, present in a linear probe-based dataset already available in the Dupret laboratory, would be suitable for recording depth estimation (Lopes-dos-Santos et al., 2023). The available recordings used various LFP-based landmarks to electrophysiologically identify the strata pyramidale, radiatum, lacunosum-moleculare, and the hippocampal fissure in the dorsal hippocampus. In these linear probe recordings, the stratum pyramidale was defined as the channel with the strongest sharp-wave ripple peak power; the mid-radiatum channel based on the strongest sink during sharp waves; and the hippocampal fissure based on the maximum theta power (**Figure 2.3.1b-g**) (Lopes-dos-Santos et al., 2023). Although distinct lacunosum-moleculare LFP profiles have not been specifically described, the middle of the stratum lacunosum-moleculare was inferred to be the channel 40-50 μm dorsal from the hippocampal fissure, defined by the maximum theta power, based on a mouse brain atlas (**Figure 2.1e-g**) (Paxinos and Franklin, 2019). On average, I found that the putative radiatum channel was located at ~180 μm (range:150 - 240 μm; 95%CI:158 – 205 μm, n=6 mice), the lacunosum-moleculare ~355 μm (range: 300 – 400 μm; 95%CI:327 – 387μm), and the hippocampal fissure

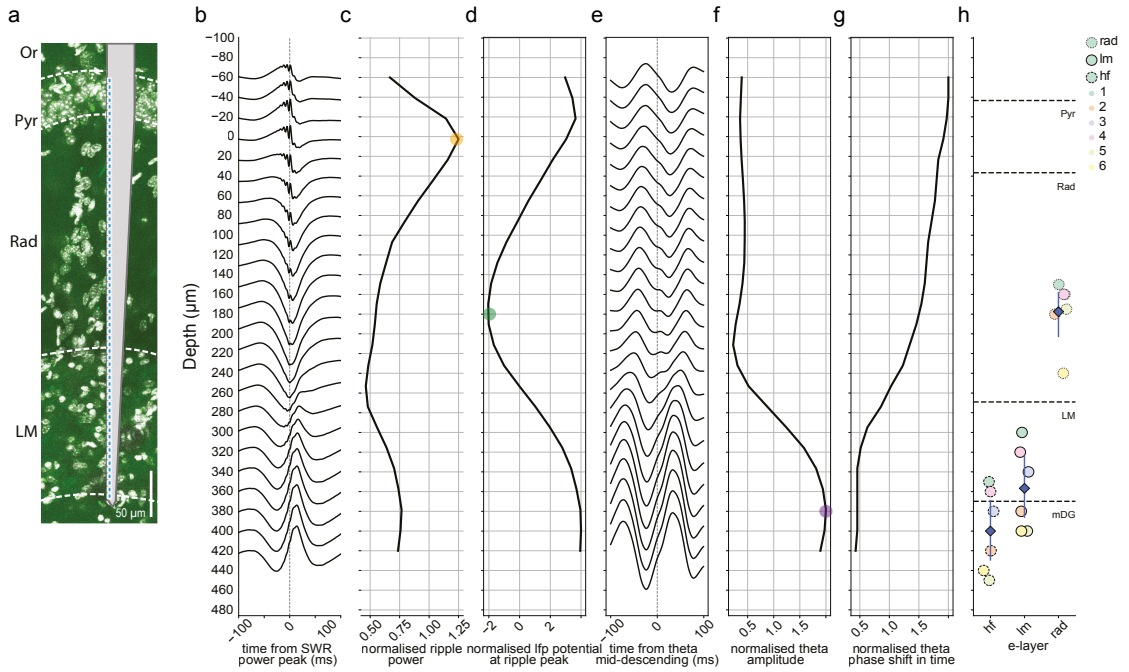


Figure 2.3.1 – Electrophysiological landmarks of distinct anatomical layers of dorsal CA1

a) Microscopy image of silicon probe track through dorsal CA1. White dashed lines indicate the layer borders. Schematic representation of the silicon probe overlayed alongside the track, scalebar 50 μm. **b**) Representative example from one mouse of ripple-triggered LFP average for all channels along the silicon probe aligned to the ripple power peaks of the channel with the maximum ripple power. **c**) Normalised ripple power across all recording channels in **a**. Note that the pyramidale channel is defined by the electrode with the maximum power. **d**) Normalised LFP amplitude for all channels in **a**. Note that the electrode with the largest negative amplitude is defined to be the centre of the stratum radiatum. **e**) Representative example from one mouse of theta-triggered LFP for all channels along the silicon probe aligned to the mid-descending phase of theta of the stratum pyramidale electrode. Note the strong amplitude increase in the bottom half of the plot. **f**) Normalised LFP amplitude for the waveforms in **d**. The electrode with the highest amplitude is allocated to the hippocampal fissure. **g**) The theta phase-shift to the pyramidale tetrode for all electrodes. Note the near-complete phase shift at the hippocampal fissure. **h**) Scatter plot representing the distance between the putative layers along the silicon probe for 6 mice mapped into an anatomical space based on the reference atlas. Note that the group means fall within the electrophysiologically defined layers. Colours represent individual mice. The marker outline indicates the putative layer along the radial axis: dotted represents Rad electrodes, solid the LM, and dashed the hippocampal fissure. Diamonds represent group means, error bars the 95%CI of the mean. Or: Oriens, Pyr: Pyramidale, Rad: Radiatum, LM: Lacunosum-Moleculare, mDG: Molecular Layer of the Dentate Gyrus.

at ~400 μm (range: 350 - 450 μm; 95%CI:372 – 432 μm) from the pyramidale channel measured along the linear probe (**Figure 2.3.1h**). Unfortunately, histological information was not available for all mice, prohibiting direct comparison between the electrode distance and the subjects' anatomy. Instead, the electrode distances were mapped onto the mouse brain reference atlas as a proxy for the expected anatomical distances between the layers (Paxinos and Franklin, 2019). This analysis revealed that the electrophysiological defined landmarks matched anatomy: The means for strata radiatum and lacunosum falling within the corresponding anatomical layers and the electrophysiologically defined hippocampal fissure only ~30 μm dorsal from the anatomical

fissure (**Figure 2.3.1h**). Together, I confirmed that earlier described correlations between LFP-based landmarks correspond to the proposed anatomical layers in our dorsal CA1 silicon probe-based dataset. This underscores that unique network patterns along the radial axis of dorsal CA1 can be used in layer-targeted recordings and make this a suitable dataset for a tetrode depth estimation template.

2.3.2 LFP-guided recording depth estimation is transferable across different recording platforms

After showing that the electrophysiological landmarks align with anatomy, I tested whether the linear probe-based template (referred to as depth estimation trajectory) developed in the Dupret laboratory was applicable to tetrodes (Lopes-dos-Santos et al., 2023). The trajectory was built based on the mean relative changes in theta and SWR events along the linear probe, aligned to the stratum pyramidale, in a linearized, lower dimensional space (**Figure 2.3.2a-d**, see **Methods**). First, tetrodes were manually positioned within the pyramidale, radiatum, and lacunosum-moleculare of dorsal CA1 by visually matching of the recorded LFPs to earlier described LFP signatures across 8 mice (maximum of 2 tetrodes per hemisphere; **Figure 2.3.2c**; see **Methods**). Interestingly, while lowering some tetrodes from the radiatum to putative lacunosum-moleculare, I observed a fourth pattern of mixed features that could only be observed across a small distance. This pattern showed a mild theta phase advancement compared to radiatum (~5 ms; ~30 ms to pyramidale theta) but displayed positive deflection at the ascending part at ~25-50 ms from the ripple power peak time. Furthermore, from this point onward the theta amplitude increased considerably. To verify the precise position of this intermediate pattern's occurrence, some tetrodes were specifically targeted to this profile in addition to the other putative layers. After all tetrodes reached the desired electrophysiological profile, the obtained LFP information was mapped onto the depth estimation trajectory, revealing that the manual LFP-guided tetrode targeting of predetermined layers aligned with the putative layers' positions in the trajectory (**Figure 2.3.2d**). In addition, without the depth estimation trajectory receiving any depth information, the transition pattern was predicted between the putative radiatum and moleculare on the depth trajectory (**Figure 2.3.2d, e**). Furthermore, to test whether the depth estimation trajectory recapitulated the

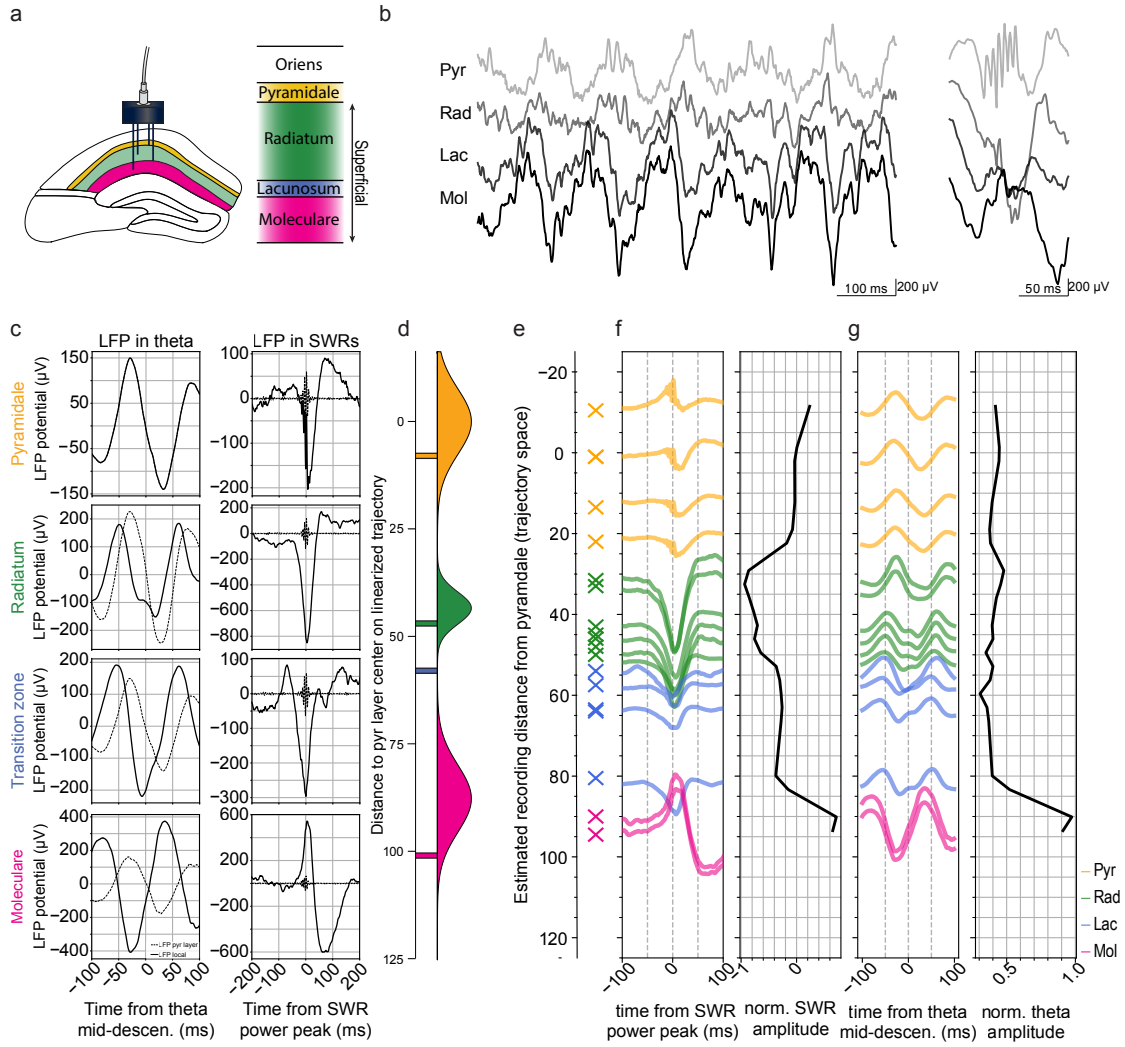


Figure 2.3.2 – LFP-guided tetrode depth estimation

a) Schematic of layer-specific tetrode targeting. Tetrodes are positioned across different layers of dorsal CA1. **b**) Simultaneously recorded, representative example of raw LFP-traces during awake exploration (left) and sharp-wave ripple during sleep (right) for a mouse with tetrodes positioned across different depths along the radial axis of dorsal CA1; scale bars 100 ms for theta and 50 ms for SWR, 200 μV. **c**) Representative examples of theta and sharp-wave ripple triggered LFP averages for tetrodes across different regions of dorsal CA1 recorded in different mice. Left: Theta triggered LFP average aligned to pyramidale theta. The solid lines indicate the locally recorded LFP, while the dashed line represents the triggered averaged of the LFP recorded in the putative pyramidale tetrode. Note the gradual phase advancement across the layers compared to the pyramidale tetrode. Right: SWR-triggered LFP average across tetrodes positioned in different regions along the radial axis of dorsal CA1. Solid lines represent locally recorded LFP, the dashed line the ripple-band filter LFP from the pyramidale tetrode. Note the change of the waveform shape across the layers compare to the pyramidale. **d**) Linearized trajectory space used to predict recording depth. The coloured bars indicate the estimated depths the four examples from **c**), colour-coding indicated the putative recording layer (pyramidale: yellow, radiatum: green, lacunosum-moleculare: magenta). The gaussians indicate the layers, note that the 'intermediate' tetrode (blue) falls in between the gaussians representing the radiatum and lacunosum moleculare. **e**) Depth estimation for all tetrodes included in this validation dataset targeted to specific domains (pyramidale: yellow, radiatum: green, transition: blue, lacunosum-moleculare: magenta). Note that the tetrodes targeted to the same domain cluster in the depth trajectory. **f**) Left: SWR triggered average LFP waveforms plotted at the corresponding depth for tetrodes represented in **e**). Colours indicate the putative layer. Right: The normalised LFP amplitude as a function of depth. Note that the most negative values around the radiatum-targeted tetrodes. **g**) Left: Theta triggered average LFP waveforms plotted at the corresponding depth for tetrodes represented in **e**) plotted at the corresponding depths. Right: normalised theta amplitude as a function of recording depth. Note the increasing amplitude as a function of depth. Pyr: Pyramidale, Rad: Radiatum, Lac: Lacunosum, Mol: Moleculare.

depth-dependent changes in the linear probes, I computed LFP amplitude for the mean theta and SWR waveforms across the estimated tetrode depths (**Figure 2.3.2e-g**). Although the depth estimation has no access to the LFP amplitudes to predict recording depth, the evolution of the amplitudes across the tetrodes resembles that of the linear probe, further underscoring the correct organisation of SWR and theta waveforms as a function of depth. Together, this shows that known LFP landmarks recorded in tetrodes map well on the linear probe-based trajectory, indicating the transferability of this approach across recording platforms; particularly tetrodes.

2.3.3 Cross-validation shows reliable LFP-guided tetrode recording depth estimation

To further validate layer assignment, I examined the presence of layer-specific gamma oscillations and performed *post hoc* histological assessment of the tetrode tracks (**Figure 2.3.3**). Earlier work from our laboratory and others has shown that different types of theta-nested gamma oscillations can be found across different CA1 layers (Colgin et al., 2009; Lopes-dos-Santos et al., 2023). To test our layer assignment, first I assessed the presence of three distinct theta-nested gammas (slow-gamma: 25-45 Hz between 140-220 degrees in theta, mid-gamma: 60-90 Hz between 15-90 degrees in theta, and fast-gamma: 100-130 Hz between 160-200 degrees in theta) in tetrodes assigned to the different layers (Lopes-dos-Santos et al., 2023). I found that, in line with earlier findings, radiatum and some intermediate tetrodes show a prominent theta-nested slow-gamma component, while moleculare neurons display a strong mid-gamma component. Unexpectedly, a superficial fast-gamma described in a previous study appeared to be primarily present in the intermediate tetrodes (Lopes-dos-Santos et al., 2023). Secondly, I performed a *post hoc* histological assessment of the tetrode tracks to validate the electrophysiologically estimated layer assignment. Examination of the tetrode tip positions confirmed that nearly all tetrodes were found in the electrophysiologically predicted layer (17/19, 89%; **Figure 2.3.3d, e**). Remarkably, tetrode tips targeted to the intermediate profile were found to be in the cell-rich upper part of the stratum lacunosum-moleculare, which has historically been described as an independent layer: the stratum lacunosum (Schaffer, 1892; Ramón y Cajal, 1904; Booker et al., 2016) (**Figure 2.3.3d, e**; see **Chapter 7**). Collectively, these analyses show that layer assignment through the depth estimation

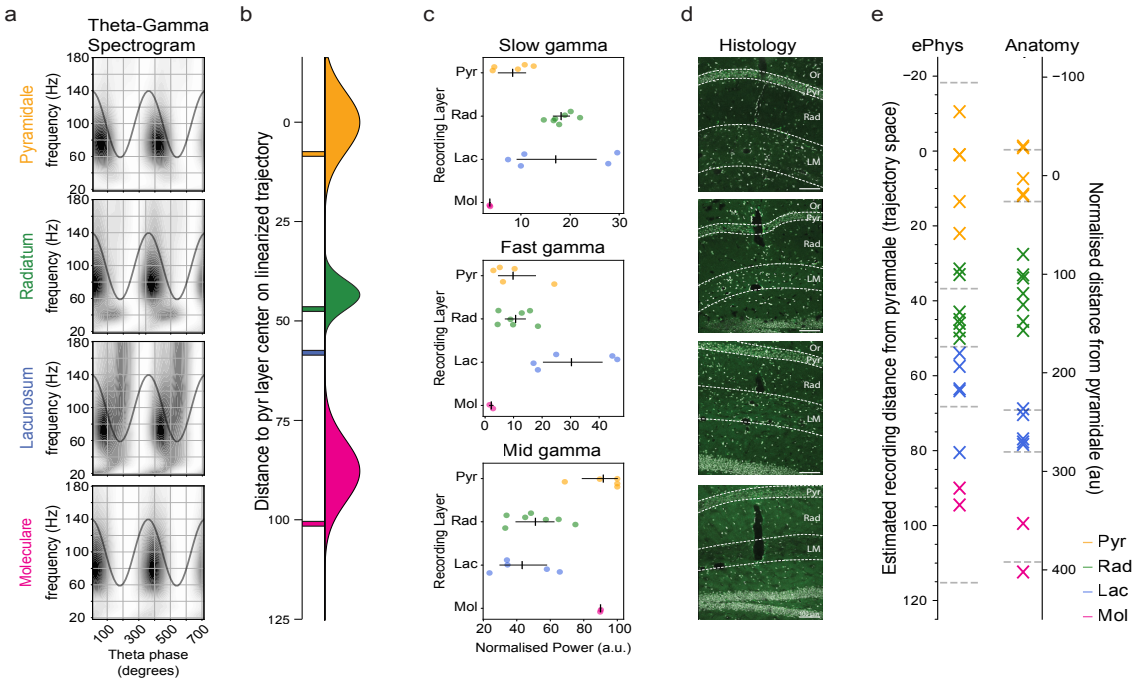


Figure 2.3.3 – Cross-validation shows valid LFP-guided layer assignment

a) Theta triggered spectrogram displaying supra-theta oscillations as a function of theta phase for the example tetrodes shown in **Figure 2.3.2c**. Data have been duplicated to show two theta cycles for illustration purposes. **b**) Depth estimation for the examples shown in **a**) projected in the trajectory space. **c**) Normalised gamma power for slow-gamma, mid-gamma, and superficial fast-gamma for all tetrodes across the four layers. Data points represent tetrodes, colour-coded based on estimated recording layer. Vertical black ticks represent group means and vertical lines the 95% CI of the mean. (Mean, 95% CI for slow gamma window: Pyr 6.33, 1.72 - 10.93; Rad 13.05, 8.44 - 17.28; Lac 15.28, 7.17 - 23.39; Mol 2.13, 2.06 - 2.19; fast gamma window: Pyr 8.04, 3.14 - 14.86; Rad 5.44, 3.79 - 7.01; Lac 28.87, 18.30 - 39.44; Mol 0.63, 0.00 - 1.26; mid gamma window: Pyr 91.37, 78.27 - 100.00; Rad 47.76, 36.06 - 59.92; Lac 42.04, 29.24 - 56.43; Mol 89.83, 89.63 - 90.04). **d**) Representative microscopy images of tetrode tracks corresponding to the example tetrodes are shown in **Figure 2.3.2c** and panel **a**). Scale bar 100 μm. **e**) Left: Scatter showing the estimated recording depth for all tetrodes. Right: The corresponding depths in normalised distance from the pyramidale in normalised anatomical space. Pyr: Pyramidale, Rad: Radiatum, Lac: Lacunosum, Mol: Moleculare.

trajectory is valid based on layer-specific theta-nested gamma oscillation as well as histological confirmation. Unexpectedly, it revealed that the stratum lacunosum features a distinct gamma oscillation, allowing it to be electrophysiologically distinguished from the strata radiatum and moleculare in the depth estimation trajectory.

2.4 Discussion

LFP-guided recording depth estimation is widely employed when interrogating layered structures such as the hippocampus and the cortex (Buzsáki et al., 1986; Lopes-dos-Santos et al., 2018, 2023; Senzai et al., 2019; Zutshi et al., 2022). Depth estimation, however, primarily relies on relative LFP changes captured through equally spaced electrodes, such as CSD analysis performed on

linear probe data. Conversely, tetrodes do not permit such analysis due to the lack of vertically aligned, equally-spaced recording sites, which makes recording depth estimation challenging. In this Chapter, I validated the LFP-based depth estimation trajectory in predicting tetrode recording depth. Accurate recording depth estimation was demonstrated by assessing independent layer-specific network events and histological examination. This recording approach revealed the ability to specifically target the 60 to 80 μm thick stratum lacunosum (Ramón y Cajal, 1904; Kitamura et al., 2014; Booker et al., 2016), underscoring its precision. Together, this work validates using the depth estimation trajectory for predicting tetrode recording depth across the radial axis of dorsal CA1.

The unique network connectivity and activity patterns across the hippocampal layers result in distinguishable local field potentials, which are grossly conserved across species (**Figure 2.3.1**) (Buzsáki, 1986; Ulyanova et al., 2018; Lopes-dos-Santos et al., 2023). By mapping the electrophysiologically defined layers along the linear probe onto an anatomical framework, I confirmed that the putative layers match the anatomical ones. However, although the means fell between the layer borders, some individual distances between layers along the probe were bigger than those in the anatomical space, which could result from several factors. First, this could be due to anatomical variation between the record mice and the reference atlas used. Second, when mapping the electrode distance onto the reference atlas, the linear probe is assumed to be aligned with the coronal orientation of the atlas. However, misalignment is likely, and such angular differences between probe and anatomical framework can artificially overestimate the distance between recorded layers. A similar overestimation can be introduced if only electrode distance is used to determine the recording layer *in vivo* rather than LFP-guided methods. Although not directly tested here for the linear probes, the tetrode data suggests that LFP-guided estimation could overcome errors introduced by anatomical variation as well as surgical procedure, and provide a more accurate depth estimation. Together, this data shows that LFP-based templates such as the depth estimation trajectory are valuable to all kinds of electrophysiological recording techniques without being limited by equally spaced recording sites.

In **section 2.3.2**, I reconstructed depth-related LFP changes along dorsal CA1 by mapping individual tetrode recordings across different mice onto the linear probe-based depth trajectory normally obtained with linear probes (**Figure 2.3.2**). The effectiveness of the tetrode depth estimation trajectory is highly dependent on the consistency of LFP relative to depth, which was evidenced by transferability of LFP patterns across mice, as the trajectory was acquired from and applied to different mice. Furthermore, LFP changes must be consistent along the medial-lateral axis of the hippocampus for cross-recording platform applicability because the trajectory is constructed using vertically spaced electrodes along a single probe, whereas tetrode positions extend across both vertical and horizontal planes. While tetrode-depth estimation works within the outlines of our tetrode positions, the depth estimation accuracy may decline with increasing distance from the original linear probe position (Schomburg et al., 2014). Differences in network connectivity and structural variation across multiple hippocampal axes can contribute to changes in LFP patterns (van Strien et al., 2009; Masurkar et al., 2017), potentially leading to estimation errors. Additionally, this trajectory was developed and designed for dorsal CA1 of mice with a C57BL/6 background. Given that network connectivity and activity patterns are not identical, it is unclear whether this specific template is directly transferable between different species (Strange et al., 2014). Nevertheless, the general approach is likely applicable to any species and other brain regions once a species or region-specific template has been generated. Thus, demonstrating the effectiveness of electrophysiologically derived trajectories lays a solid foundation for future implementation across different recording platforms.

Earlier work has shown that, besides distinct theta and SWR-related LFP patterns, different theta-nested gamma oscillations (25-150 Hz) are present along the radial axis of dorsal CA1 (Colgin et al., 2009; Lopes-dos-Santos et al., 2023). Here, I leveraged these layer-specific gammas – not used for LFP-guided depth estimation – to validate the layer assignment. Consistent with literature, I found that tetrodes assigned to strata radiatum and moleculare display stronger slow and mid-gamma oscillations compared to other layers, respectively. Interestingly, the recently described theta-nested superficial fast-gamma (~120 Hz) was consistently present in the tetrodes histologically confirmed to be in the stratum lacunosum (Lopes-dos-Santos et al., 2023). The

presence of a unique gamma profile electrophysiologically discriminated the stratum lacunosum from the strata radiatum or moleculare. Such a distinct profile implies the existence of a distinct micro-circuit in the stratum lacunosum (Chen et al., 2017), which could indicate that the stratum lacunosum might be wrongfully grouped with the moleculare as is commonly done in literature (Freund and Buzsáki, 1996; van Strien et al., 2009; Szirmai et al., 2012); see **Chapter 7** for further discussion). Furthermore, the identification of a narrow layer such as the stratum lacunosum underscores the sensitivity and replicability of the LFP-guided depth estimation. Thus, the theta-nested gamma analysis corroborates the correct layer assignment by the depth trajectory and aids in the identification of a lacunosum-specific gamma profile.

To further confirm layer assignment, I performed histological examination on all tetrodes included in this validation dataset. I confirmed that nearly all tetrode tips were present in the electrophysiologically predicted layer. However, despite minimal error, two tetrodes were found to be outside their designated layers, which could be attributed to various methodological factors. Firstly, histological examination of the tetrode tracks involves tissue fixation, typically performed using PFA. PFA is known to induce tissue shrinkage (Wehrl et al., 2015), potentially causing minor displacement of the tetrodes during this process. However, the precise and consistent positioning of tetrodes within thin layers such as the strata pyramidale and lacunosum argues against PFA-induced artifacts. Secondly, these errors could have arisen from the depth estimation. Discriminating between the strata oriens and pyramidale as well as the stratum moleculare and the outer molecular layer of the dentate is challenging using the depth estimation trajectory space solely based on theta oscillations and SWR-events (Lopes-dos-Santos et al., 2023). Interestingly, when the misaligned tetrodes were projected into the trajectory, they appeared to be closer to the putative layers' extremes, indicating that these tetrodes are recognised as 'border' cases. One could minimize potential mixing by narrowing the range that defines the putative layers along the trajectory to guarantee discrete groups. Alternatively, if higher accuracy of the trajectory is required, other layer-specific electrophysiological information, such as gamma oscillation-based information (Colgin et al., 2009; Schomburg et al., 2014; Lopes-dos-Santos et al., 2023), could be added to the depth estimation trajectory. Together, the correspondence between tetrode position

in trajectory and anatomical space corroborates the validity of LFP-guided tetrode positioning through the depth estimation trajectory in dorsal CA1.

Overall, this Chapter demonstrates the effectiveness of LFP-guided depth estimation in predicting tetrode recording depth in dorsal CA1 of the hippocampus. By leveraging an earlier-developed linear probe-based LFP trajectory, I successfully reconstructed relative LFP changes along the radial axis with tetrodes. In addition, through an independent assessment of layer-specific network events and histological examination, I validated the precision of the depth estimation trajectory, highlighting its potential for accessing CA1's full radial axis with high temporal and spatial resolution utilising tetrodes. Furthermore, the unexpected discovery of distinct layer-specific characteristics in the stratum lacunosum underscores the sensitivity and replicability of LFP-guided depth estimation as a tool. These findings emphasize the value of electrophysiological landmarks to navigate the brain during *in vivo* experiments. Together, these results show that LFP-guided depth estimation permits accurate *in vivo* access to the superficial layers of dorsal CA1, providing a solid foundation to interrogate the superficial interneurons in the following Chapters.

Chapter 3. Spike waveform characteristics of superficial interneurons

3.1 Introduction

Well-coordinated network activity is dependent on precisely orchestrated neuronal activity. To elucidate the underlying computational structures, it is important to record individual spiking activity from many neurons at high temporal resolutions. Extracellular electrophysiological recording techniques perform well at short timescales and are suitable for recording multiple neurons simultaneously (Steinmetz et al., 2018). However, action potential detection and source identification are challenging in extracellularly recorded signals (Lewicki, 1998; Hill et al., 2011; Pachitariu et al., 2016). Spike waveform shape and spike timing metrics can be useful resources for selecting valid spikes and discarding artefacts (Hill et al., 2011). In addition, spike waveforms are widely used to classify neuron types, but since these classifications often only distinguish between wide- and narrow-waveform neurons, many neuron types and regions are unrepresented in the literature (Roux et al., 2014; Petersen et al., 2021). Particularly, the heterogeneity within the interneuron class is underestimated by such crude classification approaches (Scala et al., 2021). Thus, to better understand neural circuit function, detailed spike waveform descriptions of extracellularly recorded spikes from neuron types across different anatomical layers and brain regions are required.

Despite being a powerful tool, recording and extracting valid spikes from a single source is challenging. Biophysical restraints can help segregate valid, unit-specific spikes from erroneous spikes (Hill et al., 2011). For example, the biophysical characteristics of action potential driving ion channels refrain neurons from firing action potentials within a certain refractory period (Hodgkin

and Huxley, 1990). When a unit contains a high number of spikes within this time interval, this indicates that the detected spike train is contaminated by spikes originating from neighbouring neurons or artefacts and does not represent a single source (Hill et al., 2011). Another challenge is posed by tracking neurons over longer periods. Due to the movement of the tetrodes in relation to the tissue, units can be lost during recording sessions. The stability of the recordings, as measured by the stability of the waveform and the continuous presence of the same neuron in the signal, is dependent on both the tissue composition as well as electrode characteristics (Windolf et al., 2023). Additionally, stability measures such as the variability in spike amplitude can give insights into how stable recordings are and, therefore, the reliability of the spike count and distribution over time (Hill et al., 2011). Thus, if detected spike waveforms in extracellular signals are critically assessed on validity, detecting multiple units within the same signal can be turned into one of the biggest strengths of extracellular recording techniques.

Source identification forms another challenge when utilizing large-scale extracellular recording techniques, as targets often can not be visualized. Fast potential differences, which reflect an action potential, are not exclusively generated at the axon initial segment; they can also arise from dendrites and axons. However, unlike soma-originating spikes, dendritic and axonal spikes present as positive rather than negative spikes (Lewandowska et al., 2015; Moore et al., 2017; Sun et al., 2021; Someck et al., 2023). This is even further corroborated by the positive spikes being mostly found in layers containing high dendritic and axonal content such as the oriens and radiatum of dorsal CA1 (Someck et al., 2023). These differences in spike waveform shape form an easily accessible basis to segregate somatic from non-somatic spikes. Thus, spike waveform can reflect from which neuronal subdomain a detected spike originates.

In addition, waveform shapes can inform the spike source's neural identity (Royer et al., 2012; Stark et al., 2013; Roux et al., 2014; Senzai et al., 2019). The arrival of optogenetics has boosted recent attempts to build generic libraries containing spike waveform and activity characteristics of specific molecularly defined subgroups to serve as neuronal templates for electrophysiological data (Roux et al., 2014; Petersen et al., 2021). However, these libraries are biased to spike

waveform descriptions of types and classes found in the neocortex or hippocampal stratum pyramidale, while other regions and layers remain underrepresented. In the hippocampus and cortex, for example, most neuron classification frameworks use the trough-to-peak time to split datasets into putative pyramidal and putative interneurons (Royer et al., 2012; Stark et al., 2013; Petersen et al., 2021). Although this has been well validated for fast-spiking, parvalbumin-positive interneuron types, this may be less suitable for some other members of the highly heterogenous inhibitory neuron class. *Ex vivo* whole-cell recordings with *post hoc* identification of the recorded neurons suggest that spike waveform shape is heterogeneous among interneurons and that, in the hippocampus, some interneurons share waveform characteristics with pyramidal neurons (Lacaille and Schwartzkroin, 1988a; Jiang et al., 2015; Scala et al., 2021). These observations further emphasize that currently used classification rules may not be transferable across all interneuron subtypes. Together, waveform shape can be an instrumental feature in the identification of the spike source from neuronal subdomain to different types but more elaborate waveform libraries are needed.

Dorsal hippocampal CA1 contains a variety inhibitory neurons, but detailed waveform descriptions of these neurons are limited. By performing layer-specific single-unit tetrode recordings, I built a dataset that includes over 2300 detected spike waveforms across the radial axis of dorsal CA1. In this Chapter, I assess the waveform stability, validity, and shape across different layers. This analysis revealed that units recorded across the superficial layers of dorsal CA1 are equally stable and better isolated compared to those detected in the stratum pyramidale but detection of non-somatic spikes is more likely in these layers. In addition, I show that often-used interneuron classification rules do not apply to superficial interneurons given their layer-specific waveform shapes. Lastly, I found that distinct waveform shapes are unequally distributed across different layers, possibly reflecting distinct interneuron types. Together, this data offers an elaborate description of spike waveforms detected across the radial axis of dorsal CA1, providing a large-scale reference dataset that serves as a strong foundation to study the function of superficial interneurons in dorsal CA1

3.2 Method

3.2.1 Mice

These experiments were conducted over 65 recording days using 17 male mice aged 4 to 7 months with a C57BL/6J background (**Table 3.2.1**). All mice in the experiment described below have undergone the same implantation and habituation procedure as described in **Chapter 2** (see **Methods 2.2.2 – 2.2.5**).

Mouse line	RRID	Number of mice	Genotype	Sex
C57Bl6/J	IMSR_JAX:000664	9	Wildtype	Male
NDNF-Cre	IMSR_JAX:028536	3	Heterozygote	Male
VIP-Cre	IMSR_JAX:010908	1	Heterozygote	Male
Grik4-Cre	IMSR_JAX:006474	3 1	Heterozygote Wildtype	Male

Table 3.2.1 – Overview of mice used for the superficial interneuron dataset

3.2.2 Data acquisition and recording procedures

Intracranial electrical signals, position tracking data, and tetrode positioning were acquired and performed as described in **section 2.2.6**. Every morning, stepwise tetrode positioning was followed by at least a 90-minute rest period before the recordings started. Once tetrodes were in position, the mice underwent the same behavioural protocol every recording day, depending on the cohort. Three cohorts were included in this dataset. Two cohorts were exposed to familiar and novel open fields without a specific behavioural task. The first cohort's protocol started with a 30-minute sleep session followed by a 15-minute exploration of a familiar and later a novel environment, interleaved with sleep sessions (NR1; 4 mice). The second cohort followed a similar protocol, but an additional familiar session was added and the order of the second familiar and novel sessions changed pseudo-randomly across consecutive days (NR2; 6 mice). Lastly, the third cohort participated in the continuous novel object recognition (cNOR) task of multiple sleep and exploration sessions with and without novel objects (7 mice; see **Figure 3.2.1**). A novel environment was created by varying the open field layout utilizing differently shaped insets or floor plates with different textures, as well as the introduction of novel open field boxes with the same dimensions. All analysis presented in this Chapter was performed on spike waveforms detected across all sessions. The behavioural data is not analysed in this Chapter.

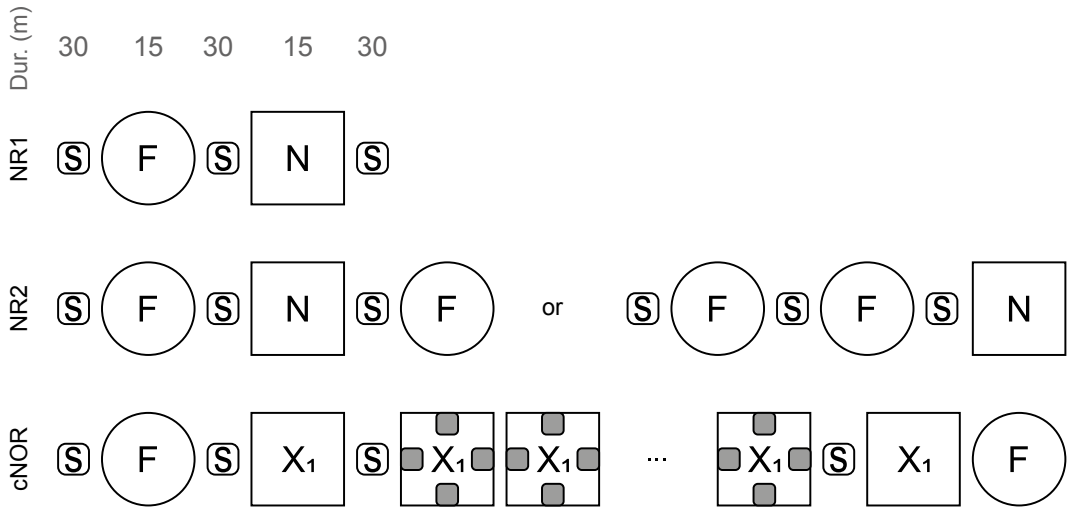


Figure 3.2.1 – Behavioural paradigms

Behaviour paradigms used for data acquisition. NR1 consists of sleep box sessions and awake exploration sessions. NR2 is based on a similar protocol with an additional exploration session. Note that the novel and familiar environments are pseudorandomised across days. Some of the mice went through the cNOR tasks in which they alternate sleep and exploration sessions with or without the presence of (novel) objects. S: sleep box, F: familiar environment, N: novel environment, X_1 is novel when the mice are introduced to the environment but remains the same throughout the recording day. Small grey boxes indicate objects.

3.2.3 Data analysis

3.2.3.1 Software

All data were analyzed using custom code in Python 3.10, with the following packages: NumPy v1.24.3, Pandas v1.5.3, SciPy v1.10.1, Matplotlib v3.7.1, and Seaborn v0.21.2.

3.2.3.2 Spike waveform detection

Spike sorting and unit isolation were performed with an automated clustering pipeline established in the Dupret laboratory implementing Kilosort via the SpikeForest framework (Pachitariu et al., 2016; van de Ven et al., 2016; Magland et al., 2020). To apply this approach to data acquired using tetrodes, the algorithm restricted templates to channels within an individual tetrode, cycling through all tetrodes. The resulting clusters were manually verified using cross-channel spike waveforms, auto-correlation histograms, and cross-correlation histograms.

3.2.3.3 Waveform measurements

Waveform analysis was performed on spike waveform identified across all sessions within the same recording day from the channel with the largest waveform amplitude.

Spike consistency

Spike consistency captures the standard deviation across all spike waveform amplitudes relative to the mean amplitude as previously described (Lopes-dos-Santos et al., 2023). In short, for each unit, the unit's mean waveform amplitude was compared with the standard deviation of all its spikes. This comparison was quantified using a waveform score, calculated as:

$$\text{wvscore} = \sqrt{\sum_{i1}^{n} \left(\frac{w_i}{\sigma_{w_i}}\right)^2 \frac{1}{n}}$$

Here, w_i represents the mean waveform value at sample i, σ_w is the standard deviation at sample i across all spikes, and n is the number of waveform samples (n=32). Units with a spike consistency score > 0.75 were excluded from further analysis.

Tetrode drift

Tetrode drift was measured as an amplitude change over time. To compute tetrode drift, the spike waveform amplitude was measured for all individual spikes assigned to a given unit and sorted based on time of occurrence. Then the slope of a regression line was obtained as a proxy for gradual amplitude changes over time. The regression line was fitted to the individual spike waveform amplitudes using the NumPy function polyfit (deg=1) and the slope was computed using NumPy's poly1d.

Refractory period violation

Refractory period violation value was defined as the percentage of inter-spike intervals <2 ms. Units with a refractory period violation value >2% were excluded.

Spike waveform characteristics

To compute spike waveform characteristics the mean waveform was computed across all recording day sessions from the tetrode channel with the highest waveform amplitude. To normalise the offset potential across waveforms the mean 'base' potential (μV) was computed by averaging the first 4 samples (0.2 ms) and subtracted from the waveform. In addition, to compute the trough-to-peak and full-width half-max time the waveform was interpolated by factor 100 using the SciPy function interpolate.interp1d (kind=quadratic). Several key waveform landmarks were identified for W(t) representing the waveform as a function of time (**Figure 3.2.2**).

Amplitude		Time		
$trough$	$= \min W(t)$	t_{trough}	$=$	$\text{argmin } W(t)$
$peak_1$	$= \max_{t<t_{trough}} W(t)$	t_{peak1}	$=$	$\text{argmax}_{t<t_{trough}} W(t)$
$peak_2$	$= \max_{t>t_{trough}} W(t)$	t_{peak2}	$=$	$\text{argmax}_{t>t_{trough}} W(t)$

$$troughhalf = \frac{trough}{2}$$

$$W(t_{cross1}), W(t_{cross2}) = trough_{half} \quad \text{with } t_{cross1} < t_{trough} < t_{cross2}$$

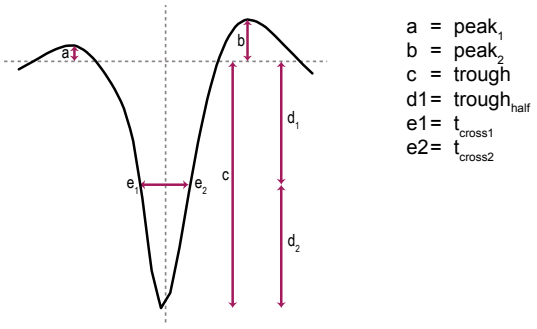


Figure 3.2.2 – Spike waveform measurements

Representative spike waveform. The vertical dashed line indicates the position around which the waveform is centred. The horizontal dashed line indicates the baseline value used to compute potential amplitudes. Arrows marked a-e represent the values obtained from the waveforms to compute different waveform measurements.

Based on the landmarks above the following waveform characteristics were computed:

The biphasic index captures the relative size of the first peak and the trough to each other. Given their non-somatic origin, units with a positive biphasic index (peak > trough) were excluded from all analyses unless stated otherwise (Someck et al., 2023):

$$\textit{Biphasic index} = \frac{\text{peak1} - |\text{trough}|}{\text{peak1} + |\text{trough}|}$$

Shoulder asymmetry was used to describe the relative size of the first peak (left shoulder) and the second peak (right shoulder) (Csicsvari et al., 1998):

$$\textit{Shoulder Asymmetry} = \frac{\text{peak1} - \text{peak2}}{\text{peak1} + \text{peak2}}$$

Trough-to-peak time describes the time difference between the spike waveform trough and the second peak.

$$\textit{Trough-to-Peak time} = t_{peak2} - t_{trough}$$

The full-width half-max describes the duration between the descending and ascending parts of the trough at 50% of the trough's maximum absolute amplitude.

$$\textit{Full-Width Half-Max} = t_{cross2} - t_{corss1}$$

3.2.3.4 Unit classification

Units recorded in stratum pyramidale were classified in putative pyramidal neurons and putative pyramidale interneurons as previously described (Lopes-dos-Santos et al., 2023). In short, units were split based on trough-to-peak time thresholds derived from a 1-dimensional 2-component Gaussian Mixture Model trained on a pre-existing dataset in the laboratory, with longer trough-to-peak times being classified as putative pyramidal neurons and shorter times as interneurons.

3.2.3.5 Waveform characteristics dimensionality reduction and structure analysis

To project the waveform characteristics in a lower dimensional space, four spike waveform characteristics (biphasic index, shoulder asymmetry, trough-to-peak time, and full-width half-max) were individually z-scored using SciPy stats.zscore function and concatenated so that every

unit was represented by all four different waveform measures. Dimensionality reduction was performed through UMAP (metric=euclidean, min_dist=.15, n_neighbors=10, n_components=2, random_state=25). The structure index was used to examine the presence of a layer-based structure in the UMAP manifold as described in (Sebastian et al., 2024). This measure describes the probability of a given data point being close to data points representing the same class versus points representing other classes. A high structure index indicates stronger clustering of data points from the same class in the lower dimensional space.

3.2.3.6 Waveform-based depth prediction

Two different types of classifiers from the sklearn package were used to predict recording depth at a single spike waveform level. The dataset was balanced by subsampling 115 neurons per layer across all mice. To prevent any overlap between the training and testing set, each classifier was trained on data from all but one mouse and data from the remaining mouse was used in the testing set. This procedure was repeated for all mice. For the **Naive Bayes Classification**, the GaussianNB function from the sklean naive_bayes module was used (parameters: priors=None). For the **k-Nearest Neighbors classifier**, the KNeighborsClassifier function from the neighbors module was used (parameters: n_neighbors=10, *, weights='uniform', algorithm='auto'). Mutual information (MI) was computed based on the confusion matrix which was composed using the confusion_matrix function from the sklearn.metrics module and the accuracy score was computed using the accuracy_score function from the same module. Mean and 95% confidence intervals for the MI and accuracy were computed across MI and accuracy distributions derived from 1000 times balanced, random subsampling 115 neurons per layer without replacement.

3.2.3.7 Spike waveform clustering

To identify clusters in the UMAP embedding (see **section 3.2.3.4**), DBSCAN was chosen over centroid and Gaussian-based methods as it does not assume cluster shape. First, different values for epsilon were assessed for a minimal number of 12 samples per cluster (10% of the smallest layer-based group). To do so, both the Silhouette Score (silhouette_score from sklearn.metrics) and the k-Distance Plot (NearestNeighbors from sklearn.neighbors) were employed (**Figure**

3.2.3). Both tests converged on an epsilon of 0.95. In the silhouette score assessment, 0.95 appeared to be the largest epsilon (larger epsilon will result in fewer clusters) with the highest silhouette score (indicating the best-segregated clusters). The k-Distance assessment showed the steepest increase around 0.95 indicating this value to be most suited. Then DBSCAN clustering was performed using the DBSCAN function from sklearn.cluster package (parameters: eps=.95, min_samples=12).

3.2.3.8 Statistical testing

Statistical testing was performed using functions from the scypi.stats package and custom code to perform permutation testing and generate bootstrapped confidence intervals.

Permutation of difference in the mean

Statistical testing was performed through permutation testing of the difference in the mean or median. Specifically, the actual mean difference between the two groups is compared to a null distribution. The null distribution was generated by computing the mean difference between two groups of the same size as the original groups but composed of randomly assigned data points 10,000 times. For paired testing, the null distribution was generated by randomly flipping signs of the differences across the group. The p-value was calculated as the probability of occurrence of the actual mean difference in the null distribution.

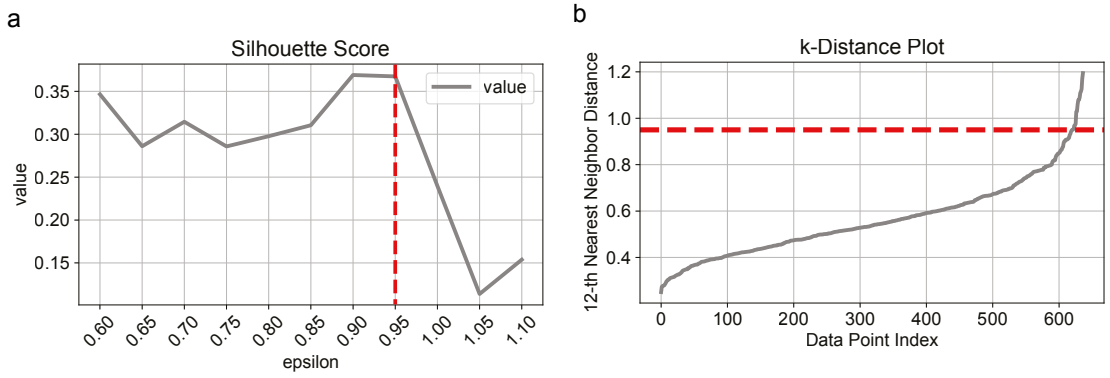


Figure 3.2.3 – Optimizing spike waveform clustering parameter space

a) Silhouette score computed for different values of epsilon. Higher silhouette score values represent better clustering. Red dashed line indicates the position of the highest silhouette score intersecting with the largest value for epsilon. **b**) k-Distance plot showing the cumulative distance of the 12th nearest neighbour per data point in the lower-dimensional UMAP space (see figure 3.3.2.2). Red dashed line indicates the 0.95 threshold obtained with the silhouette score method. The rapid change in slope of the k-Distance plot at the 0.95 thresholds supports this value to be a suitable value for epsilon.

Bootstrapped confidence interval of the mean

To compute the confidence intervals of the mean for individual groups, the mean was computed of a randomly resampled group with equal size as the original data, which was generated using the random.choice function from NumPy with replacement. The resampling was repeated 10,000 times and the 2.5th and 97.5th percentile from the resulting means was taken as the confidence interval of the mean.

3.3 Results

3.3.1 Spike waveform validation and stability across different layers in dorsal CA1

In this Chapter, I assessed the wavefroms of units recorded across dorsal CA1 layers using the depth trajectory to navigate tetrode positioning (**Figure 3.3.1c-e**). Since no elaborate tetrode-based dataset on superficial neurons was available, I first assessed the number of units recorded across different layers and mice, quality control metrics, as well as their stability over time.

After spike sorting (see **Methods**), a total of 2486 units were found across the strata Pyramidale, Radiatum, Lacunosum, and Moleculare in 17 mice, over 823 tetrodes from 65 recording days (**Figure 3.3.1a-f**). Most units per tetrode were found in the pyramidal layer (~6 units per tetrode on average) while this number rapidly dropped off as tetrodes moved into the superficial layers to ~1 unit per tetrode (**Figure 3.3.1f**). It is important to note, however, spikes were actively sought to be present in the signal during tetrode positioning, and, therefore the number of units found may not reflect a random sampling across depth (see **Methods**). Although not every recording day captured units across all layers, nearly all individual mice contributed to units across the different layers (**Figure 3.3.1b**), indicating that pyramidale, as well as superficial units, are detected across different mice. Together, this dataset contains a substantial amount of simultaneously recorded units found across different CA1 layers sampled across different mice.

In addition to curation during spike sorting, our lab uses a custom quality control pipeline to assess inter-spike variability over time and refractory period violations (see **section 3.2.3**). Since

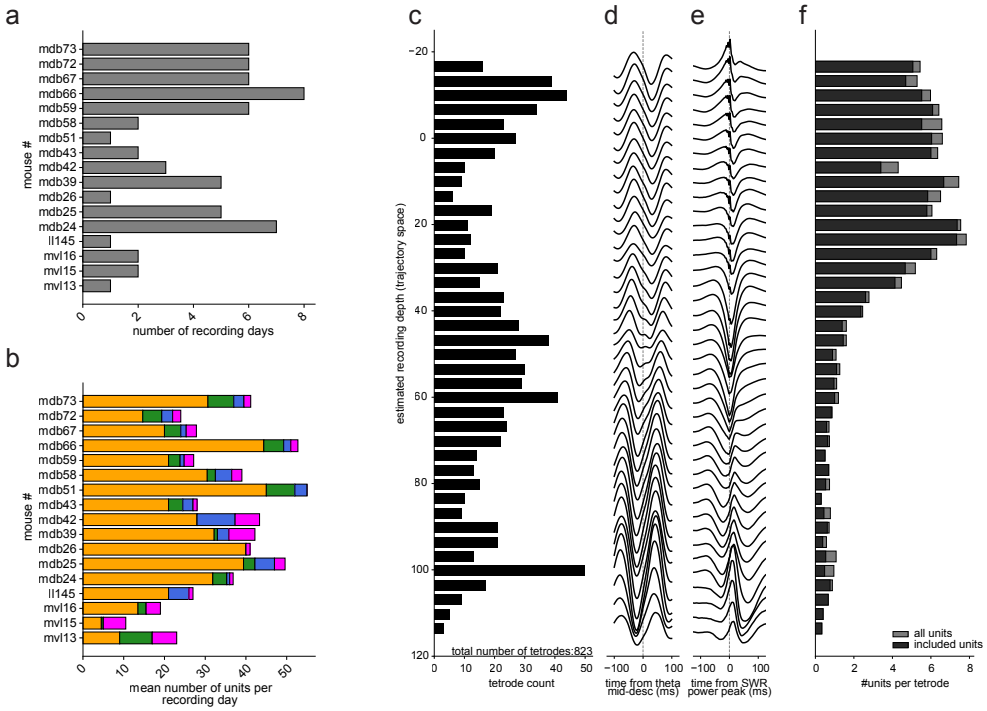


Figure 3.3.1 – Number of recorded units as a function of depth

a) Bar graph showing the number of recording days per mouse included in the dataset. **b**) Bar graph indicating the mean number of units recorded per mouse across different layers; yellow: pyramidale, green: radiatum, blue: lacunosum, magenta: moleculare. Counts for the stratum pyramidale include both putative pyramidal neurons and interneurons. Note that nearly all mice contributed to neurons across all layers. **c**) The number of tetrodes allocated to distinct depth bins by the recording depth estimation algorithm. **d**) Mean theta triggered LFP for all tetrodes per depth bin. All channels along the radial axis were aligned to the mid-descending phase of theta of the stratum pyramidale tetrode. Note amplitude and phase changes as a function of depth resembling a pattern observed in silicon probe recordings (see **Chapter 2**). **e**) Mean ripple triggered LFP for all tetrodes per depth bin. All channels along the radial axis were aligned to the ripple power peak of ripples detected in the stratum pyramidale tetrode. Note the changes in amplitude, shape, and polarity of the sharp-waves as a function of depth. This pattern resembles those observed in silicon probe recordings (see **Chapter 2**). **f**) Bar graph indicating the average number of units recorded per tetrode per depth bin. Height of the grey bars indicates all detected units. Dark bars represent the proportion of clusters passing quality control.

this pipeline is specifically developed for units in the stratum pyramidale, its applicability to superficial layers is uncertain. Therefore, I compared the computed quality control metrics for superficial layers with those in the pyramidale (**Figure 3.3.2**). To assess inter-spike waveform stability over time a waveform consistency score is computed capturing the mean waveform amplitude relative to the standard deviation across all spikes. The number of units violating the spike consistency threshold was not significantly different across layers (Chi-squared test statistic=2.353, pval=0.503, dof=3) as well as the mean spike waveforms consistency across layers (ANOVA statistic=1.713, pval=0.162; **Figure 3.3.2d**). In addition, by measuring the magnitude of spike waveform amplitude change over time, I found no indication of differential tetrode drift

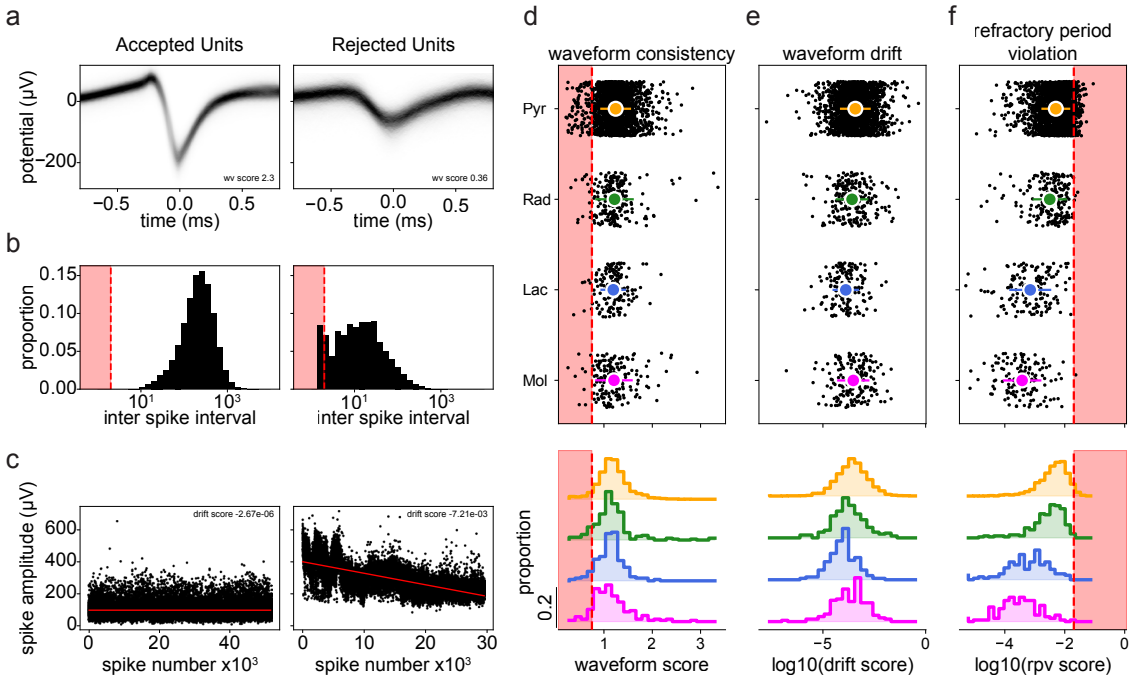


Figure 3.3.2 – Spike waveform stability and quality control

a) Heatmap of superimposed waveforms of two example units (left: accepted unit with waveform consistency score of 2.3, right: rejected unit with waveform consistency score of .36). Note the higher waveform-to-waveform variability in the rejected unit (right). **b**) Interspike interval histograms for two example units (left: accepted, right: rejected). The rejected unit violates the spike refractory period with >2% of the interspike intervals being below 2ms. Red dashed line and shaded area indicate the intervals < 2 ms. **c**) Spike amplitudes for two example units across the full recording session. Black dots represent the amplitude for every individual spike of the same neuron. Red line depicts the fitted regression on the spike amplitude over consecutive spikes. Note the stable waveform amplitude for the left unit, while the right unit shows a prominent amplitude change over time indicative of an unstable recording. **d**) Top: Waveform consistency score for all units. Black dots represent individual neurons per layer and coloured markers the mean and standard deviation (yellow: pyr, green: rad, blue: lac, magenta: mol). Bottom: Histograms of the waveform consistency score per layer. The red-shaded area indicates the violation range. The number of units violating the spike consistency threshold was not significantly different across layers (Chi-squared test statistic=2.353, pval=0.503, dof=3) as well as the mean spike waveforms consistency across layers (ANOVA statistic=1.713, pval=0.162). **e**) Same as **d**) for waveform drift representing waveform amplitude change over time for all layers. Waveform drift was not significantly different across layers (ANOVA statistic=0.290, pval=0.833). **f**) Same as **d**) for refractory period violations. The occurrence of refractory period violations was significantly different across layers (Chi-squared test statistic=26.054, pval<10^{-5}, dof=3), as well as the mean refractory period violation value, which gradually decrease as a function of depth (ANOVA statistic=93.245, pval<10^{-5})

across layers (ANOVA statistic=0.290, pval=0.833; **Figure 3.3.2e**). These two measures show that spike detection was stable across time and layers. Furthermore, the refractory period violation value (defined as >2% of the inter-spike intervals < 2 ms) is normally computed to identify poorly isolated units in the dataset. When computed across the radial axis of CA1, a layer-dependent difference was observed in the number of violations (Chi-squared test statistic=26.054, pval<10^{-5}, dof=3; **Figure 3.3.2f**). Most units violating the refractory period threshold were found in the

stratum pyramidale (~6% of all units), while only <1.5% units violated this threshold in the individual superficial layers (**Figure 3.3.2f**). The mean refractory period violation value gradually decreased over depth (ANOVA statistic=93.245, pval<10^{-5}; **Figure 3.3.2f**), indicating that the number of units with spike trains containing interfering spikes is lower in the most superficial layers compared to the pyramidale. Together, this data shows that units recorded in the superficial layers are as stable as those in the pyramidale and their spike waveforms better isolated.

Previous literature describes the occurrence of non-somatic spikes, which present as positive spikes and are mostly seen in regions with high dendritic and axonal content (Moore et al., 2017; Someck et al., 2023). To examine the occurrence of positive spikes in the current dataset, I computed the biphasic index for individual units (see **Methods**), which captures the relative amplitude of the first peak versus the waveform trough (**Figure 3.3.3a, b**). This analysis revealed that the likelihood of recording a positive spike (positive biphasic index; first waveform peak > trough) was not equally distributed across the different layers, with the highest detection probability in the stratum moleculare (~20%), followed by radiatum and lacunosum with 14% and 15%, respectively, and the lowest in the pyramidale (4%; Chi-squared statistic=27.482, pval<10^{-5}; **Figure 3.3.3c**). Furthermore, positive spikes represented ~5% (101 / 2251) of all detected units (**Figure 3.3.3a**). When grouped per recording layer, the largest proportion of positive spikes among the recorded unit was found in the stratum moleculare 28% (46/166), followed by the lacunosum 15% (22/151) and radiatum rad 11% (24/219), and the lowest proportion in the stratum pyramidale 0.8% (14/1808). Together, these results show that positive spikes are recorded along the full radial axis of dorsal CA1 but the recording probability and the proportions of positive spikes are skewed to the superficial layers.

Spike waveform can predict the class of the neurons from which the spike originates (Henze et al., 2000; Petersen et al., 2021). Spike waveform classification is employed to segregate putative pyramidal neurons from interneurons using a waveform shape-based classification algorithm (see **Methods**; **Figure 3.3.3e**). However, the neuron classification thresholds used in the Dupret laboratory were specifically optimised and validated for the stratum pyramidale and the extent

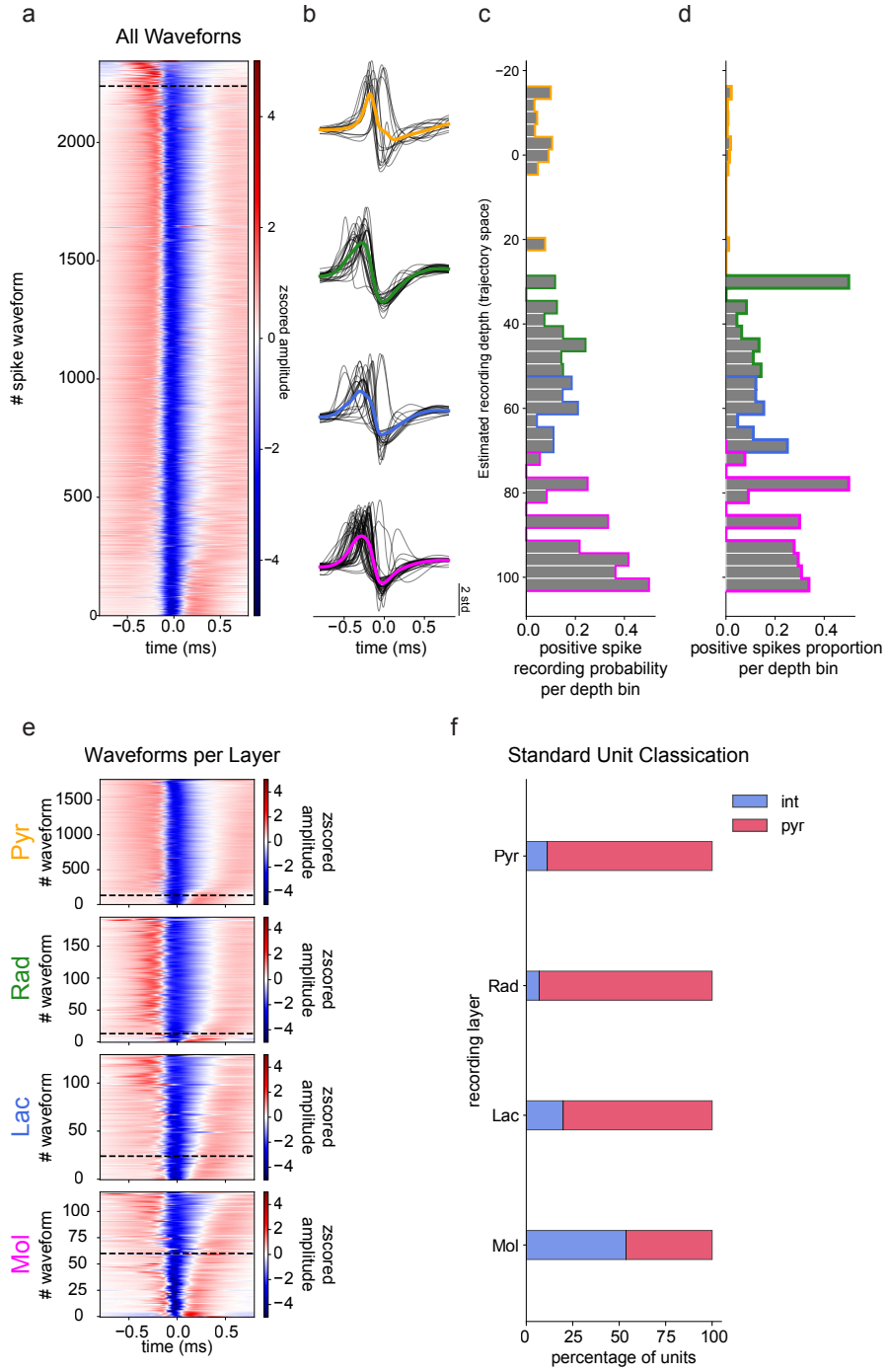


Figure 3.3.3 – Spike waveform sources across subdomains and major neuron classes

a) Colour plot representing individual mean spike waveforms per row for all units sorted based on biphasic index with the highest biphasic indices at the top of the plot and the lowest at the bottom. Dashed line indicates the biphasic index threshold, waveforms above the threshold are considered positive spikes. Colour bar indicated z-scored waveform amplitude. All spike waveforms are centred at their minimum amplitude value (deepest part of the trough). **b**) Spike waveforms of positive spikes per layer. Mean waveform indicated in colour (pyr: yellow, rad: green, lac: blue, and mol: magenta) Individual waveforms are depicted in grey. **c**) Bar graph indicating the proportion of positive spikes per tetrode per depth bin. Coloured envelope indicates to which layer the corresponding bars belong, with similar colour coding as in **b**). Recording probability of positive spikes in unequally distributed across the distinct layers (Pyr 5%, Rad 14%, Lac 15%, Mol 21%; Chi-squared statistic=23.799, pval<10^{-5}). Note the gap in recording probability of positive spike in the stratum pyramidale. **d**) Bar graph showing the proportion of positive spikes across all recorded units per depth bin. Coloured envelope **»**

» indicates to which layer the corresponding bars belong, with similar colour coding as in **b**). (Pyr 0.8%, Rad 11%, Lac 15%, Mol 28%). Note the low proportion of positive spikes per depth bin. **e**) Colour plots showing mean spike waveforms per layer sorted based on trough-to-peak time. Every row depicts an individual mean waveform. Dashed lines indicate the trough-to-peak threshold used to discriminate putative pyramidale cells from putative pyramidale interneurons. Colour bar indicates the z-scored spike waveform amplitude. **f**) Bar graph showing unit classification (red: putative pyramidal neurons, blue: putative interneurons) based on the trough-to-peak threshold optimized for stratum pyramidale units. Note that, according to this classification rule the majority of superficial units would be classified as putative pyramidal neurons.

to which these thresholds are transferable to superficial interneurons is unclear (Lopes-dos-Santos et al., 2023). In the stratum pyramidale, ~10% (202/1792) of the classified units were classified as interneurons, which is in line with earlier findings (Henze et al., 2000; Royer et al., 2012). Surprisingly, I found that only a minority of the superficial units would be classified as interneurons when the spike width threshold estimated for pyramidale interneurons was applied: around 7% (12/173) in strata radiatum, 20% (22/111) in lacunosum, and ~54% (51/95) in moleculare (**Figure 3.3.3f**). Since nearly all superficial neurons are GABAergic (Freund and Buzsáki, 1996), these results indicate that superficial interneuron waveform characteristics differ from those in pyramidale. Thus, superficial interneurons do not follow the same classification rules as pyramidale interneurons.

In summary, I examined whether recording stability assumptions and quality control metrics developed and validated for the stratum pyramidale apply to units recorded in the superficial layers of dorsal CA1. This analysis revealed that the number of units detected is lower in superficial layers, but the recordings are equally stable, and waveforms are better isolated compared to stratum pyramidale. Furthermore, spike waveforms detected in the superficial layers are more often from non-somatic origin, and superficial somatic spikes do not follow standard pyramidale interneuron classification rules. Overall, this indicates that superficial layers can be reliably recorded.

3.3.2 Spike waveform characteristics differ across the radial axis of dorsal CA1

In **section 3.3.1**, I showed that standard spike waveform classification metrics do not apply to superficial interneurons, indicating that superficially recorded waveforms may differ in shape. Here, I examine the differences in interneuron spike waveform shapes across the layers of dorsal

CA1 by describing various waveform characteristics. In this section, I focus on the superficial and pyramidale interneurons (see **Methods**). Note that unit classification was only applied to the stratum pyramidale, all valid neurons detected in the superficial layers were included in this analysis. I found that superficial waveforms have unique characteristics and are distinguishable across layers, which eventually may aid in discriminating distinct interneuron types.

To capture waveform differences, I computed and compared several waveform metrics representing amplitude and duration across depth (**Figure 3.3.4**). To describe spike waveform amplitudes, I computed the biphasic index and shoulder asymmetry (also known as spike asymmetry). The biphasic index measures whether spike waveform has a dominant positive or

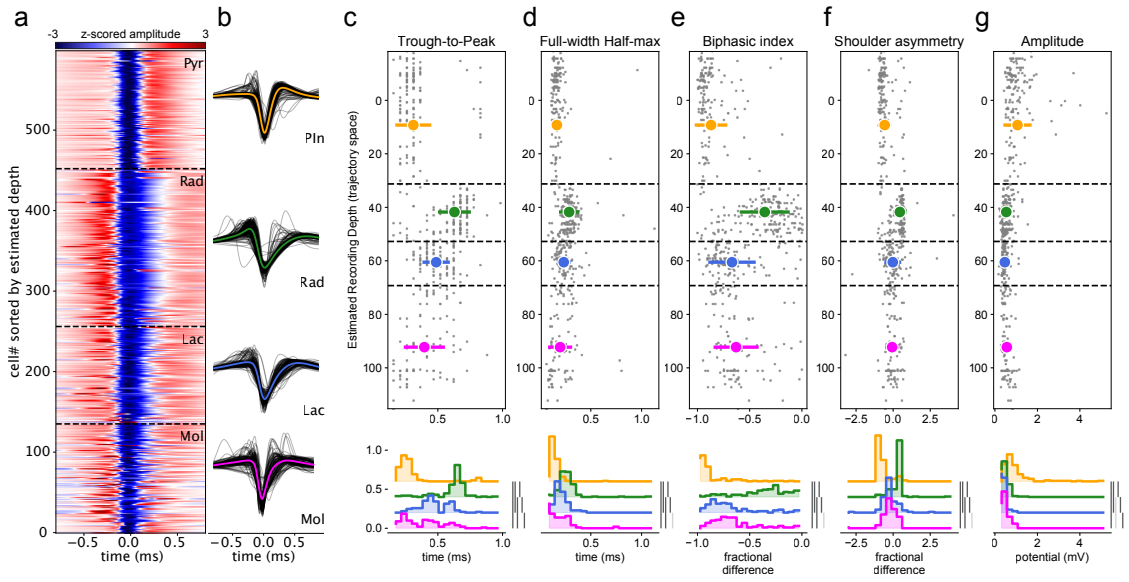


Figure 3.3.4 – Distinct waveform shapes in different layers of dorsal CA1

a) Colour plots showing mean spike waveforms of interneurons per layer sorted as a function of depth. Every row represents an individual neuron. Dashed lines indicate the layer borders. Colour bar indicates the z-scored spike waveform amplitude. Note the differences in width and spike-shoulder shapes. **b**) Mean spike waveforms of interneurons per layer. Mean waveform indicated in colour (pyr: yellow, rad: green, lac: blue, and mol: magenta) Individual waveforms are depicted in grey. **c**) Top: Scatter plot showing the trough-to-peak time for interneurons as a function of estimated recording depth in trajectory space. Coloured circles indicate the mean and the whiskers depict the standard deviation. Bottom: histogram of the trough-to-peak distribution per layer. Note the trimodal distribution in the stratum moleculare. Dark vertical lines indicate significant differences between the groups. **d**) Same as **c**) for full-width half-max of the mean spike waveform **e**) Same as **c**) for biphasic index for the mean spike waveform **f**) Same as **c**) for the shoulder asymmetry (relative amplitude of the left shoulder compared to the right shoulder) the mean spike waveform, with positive values indicating a higher left shoulder and negative values a higher right shoulder. **g**) Same as **c**) for the mean spike waveform amplitude.

negative deflection reflected by a positive or negative value, respectively. The biphasic index of pyramidale interneurons was significantly lower than that of the superficial layers (mean: -0.86, 95%IC: -0.89 – -0.84). On average, the most negative values among the superficial layers were found in the stratum lacunosum (mean: -0.65, 95%IC: -0.70 – -0.61) followed by the moleculare (mean: -0.63, 95%IC: -0.67 – -0.60) and radiatum (mean: -0.35, 95%IC: -0.39 – -0.32). This indicates that pyramidale and lacunosum neuron waveforms have a less pronounced peak before the trough (**Figure 3.3.4e**). In addition, I computed the shoulder asymmetry, a measure capturing the size of the peak before the trough (left shoulder) relative to the one after the trough (right shoulder). Interneurons in the pyramidale displayed the most negative shoulder asymmetry values (mean: -0.56, 95%IC: -0.62 – -0.49), indicating a more prominent right peak compared to the left. Neurons in the stratum lacunosum (mean: 0, 95%IC: -0.10 – 0.11) and moleculare (mean: -0.04, 95%IC: -0.13 – 0.05) had values closer to zero, reflecting a more symmetrical waveform, while the stratum radiatum was dominated by neurons with a more pronounced left peak (mean: 0.45, 95%IC: 0.39 – 0.51; **Figure 3.3.4f**). Furthermore, to capture waveform durations, trough-to-peak time and full-width half-max duration were measured for all waveforms across the layers. Pyramidale interneurons showed short trough-to-peak time (mean: 0.31, 95%IC: 0.29 – 0.33 ms), while radiatum neurons have the longest times (mean: 0.68, 95%IC: 0.62 – 0.78 ms), indicative of narrow and wide waveforms, respectively. The mean trough-to-peak times found in the strata lacunosum (mean: 0.50, 95%IC: 0.48 – 0.52 ms) and moleculare (mean: 0.41, 95%IC: 0.38 – 0.44 ms) fell between those of the pyramidale and radiatum, but their distributions were more heterogeneous (interquartile range: PIn 0.25 – 0.32 ms, Rad 0.62 – 0.70 ms versus Lac 0.42 – 0.60 ms, Mol 0.26 – 0.53 ms; **Figure 3.3.4c**). The full-width half-max, which is related to the trough-to-peak time but captures different phases of the spike showed a similar effect, with pyramidale interneurons having the shortest latencies (mean: 0.16, 95%IC: 0.15 – 0.17 ms), radiatum the longest (mean: 0.28, 95%IC: 0.27 – 0.29 ms), and lacunosum and moleculare intermediate means (Lac mean: 0.24, 95%IC: 0.22 – 0.24 ms; Mol mean: 0.20, 95%IC: 0.18 – 0.22 ms) across a heterogeneous population (**Figure 3.3.4d**). Together, these results show that neurons with distinct waveform characteristics are differentially distributed along the radial axis of dorsal CA1.

To further corroborate waveform differences, I tested whether a spike waveform holds enough information to predict its recording layer at a single-neuron resolution rather than group means. First, I projected four different (biphasic index, shoulder asymmetry, trough-to-peak time, full-width half-max) waveform metrics into a lower dimensional space (UMAP) and quantified whether a layer-based structure is present (**Figure3.3.5a**). The structure index, measuring the likelihood of a data point being close to data points from the same category (Sebastian et al., 2024), revealed that neurons from the same layer cluster above chance level (SI: 0.53, pval<10^{-5}), which indicated that waveforms within the same layer are more similar than across layers. Second, I trained a classifier to predict the recording layer on a neuron-by-neuron basis. To ensure no overlap between training and testing sets, the classifier was trained on data from 16 mice and tested on the remaining data from the 17th mouse, rotating across all mice. Based on their waveform characteristics, the Naive Bayes (NB) classifier correctly classified pyramidale and radiatum neurons above chance but performed less well for lacunosum and moleculare neurons (MI mean:0.45, 95%CI:0.37 – 0.52, pval<10^{-5}; accuracy mean:0.55, 95%CI:0.50 – 0.59, pval<10^{-5}; **Figure 3.3.5b, d-f**). Interestingly, the classifier was more likely to misclassify moleculare and lacunosum neurons compared to the misclassification of pyramidale or radiatum neurons (**Figure 3.3.5b**). Given this result and the identified waveform heterogeneity in the strata lacunosum and moleculare (**Figure 3.3.4**), I hypothesized that the observed multimodal distributions might interfere with the NB classifier's model fitting, as these classifiers are less effective at handling within-group heterogeneity. To test this possibility, the same classification procedure was performed while utilizing a classifier less susceptible to within-group variation, such as the k-Nearest Neighbours (kNN) classifier. The kNN classifier successfully differentiated interneurons from the recorded layers based on their waveform characteristics above chance level (MI mean:0.61, 95%CI:0.55 – 0.68, pval<10^{-5}; accuracy mean:0.65, 95%CI:0.63 – 0.68, pval<10^{-5}; **Figure 3.3.5c, h-j**). Direct comparison of the mutual information as well as the accuracy revealed that the kNN outperformed the NB classifier (MI difference 0.16, pval<10^{-5}; accuracy difference 0.10, pval<10^{-5}; **Figure 3.3.5g, k**). Both classifiers performing above chance underscores that the recording layer can be predicted based on individual waveforms. However, given the classifiers' characteristics, better performance of the kNN classifier is in line with the observed within-group heterogeneity, suggesting that several

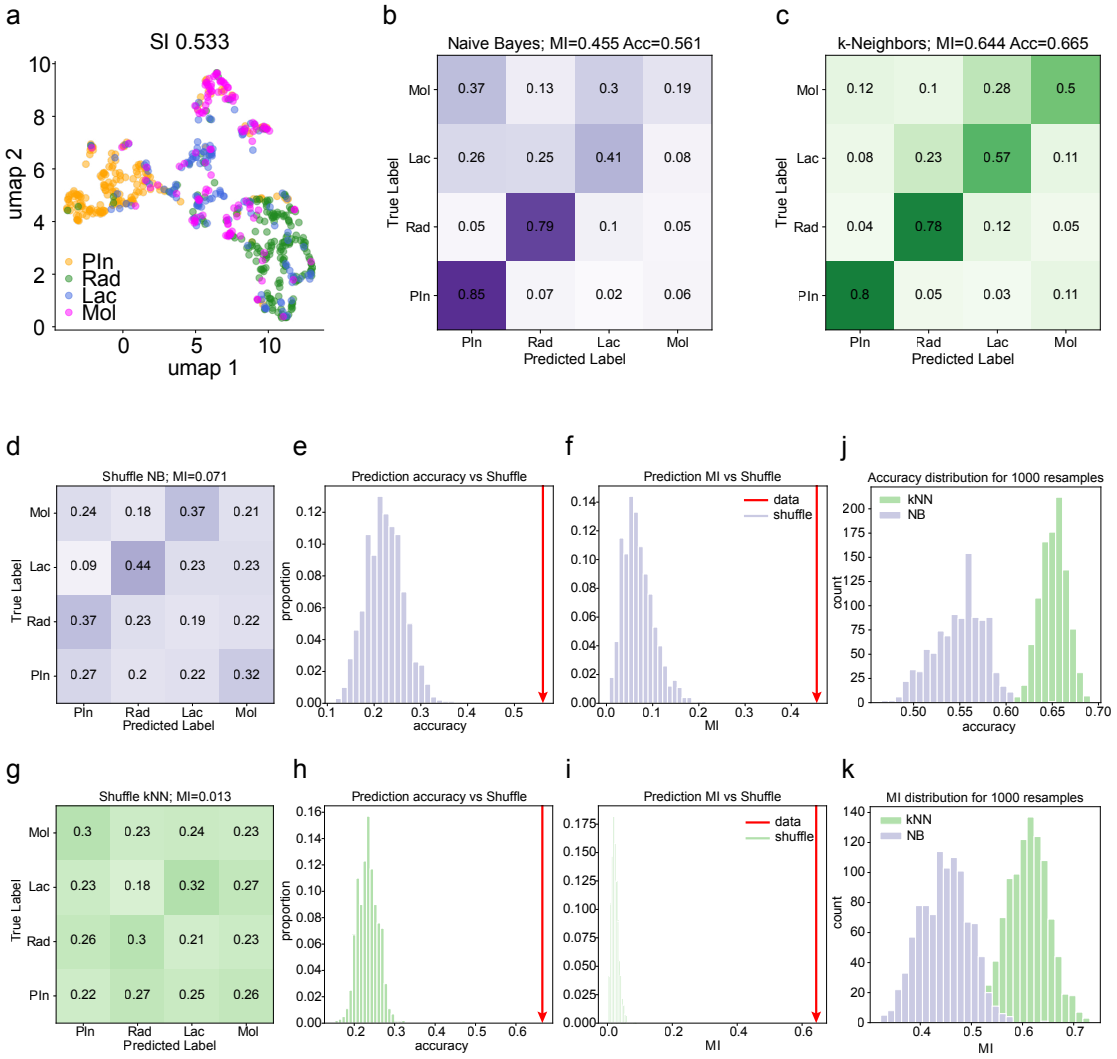


Figure 3.3.5 – Spike waveform shapes cluster along the radial axis of dorsal CA1

a) UMAP embedding of spike waveform characteristics. Data points represent individual neurons colour-coded for the layer in which they were recorded (Pyr: yellow, Rad: green, Lac: blue, Mol: magenta). Note that colour coding reveals layer-based clusters, also reflected by the structure index (SI). **b**) Confusion matrix for the Naïve Bayes Classifier predicting estimated recording layer based on waveform characteristics. Values represent the probability of correctly predicting the recording layer compared to the known labels. Prediction accuracy (Acc) of the classifier was 0.561 across all layers. The Mutual information (MI) between the predicted and true layers was 0.455. Note that the accuracy per layer is highest for the stratum pyramidale and radiatum, which drops below change levels for the stratum moleculare. **c**) Same as in **b**) for k-Nearest Neighbor Classifier. Values represent the probability of correctly predicting the recording layer compared to the known labels. Prediction accuracy (Acc) of the classifier was 0.665 across all layers. The Mutual information (MI) between the predicted and true layers was 0.644. Note that the accuracy per layer is highest for the stratum pyramidale and radiatum, but in contrast to the NB Classifier, the prediction accuracy is maintained for the strata lacunosum and moleculare. **d**) Example confusion matrix of the Naïve Bayes Classifier (as in **b**) predicting estimated recording layer based on waveform characteristics but trained on a single shuffled dataset. Shuffle was generated by permutating the labels in the training set. Note the drop in both Acc and MI compared to **b**) as well as the prediction probability at the diagonal to chance level of 0.25 for all layers. **e**) Histogram showing the distribution of the NB classifier prediction accuracy for 1000 shuffled datasets (purple) against the true prediction accuracy (red arrow) related to the confusion matrix in **b**). **f**) Same as in **e**) for the mutual information between the true and NB classifier predicted labels for the shuffled distribution and the true value (red arrow) related to the confusion matrix in **b**). »

» **g**) Example confusion matrix of the k-Nearest Neighbor Classifier (as in **c**) predicting estimated recording layer based on waveform characteristics but trained on a single shuffled dataset. Note the drop in both Acc and MI compared to **c**) as well as the prediction probability at the diagonal to chance level of 0.25 for all layers. **h**) Histogram showing the distribution of the kNN classifier prediction accuracy for the shuffled datasets (green) against the true prediction accuracy (red arrow) related to the confusion matrix in **c**). **i**) Same as in **h**) for the mutual information between the true and kNN classifier predicted labels for the shuffled distribution and the true value (red arrow) related to the confusion matrix in **c**). **j**) Distributions of classification accuracies for the NB classifier and the kNN classifier based on 1000 resamples of the interneuron population across the different layers. The number of included neurons was balanced across layers. The mean accuracy of the kNN is significantly higher compared to the NB classifier. **k**) Same as in **j**) for mutual information for the NB classifier and the kNN classifier. All layers are equally represented. The mean accuracy of the kNN is significantly higher compared to the NB classifier.

distinct waveform shapes may be present within the same layer. Together, these results suggest that layers in dorsal CA1 contain various neurons with distinct waveform shapes.

To summarize, here I assessed the waveform shapes across different depths on the radial axis in dorsal CA1. This revealed that waveform characteristics differ over depth with on average narrower spike waveforms and lower peak-trough amplitude ratios the further away units are recorded from the stratum pyramidale. Furthermore, waveform shapes show a layer-based clustering when projected into a lower dimensional space, and individual waveforms contain sufficient information to predict recording depth. Together, these data suggest that specific waveform differences are related to recording depth and could be informative for neural type classification.

3.3.3 Spike waveform clustering reveals heterogeneous spike waveform population

The performance differences between classifiers suggest that strata lacunosum and moleculare harbour a more heterogeneous population compared to the strata pyramidale and radiatum. To test this hypothesis beyond the single value characteristics presented in **section 3.3.2**, I perform interneuron spike waveform clustering and assess the presence of distinct spike waveform clusters across different CA1 layers (see **Methods**). Clustering revealed six clusters across all detected interneurons in dorsal CA1 (**Figure 3.3.6a-b**). Visual inspection of the waveforms showed that the clusters differed mostly in waveform width, shoulder amplitude, and shoulder asymmetry

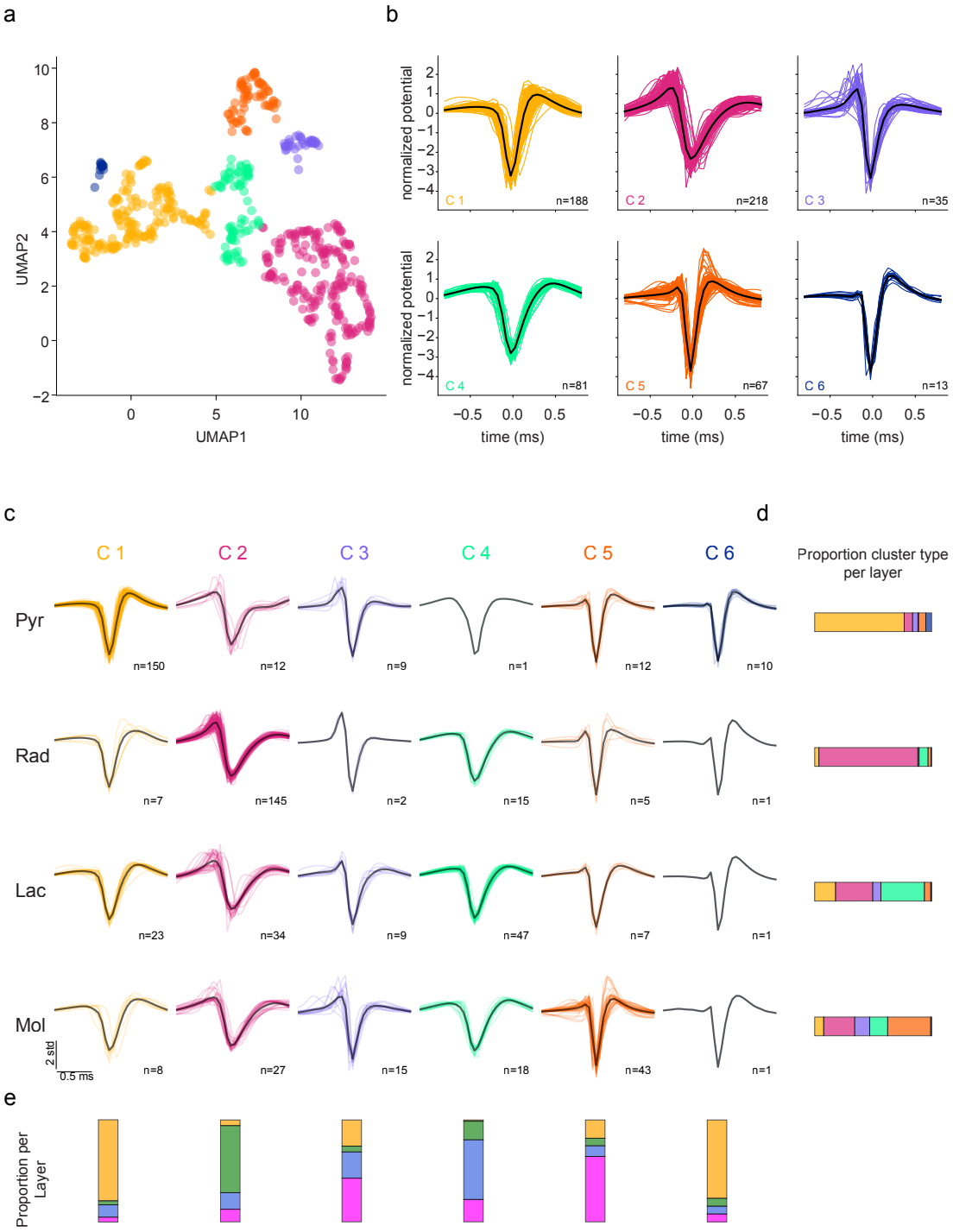


Figure 3.3.6 – Spike waveform shape clusters distribute differently across distinct layers of dorsal CA1

a) UMAP embedding of waveform characteristics. Colour coding indicates waveform cluster yellow: cluster 1, pink: cluster 2, purple: cluster 3, light green: cluster 4, orange: cluster 5, and dark blue: cluster 6. **b**) Mean waveforms per waveform cluster. Mean waveform per waveform cluster in black, waveforms of individual neurons are depicted in the cluster colour. Number of neurons per cluster is annotated in the bottom right corner. Colour coding as in **a**). **c**) Mean waveforms per waveform cluster per recording layer. Rows present the waveforms per cluster recorded in a particular layer. Mean waveform per waveform cluster in black, waveforms of individual neurons are depicted in the cluster colour. Number of neurons per cluster is annotated in the bottom right corner. »

» **d**) The proportion of neurons belonging to a particular cluster for every recording layer. Colours correspond to the cluster colours as in **a-c**). Note the higher heterogeneity in the strata lacunosum and moleculare. **e**) The proportion of neurons recorded in a particular layer for every waveform cluster. Colours indicate the layer (yellow: pyramidale, green: radiatum, blue: lacunosum, magenta: moleculare). Note that some clusters are not equally distributed across layers.

(**Figure 3.3.6b**). Waveform Cluster 1 displayed a narrow waveform with a flat first shoulder (left peak before the negative deflection) and a prominent right shoulder. Cluster 1 was the second largest cluster consisting of 46.4% of all waveforms, and 79.4% of all cluster 1 waveforms found in stratum pyramidale (**Figure 3.3.6c, e**). Cluster 2, the largest cluster (53.8%), was characterised by a prominent left shoulder, a wide waveform, and a broad rounded right shoulder (**Figure 3.3.6a**). Similar to cluster 1, the vast majority of cluster 2 waveforms were found in one layer: the stratum radiatum (65.7%; **Figure 3.3.6c, e**). In addition, out of all waveforms detected in radiatum, 84.6% belonged to cluster 2 (**Figure 3.3.6c, d**). Cluster 3 represents a smaller cluster (8.6% of all interneurons) and can be distinguished based on the prominent sharp left shoulder, a narrow waveform, and an angular but flat right shoulder (**Figure 3.3.6b**). In contrast to earlier clusters, cluster 3 spike waveforms were distributed across multiple layers (Pyr: 25.7%, Rad:5.7%, Lac:25,7%, and Mol:42.9%; **Figure 3.3.6e**). Out of all waveforms, 20% was allocated to cluster 4, which was characterised by flat and round left and right shoulders, and a wide waveform. As for cluster 1 and 2, cluster 4 waveforms were biased to one layer, with most detected waveforms found in stratum lacunosum (58.5%), while virtually absent in stratum pyramidale (1.2%; Rad:18.3%, Lac:22.0%; **Figure 3.3.6c-e**). Cluster 5 had a narrow waveform, with a sharp but low amplitude left shoulder, and a prominent right shoulder. Despite some similarities with cluster 1's waveform, members of this cluster are mostly found in stratum moleculare (64.2%) and to a lesser extent in pyramidale (17.9%), radiatum (7.5%), and lacunosum (10.4%; **Figure 3.3.6b-c**, **e**). Lastly, cluster 6, a cluster sharing traits with cluster 1, has a narrow appearance a left angular left shoulder and a prominent, pointy right shoulder. This cluster comprised of the fewest number of spike waveforms and nearly all were found in the stratum pyramidale (Pyr: 76.9% 10/13; (**Figure 3.3.6b-c**, **e**). With different waveform clusters found across different layers, I assessed the waveform heterogeneity per layer (**Figure 3.3.6d**). This revealed that stratum pyramidale (C1: 76.5%, C2: 7.1%, C3: 4.6%, C4: 0.5%, C5: 6.1%, and C6: 5.1%) and radiatum (C1: 3.6%, C2:

84.6%, C3: 1.0%, C4: 7.7%, C5: 2.6%, and C6: 0.5%) were mostly populated by spike waveforms from one cluster, while stratum lacunosum (C1: 17.8%, C2: 31.8%, C3: 7.0%, C4: 37.2%, C5: 5.4%, and C6: 0.8%) and moleculare (C1: 7.7%, C2: 26.5%, C3: 12.8%, C4: 15.4%, C5: 36.8%, and C6: 0.9%) housed multiple clusters (**Figure 3.3.6d**). Together, these data further underscore that the dorsal CA1 superficial interneuron population displays distinct spike waveforms that are not equally distributed across the layers. These different waveforms may reflect distinct neuronal types. Overall, this analysis shows that spike waveforms in stratum pyramidale and radiatum are less heterogeneous compared to the strata lacunosum and moleculare.

In summary, I clustered interneurons recorded in dorsal CA1 based on their waveform characteristics. This revealed 6 clusters varying most in the duration and shoulder amplitude. Interestingly, these clusters were not equally distributed across different layers. This results in differences between the heterogeneity of waveforms found per layer, with the most heterogeneous groups being found in the most superficial layers. Together, these data confirmed that distinct waveform shapes differentially distribute along the radial axis of dorsal CA1.

3.4 Discussion

In this Chapter, I recorded from superficial interneurons utilising our tetrode-depth estimation approach (see **Chapter 2**) to navigate the strata pyramidale, radiatum, lacunosum, and moleculare, which resulted in a substantial number of simultaneously recorded units across these layers in freely moving mice and provided a global scaffolding aidding direct comparison between mice. I explored the stability and validity of the units recorded as well as the spike waveform shapes across the different layers. This analysis revealed that units recorded across the superficial layers are equally stable and better isolated compared to the pyramidale units. In addition, waveform clustering showed that the most superficial layers feature multiple waveform types. Together, this indicated that distinct waveform types cluster across depth.

By mapping recorded neurons into a depth estimation space, I found a stark contrast between the number of recorded units per tetrode in the stratum pyramidale compared to the superficial layers.

Stratum pyramidale tetrodes recorded most units and pyramidal neuron/interneuron ratios matched earlier reports (Henze et al., 2000; Royer et al., 2012). For the superficial layers, the expected number of detected neurons per recording site has, to my knowledge, not yet been reported. Nevertheless, the sharp decrease in the number of recorded neurons across the superficial layers compared to the stratum pyramidale aligns with the estimated neuron densities in these regions (Bezaire and Soltesz, 2013). The reported global estimates, however, suggest that the number of neurons declines as a function of distance from the pyramidale (Bezaire and Soltesz, 2013), which is not reflected by this dataset. This decline may not be observed due to the targeted recordings rather than random sampling along the axis. Alternatively, electrophysiological differences could introduce differential detection levels in different layers. Due to the extracellularly recorded signals containing mixed electrical activity, spike sorting may be biased towards neurons that would be more easily discriminable from the background activity, such as those with larger intrinsic spike waveform amplitudes (Ye et al., 2023). The spike waveforms in the stratum moleculare for example are smaller than those in the pyramidale, most likely reflecting neuronal subtypes with differences in soma size (Price, 2005; Capogna, 2011). Furthermore, spike waveform amplitudes are dependent on the distance of the soma to the recording electrode (Buzsáki et al., 2012), which may result in different soma-to-electrode distance detection ranges across different neuronal types. Together, the different number of units recorded along the radial axis is most likely driven by layer-specific cell densities, but to a lesser extent may be influenced by subtype-specific intrinsic electrophysiological characteristics that bias detection probability.

Spike detection in extracellularly recorded signals is challenging, especially in freely moving mice, given that the spikes need to be extracted from a noisy signal dominated by population currents and movement-related artefacts (Lewicki, 1998; Pachitariu et al., 2024). Two problems that may interfere with reliable spike detection are the recording stability as well as the spike validity. Given that I record from different layers with different properties it would have been possible that recordings are not equally stable across the layers. Stability measures, however, reveal that the spike waveform amplitudes do not show any signs of differential tetrode drift or instability, indicating equally stable recordings across all layers. Even though spike waveforms

are equally stable, the source of the detected spike waveforms could still be of non-neuronal or non-somatic origin, such as positive spike waveforms, which are considered to have axonal or dendritic sources (Sun et al., 2021; Someck et al., 2023). The highest number of positive spikes were detected in CA1's input layers, supporting the idea that positive spikes are non-somatic. Furthermore, spike isolation is another challenge in extracellular recordings given that the origin of the spike needs to be reconstructed based on the spike waveform across different channels (Lewicki, 1998; Pachitariu et al., 2024). Refractory period violation scores, which are assumed to be caused by mis-clustered spikes originating from other neurons or invalid, artefactual spikes (Hill et al., 2011), suggest that superficial interneurons are better isolated compared to those detected in the pyramidale. The better-isolated superficial are likely a result of the low neuron densities in these layers. Thus, superficial interneurons can be reliably recorded over hours using tetrodes and succesfully isolated from multi-source signals.

Alongside the challenges of detecting spikes, extracellular recordings do not easily permit discrimination between different neuron types due to the 'blind' character of this recording approach. In literature, this challenge has been taken on by attempts to discriminate neuronal types based on distinct spike waveform shapes (Roux et al., 2014; Petersen et al., 2021; Sun et al., 2021; Ye et al., 2023). By combining electrophysiological recordings with optogenetics it has been confirmed that specific neuronal categories can be discriminated based on spike waveform (Petersen et al., 2021; Ye et al., 2023). Given that, in contrast to amplitude, shoulder asymmetry and spike width do not seem to be affected by the distance between the electrode and the recorded neuron, these features may be most suitable to infer neuronal types (Stark et al., 2013; Weir et al., 2015; Petersen et al., 2021; Lopes-dos-Santos et al., 2023). The most common neuron classification applied to electrophysiological data is the split between putative pyramidal neurons and inhibitory groups based on spike waveform width, among which trough-to-peak time (Stark et al., 2013; Petersen et al., 2021; Lopes-dos-Santos et al., 2023). However, most of these classification rules, especially for the hippocampus, have been designed for the stratum pyramidale and, up until now, it has been unclear whether these rules are generalisable across regions and layers. Interestingly, the custom classification model available in the laboratory labelled only a minority of the neurons

recorded in the superficial layers as putative interneurons (Lopes-dos-Santos et al., 2023), while in literature nearly all neurons in the superficial layers are GABAergic (Freund and Buzsáki, 1996; Klausberger and Somogyi, 2008). This mismatch indicates that superficial interneurons do not follow the same classification rules as pyramidale interneurons. This is further emphasized when spike waveform characteristics are compared across layers, which shows that distinct waveform features are significantly different across layers (**Figure 3.3.4**). These different waveforms could possibly be leveraged to guide neuron classification in extracellular recording along the radial axis of dorsal CA1.

Dorsal CA1 houses a plethora of different interneuron types and layer-specificity of these interneuron types, which are mostly based on molecular expression patterns or morphology, has been extensively reported in literature (Freund and Buzsáki, 1996; Pelkey et al., 2017; Booker and Vida, 2018). Given that different cell types can display unique spike waveform shapes (Stark et al., 2013; Roux et al., 2014; Petersen et al., 2021; Scala et al., 2021), the spike waveform differences found in this Chapter may reflect different interneuron types across the different layers. As suggested by the lack of transferability of the neuron classification rules, spike waveforms across the superficial layers differ from those of pyramidale interneurons. Furthermore, when projecting the spike waveforms into a lower dimensional space, individual spike waveforms form clusters together based on layer, which may reflect distinct interneuron types found in literature (Freund and Buzsáki, 1996; Pelkey et al., 2017; Booker and Vida, 2018). In addition, one waveform holds enough information to predict the recording layer above chance levels. These different analyses indicate that waveforms from the same layer are more similar to each other compared to those from other layers. This does not imply, however, that all spike waveforms in a given layer are the same. Interestingly, the kNN classifier performed better compared to the NB classifier, especially in discriminating lacunosum from moleculare neurons. The NB classifier misclassifying interneurons recorded across the most superficial layers could be a result of spike waveforms across these layers being similar. However, if this were the case, one would expect the kNN classifier to fail too. The kNN classifier successfully discriminating between lacunosum and moleculare above chance level argues against a lack of discriminative features

between neurons recorded in these layers. Alternatively, failure of the NB classifier and not the kNN classifier could be evidence of more varying populations in lacunosum and moleculare. The NB classifier, for example, intrinsically does not work well on heterogeneous populations, while the kNN classifier is more resistant to within-group heterogeneity. The idea that classifier performance differences could be caused by population heterogeneity is further supported by variation between waveform characteristics across individual neurons (see **section 3.3.2** and **3.3.3**). Together, my results suggest that superficial interneurons display a vast heterogeneity in waveform characteristics which cluster at different depths along the radial axis of dorsal CA1 and may reflect distinct interneuron types.

Different interneuron types have been described across all CA1 layers (Freund and Buzsáki, 1996; Somogyi and Klausberger, 2005; Pelkey et al., 2017; Booker and Vida, 2018), but spike waveform clustering revealed little heterogeneity in the strata pyramidale and radiatum (**Figure 3.3.3**). Several factors could cause this lack of variety. First, in the laboratory's preprocessing pipeline, units recorded in the pyramidale are split into putative pyramidal neurons and interneurons based on trough-to-peak time (see **Methods**), which reduces the perceived heterogeneity in this layer. Second, the main occupiers of the strata oriens and pyramidale – PV-positive and SST-positive neurons – are not equally distributed among these layers. SST-positive neurons are biased towards the oriens (Somogyi and Klausberger, 2005; Chamberland et al., 2024), while my recordings mostly targeted the pyramidale, possibly resulting in an underrepresentation of members from the SST-positive family. Alternatively, the discrepancy between the known number of interneuron types and the number of detected waveform clusters in the pyramidale could result from different types in this layer having more similar waveforms. PV-positive and SST-positive neurons are the main occupiers of the strata oriens and pyramidale and can be found closer in transcriptomic space compared to other types (Harris et al., 2018). Given that transcriptomic profiles are closely related to action potential shape (Földy et al., 2016), it could be possible that pyramidale interneurons display more subtle differences compared to distinct superficial interneurons types, as has been reported in the cortex (Scala et al., 2021; Bugeon et al., 2022). In addition, a broad range of waveforms was included in my clustering analysis. This possibly forces waveforms into coarser

clusters, concealing subgroups featuring nuanced differences. Together, several methodological and biophysical factors, or a combination thereof, can cause a lower waveform variability in strata pyramidale than expected based on previously defined types.

Similar waveforms do not exclude the possibility of originating from different types, differing waveforms, however, are likely to represent different neuronal groups (Petersen et al., 2021; Scala et al., 2021). Therefore, the spike waveform heterogeneity in stratum lacunosum and moleculare may reflect the diverse population residing in these layers but ground-truth data to assign waveform to the appropriate types is not available. Since spiking characteristics of distinct hippocampal types are known (Klausberger and Somogyi, 2008), spike waveform clustering could be aided by spiking characteristics, such as firing rate, bursting, or other autocorrelation patterns, to improve neuronal type identification (Royer et al., 2012; Roux et al., 2014). Experiments combining extracellular recordings and type-specific identification, such as opto-tagging approaches, are required to further refine our understanding of spike waveform and neuron type relationships and serve as ground truth in extracellular waveform identification libraries. Furthermore, it has been proposed that higher-density extracellular recordings are more suited to discriminate between subtle spike waveform differences (Ye et al., 2023), which may further improve waveform-based identification. In conclusion, spike waveform shapes reflect distinct neuron types and, despite requiring refinement in the future, could aid neuron type identification in extracellular recordings.

In summary, in this Chapter, I simultaneously recorded from over ~2500 units across different layers of dorsal CA1 and assessed the spike waveform stability, validity, and characteristics. I found that units recorded in the superficial layers of dorsal CA1 are equally stable and better isolated compared to the stratum pyramidale but tend to be more often from non-somatic origin. Furthermore, superficial interneuron waveform shapes are significantly different from those in the stratum pyramidale, which prevents the usage of standard interneuron classification rules. Interestingly, different layers feature unique waveform shapes, which could reflect distinct neuronal types across the layers. Together, the simultaneous recordings along with the depth estimation framework allowed me to pool data across multiple mice and recording days, as well

as the proven quality of the recordings and distinct waveform shapes, form a strong foundation to further study superficial interneurons and their role in dorsal CA1.

Chapter 4. Spike characteristics of superficial interneurons in dorsal CA1 are spatially organised

4.1 Introduction

Interneurons play a key role in the hippocampal network and are thought to guide information processing (Lapray et al., 2012; Royer et al., 2012; Siwani et al., 2018; Sakalar et al., 2022; Bilash et al., 2023). The large variety of interneuron types comes with stark differences in spiking characteristics, which may reflect distinct roles in shaping the hippocampal input-output function (Somogyi and Klausberger, 2005; Booker and Vida, 2018). Within the same type, neurons can show varying spiking behaviour in specific brain states, network events, or behaviour (Somogyi and Klausberger, 2005; Mizuseki and Miyawaki, 2017). Varying spiking behaviour under particular conditions signals, and likely supports, distinct network operations tailored to online demands such as memory encoding, retrieval, or consolidation. How interneurons play a role in shaping and supporting such processes is not fully understood. However, gaining insights into interneurons across CA1 layers during different brain and network states may provide answers.

Given that hippocampal interneurons have been shown to exert strong inhibitory control over pyramidal neurons (Grienberger et al., 2017; Valero et al., 2022), interneuron activity patterns may provide clues to better understand the function of distinct types. Spike characteristics of hippocampal neurons are often studied during oscillatory network events such as theta oscillations and sharp-wave ripples, which are most abundant during awake exploration and slow-wave sleep, respectively (Colgin, 2016). While pyramidal neurons tend to show more homogeneous population activity in such events (Csicsvari et al., 1999), interneurons display a wide array

of spiking activity (Klausberger and Somogyi, 2008). Different interneuron types have been shown to preferentially spike in separate phases of theta and display varying coupling strength (Klausberger et al., 2003; Klausberger, 2005; Fuentealba et al., 2008, 2010; Lapray et al., 2012). In sleep, sharp-wave ripples engage interneurons differentially, with most neurons responding to ripples with a spike rate increase, while others maintain their baseline firing rates (Lapray et al., 2012; Katona et al., 2014; Geiller et al., 2020; Dudok et al., 2021a, 2021b; Rangel Guerrero et al., 2024). Additionally, interneurons found in CA1's deeper layers show remarkable differences in firing rate and timing between awake and sleep states (Lapray et al., 2012; Katona et al., 2014). Together, this underscores the heterogeneous nature of interneuron activity, highlighting the importance of studying the spiking characteristics of interneurons to unravel their distinct roles in hippocampal function.

Despite interneurons in the hippocampus being subjects of many studies, historically the focus lies on interneurons in the deep layers, the strata pyramidale and oriens (Csicsvari et al., 1999; Royer et al., 2012; Dupret et al., 2013; Dudok et al., 2021b). Studies reporting on superficial interneurons mostly utilise *ex vivo*, juxta-cellular, or optical recording methods and genetic-targeting approaches, which restrain the subjects of study to single neurons or specific, molecularly defined, subpopulations (Vida et al., 1998; Price, 2005; Dudok et al., 2021a; Sakalar et al., 2022; Rangel Guerrero et al., 2024). To better understand the role of superficial interneurons in a network-wide framework, it is essential to record different types simultaneously. A recent study has attempted to take on this task by utilizing a pan-interneuron calcium imaging approach with *post hoc* molecular identification (Geiller et al., 2020). Despite this unprecedented opportunity to study interneurons in a global interneuron framework, calcium imaging restrained the temporal resolution and does not permit examination of spike dynamics at sub-theta or sharp-wave timescales. For these timescales, electrophysiological recordings would be more appropriate. Thus, more detailed studies are required to better understand the function of superficial interneurons in the context of their local circuitry.

Here, I try to understand the activity patterns of superficial interneurons in relation to the

well-studied interneurons in the stratum pyramidale and local network oscillations, utilising layer-targeted tetrode recordings. This approach permits studying all superficial interneurons from microcircuit to behavioural timescales across mice. I found that superficial interneurons display varying, layer-specific spike characteristics in time, oscillations, and behaviour and exhibit unique properties compared to pyramidale interneurons. Furthermore, superficial interneurons could be clustered in electrophysiologically defined subpopulations, some of which closely resemble spiking characteristics of previously defined interneuron types. Together, these characteristics form a solid foundation to further elucidate the function of superficial interneurons in the hippocampal network.

4.2 Methods

4.2.1 Mice, surgical procedure, and data acquisition

For this Chapter, the same dataset as presented in Chapter 3 was used, see the Methods section of Chapters 2 and 3 for a description of the included mice (**section 3.2.1**; **Table 3.2.1**), surgical and habituation procedures (**sections 2.2.2 - 2.2.5**), electrophysiological and tracking data acquisition methods (**section 2.2.6**), and behavioural protocol (**section 3.2.2**). In short, 17 mice were intracranially recorded using 14-tetrode microdrives over a total of 65 recording days (maximum 8 days per mouse). Mice were allowed to explore either familiar and novel open fields interleaved with sleep sessions or performed the cNOR task.

4.2.2 Data analysis

4.2.2.1 Software

All data were analyzed using custom code in Python 3.10, with the following packages: NumPy v1.24.3, Pandas v1.5.3, SciPy v1.10.1, Matplotlib v3.7.1, and Seaborn v0.21.2.

4.2.2.2 Data pre-processing and quality control

Signal pre-processing, spike sorting, and quality control were performed as described in Chapter 3. In short, after manual curation of the spike sorting, custom quality control filters were applied as well as a classification algorithm to segregate putative pyramidal neurons from putative pyramidal

interneurons (**section 3.2.3**, see also **section 3.3.1** for validation of these measures in superficial interneurons). Quality control was focussed on waveform shape and recording stability. Units with a biphasic index > 0, refractory period violation value >2%, and spike consistency value > 0.75 were excluded.

4.2.2.3 Detecting theta oscillations and sharp-wave ripples

Theta and sharp-wave ripple detection was performed as described in **sections 2.2.7.3** and **2.2.7.4**, and by Lopes-dos-Santos et al. 2023.

4.2.2.4 Detecting gamma oscillations

First, the tetrode closest to the estimated layer centre corresponding to the gamma of interest (slow-gamma: radiatum, mid-gamma: moleculare, superficial fast-gamma: lacunosum, pyramidale fast gamma: pyramidale) was selected per recording day for each hemisphere. If no tetrodes were found in the gamma-related layer, analysis of this gamma band was omitted for the corresponding hemisphere. Then, LFP signals were filtered for the gamma frequency bands (slow-gamma: 20-45Hz, mid-gamma: 50-100Hz, and fast gammas: 100-250Hz) using a 4th order Butterworth filter (butter function from the scipy signals package) as described in Lopes-dos-Santos et al., 2023. To extract instantaneous amplitude and phase, a Hilbert transform (hilbert function from the scipy signal package) was performed on the filtered signals. The top 25% of the strongest gamma amplitude theta cycles were selected to compute the gamma trough-triggered averages, spike-phase distributions, mean spike phase, and coupling strength.

4.2.2.5 Computing spike timing characteristics

Firing rates

Firing rates were computed over all awake and sleep sessions (**Figure 4.3.1**), within theta cycles (**Figure 4.3.3**), in sharp-wave ripples, or pre-ripple periods (**Figure 4.3.6**). For firing rates across the sessions, awake and sleep sessions were segregated. Then, the number of detected spikes was divided by the session length per session. When multiple sessions per state were included the weighted average of the firing rates was taken. The average rate across the theta cycle-triggered

instantaneous firing rate was used to obtain the firing rate within theta cycles. For firing rates within and before ripples, the ripple-triggered instantaneous firing rates were split into the average rate within the ripple window (20ms centred around the ripple power peak), and the average rate across a window from -500 to -200ms before the ripple, respectively.

Median inter-spike interval

The median inter-spike interval (median ISI) was computed as the median over the inter-spike intervals per neuron per recording session, across either awake or sleep recording sessions. When multiple sessions were included, an average weighted by session length was taken across the sessions within the same state.

Burst index

The Burst index was computed as the proportion of inter-spike intervals <8ms out of all inter-spike intervals per neuron per session, for all sessions. When multiple sessions were included, an average weighted by session length was taken across the sessions within the same state.

Coefficient of Variance

The coefficient of variance (CV) was computed as the standard deviation of the inter-spike intervals divided by the mean per neuron per session.

$$CV = \frac{std}{mean}$$

Coefficient of Variance 2

In addition to the CV, the coefficient of variance 2 (CV2) was computed to account for temporary changes in firing rate deviating from a baseline state, for example, during behaviourally driven epochs while still capturing burst-like spiking behaviour (Holt et al., 1996; Levenstein et al., 2021). In brief, the absolute difference between two subsequent ISI is multiplied by 2 and divided by the sum of the two ISIs, which are then averaged to reduce this measure to a single value per neuron.

$$CV2 = \frac{1}{\mathrm{n} - 1} \sum_{i=1}^{n-1} \frac{2 \bullet |ISI_{i+1} - ISI_i|}{ISI_{i+1} + ISI_i}$$

Mean theta phase

To correct for the asymmetrical shape of theta oscillations, which results in an overrepresentation of part of the theta phases in time, the theta cycle was binned in 64 bins, and the spike probability per phase bin was normalised to the phase count in the corresponding bin (Lopes-dos-Santos et al., 2023).

Theta coupling strength

Theta coupling strength was computed using the mean vector length, with each phase bin centre weighted by its assigned probability (Lopes-dos-Santos et al., 2023).

Gamma trough-triggered LFP and spike averages

Gamma trough-triggered LFP and spike averages are obtained by averaging LFP signal or spike activity centred around a single trough per gamma burst detected in selected theta cycles (see **section 4.2.2.4**).

Mean gamma phase, coupling strength and spike-phase distribution

Spike-phase distributions, mean spike phase, and coupling strength (mean vector length) are computed by extracting the spike phases per neuron for the selected theta cycles (see **section 4.2.2.4**). To construct spike-phase distributions, the spike probability per phase bin was computed over 16 equally spaced phase bins.

Spike probability in theta and sharp-wave ripple

Spike probability was computed as the proportion of theta cycles or sharp-wave ripples a neuron was active out of all theta cycles/sharp-wave ripples in the session.

Ripple response score

The ripple response score was computed as the mean z-scored firing rate of the ripple-triggered average in a 10-ms window centred around the ripple power peak.

Peak and mean spike number in ripples

The peak number was determined as the 95th percentile of the number of spikes per ripple across all ripples per neuron. While the mean spike number represented the average number of spikes per ripple.

4.2.2.6 Speed modulation analysis

Speed was computed as the distance travelled in pixels per tracking sample and converted to centimetres per second. To identify speed transitions, candidate transitions were identified as points in time where the speed exceeded or dropped below 4 cm/s for slow-fast and fast-slow transitions, respectively. Transition points were included if the average speed was below the speed threshold for 3 seconds before and 3 seconds above the threshold after the transition (slow-fast) or 3 seconds above the threshold before and below 3 seconds after the transition (fast-slow). Speed transition triggered averaged were obtained by down sampling the spike trained to the tracking sampling rate and averaging the activity in a 15-second window around the transition.

Spike rate changes before and after transitions were calculated as follows:

$$spike\ change = \frac{activity_{post} - activity_{pre}}{activity_{baseline}}$$

With $activity_{pre}$ being the mean spike activity over 3 seconds before the speed transition (t_0-3 to t_0), $activity_{post}$ the mean spike activity over 3 seconds after the speed transition (t_0 to t_0+3), and $activity_{baseline}$ the mean activity in a baseline window ($t< t_0$-5 and $t> t_0$+5). In addition, Speed modulation was computed by obtaining Spearman's correlations coefficient across the instantaneous speed and spiking activity at a 1250 Hz sampling rate over the awake exploration sessions.

4.2.2.7 Clustering neurons based on spiking characteristics

Parameterisation and clustering were performed as described in Chapter 3 (see **section 3.2.3.7**). Here the following parameters were used: UMAP function with metric=euclidean, min_dist=.15, n_neighbors=15, n_components=2, random_state=25 and DBSCAN function with parameters: eps=.7, min_samples=15.

4.2.3 Statistical testing

Permutation testing and bootstrapped confidence intervals were obtained as described in Chapter 3 (see **section 3.2.3.8**). For all correlations, spearman's correlation coefficient was computed using Scipy's spearmanr function from the statistical functions module unless stated otherwise. Significance was assessed by obtaining a control distribution by computing the Spearman correlation between one original vector and one shuffled vector, which is repeated 1000 times. The p-value was calculated based on the probability of occurrence compared to the control distribution.

4.3 Results

4.3.1 Superficial interneurons display distinct temporal spike structures

To examine spike timing characteristics of superficial and pyramidale interneurons, I computed four spike timing characteristics across different layers in both awake exploration and sleep on my previously acquired multi-layer tetrode-based recording dataset (**Chapter 3**; **Figure 4.3.1a-g**). First, I examined firing rate across awake sessions, which revealed that pyramidale interneurons display the highest firing rates across all layers, with rates ranging from ~3 to ~20 Hz (median 9.5, 1st and 3rd quartiles 3.6 - 21.2 Hz). Superficial interneuron rates were lower and ranged from ~0.5 to ~10 Hz. Lacunosum neurons showed the highest rates among superficial interneurons (median 4.4, 1st and 3rd quartiles 1.3 - 9.0 Hz), followed by neurons in the moleculare and radiatum neurons (median, 1st and 3rd quartiles Mol: 2.0, 0.6 - 5.8; Rad: 1.0, 0.5 - 2.6 Hz; **Figure 4.3.1c, f**). In sleep, a similar structure was seen with the highest rates found in pyramidale interneurons (median 7.3, 1st and 3rd quartiles 2.7 - 13.8 Hz), followed by lacunosum, moleculare, and radiatum interneurons with the lowest median rates (median, 1st and 3rd quartiles Lac: 2.8, 0.9 - 6.8; Mol: 1.3, 0.4 - 3.8; Rad: 1.1, 0.7 - 2.5 Hz; **Figure 4.3.1d, g**).

Second, I computed the burst index, which captured the proportion of spikes belonging to a burst versus independent spikes (see **Methods**). This analysis revealed that the pyramidale interneuron population had the highest median burst index (median proportion 0.08, 1st and 3rd quartiles 0.033 - 0.148), indicating that this group has the largest proportion of bursts occurring during the

awake sessions (**Figure 4.3.1c, f**). Among the superficial interneurons, radiatum neurons were most bursty (median proportion 0.05, 1st and 3rd quartiles 0.025 – 0.091). Although the median burst index was similar for lacunosum and moleculare neurons, the latter group covered a wider range and displayed a bimodal distribution, with a portion of the neurons reaching more than 10% of their spikes being part of a burst (median proportion, 1st and 3rd quartiles Lac: 0.014, 0.006 – 0.036; Mol: 0.014, 0.005 – 0.074; **Figure 4.3.1c, f**). During sleep sessions, a similar relationship in burst index was found between the different layers. In the moleculare layer, a bimodal distribution was observed, with one portion aligning with the lacunosum neurons and a smaller portion of cells with >10% of their spikes being part of a burst (median proportion, 1st and 3rd quartiles PIn 0.095, 0.047 – 0.175; Rad 0.070, 0.038 – 0.111; Lac 0.012, 0.005 – 0.027; Mol 0.011, 0.004 – 0.062; **Figure 4.3.1d, g**).

Third, I computed the coefficient of variance (CV) and CV2 for sleep and awake states, both measures of spike regularity (**Table 4.3.1**, **Figure 4.3.1c-d**, **f-g**). The high CV values for radiatum and moleculare neurons during the awake state indicate that the spike trains of these groups display high variability, while lacunosum neurons have more regular spike patterns (median CV, 1st and 3rd quartiles PIn 1.295, 1.207 – 1.469; Rad 1.608, 1.336 – 1.987; Lac 1.221, 1.094 – 1.396; Mol 1.540, 1.199 – 2.189; **Table 4.3.1**). Interestingly, while CV2 followed the pattern revealed by CV analysis for pyramidale, radiatum, and lacunosum neurons, the moleculare population showed a median CV2 closer to 1, indicating that the high variability is more likely due to slower firing rate changes across the session rather than bursting (median CV2, 1st and 3rd quartiles PIn 0.985, 0.929 – 1.023; Rad 1.190, 1.135 – 1.253; Lac 0.984, 0.920 – 1.046; Mol 1.038, 0.955 – 1.149; **Figure 4.3.1c-d**, **f-g**). During sleep CV and CV2 patterns were very similar to those in awake (**Figure 4.3.1 c-d, f-g** and **Table 4.3.1**).

Lastly, I examined the ISI distributions in awake and sleep sessions. As a group, pyramidale interneurons showed short median ISIs (median 55.6, 1st and 3rd quartiles 25.0 - 176.4 ms),but appeared to consist of two populations, one with shorter ISIs with a peak around ~30 ms, while the second group had a peak at ~100 ms accompanied by a peak within the burst

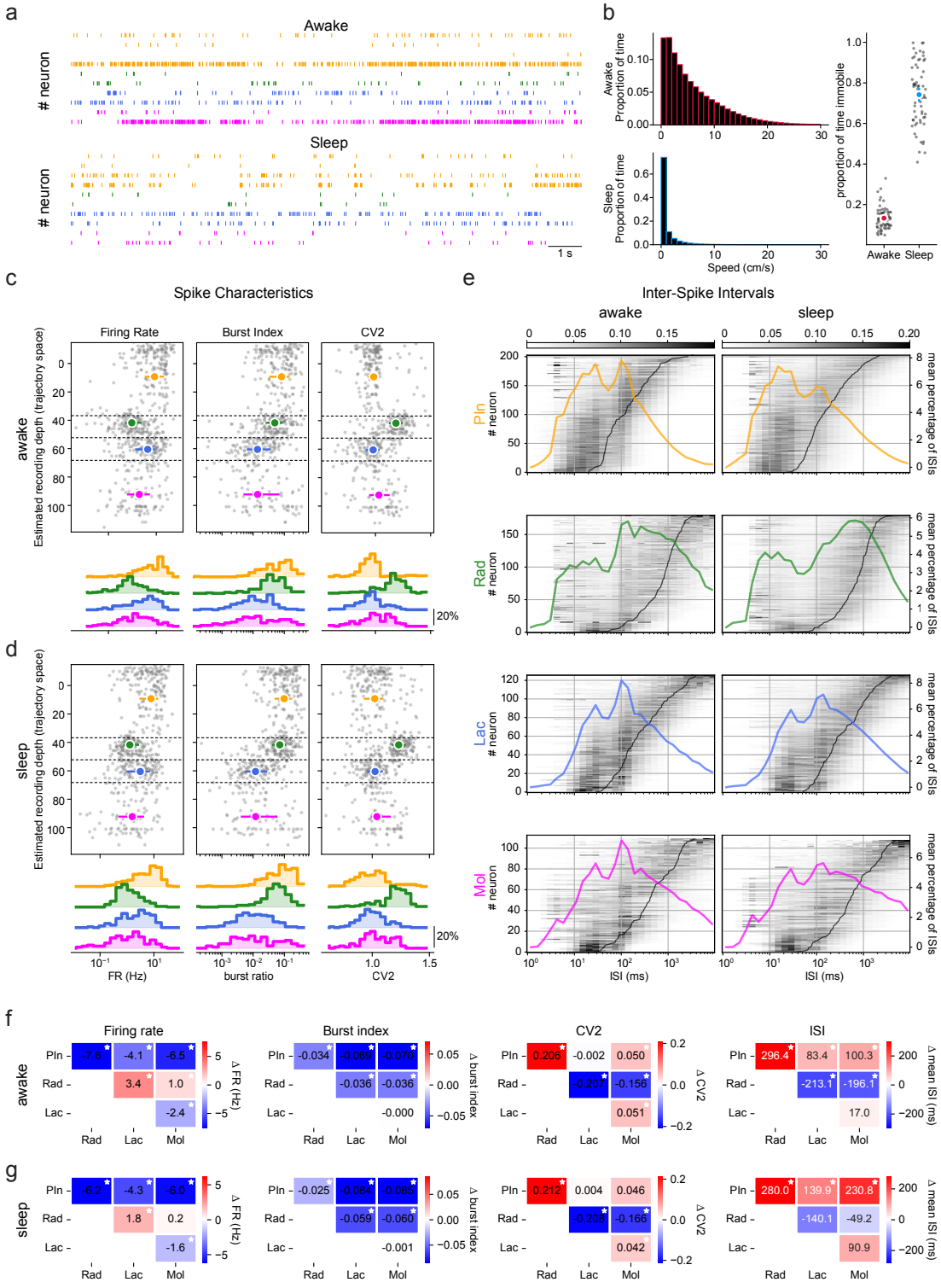


Figure 4.3.1 – Superficial interneurons display varying spike characteristics

a) Raster plot showing 15 seconds of simultaneously recorded neurons across nearly all layers. Tick colours indicate recording group (PIn: yellow, Rad: green, Lac: blue, Mol: magenta) for an awake and sleep session. **b**) Movement analysis confirms that the behavioural profile fits respective session types. Left: Histogram of the speed across the session for awake (red) and sleep (blue) sessions averaged across mice. Note the large variability of speeds in the awake session compared to the sleep session. Right: The proportion of time the mice were immobile (speed <1 cm/s). Individual data points represent the average per recording day, coloured marker indicates the group mean and the whiskers the 95%CI of the mean. »

» Mean proportion of time immobile, 95%CI of the mean: awake 0.12, 0.12 – 0.15; sleep 0.74, 0.71 – 0.78. **c**) Top: Scatter plots show firing rate (left), burst index (middle), and CV2 (right) as a function of estimated recording depth in the awake sessions. Datapoints represent individual neurons, coloured circles indicate the group median per layer-group, and the whiskers the 25th-75th percentiles. Colour-coding as in **a**) Bottom: histogram of the data presented in the top plot per layer-groups, colour code as in **a**). See **Table 4.3.1** for corresponding statistics. **d**) Same as in **c**) for the sleep sessions. See **Table 4.3.1** for corresponding statistics **e**) Heatmaps showing the inter-spike interval distributions for interneurons recorded across different layers for awake (left) and sleep (right) sessions. Rows represent inter-spike intervals (ISIs) of individual neurons sorted by median, shades indicate the percentage of ISIs per bin. The black line shows the median per neuron, and the coloured line the group average percentage; colour-coding as in **a**). For illustration purposes, the ISIs exceeding the histogram boundaries (1ms – 10s) were not included in the histograms. Note the subpopulations with different ISI patterns in pyramidale, lacunosum, and moleculare, while radiatum neurons are more homogeneous. Group median ISI awake: median, 25th – 75th percentile (ms); PIn 55.6, 25.0 – 176.4; Rad 352.0, 139.0 – 817.4; Lac 138.9, 67.3 – 475.6; Mol 184.8, 54.7 – 760.3. Group median ISI sleep: median, 25th – 75th percentile (ms); PIn 57.4, 23.975 – 197.742; Rad 348.8, 137.3 – 622.2; Lac 197.3, 85.1 – 736.3; Mol 292.9, 74.5 – 1336.3. **f**) Heatmaps that show the median difference between layer groups across different characteristics for awake sessions. Values indicate the median difference (column group minus row group) and stars indicate significant differences. The p-values were obtained by permutation testing. The significance threshold was corrected for the number of comparisons per characteristic and brain state (threshold = 0.0083) Firing Rate, median difference (Hz), p-val: PIn vs Rad -7.6, $<10^{-5}$; PIn vs Lac -4.1, $<10^{-5}$; PIn vs Mol -6.5, $<10^{-5}$; Rad vs Lac 3.4, $<10^{-5}$; Rad vs Mol 1.0, $<10^{-5}$; Lac vs Mol -2.4, $<10^{-5}$. Burst index, median difference, p-val: PIn vs Rad -0.034, $<10^{-5}$; PIn vs Lac -0.069, $<10^{-5}$; PIn vs Mol -0.070, $<10^{-5}$; Rad vs Lac -0.036, $<10^{-5}$; Rad vs Mol -0.036, $<10^{-5}$; Lac vs Mol 0.0, 0.407. CV2, median difference, p-val: PIn vs Rad -0.206, $<10^{-5}$; PIn vs Lac -0.002, 0.474; PIn vs Mol 0.050, $<10^{-5}$; Rad vs Lac -0.207, $<10^{-5}$; Rad vs Mol -0.156, $<10^{-5}$; Lac vs Mol 0.051, $<10^{-5}$. ISI (ms), median difference, p-val: PIn vs Rad 296.4.1, $<10^{-5}$; PIn vs Lac 83.4, $<10^{-5}$; PIn vs Mol 100.3, $<10^{-5}$; Rad vs Lac -213.1, $<10^{-5}$; Rad vs Mol -196.1, 0.001; Lac vs Mol 17.0, 0.330. **g**) Same as in **f**) for the sleep sessions. Firing Rate, median difference (Hz), p-val: PIn vs Rad -6.2, $<10^{-5}$; PIn vs Lac -4.3, $<10^{-5}$; PIn vs Mol -6.0, $<10^{-5}$; Rad vs Lac 1.8, $<10^{-5}$; Rad vs Mol 0.2, 0.169; Lac vs Mol -1.6, $<10^{-5}$. Burst index, median difference, p-val: PIn vs Rad -0.025, $<10^{-5}$; PIn vs Lac -0.084, $<10^{-5}$; PIn vs Mol -0.085, $<10^{-5}$; Rad vs Lac -0.059, $<10^{-5}$; Rad vs Mol -0.060, $<10^{-5}$; Lac vs Mol -0.001, 0.381. CV2, median difference, p-val: PIn vs Rad -0.212, $<10^{-5}$; PIn vs Lac 0.004, 0.456; PIn vs Mol 0.046, 0.012; Rad vs Lac -0.208, $<10^{-5}$; Rad vs Mol -0.166, $<10^{-5}$; Lac vs Mol 0.042, 0.007. ISI (ms), median difference, p-val: PIn vs Rad 280.0, $<10^{-5}$; PIn vs Lac 139.9, $<10^{-5}$; PIn vs Mol 230.8, $<10^{-5}$; Rad vs Lac -140.1, 0.014; Rad vs Mol -49.2, 0.184; Lac vs Mol 90.9, 0.198.

range for some neurons (**Figure 4.3.1e**). The radiatum population had longer ISIs and showed a more homogeneous pattern across individual neurons, with the most prominent peak around 100-millisecond inter-spike intervals (median 352.0, 1st and 3rd quartiles 139.0 – 817.4 ms). Lacunosum neurons showed longer median ISIs of ~140 ms (median 138.9, 1st and 3rd quartiles 67.3 – 475.6 ms) but displayed a wide range. Visual inspection showed that one part of the lacunosum neurons displayed two prominent ISI peaks around 30 and 100 ms, while the other part showed longer median ISIs of ~1 second. The moleculare group had a median ISI of ~180 ms with an interquartile range of ~700 ms (median 184.8, 1st and 3rd quartiles 54.7 – 760.3 ms). Closer inspection showed that the wide range arose from three different ISI patterns. The first two

	Awake			Sleep		
Firing Rate (Hz)	**Median**	**25th percentile**	**75th percentile**	**Median**	**25th percentile**	**75th percentile**
PIn	9.7	3.6	21.2	7.3	2.7	13.8
Rad	1.0	0.5	2.6	1.1	0.7	2.5
Lac	4.4	1.3	9.0	2.9	0.9	6.8
Mol	2.0	0.6	5.8	1.4	0.4	3.8
Median ISI (ms)						
PIn	55.6	25.0	176.4	57.4	24.0	197.7
Rad	352.0	139.0	817.4	348.8	137.3	622.2
Lac	138.9	67.3	475.6	197.3	85.1	736.3
Mol	184.8	54.7	760.3	292.9	74.5	1336.3
Burst Index						
PIn	0.08	0.033	0.148	0.095	0.047	0.175
Rad	0.05	0.025	0.091	0.07	0.038	0.111
Lac	0.014	0.006	0.036	0.012	0.005	0.027
Mol	0.014	0.005	0.074	0.011	0.004	0.062
CV						
PIn	1.295	1.207	1.469	1.771	1.575	2.156
Rad	1.608	1.336	1.987	1.691	1.525	1.945
Lac	1.221	1.094	1.396	1.371	1.261	1.638
Mol	1.54	1.199	2.189	1.802	1.39	2.389
CV2						
PIn	0.985	0.929	1.023	1.019	0.926	1.102
Rad	1.19	1.135	1.253	1.232	1.172	1.295
Lac	0.984	0.92	1.046	1.024	0.952	1.09
Mol	1.038	0.955	1.149	1.066	0.996	1.184

Table 4.3.1 – Spike timing characteristics in awake and sleep

The table shows spike characteristics per interneuron group across different brain states

subgroups were similar to those described for the lacunosum population, while the third subgroup appeared to have a higher portion of ISIs in the bursts range and most ISI remained below ~120 ms. In awake sessions, the median ISI significantly differed between all groups except the lacunosum and moleculare neurons (**Figure 4.3.1f**). Conversely, in sleep, only the stratum pyramidale ISIs differed from the other groups (**Figure 4.3.1e**), while no significant ISI differences were observed between superficial interneurons (median, 1st and 3rd quartiles (ms); PIn 57.4, 23.975 – 197.742; Rad 348.8, 137.3 – 622.2; Lac 197.3, 85.1 – 736.3; Mol 292.9, 74.5 – 1336.3). Together, these four spike-timing characteristics show that neurons display distinct profiles across different CA1 layers and brain states.

4.3.2 Superficial interneurons show distinct spike timing characteristics in distinct brain states

Between awake and sleep states brain activity changes dramatically (Varga et al., 2012). To directly compare spike timing characteristics between awake and sleep, I examined changes in neuronal firing patterns in across brain states (**Figure 4.3.2**). In line with earlier reports (Lapray et al., 2012), pyramidale interneurons showed a higher firing rate in awake versus sleep states.

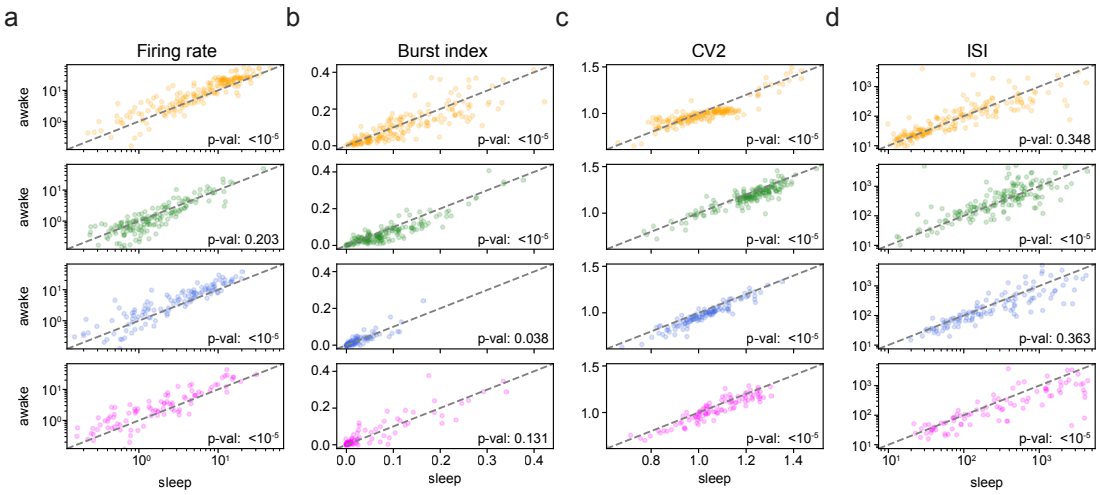


Figure 4.3.2 – Superficial interneuron spike characteristics differ across brain states

a) Scatter plots showing firing rates for awake sessions against sleep sessions per recording layer group. Data points represent individual neurons, colour coding indicates group (PIn: yellow, Rad: green, Lac: blue, Mol: magenta). The p-values are obtained through paired permutation testing between awake versus sleep sessions per layer group. Median firing rate differences (Hz; awake minus sleep), p-value: PIn 3.5, $<10^{-5}$; Rad 0.1, 0.203; Lac 1.9, $<10^{-5}$; Mol 1.7, $<10^{-5}$. **b**) Same as in **a**) for burst index. Burst index differences (awake minus sleep) median, p-value: PIn –0.015, $<10^{-5}$; Rad –0.015, $<10^{-5}$; Lac 0.002, 0.038; Mol 0.004, 0.131. **c**) Same as in **a**) for CV2. CV2 differences (awake minus sleep) median, p-value: PIn -0.028, $<10^{-5}$; Rad -0.030, $<10^{-5}$; Lac -0.038, $<10^{-5}$; Mol -0.034, $<10^{-5}$. **d**) Same as in **a**) for median ISI. Median ISI differences (ms; awake minus sleep) median, p-value: PIn –15.1, 0.348; Rad 273.4, $<10^{-5}$; Lac –29.9, 0.363; Mol –507.0, $<10^{-5}$.

Among the superficial interneurons, the lacunosum and moleculare neurons showed similar behaviour, and radiatum neurons did not change their firing rates significantly (median difference (Hz), p-value PIn 3.5, $<10^{-5}$; Rad 0.1, 0.203; Lac 1.9, $<10^{-5}$; Mol 1.7, $<10^{-5}$; **Figure 4.3.2a**). When comparing burst index, pyramidale interneurons showed a reduction in awake versus sleep sessions, indicating fewer ISIs in the burst range during awake states. Radiatum neurons showed a similar effect of state on burst index. The other superficial groups, however, showed no significant difference in burst index between awake and sleep (median difference, p-value: PIn –0.015, $<10^{-5}$; Rad –0.015, $<10^{-5}$; Lac 0.002, 0.038; Mol 0.004, 0.131; **Figure 4.3.2b**). The rhythmicity measure CV2 was significantly different for both pyramidale and superficial interneurons between awake and sleep, with all neuron groups showing lower CV2 during awake (median difference, p-value: PIn -0.028, $<10^{-5}$; Rad -0.030, $<10^{-5}$; Lac -0.038, $<10^{-5}$; Mol -0.034, $<10^{-5}$; **Figure 4.3.2c**). This indicates that interneuron spiking is more regular in awake versus sleep sessions across all recorded layers. Lastly, the median inter-spike intervals did not significantly change for pyramidale layer interneurons and lacunosum neurons, while radiatum median ISI

were higher in awake and moleculare lower in awake sessions (median difference (ms), p-value: PIn –15.1, 0.348; Rad 273.4, $<10^{-5}$; Lac –29.9, 0.363; Mol –507.0, $<10^{-5}$; **Figure 4.3.2d**). This showed that the ISI distributions change for some populations between awake and sleep, with radiatum neurons displaying longer and moleculare shorter ISIs in awake states. Together, these results show that spike rates and timing differentially change between awake and sleep states across the layers of the dorsal CA1.

4.3.3 Superficial interneurons display differential spiking behaviour in theta oscillations

Theta oscillations dominate the hippocampal LFP during awake exploration (Buzsáki, 2002). Hippocampal neurons have been shown to lock to these oscillations at different phases and strengths (Klausberger and Somogyi, 2008). To assess the behaviour of superficial interneurons in theta oscillations, I computed theta-associated firing rates, theta-coupling strength, and preferred phase for neurons across different recording layers (**Figure 4.3.3**). Pyramidale interneurons showed highest firing rates (mean 14.0, 95%CI of the mean 12.3 – 15.7 Hz). Across the superficial layers lacunosum and moleculare neurons had the highest rates and radiatum neurons the lowest (mean, 95%CI of the mean (Hz) Rad 2.6, 1.9 – 3.5; Lac 6.5, 5.3 – 7.6; Mol 4.9, 3.7 – 6.4; **Figure 4.3.3a-c**). For every individual neuron, the spike probability was computed as a function of phase (**Figure 4.3.3a, b**), which revealed that neurons display differential spiking behaviour in theta cycles across the different hippocampal layers. Pyramidale interneurons formed a homogeneous population preferentially spiking around the through of stratum pyramidale theta (mean 178.8°, 95%CI 174.9 –182.6°; **Figure 4.3.3a, b**). Conversely, across all superficial layers, a more heterogeneous population emerged showing a global pattern of gradual spike advancement in theta as a function of recording depth ranging from mean theta phase of ~220° in the radiatum to ~125° in moleculare (**Figure 4.3.3a-c**). Within the superficial layers, lacunosum and moleculare populations showed higher variability in mean theta phase evidenced by the larger confidence intervals of the mean, while nearly all radiatum neurons preferred spiking after the through (mean theta phase (degrees), 95%CI Rad 216.6, 209.7 – 223.2; Lac 177.2, 157.9 – 194.9; Mol 125.5, 109.0 – 142.1. In addition, I examined the theta coupling strength. Radiatum neuron spikes

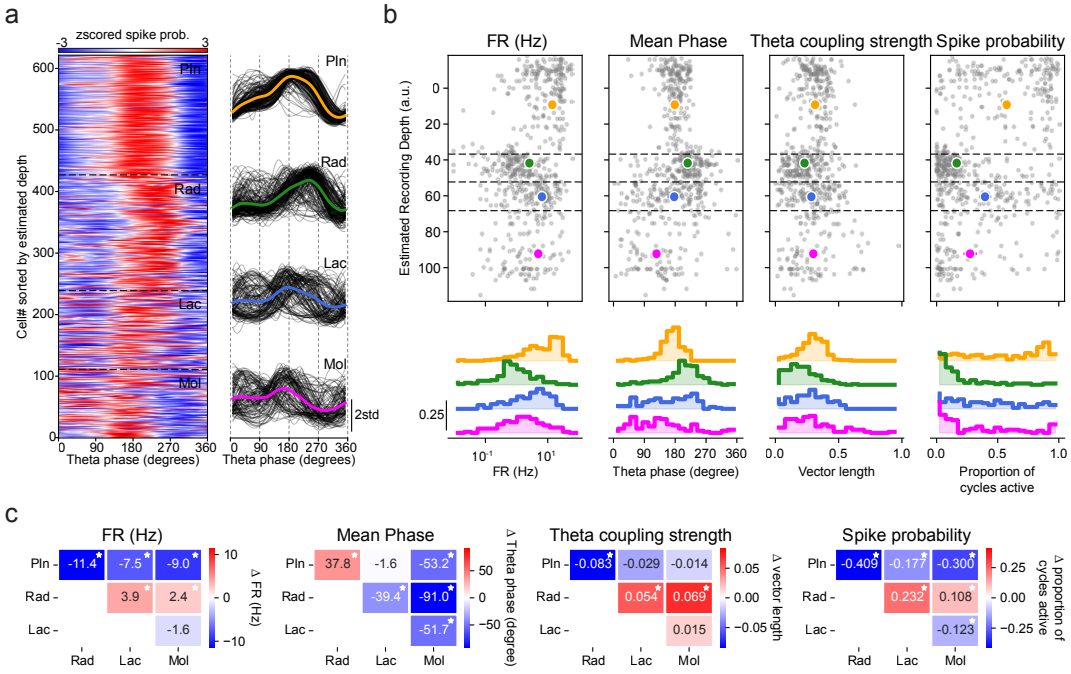


Figure 4.3.3 – Superficial interneurons display varying spiking behaviour in theta cycles

a) Left: Heatmap of the spike probability per neuron (rows) in theta oscillations (0 degrees represents the theta cycle peak) sorted based on estimated recording depth (in trajectory space). Dashed lines indicate the estimated layer borders. Right: Z-scored spike probability as a function of theta phase per recording layer group. The coloured lines indicate the group mean, and the black lines individual neurons. Colour-coding represents the recording layer (pyramidale: yellow, radiatum: green, lacunosum: blue, moleculare: magenta) **b**) Top: Scatter plots show different theta-related spike characteristics as a function of estimated recording depth. Datapoints represent individual neurons, coloured circles indicate the group mean, and the whiskers the 95%CI of the mean. Colour-coding as in **a**) Bottom: histogram of the data presented in the top plot per layer-groups, colour code as in **a**). Firing Rate: mean, 95%CI (Hz) PIn 14.0, 12.3 – 15.7; Rad 2.6, 1.9 – 3.5; Lac 6.5, 5.3 – 7.6; Mol 4.9, 3.7 – 6.4. Mean theta phase: mean, 95%CI (degrees) PIn 178.8, 174.9 – 182.6; Rad 216.6, 209.7 – 223.2; Lac 177.2, 157.9 – 194.9; Mol 125.5, 109.0 – 142.1. Theta coupling strength: mean, 95%CI PIn 0.314,0.300 – 0.327; Rad 0.231, 0.214 – 0.248; Lac 0.285, 0.259 – 0.309; Mol 0.299, 0.268 – 0.333. Spike probability: mean, 95%CI of the mean PIn 0.573, 0.530 – 0.617; Rad 0.165, 0.136 – 0.195; Lac 0.396, 0.346 – 0.447; Mol 0.273, 0.220 – 0.329. **c**) Heatmaps that show the mean difference between layer groups across different theta-related firing characteristics. Values indicate the mean difference (column group minus row group) and stars indicate significant differences. The p-values were obtained by permutation testing. The significance threshold was corrected for the number of comparisons per characteristic (p-value threshold = 0.0083) Firing Rate: mean difference (Hz), p-value: PIn vs Rad -11.4, $<10^{-5}$; PIn vs Lac -7.5, $<10^{-5}$; PIn vs Mol -9.0, $<10^{-5}$; Rad vs Lac 3.9, $<10^{-5}$; Rad vs Mol 2.4, 0.001; Lac vs Mol -16, 0.044. Mean theta phase: mean difference (degrees), p-value: PIn vs Rad -37.8, $<10^{-5}$; PIn vs Lac -1.6,0.384; PIn vs Mol 53.2, $<10^{-5}$; Rad vs Lac -39.4, $<10^{-5}$; Rad vs Mol -91.0, $<10^{-5}$; Lac vs Mol -51.7, $<10^{-5}$. Theta coupling strength: mean difference, p-value: PIn vs Rad -0.083 $<10^{-5}$; PIn vs Lac -0.029, 0.015; PIn vs Mol -0.014, 0.182; Rad vs Lac 0.054, $<10^{-5}$; Rad vs Mol 0.0689, $<10^{-5}$; Lac vs Mol 0.015, 0.240. Spike probability: mean difference, p-value: PIn vs Rad -0.409, $<10^{-5}$; PIn vs Lac -0.177, $<10^{-5}$; PIn vs Mol -0.300, $<10^{-5}$; Rad vs Lac 0.232, $<10^{-5}$; Rad vs Mol 0.108, $<10^{-5}$; Lac vs Mol -0.123, $<10^{-5}$.

coupled least to theta oscillations, while pyramidale, lacunosum and molecular populations show comparable mean coupling strengths (mean vector length, 95%CI of the mean PIn 0.314, 0.300 – 0.327; Rad 0.231, 0.214 – 0.248; Lac 0.285, 0.259 – 0.309; Mol 0.299, 0.268 – 0.333; **Figure 4.3.3b, c**). Lastly, I assessed the spike probability of each neuron in theta cycles. Pyramidale and lacunosum interneurons showed high spike probabilities with spikes in ~40 - 60% of the cycles, with some neurons reaching nearly one spike per cycle (mean probability, 95%CI PIn 0.573, 0.530 – 0.617; Lac 0.396, 0.346 – 0.447). Conversely, neurons in strata radiatum and moleculare were less likely to spike in theta cycles with, on average, spiking in less than 15% and 30% of the cycles, respectively (mean probability, 95%CI Rad 0.165, 0.136 – 0.195; Mol 0.273, 0.220 – 0.329; **Figure 4.3.3b, c**). Together, this data shows that superficial interneurons behave differently in theta cycles compared to pyramidale neurons and display layer-specific characteristics.

4.3.4 Superficial interneurons display differential spiking patterns in theta-nested gamma oscillations

In Chapter 2, I describe distinct gamma oscillations found across different CA1 layers (**Figure 2.3.3**; Lopes-dos-Santos et al., 2023), which have been shown to dictate hippocampal activity patterns at sub-theta time scales (Tukker et al., 2007; Sakalar et al., 2022; Lopes-dos-Santos et al., 2023). To examine the relationship between superficial interneurons and theta-nested gamma oscillations, I computed mean spike phase and coupling strength for neurons across different recording layers and gamma rhythms (see **Methods**). Pyramidale fast gamma mostly engaged pyramidale interneurons (PIn mean vector length 0.186, 95%CI 0.161 – 0.211), while superficial interneurons displayed low coupling strengths (mean vector length, 95%CI: Rad 0.079, 0.069 – 0.089; Lac 0.047, 0.040 – 0.055; Mol 0.070, 0.055 – 0.087; **Figure 4.3.4a-c, e**). Furthermore, pyramidal layer interneurons preferred to spike at the ascending phase of pyramidale fast-gamma (PIn mean phase 247.8, 95%CI 238.0 – 257.2 in degrees), followed by radiatum neurons (Rad mean phase 281.5, 95%CI 250.5 – 316.5 in degrees), while lacunosum and moleculare neurons displayed dispersed patterns evidenced by the large confidence intervals (mean phase, 95%CI (degrees): Lac 2.4, 0.7 – 359.3; Mol 355.1, 0.7 – 359.0; **Figure 4.3.4c, d**). Slow-gamma (detected in stratum radiatum) analysis revealed that neurons across all layers couple strongly to

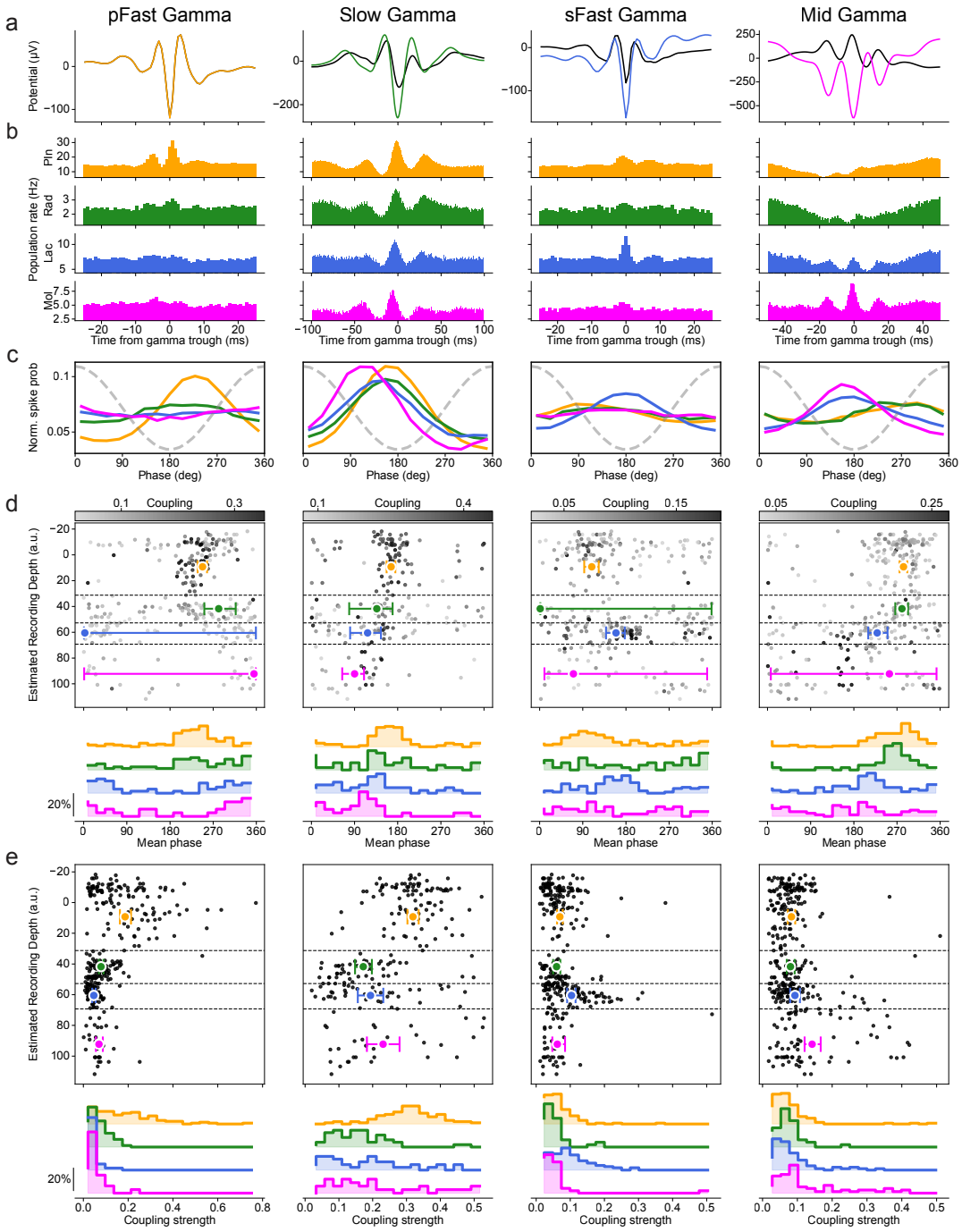


Figure 4.3.4 – Superficial interneurons display differential coupling to theta-nested gamma oscillations in CA1

a) Gamma trough-triggered LFP average for the tetrode in the gamma-associated layer (pyramidale fast gamma in pyramidale: yellow, slow gamma in radiatum: green, superficial fast gamma in lacunosum: blue, mid gamma in moleculare: magenta) and tetrode in stratum pyramidale (black). **b**) Gamma trough-triggered spike average for neurons across different recording layers (PIn: yellow, Rad: greed, Lac: blue, and Mol: magenta) in gamma oscillations corresponding to columns in **a**). Note the oscillatory pattern in spiking activity despite a single trigger (the largest gamma trough) per theta cycle. **c**) Spike-phase probability for neurons across different recording layers in gamma oscillations corresponding to columns in **a**). Lines show a population-average, in which data per neuron is weighted by its coupling strength, colour code same as in **b**). **d**) Top: Scatter plots showing the mean gamma phase as a function of estimated recording depth across different theta-nested gammas, with the columns corresponding to **a**). Datapoints represent individual »

» neurons with shading indicating coupling strength. Coloured circles indicate the group mean, and the whiskers 95% CI of the mean. Bottom: Histogram of data presented in the scatter plot per layer groups, colour-coding as in **b**). Mean gamma phase per recording layer (mean, 95% CI in degrees) Pyramidale fast gamma: PIn 247.8, 238.0 – 257.2; Rad 281.5, 250.5 – 316.5; Lac 2.4, 0.7 – 359.3; Mol 355.1, 0.7 – 359.0. Slow gamma: PIn 166.3, 156.1 – 175.6; Rad 136.4, 83.5 – 172.0; Lac 117.2, 83.3 – 144.1; Mol 90.1, 65.4 – 109.6. Superficial fast gamma: PIn 108.7, 93.9 – 124.1; Rad 1.2, 1.4 – 358.7; Lac 159.3, 137.3 – 180.0; Mol 70.4, 8.7 – 349.2. Mid gamma: PIn 283.6, 275.7 – 291.8; Rad 280.4, 267.2 – 293.0; Lac 228.7, 211.0 – 249.4; Mol 254.2, 7.7 – 353.0. **e**) Top: Scatter plots showing coupling strength as a function of estimated recording depth across different theta-nested gammas, with the columns corresponding to **a**). Datapoints represent individual neurons, coloured circles indicate the group mean, and the whiskers 95% CI of the mean. Bottom: Histogram of data presented in the scatter plot per layer groups, colour-coding as in **b**). Gamma coupling strength per recording layer (mean, 95% CI); Pyramidale fast gamma: PIn 0.186, 0.161 – 0.211; Rad 0.079, 0.069 – 0.089; Lac 0.047, 0.040 – 0.055; Mol 0.070, 0.055 – 0.087. Slow gamma: PIn 0.319, 0.302 – 0.336; Rad 0.172, 0.148 – 0.199; Lac 0.194, 0.154 – 0.230; Mol 0.231, 0.184 – 0.277. Superficial fast gamma: PIn 0.069, 0.062 – 0.079; Rad 0.060, 0.050 – 0.071; Lac 0.104, 0.091 – 0.116; Mol 0.062, 0.047 – 0.085. Mid gamma: PIn 0.083, 0.073 – 0.093; Rad 0.080, 0.070 – 0.092; Lac 0.093, 0.080 – 0.108; Mol 0.142, 0.119 – 0.166.

this oscillation, with pyramidale interneurons displaying the strongest coupling followed by the superficial interneurons (mean vector length, 95%CI: PIn 0.319, 0.302 – 0.336; Rad 0.172, 0.148 – 0.199; Lac 0.194, 0.154 – 0.230; Mol 0.231, 0.184 – 0.277; **Figure 4.3.4a-c, e**). The strong coupling is further corroborated by the oscillatory pattern seen in the gamma trough-triggered spiking activity, which displayed multiple peaks despite being triggered by a single trough per gamma burst (see **Methods**). While neurons across all layers were modulated by slow-gamma, most lacunosum and moleculare neurons preferred the descending phase of slow gamma, while most pyramidale interneuron spikes predominantly populated the trough (mean phase, 95%CI (degrees): PIn 166.3, 156.1 – 175.6; Rad 136.4, 83.5 – 172.0; Lac 117.2, 83.3 – 144.1; Mol 90.1, 65.4 – 109.6; **Figure 4.3.4c, d**). Furthermore, neurons in the stratum lacunosum displayed the strongest coupling to the in-lacunosum detected superficial fast-gamma (Lac mean vector length 0.104, 95%CI 0.091 – 0.116), followed by stratum pyramidale interneurons. Stratum pyramidale, radiatum, and moleculare neurons, on the other hand, displayed a lower coupling to superficial fast-gamma (mean vector length, 95%CI: PIn 0.069, 0.062 – 0.07; Rad 0.060, 0.050 – 0.071; Mol 0.062, 0.047 – 0.085; **Figure 4.3.4a-c, e**). Stratum pyramidale interneuron preceded stratum lacunosum neurons in superficial fast-gamma phase, which populated the mid-descending phase and trough (mean phase, 95%CI (degrees): PIn 108.7, 93.9 – 124.1; Lac 159.3, 137.3 – 180.0; **Figure 4.3.4c, d**), respectively. In contrast, the mean phase of stratum radiatum and moleculare

neurons was dispersed across the superficial fast-gamma cycle (mean phase, 95%CI (degrees): Rad 1.2, 1.4 – 358.7; Mol 70.4, 8.7 – 349.2; **Figure 4.3.4c, d**). For mid-gamma oscillations, stratum moleculare neurons showed the strongest coupling (Mol mean vector length 0.142, 95%CI 0.119 – 0.166), compared to neurons across other layers (mean vector length, 95%CI: PIn 0.083, 0.073 – 0.093; Rad 0.080, 0.070 – 0.092; Lac 0.093, 0.080 – 0.108; **Figure 4.3.4a-c, e**). While the mean preferred phase moleculare neuron population was dispersed across the mid-gamma cycle (Mol mean phase 254.2, 95%CI 7.7 – 353.0 in degrees), the neurons coupling strongest to this oscillation tend to prefer the late-descending phase (**Figure 4.3.4d**). Additionally, neurons across the other layers displayed a progressive phase delay from stratum lacunosum to stratum pyramidale (mean phase, 95%CI: PIn 283.6, 275.7 – 291.8; Rad 280.4, 267.2 – 293.0; Lac 228.7, 211.0 – 249.4; **Figure 4.3.4c, d**). Together, these data show that pyramidale and superficial interneurons differentially engage with local CA1 theta-nested gamma oscillations.

4.3.5 Superficial interneurons correlate differentially to speed

Hippocampal interneurons have been shown to differentially couple to the mouse's running speed (Dudok et al., 2021a; Rangel Guerrero et al., 2024). To investigate how superficial neuron firing rates correlate to speed, I analysed spike rate responses around start/stop transitions and examined the speed-spike rate correlations (**Figure 4.3.5a-h**). Pyramidale interneurons showed a homogeneous population which bidirectionally responded to start/stop transitions, with most neurons signalling Start transitions with a strong spike rate increase (positive response 88%; normalised mean spike change PIn 20.7, 95%CI 18.7 – 22.6) and Stop transitions with a decreased spike rate (negative response 88%; normalised mean spike change PIn -16.8, 95%CI -14.9 – -18.7; **Figure 4.3.5c-e**). Besides speed transitions, pyramidale interneurons showed a strong relationship between spike rates to speed as evidenced by the positive speed correlations (mean speed correlation, 95%CI 0.71, 0.63 – 0.77; **Figure 4.3.5f**). Among the superficial neurons, more heterogeneous responses were found, with neurons either increasing rate, decreasing rate, or non-responding around speed transitions (**Figure 4.3.5c-e**). Radiatum and lacunosum interneurons showed lower mean spike changes around both start and stop transitions (normalised mean spike change, 95%CI: Start Rad 5.4, 2.2 – 8.2; Lac 3.5, 0.41 – 6.6; Stop: Rad -3.0, -0.3 – -6.0; Lac –4.3, -1.3 – 7.1; **Figure 4.3.5c-**

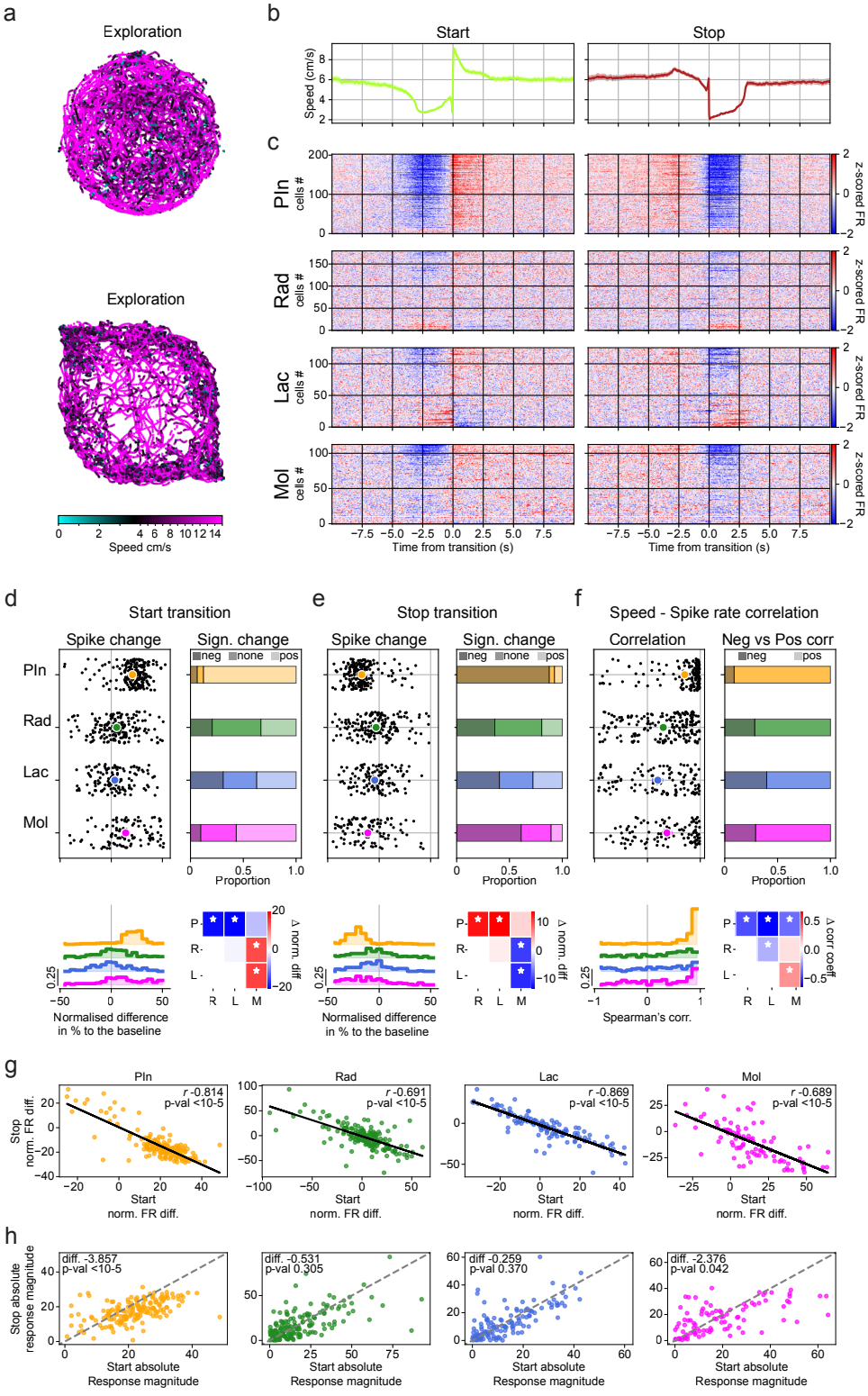


Figure 4.3.5 – Superficial interneurons correlate differently to speed

a) Examples of exploration sessions in different environments showing the mouse position tracking over time with instantaneous speed indicated by colours (colourmap is centred around 4 cm/s, with lower speeds in cyan and faster in magenta). Note the frequent speed transitions across the environment. **b**) Instantaneous speed triggered by speed transitions from slow to fast (Start; green) and from fast to slow (Stop; red). Note the sharp acceleration and deceleration around 0 ms from the transition. The solid line represents the mean speed across all mice and the shaded area indicates the 95%CI. »

» **c**) Speed transition-triggered neuronal activity shows speed-correlated activity patterns. Speed transition-triggered neuronal activity per neuron (rows) per recording layer centred around the start (left) and stop transitions (right). Neurons are sorted based on speed modulation (shown in **f**). Note the differential responses across the layers to speed transitions. **d**) Top left: Scatter plot showing normalized spike changes as a difference in percentage to the baseline activity for the start transitions. Individual data point represents neurons, the coloured data points the group means and the whiskers the 95%CI. Bottom left: histograms presenting the data from the corresponding scatter plot per recording layer, scalebar represents a proportion of 0.25. Mean spike change for start transitions, 95%CI; PIn 20.7, 18.7 – 22.6; Rad 5.4, 2.2 – 8.2; Lac 3.5, 0.41 – 6.6; Mol 14.1, 9.9 – 18.3. Top right: Bar graph showing the proportions of significantly positive (lightest shade), negative (darkest shade), and non-modulated (middle shade) neurons per interneuron group. Proportion negatively, none, positively modulated neurons: PIn 0.06, 0.06, 0.88; Rad 0.21, 0.46, 0.33; Lac 0.31, 0.32, 0.37; Mol 0.10, 0.33, 0.57. Recording layer is indicated by the bar colours (PIn: yellow, Rad: green, Lac: blue, Mol: magenta). Bottom right: Heatmap showing pairwise mean differences in spike rate change between interneuron groups (column group - row group). Colour indicates the difference, the star indicates significance. The p-value is obtained through permutation testing. Mean difference, p-val: PIn vs Rad -19.2, $<10^{-5}$; PIn vs Lac -20.1, $<10^{-5}$; PIn vs Mol -5.0, 0.036; Rad vs Lac -0.9, 0.400; Rad vs Mol 14.2, $<10^{-5}$; Mol vs Lac 15.0, $<10^{-5}$. **e**) Same as in **d**) for spike rate changes at Stop transitions. Scatter top left: Mean spike rate change, 95%CI; PIn -16.8, -14.9 – -18.7; Rad -3.0, -0.3 – -6.0; Lac –4.3, -1.3 – 7.1; Mol –11.0, -6.9 – -14.7. Bar plot top right: Proportion negatively, none, positively modulated neurons: PIn 0.88, 0.05, 0.07; Rad 0.36, 0.44, 0.20; Lac 0.40, 0.32, 0.28; Mol 0.61, 0.28, 0.11. Heatmap bottom right: Mean difference, p-val: PIn vs Rad 12.7, $<10^{-5}$; PIn vs Lac 13.7, $<10^{-5}$; PIn vs Mol 2.3, 0.161; Rad vs Lac 1.0, 0.426; Rad vs Mol -10.4, 0.006; Mol vs Lac -11.4, $<10^{-5}$. **f**) Same as in **d**) for Spearman's correlation coefficient between speed and spike rate across the sessions per interneuron group. Scatter top left: Mean correlation coefficient, 95%CI: PIn 0.71, 0.63 – 0.77; Rad 0.30, 0.22 – 0.38; Lac 0.20, 0.09 – 0.31; Mol 0.37, 0.27 – 0.47. Top right: Bar graph presenting the proportions of neurons negatively correlated (dark shades) and positively correlated (light shades). Proportion of negatively correlated neurons per group: PIn 0.09; Rad 0.28; Lac 0.40; Mol 0.29. Heatmap bottom right: Mean difference, p-val: PIn vs Rad -0.454, $<10^{-5}$; PIn vs Lac -0.660, $<10^{-5}$; PIn vs Mol -0.377, $<10^{-5}$; Rad vs Lac -0.206, 0.002; Rad vs Mol 0.078, 0.120; Mol vs Lac 0.283, $<10^{-5}$. **g**) Scatter plots per interneuron group which show Pearson's correlation between the spike rate change in Stop transitions and Start transitions. Individual data points represent neurons. The p-values are obtained through permutation testing, with the null distribution generated under the assumption that Start/Stop-group labels are ambiguous. **h**) Scatter plots per interneuron group depicting the response magnitudes (absolute spike rate change) in Start versus Stop transitions. Individual data points represent neurons. The p-values are obtained through permutation testing, with the null distribution generated under the assumption that Start/Stop-group labels are ambiguous. Note that the rate change magnitude is larger for Start than Stop transitions in pyramidale interneurons, with a trend in stratum moleculare. The p-value threshold was set at 0.013.

e). However, in both groups, a substantial number of neurons showed significant spike changes around start and stop transitions (Proportion positive, no, negative spike change Start: Rad 0.21, 0.46, 0.33; Lac 0.31, 0.32, 0.37; Stop: Rad 0.36, 0.44, 0.20; Lac 0.40, 0.32, 0.28; **Figure 4.3.5c-e**). The existence of counteracting groups was also reflected by lower mean speed-spike correlations and larger numbers of anti-correlated neurons (Mean correlation coefficient, 95%CI Rad 0.30, 0.22 – 0.38; Lac 0.20, 0.09 – 0.31; proportion of negatively correlated neurons Rad 0.28; Lac 0.40; **Figure 4.3.5f**). In contrast, moleculare interneurons showed higher mean spike rate changes in start/stop transitions and a higher positive speed-spike correlation (normalised mean spike

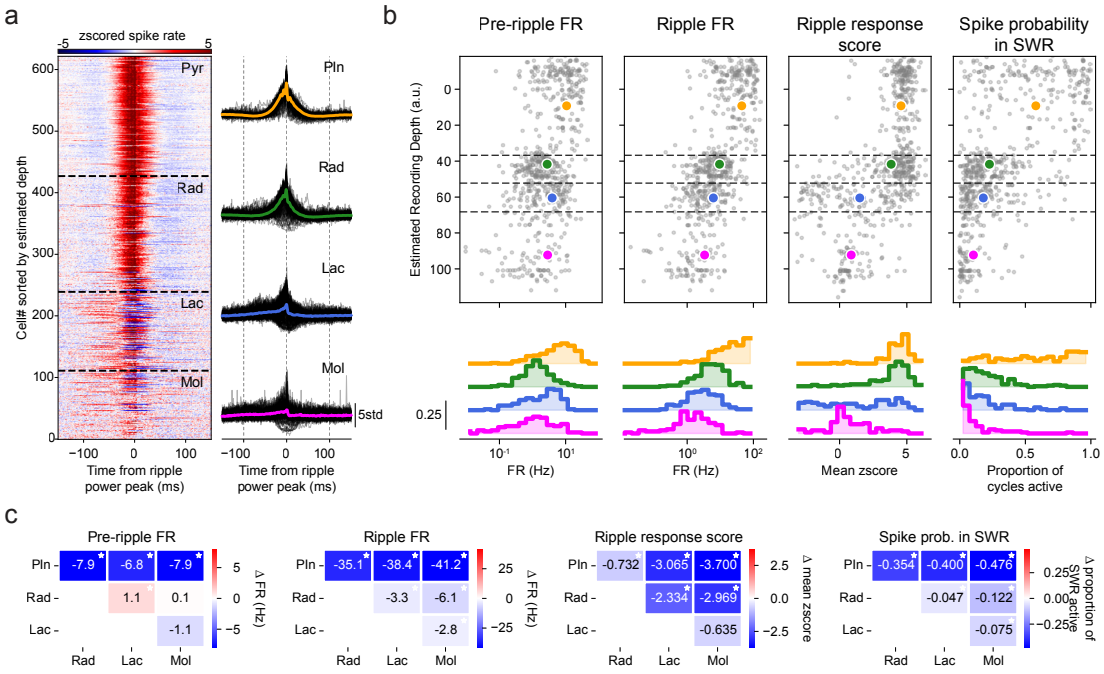


Figure 4.3.6 – Superficial interneurons display varying spiking behaviour in sharp-wave ripples

a) Left: Heatmap of the spike rate per neuron (rows) in sharp-wave ripples sorted based on estimated recording depth (in trajectory space). Dashed lines indicate the estimated layer borders. Note the heterogenous spike behaviour in stratum lacunosum and moleculare. Right: Z-scored spike rate centres around the ripple power peak per recording layer group. The coloured lines indicate the group mean, and the black lines individual neurons. Colour-coding represents the recording layer (pyramidale: yellow, radiatum: green, lacunosum: blue, moleculare: magenta). **b**) Top: Scatter plots show different sharp-wave ripple-related spike characteristics as a function of estimated recording depth. Datapoints represent individual neurons, coloured circles indicate the group mean, and the whiskers the 95%CI. Colour-coding as in **a**) Bottom: histogram of the data presented in the top plot per layer-groups, colour code as in **a**). Pre-ripple firing rate: mean, 95%CI (Hz) PIn 10.7, 9.4 – 12.0; Rad 2.8, 2.2 – 3.4; Lac 3.9, 3.3 – 4.6; Mol 2.9, 2.1 – 3.7. Ripple firing rate: mean, 95%CI (Hz) PIn 44.6, 39.5 – 49.8; Rad 9.5, 8.17 – 11.0; Lac 6.2, 4.9 – 7.7; Mol 3.4, 2.5 – 4.5. Ripple response score: mean, 95%CI PIn 4.56, 4.44 – 4.68; Rad 3.83, 3.57 – 4.08; Lac 1.50, 1.04 – 1.96; Mol 0.86, 0.54 – 1.19. Spike probability in ripples: mean, 95%CI PIn 0.58, 0.54 – 0.62; Rad 0.23, 0.20 – 0.25; Lac 0.18, 0.15 – 0.21; Mol 0.10, 0.08 – 0.13. **c**) Heatmaps that show the mean difference between layer groups across different ripple-related firing characteristics. Values indicate the mean difference (column group minus row group) and stars indicate significant differences. The p-values were obtained by permutation testing. The significance threshold was corrected for the number of comparisons per characteristic (p-value threshold = 0.0083) Pre-ripple firing rate: mean difference (Hz), p-value: PIn vs Rad -7.9, $<10^{-5}$; PIn vs Lac -6.8, $<10^{-5}$; PIn vs Mol -7.9, $<10^{-5}$; Rad vs Lac 1.1, 0.005; Rad vs Mol 0.1, 0.427; Lac vs Mol -1.1, 0.019. Ripple firing rate: mean difference (Hz), p-value: PIn vs Rad -35.1, $<10^{-5}$; PIn vs Lac -38.4, $<10^{-5}$; PIn vs Mol -41.2, $<10^{-5}$; Rad vs Lac -3.3, $<10^{-5}$; Rad vs Mol -6.1, $<10^{-5}$; Lac vs Mol -2.8, 0.001. Ripple response score: mean difference, p-value: PIn vs Rad -0.73, $<10^{-5}$; PIn vs Lac -3.07, $<10^{-5}$; PIn vs Mol -3.70, $<10^{-5}$; Rad vs Lac -2.33, $<10^{-5}$; Rad vs Mol -2.97, $<10^{-5}$; Lac vs Mol -0.64, 0.016. Spike probability in ripples: mean difference, p-value: PIn vs Rad -0.35, $<10^{-5}$; PIn vs Lac -0.40, $<10^{-5}$; PIn vs Mol -0.48, $<10^{-5}$; Rad vs Lac -0.05, 0.007; Rad vs Mol -0.12, $<10^{-5}$; Lac vs Mol -0.08, 0.016.

change, 95%CI Start 14.1, 9.9 – 18.3; Stop–11.0, -6.9 – -14.7; Mean correlation coefficient, 95%CI 0.37, 0.27 – 0.47; **Figure 4.3.5c-f**), and similar to pyramidale interneurons, moleculare neurons comprised a larger population that responded positively to start transitions (Proportion positive, no, negative spike change Start 0.10, 0.33, 0.57; Stop 0.61, 0.28, 0.11; proportion of negatively correlated neurons Mol 0.29; **Figure 4.3.5c-f**). Next, I examined whether pair-wise responses in start and stop transitions were correlated. Across all layers, start/stop transition spike rate changes were highly anti-correlated, indicating that neurons with the largest spike rate increases in start transitions showed the strongest rate reduction in stop transitions (**Figure 4.3.5g**). Lastly, I examined the rate change magnitude between start and stop transitions, which showed that pyramidale interneurons display larger rate increases in start transitions than rate reduction in stop transitions (**Figure 4.3.5h**). A similar trend was seen for moleculare neurons, while radiatum and lacunosum neurons showed symmetric responses (**Figure 4.3.5h**). Together, these data show that pyramidale and moleculare neuron spiking activity show a positive correlation with speed, while radiatum and lacunosum neurons display more varied responses, indicating diverse speed-spike relationships across distinct CA1 layers.

4.3.6 Superficial interneurons display differential spiking behaviour in sharp-wave ripples

Interneurons have been shown to respond to hippocampal sharp-wave ripples differentially (Klausberger and Somogyi, 2008). To examine this variability, I computed firing rates of pyramidale and superficial interneurons in and around ripples during sleep (**Figure 4.3.6**, see **Methods**). Pyramidale interneurons showed the highest firing rates in both pre-ripple periods as well as in ripples. While, across superficial layers, lacunosum neurons had the highest firing rates in pre-ripple periods and radiatum neurons in ripples (Pre-ripple mean rate, 95%CI PIn 10.7, 9.4 – 12.0; Rad 2.8, 2.2 – 3.4; Lac 3.9, 3.3 – 4.6; Mol 2.9, 2.1 – 3.7; Ripple mean rate, 95%CI PIn 44.6, 39.5 – 49.8; Rad 9.5, 8.17 – 11.0; Lac 6.2, 4.9 – 7.7; Mol 3.4, 2.5 – 4.5; **Figure 4.3.6a-c**; **Table 4.3.2**). In sharp-wave ripples, nearly all interneurons in the strata pyramidale and radiatum increased their firing rates compared to the pre-ripple rate (proportion positively responding PIn 0.97, Rad 0.89; **Figure 4.3.6a, b**; **Table 4.3.2**), which was further reflected by high positive ripple

	Mean	25th percentile	75th percentile
Pre-ripple FR (Hz)			
PIn	10.7	3.2	15.1
Rad	2.8	0.9	3.1
Lac	3.9	0.9	5.9
Mol	2.9	0.4	3.1
Ripple FR (Hz)			
PIn	44.6	13.2	68.4
Rad	9.5	3.6	11.8
Lac	6.2	1.8	8.1
Mol	3.4	0.9	4.1
Spike probability in Ripples (proportion)			
PIn	0.580	0.314	0.866
Rad	0.226	0.104	0.301
Lac	0.179	0.064	0.237
Mol	0.104	0.020	0.136
Mean number of spikes per ripple (n spikes)			
PIn	1.6	0.4	2.6
Rad	0.4	0.1	0.4
Lac	0.2	0.1	0.3
Mol	0.1	0.0	0.2
Peak spike number in ripples (n spikes)			
PIn	4.1	2.0	6.0
Rad	1.6	1.0	2.0
Lac	1.1	0.5	1.5
Mol	0.7	0.0	1.0
Ripple response score (rrs; mean z-score ripple peak)			
PIn	4.564	4.3	5.055
Rad	3.833	3.367	5.042
Lac	1.499	-1.07	3.888
Mol	0.864	0.08	1.91
Ripple response (proportion)			
	Reduction (rrs < -1.5)	No-response (-1.5 < rrs < 1.5)	Increase (rrs > 1.5)
PIn	0.0	0.030	0.970
Rad	0.028	0.083	0.889
Lac	0.183	0.325	0.492
Mol	0.080	0.602	0.319

Table 4.3.2 – Spike characteristics in sharp-wave ripples

The table shows spike characteristics per interneuron group
rrs = ripple response score

response scores (Ripple response score mean, 95%CI PIn 4.56, 4.44 – 4.68; Rad 3.83, 3.57 – 4.08; **Figure 4.3.6a, b**; **Table 4.3.2**). Pyramidale interneurons fired consistently multiple spikes per ripple, while superficial interneurons spiked less than 1 spike per ripple (Mean per ripple PIn 1.6, Rad, 0.4, Lac 0.2, Mol 0.1; **Table 4.3.2**). Stratum lacunosum and moleculare showed more heterogeneous responses, as these layers also comprised neurons that did not respond or reduced their rates in ripples (**Figure 4.3.6a-c**). In addition, this was reflected by the significantly lower firing rates and ripple response scores (Ripple response score mean, 95%CI Lac 1.50, 1.04 – 1.96; Mol 0.86, 0.54 – 1.19; **Figure 4.3.6a-c**). Interestingly, the stratum lacunosum housed most rate-reducing neurons (proportion PIn 0.0, Rad 0.028, Lac 0.183, Mol 0.080), while most non-responsive neurons were recorded in the moleculare (proportion PIn 0.030, Rad 0.083, Lac 0.325, Mol 0.602; **Figure 4.3.6a-c**; **Table 4.3.2**). In addition, the probability of neurons spiking

in a sharp-wave ripple event varied across the different layers, with pyramidale interneurons spiking in more than half of the ripples, while the spike probability in ripples reduced with depth (**Figure 4.3.6b, c**). Together, these data show that superficial and pyramidale interneurons respond differently to sharp-wave ripples and that engagement of neurons by sharp-wave ripples varies across layers.

4.3.7 Superficial interneurons cluster based on spike characteristics

In the previous sections, I showed that superficial interneurons comprise a heterogeneous population based on individual characteristics. To examine whether neuronal subpopulations display a 'feature signature', I performed dimensionality reduction and clustering based on five electrophysiological characteristics described above; namely, theta firing rate, mean theta phase, speed modulation, SWR firing rate, and ripple response score (**Figure 4.3.7**; **Table 4.3.3**). This analysis resulted in 7 electrophysiological clusters (e-clusters; **Figure 4.3.7a, b**). Unsurprisingly, these groups were distinguishable based on most characteristics used for clustering, showing largely different firing rates in theta and sharp-wave ripples, mean theta phase, and ripple response score (**Figure 4.3.7c**; **Table 4.3.3**, **Table 4.3.4**). Speed modulation was more variable within the groups, as reflected by overlapping distributions between clusters (**Figure 4.3.7c**). Cluster 1 comprised a homogeneous population characterised by high firing rates (Mean, 95%CI 20.7, 19.1 - 22.3 Hz; **Figure 4.3.7c**; see **Table 4.3.3** for descriptive statistics), preferentially firing just after the theta trough (Mean, 95%CI 187.1, 181.7 – 192.3 degrees), strong positive speed-spike correlations (Mean, 95%CI 0.912, 0.865 – 0.950), and strongly responding to ripples (Mean, 95%CI 4.756, 4.647 – 4.855). Cluster 2 was the most populated cluster and displayed lower firing rates compared to cluster 1 (Mean, 95%CI 6.6, 5.6 – 7.8 Hz), fired before the theta trough (Mean, 95%CI 159.0, 153.0 – 164.3 degrees), and responded strongly to ripples (Mean, 95%CI 3.952, 3.756 – 4.124). Clusters 3 and 4 showed low firing rates (Mean, 95%CI: Cluster 3: 1.3, 1.0 – 1.7; Cluster 4: 1.5, 1.1 – 1.9 Hz), preferred to spike at the ascending phase of theta (Mean, 95%CI Cluster 3: 231.4, 225.8 – 237.0; Cluster 4: 238.2, 230.3 – 246.9 degrees), and responded to ripples (Mean, 95%CI Cluster 3: 4.258, 4.130 – 4.384; Cluster 4: 3.178, 2.809 – 3.625), but differed in speed modulation with 3 being positively and 4 negatively correlated (Mean, 95%CI Cluster 3:

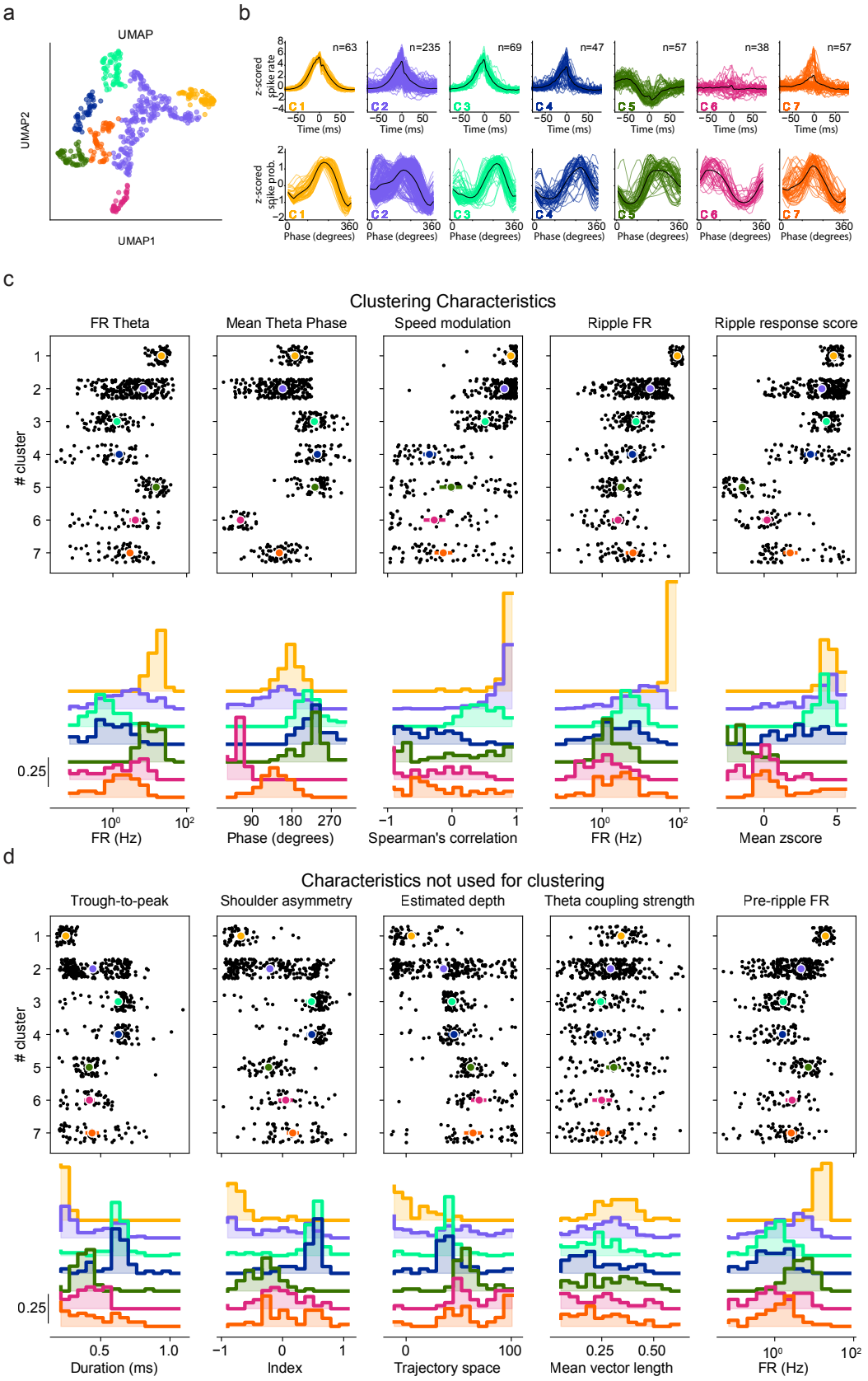


Figure 4.3.7 – Superficial interneurons can be clustered in electrophysiologically distinct groups

a) Scatter plot showing individual neurons projected into a lower-dimensional space based on UMAP embedding and DBSCAN clustering. Colour-coding indicates cluster as in **b**). »

» **b**) Top: line plots showing the z-scored instantaneous firing rates centred around the ripple power peak for different clusters. The black line indicates the mean and the coloured lines individual neurons. Bottom: same as top panels for the z-scored spike probability in theta cycles. **c**) Strip plots (top) showing different clusters across the features used for clustering. Data points indicate individual neurons, coloured points group means and the whiskers the 95% CI. Bottom: histograms depicting cluster distributions. Colour coding is the same as in **b**). see **Table 4.3.3** for corrsponding statistics. **d**) Same as in **c**) for features not included in clustering. Strip plots show different clusters across the features used for clustering. Data points indicate individual neurons, coloured points group means and the whiskers the 95% CI of the mean. Bottom: histograms depicting cluster distributions. Colour coding is the same as in **b**). see **Table 4.3.3** for corrsponding statistics.

Cluster	Mean	95%CI	
Theta firing rate			
1	20.7	19.1	22.3
2	6.6	5.6	7.8
3	1.3	1.0	1.7
4	1.5	1.1	1.9
5	14.9	13.0	17.0
6	4.1	2.7	5.5
7	2.9	2.3	3.6
Mean theta phase (degrees)			
1	187.1	181.7	192.3
2	159.0	153.0	164.3
3	231.4	225.8	237.0
4	238.2	230.3	246.9
5	232.8	224.2	240.6
6	62.6	56.4	68.9
7	151.3	143.1	160.1
Speed-spike rate correlation			
1	0.912	0.865	0.95
2	0.812	0.783	0.839
3	0.514	0.463	0.566
4	-0.351	-0.454	-0.252
5	-0.014	-0.189	0.159
6	-0.277	-0.447	-0.105
7	-0.136	-0.277	0.009
Ripple firing rate (Hz)			
1	84.8	80.0	90.1
2	17.0	15.3	18.9
3	7.4	6.4	8.4
4	6.0	4.4	7.9
5	3.1	2.5	3.7
6	2.6	1.8	3.5
7	6.2	4.1	8.5
Ripple response score			
1	4.756	4.647	4.855
2	3.952	3.756	4.124
3	4.258	4.13	4.384
4	3.178	2.809	3.625
5	-1.508	-1.772	-1.23
6	0.197	-0.159	0.57
7	1.779	1.296	2.274

Cluster	Mean	95%CI	
Trough-to-peak time (ms)			
1	0.249	0.239	0.259
2	0.444	0.421	0.467
3	0.627	0.598	0.656
4	0.627	0.588	0.664
5	0.418	0.392	0.443
6	0.419	0.383	0.456
7	0.438	0.392	0.489
Spike waveform shoulder asymmetry			
1	-0.682	-0.736	-0.617
2	-0.207	-0.278	-0.142
3	0.474	0.388	0.552
4	0.479	0.4	0.547
5	-0.228	-0.289	-0.158
6	0.052	-0.061	0.173
7	0.167	0.066	0.265
Estimated recording depth (trajectory space)			
1	5.1	1.0	9.3
2	35.6	31.2	40.4
3	43.6	40.2	46.8
4	45.5	40.3	50.6
5	61.4	57.6	65.2
6	69.5	62.3	77.1
7	63.7	54.9	72.1
Theta coupling strength (vector length)			
1	0.343	0.322	0.364
2	0.292	0.279	0.309
3	0.245	0.219	0.273
4	0.24	0.211	0.273
5	0.308	0.272	0.343
6	0.25	0.201	0.295
7	0.251	0.218	0.284
Pre-ripple firing rate (Hz)			
1	19.3	17.7	20.9
2	4.6	4.1	5.2
3	1.6	1.4	2.0
4	1.6	1.2	2.0
5	7.1	6.0	8.3
6	2.8	1.9	3.7
7	2.6	1.9	3.6
Burst index			
1	0.151	0.135	0.168
2	0.068	0.058	0.079
3	0.074	0.059	0.09
4	0.075	0.056	0.095
5	0.042	0.032	0.053
6	0.047	0.029	0.07
7	0.103	0.079	0.129

Table 4.3.3 – Spike characteristics of electrophysiological clusters

The table shows spike characteristics per feature and cluster corresponding to **Figure 4.3.7**.

	Mean difference						p-values						
Theta firing rate (Hz)													
Cluster	2	3	4	5	6	7	Cluster	2	3	4	5	6	7
1	-14.4	-20.0	-19.8	-6.3	-17.3	-18.4	1	$<10^{-5}$	$<10^{-5}$	$<10^{-5}$	$<10^{-5}$	$<10^{-5}$	$<10^{-5}$
2		-5.6	-5.4	8.0	-2.9	-4.0	2		$<10^{-5}$	$<10^{-5}$	$<10^{-5}$	0.013	$<10^{-5}$
3			0.1	13.6	2.7	1.5	3			0.304	$<10^{-5}$	$<10^{-5}$	$<10^{-5}$
4				13.5	2.5	1.4	4				$<10^{-5}$	$<10^{-5}$	$<10^{-5}$
5					-10.9	-12.1	5					$<10^{-5}$	$<10^{-5}$
6						-1.1	6						0.068
Mean theta phase (degrees)													
	2	3	4	5	6	7		2	3	4	5	6	7
1	-28.4	46.4	54.9	46.7	-129.7	-35.7	1	$<10^{-5}$	$<10^{-5}$	$<10^{-5}$	$<10^{-5}$	$<10^{-5}$	$<10^{-5}$
2		74.9	83.4	75.1	-101.3	-7.3	2		$<10^{-5}$	$<10^{-5}$	$<10^{-5}$	$<10^{-5}$	0.136
3			8.5	0.3	-176.2	-82.2	3			0.072	0.485	0.003	$<10^{-5}$
4				-8.2	-184.7	-90.6	4				0.105	0.158	$<10^{-5}$
5					-176.4	-82.4	5					0.022	$<10^{-5}$
6						94.0	6						$<10^{-5}$
Speed-spike rate correlation													
	2	3	4	5	6	7		2	3	4	5	6	7
1	-0.104	-0.403	-1.269	-0.981	-1.264	-1.053	1	$<10^{-5}$	$<10^{-5}$	$<10^{-5}$	$<10^{-5}$	$<10^{-5}$	$<10^{-5}$
2		-0.299	-1.164	-0.877	-1.160	-0.949	2		$<10^{-5}$	$<10^{-5}$	$<10^{-5}$	$<10^{-5}$	$<10^{-5}$
3			-0.865	-0.578	-0.861	-0.650	3			$<10^{-5}$	$<10^{-5}$	$<10^{-5}$	$<10^{-5}$
4				0.287	0.005	0.215	4				0.004	0.483	0.009
5					-0.283	-0.072	5					0.017	0.256
6						0.211	6						0.028
Ripple firing rate (Hz)													
	2	3	4	5	6	7		2	3	4	5	6	7
1	-73.3	-83.0	-84.5	-87.3	-88.0	-84.5	1	$<10^{-5}$	$<10^{-5}$	$<10^{-5}$	$<10^{-5}$	$<10^{-5}$	$<10^{-5}$
2		-9.7	-11.2	-14.0	-14.7	-11.2	2		$<10^{-5}$	$<10^{-5}$	$<10^{-5}$	$<10^{-5}$	$<10^{-5}$
3			-1.5	-4.3	-5.0	-1.5	3			0.065	$<10^{-5}$	$<10^{-5}$	0.097
4				-2.8	-3.5	0.0	4				0.001	$<10^{-5}$	0.500
5					-0.7	2.8	5					0.099	0.006
6						3.5	6						0.002
Ripple response score													
	2	3	4	5	6	7		2	3	4	5	6	7
1	-0.794	-0.496	-1.596	-6.466	-4.577	-2.846	1	$<10^{-5}$	$<10^{-5}$	$<10^{-5}$	$<10^{-5}$	$<10^{-5}$	$<10^{-5}$
2		0.298	-0.802	-5.672	-3.783	-2.052	2		0.034	$<10^{-5}$	$<10^{-5}$	$<10^{-5}$	$<10^{-5}$
3			-1.100	-5.970	-4.081	-2.350	3			$<10^{-5}$	$<10^{-5}$	$<10^{-5}$	$<10^{-5}$
4				-4.869	-2.981	-1.250	4				$<10^{-5}$	$<10^{-5}$	$<10^{-5}$
5					1.888	3.620	5					$<10^{-5}$	$<10^{-5}$
6						1.731	6						$<10^{-5}$

Table 4.3.4 – Comparative statistics of electrophysiological cluster spike characteristics

The table shows the pair-wise mean differences between clusters (column group minus row group) and the corresponding p-value on the right. Significance level was corrected for multiple testing per feature and was set at 0.002. Data corresponds to **Figure 4.3.7**. Table is continued at the next page.

0.514, 0.463 – 0.566; Cluster 4: -0.351, 0.252 – -0.454). Notably, clusters 5 and 6 showed distinct activity patterns in sharp-wave ripples, with cluster 5 including neurons reducing their spike rates in ripples and cluster 6 non-responsive neurons (Mean, 95%CI Cluster 5: -1.508, -1.772 – -1.230; Cluster 6: 0.197, -0.159 – 0.570), while other clusters mostly contained ripple-responding neurons. Cluster 7 seemed to overlap most with cluster 4 but showed a different mean theta phase and more non-responding neurons in ripples (Mean theta phase, 95%CI 151.3, 143.1 – 160.1 degrees; Ripple response score 1.779, 1.296 – 2.274). To further validate the clusters, I compared characteristics not included in the clustering (**Figure 4.3.7d**). Interestingly, clusters appeared to have different spike waveform characteristics (see also **Chapter 3**) and occupied different spaces along the radial axis of dorsal CA1 (estimated recording depth; **Figure 4.3.7d, s**ee **Table 4.3.4** for comparative statistics). Conversely, theta coupling strength did not differentiate between the

	Mean difference						p-values						
Trough-to-peak time (ms)													
Cluster	2	3	4	5	6	7	Cluster	2	3	4	5	6	7
1	0.238	0.378	0.370	0.169	0.201	0.214	1	<10-5	$<10^{-5}$	$<10^{-5}$	$<10^{-5}$	$<10^{-5}$	$<10^{-5}$
2		0.140	0.132	-0.069	-0.037	-0.024	2		0.007	0.081	0.081	0.387	0.454
3			-0.008	-0.209	-0.178	-0.164	3			0.360	$<10^{-5}$	$<10^{-5}$	$<10^{-5}$
4				-0.201	-0.169	-0.156	4				$<10^{-5}$	$<10^{-5}$	$<10^{-5}$
5					0.032	0.045	5					0.163	0.179
6						0.013	6						0.434
Spike waveform shoulder asymmetry													
	2	3	4	5	6	7		2	3	4	5	6	7
1	0.500	1.185	1.257	0.413	0.766	0.821	1	$<10^{-5}$	$<10^{-5}$	$<10^{-5}$	$<10^{-5}$	$<10^{-5}$	$<10^{-5}$
2		0.685	0.757	-0.087	0.266	0.321	2		$<10^{-5}$	$<10^{-5}$	0.155	0.004	$<10^{-5}$
3			0.072	-0.772	-0.419	-0.365	3			0.199	$<10^{-5}$	$<10^{-5}$	$<10^{-5}$
4				-0.844	-0.491	-0.437	4				$<10^{-5}$	$<10^{-5}$	$<10^{-5}$
5					0.353	0.407	5					$<10^{-5}$	$<10^{-5}$
6						0.054	6						0.291
Estimated recording depth (trajectory space)													
	2	3	4	5	6	7		2	3	4	5	6	7
1	31	40	42	58	65	65	1	$<10^{-5}$	$<10^{-5}$	$<10^{-5}$	$<10^{-5}$	$<10^{-5}$	$<10^{-5}$
2		9	11	27	34	35	2		0.012	0.012	$<10^{-5}$	$<10^{-5}$	$<10^{-5}$
3			2	18	25	25	3			0.255	$<10^{-5}$	$<10^{-5}$	$<10^{-5}$
4				16	23	23	4				$<10^{-5}$	$<10^{-5}$	$<10^{-5}$
5					7	7	5					0.054	0.064
6						0	6						0.473
Theta coupling strength (vector length)													
	2	3	4	5	6	7		2	3	4	5	6	7
1	-0.04	-0.10	-0.10	-0.04	-0.08	-0.09	1	0.006	$<10^{-5}$	$<10^{-5}$	0.034	0.002	$<10^{-5}$
2		-0.06	-0.06	0.00	-0.04	-0.04	2		$<10^{-5}$	0.001	0.396	0.060	0.012
3			0.00	0.06	0.02	0.01	3			0.460	0.005	0.243	0.294
4				0.06	0.02	0.01	4				0.008	0.253	0.272
5					-0.04	-0.05	5					0.109	0.032
6						-0.01	6						0.414
Pre-ripple firing rate (Hz)													
	2	3	4	5	6	7		2	3	4	5	6	7
1	-16.1	-19.2	-19.3	-13.8	-18.3	-18.3	1	$<10^{-5}$	$<10^{-5}$	$<10^{-5}$	$<10^{-5}$	$<10^{-5}$	$<10^{-5}$
2		-3.1	-3.2	2.3	-2.2	-2.2	2		$<10^{-5}$	$<10^{-5}$	0.002	0.001	$<10^{-5}$
3			-0.1	5.4	0.9	0.9	3			0.346	$<10^{-5}$	0.014	0.016
4				5.5	1.0	1.0	4				$<10^{-5}$	0.019	0.016
5					-4.5	-4.5	5					$<10^{-5}$	$<10^{-5}$
6						0.0	6						0.477
Burst index													
	2	3	4	5	6	7		2	3	4	5	6	7
1	-0.080	-0.077	-0.070	-0.109	-0.105	-0.048	1	$<10^{-5}$	$<10^{-5}$	$<10^{-5}$	$<10^{-5}$	$<10^{-5}$	0.002
2		0.003	0.010	-0.029	-0.025	0.033	2		0.386	0.235	0.002	0.047	0.012
3			0.007	-0.032	-0.028	0.030	3			0.310	$<10^{-5}$	0.019	0.023
4				-0.039	-0.035	0.023	4				0.001	0.020	0.114
5					0.004	0.061	5					0.355	$<10^{-5}$
6						0.057	6						0.001

Table 4.3.4 – Comparative statistics of electrophysiological cluster spike characteristics - continued

groups (**Figure 4.3.7d, s**ee **Table 4.3.4**). Overall, this indicates that different characteristics can form 'feature signatures' grouping superficial interneurons into electrophysiologically distinct groups which spatially segregate along CA1's radial axis.

4.4 Discussion

In this Chapter, I analysed simultaneously recorded CA1 interneuron activity at a temporal resolution of individual spikes, utilising layer-targeted tetrode recordings. This revealed that superficial interneurons exhibit unique electrophysiological signatures across hippocampal layers. Furthermore, superficial interneurons showed changes in their spiking behaviour between awake and sleep states, differentially engaged in network events such as sharp-wave ripples and theta oscillations, and varied in their relationship with movement. Together these findings emphasise

the heterogeneous nature of the hippocampal interneuron population and highlight previously underappreciated neuron populations in the most superficial layers of dorsal CA1.

It is well-known that hippocampal interneurons display a wide variety of spike timing characteristics (Klausberger and Somogyi, 2008), which are thought to provide clues to the network function they fulfil (Kepecs and Fishell, 2014). The data in this Chapter showed a wide range of spike rates across the interneuron population, which is in line with earlier reports on interneurons in dorsal CA1 (Klausberger, 2005; Fuentealba et al., 2010; Lapray et al., 2012; Katona et al., 2014; Rangel Guerrero et al., 2024). However, firing rates, inter-spike intervals, and rhythmicity measures revealed layer-based differences when I organised neurons based on recording depth. Despite nearly all neurons showing ISI peaks in the theta range, different ISI patterns emerged across layers, likely reflecting differential interneuron participation in other hippocampal rhythms (Colgin, 2016). Furthermore, I found a substantial proportion of burst-like (<8 ms) ISIs in stratum pyramidale, radiatum, and moleculare, while bursting is generally seen as a feature of pyramidal neurons (Grienberger et al., 2017; Petersen et al., 2021). However, burst-like ISIs have been previously reported for a subpopulation of deep CA1 interneurons (Csicsvari et al., 1999; Katona et al., 2014). These burst-like patterns may reflect genuine cell-intrinsic bursting but, given the burst detection criteria (ISI<8ms), participation in subsequent fast-gamma cycles (~5 ms-intervals) provides an alternative explanation (Lopes-dos-Santos et al., 2023). Together, overall spike timing and pattern analysis showed that interneurons display layer-specific spiking behaviour, which underscores the large heterogeneity between hippocampal interneurons and suggests spatial organisation of distinct network functions.

The recorded interneurons switched spiking behaviour in different brain states, as described previously (Lapray et al., 2012; Varga et al., 2012; Katona et al., 2014; Francavilla et al., 2018). Such changes were evident across all layers while the identified layer-based activity structure remained intact, indicating that activity pattern switching is globally directed. Conversely, layer-specific differences are more likely to arise from neuron intrinsic properties (Armstrong and Soltesz, 2012). Interneurons in the stratum oriens and lacunosum have been shown to express

particular neuromodulatory receptors (Chapman and Lacaille, 1999b; Buhler and Dunwiddie, 2002; Leão et al., 2012; Wyskiel and Andrade, 2016; Francavilla et al., 2018), resulting in distinct state-dependent spike patterns (Palacios-Filardo et al., 2021; Szabo et al., 2022). Additionally, interneuron behaviour depends on afferents they receive and can be differentially affected by the same upstream region (Milstein et al., 2015; Basu et al., 2016; Palacios-Filardo et al., 2021). Such neuron-specific characteristics combined with layer-specific afferents may result in layer-specific patterns found here. Together, these multi-interneuron recordings revealed layer-specific state-dependent spike characteristics, indicating layer-based differential network functions between brain states.

Several interneurons have been shown to preferentially spike in different phases of theta oscillations (Klausberger and Somogyi, 2008). I find a large variability between the mean spike-phase in theta across the recorded interneurons, reflecting the earlier reports (Fuentealba et al., 2008, 2010; Lapray et al., 2012; Katona et al., 2014). However, when sorted based on recording depth, I found that the mean spike phase of interneurons tends to advance in theta as a function of depth. These results could represent different interneuron types occupying different spaces along the radial axis of dorsal CA1. Alternatively, interneurons could follow the excitatory inputs which show a similar pattern with the most distal input arriving around the theta peak and moving towards the stratum pyramidale over the course of the theta cycle (Liao et al., 2024). Additionally, the theta coupling strength indicates that most neurons have well-defined parts of the cycle in which they are active. Combined with the layer-specific preferred phases, these findings could support the notion that hippocampal interneuron activity tiles the theta cycle to constrain pyramidal neuron activity in the trough (Somogyi and Klausberger, 2005; Klausberger and Somogyi, 2008). However, except for lacunosum neurons, few superficial interneurons faithfully spike in nearly every theta cycle, making it less likely that individual neurons are responsible for constraining pyramidal spiking in such manner. Alternatively, superficial interneurons could collectively perform this task, or their activity is not only intended to regulate pyramidal neuron output directly but to control inputs (Milstein et al., 2015; Palacios-Filardo et al., 2021; Bilash et al., 2023). Overall, this data revealed a layer- and recording depth-specific structure of superficial interneuron activity in theta cycles.

Interneuron activity and speed are correlated (Turi et al., 2019; Geiller et al., 2020; Dudok et al., 2021a; Rangel Guerrero et al., 2024). Superficial interneurons were differently related to speed, with the majority being positively correlated but depending on the layer up to ~40% showed a negative correlation to speed. This proportion is ~4 times higher than previously reported by Geiller and colleagues (Geiller et al., 2020). This study reported ~10% of neurons to be negatively correlated, which resembles the proportions found here in the stratum pyramidale. These discrepancies could originate from the fact that the detected neurons in the latter study seem to be biased toward the deeper layers of CA1. Across the superficial layers the number of negatively correlated neurons is highest in stratum lacunosum, a region well populated by cholecystokinin-positive interneurons, of which most are active during immobility (Dudok et al., 2021a; Rangel Guerrero et al., 2024). Interestingly, the stratum moleculare does not harbour neurons with such strong anti-correlation as strata radiatum and lacunosum, which is in line with the lack of CCK-positive neurons in this layer. Although molecular identity cannot be confirmed in the current experiments, it is likely that, at least part of the negatively correlated neurons belongs to the CCK-positive population. Notably, the largest proportion of strongly positively correlated interneurons was found in the strata pyramidale and moleculare, while the most heterogenous responses were found in the stratum lacunosum. It is unclear what drives these differences but given heterogeneous responses within the same layer, it is most likely that these differences are driven by cell intrinsic properties such as the expression of specific neuromodulatory receptors, or targeted inhibition (Armstrong and Soltesz, 2012; Melzer et al., 2012; Wyskiel and Andrade, 2016; Bilash et al., 2023). Overall, this data shows that neurons in the superficial layers display varying relationships with speed with the most heterogeneous population in the stratum lacunosum.

Sharp-wave ripples and sleep play an important role in memory consolidation and are associated with high-activity bursts (Buzsáki, 2015; van de Ven et al., 2016). Orchestrating this activity is essential and the emergence and termination likely rely on interneurons. Interneurons across CA1 have been shown to differently engage with sharp-wave ripples ranging from strong activity to being silenced during ripples (Klausberger and Somogyi, 2008). The interneurons recorded here, show similar responses but when organised as a function of depth an interesting pattern

emerged. While most neurons in the deep layers – the layers directly receiving strong inputs driving the ripples – show increased activity during the ripples, the neurons in lacunosum and moleculare comprised a substantial number of neurons that did not respond or even reduced their spiking activity. Although it is unclear why these neurons do not engage, it is hypothesised that the lack of inhibition on pyramidal neurons' distal dendrites facilitates plasticity and aids memory consolidation (Klausberger, 2009). In addition, the ripple-inhibited lacunosum interneurons increase their firing rate just before the ripple emerges in CA1, which could indicate that these interneurons put a temporary break on the strong inhibitory control and generate a window of opportunity for ripples to emerge (Evangelista et al., 2020), while their silence is essential to terminate the ripple. Lastly, the lack of ripple engagement in the moleculare could reflect reduced input onto this region (Liao et al., 2024). Overall, these data show that ripple responses are spatially well-organised and expand our understanding of local network computation during sharp-wave ripples.

In literature, defined interneuron types tend to present with distinct electrophysiological signatures representing a set of specific features. To examine how all the individual features assessed in this Chapter converge on individual neurons, I generated neuron clusters based on 5 predefined firing features. Interestingly, some obtained clusters seemed to relate to previously defined interneuron types. For example, the high firing rates, theta trough-firing, ripple-responding, and narrow waveform neurons in Cluster 1 likely comprise parvalbumin-positive basket cells (Lapray et al., 2012). Cluster five's theta-ascending, ripple-inhibited neurons mostly found in stratum lacunosum could represent a subpopulation of CCK-positive neurons (Klausberger, 2005; Dudok et al., 2021a). Additionally, Cluster 6 comprises theta-peak, ripple non-responding, neurons that are mostly found in the superficial layers, which strongly resemble features of neurogliaform neurons in CA1 (Sakalar et al., 2022). Due to the higher variability in Cluster 2, assigning one putative type is challenging as it displays features that fit CCK-basket, Ivy, and bistratified cells (Klausberger, 2005; Fuentealba et al., 2008; Katona et al., 2014). Notably, most clusters occupied specific regions along the radial axis of dorsal CA1, suggesting that electrophysiological signatures are not randomly dispersed across layers, consistent with results in Chapter 3 of spatially

clustered spike waveforms. However, whether these groups have differential functional network implications remains to be elucidated. Together, distinct electrophysiological characteristics converge on specific interneuron populations, likely reflecting described interneuron types.

In conclusion, leveraging layer-targeted tetrode recordings, I examined electrophysiological characteristics of hippocampal interneurons, which revealed a layer-based structuring of distinct characteristics. The layer-specific differences could be driven by uneven dispersion of interneuron types (Klausberger and Somogyi, 2008; Booker and Vida, 2018), while position-specific network connectivity dictating activity patterns may provide an alternative explanation (Kepecs and Fishell, 2014; Milstein et al., 2015; Tzilivaki et al., 2023). Nevertheless, these stark differences between interneuron spike characteristics across different layers indicate that inhibitory network function is spatially organised. Ultimately, these results underscore the intricate organisation of interneuron participation in the hippocampal network and lead to a better understanding of interneuron function.

Chapter 5. Superficial interneurons are differently targeted by CA3 and EC

5.1 Introduction

The hippocampus is a pivotal region for memory formation. It is a higher-order processing domain multiplexing high-dimensional sensory signals with previously stored information (Strange et al., 2014). Inevitably, the hippocampus receives a variety of afferents from different areas in the brain, all sending information that requires local orchestration (Witter et al., 2000; van Strien et al., 2009). Two well-known input regions to the CA1 region of the hippocampus are the intrahippocampal CA3 region and the extrahippocampal entorhinal cortex (Kajiwara et al., 2008; van Strien et al., 2009; Strange et al., 2014). Interestingly, the axonal projections remain highly segregated up until they reach the pyramidal neuron dendrites in CA1, with entorhinal cortex (EC) synapsing onto the distal part of the pyramidale dendrite in strata lacunosum and moleculare, and CA3 on the proximal dendrites in stratum radiatum (Kajiwara et al., 2008). Additionally, CA3 and EC are suggested to carry different information types (Hasselmo et al., 2002; Zutshi et al., 2022). Due to the varying electrogenesis rules along the pyramidal dendrites as well as specific subdomain-specific targeting by interneurons (Somogyi and Klausberger, 2005; Larkum et al., 2022), spatial segregation of CA3 and EC input likely plays a functional role in information processing by CA1 pyramidal neurons. Together, the spatial segregation of distinct inputs potentially allows the local CA1 network to control which input streams it is reading from.

The dendritic structure of hippocampal pyramidal neurons, combined with the afferents and interneurons targeting specific dendritic subdomains, facilitates information processing (Spruston, 2008; Lovett-Barron et al., 2012; Bilash et al., 2023). Inhibitory innervation supports

local dendritic computation by local shunting of excitatory currents, spatially and temporally constraining depolarising currents, and regulating the dendritic spike generation (Lovett-Barron et al., 2012; Palmer et al., 2012b, 2012a; Bloss et al., 2016; Shin et al., 2021; Bilash et al., 2023). Interneuron type-specific targeting of pyramidal neuron dendrites (Klausberger, 2009), suggests that these neurons can differentially influence and compartmentalise dendritic computations (Bloss et al., 2016). Furthermore, since most interneurons' somata and dendrites are found in the input layers of dorsal CA1, it is suggested that these interneurons mostly facilitate feed-forward inhibition (Buzsáki, 1984; Kullmann, 2011). Specialised dendritic targeting combined with feedforward connectivity patterns has led to the idea that these superficial interneurons could 'gate' the incoming information streams (Leão et al., 2012; Milstein et al., 2015; Basu et al., 2016; Grienberger et al., 2017). However, to better understand how these interneurons gate and aid information processing, it is essential to elucidate how superficial interneurons are recruited by their major afferents.

Ex vivo work has shown that interneurons receive inputs from Schaffer collateral or Perforant path-associated afferents (Price, 2005; Milstein et al., 2015; Basu et al., 2016), which originate from CA3 and EC, respectively. Some reports suggest that CA1 interneurons are not equally targeted along the radial axis, resulting in differential recruitment by CA3 or EC inputs (Kajiwara et al., 2008; Milstein et al., 2015). Conversely, other reports imply that interneuron soma location is not relevant for interneuron recruitment given their widely distributed dendritic arborization (Klausberger, 2005; Somogyi and Klausberger, 2005). However, if subsets of interneuron types are differentially recruited by distinct inputs, then these interneurons could form local subnetworks. Depending on axonal targeting pattern of recruited interneurons, their activity could bias the CA1 network to one of multiple 'competing' input sources (Leão et al., 2012; Lovett-Barron et al., 2014; Basu et al., 2016). In addition, it is suggested that neuromodulatory influence, such as acetylcholine release, can prioritise specific inputs either directly or through modulation of interneuron activity (Palacios-Filardo et al., 2021). This neuromodulation-specific effect on interneuron activity adds an extra dimension to the flexibility of the hippocampal network under distinct behavioural states (Chapman and Lacaille, 1999; Wyskiel and Andrade, 2016; Szabo et

al., 2022). Overall, interneurons are important regulators of the CA1 circuitry with superficial interneurons being perfectly positioned to regulate information flow from CA1 afferents to local pyramidal neurons. However, the intricate interplay between remote excitatory, inhibitory, and neuromodulatory input sources as well as local interneurons, and pyramidal neuron output in dorsal CA1 is not well understood.

Although it has been shown that CA3 and EC afferents recruit interneurons (Price, 2005; Milstein et al., 2015; Basu et al., 2016), these earlier reports are limited by the number of interneurons examined or tend to focus on a single interneuron type. Furthermore, most studies rely on electrophysiological recordings combined with electrical afferent stimulation (Lacaille and Schwartzkroin, 1988; Price, 2005). Although often presented as input-specific, this type of stimulation can activate any axon terminal despite its origin (Wouterlood et al., 1990; Dolleman-van der Weel et al., 2017). To gain an unbiased and input-specific overview of how CA3 and EC recruit local CA1 interneurons, I performed dorsal CA1-wide, interneuron-specific, anterograde transsynaptic tracing as well as *in vivo* electrophysiological connectivity mapping and found that CA3 and entorhinal cortex predominantly recruit interneurons with somata located in their target layers, stratum radiatum and lacunosum/moleculare, respectively. Furthermore, anatomical assessment suggested that the recruited populations comprise distinct but overlapping interneuron groups, and converge on the stratum lacunosum. Lastly, I found that interneuron recruitment by these major afferents was brain and network state-dependent, suggesting flexible information transfer. Together, these findings show that CA3 and EC recruit distinct but overlapping populations of local interneurons in CA1.

5.2 Methods

5.2.1 Animals

This study used fifteen male mice, aged 4 to 7 months, on a C57BL/6J genetic background (**Table 5.2.1**). Implanted mice were group-housed until the surgical procedure and single-housed after, while intracranially injected mice were housed in pairs after the surgery. All mice had access to food and water ad libitum, chew sticks, and nesting material and were held in individually

ventilated cages on a 12/12h light/dark cycle (lights on at 07:00), 19–23°C ambient temperature and 40–70% humidity. All experimental procedures performed in this study followed the Animals (Scientific Procedures) Act, 1986 (United Kingdom) and underwent ethical review by the Animals in Science Regulation Unit of the UK Home Office.

Mouse line	RRID	Number of mice	Genotype	Sex
Vgat-Cre	IMSR_JAX:016962	10	Heterozygote	Male
Grik4-Cre	IMSR_JAX:006474	2 1	Heterozygote Wildtype	Male
C57Bl6/J	IMSR_JAX:000664	2	Wildtype	Male

Table 5.2.1 – Mice used for anatomical and functional mapping experiments

5.2.2 Viruses

For anterograde tracing, heterozygote Vgat-cre mice were intracranially injected with three independent constructs to label anterogradely targeted GABAergic neurons in CA1 specifically (Zingg et al., 2017, 2020) (**Table 5.2.2**). To do so, a custom-made Cre-dependent FLPo-recombinase (AAV1-EF1a-cDIO-FLPo-Myc) was delivered into either CA3 or entorhinal cortex and a FLPo-dependent yellow fluorescent protein to CA1 (AAV5-EF1a-fDIO-EYFP-WPRE). In the first two injected subjects, a tdTomato-carrying construct was mixed in 1:1 ratio with the AAV1 construct to ensure injection site-visualization. For functional connectivity mapping, Grik4-cre heterozygote mice were injected in CA3 with a Cre-dependent Channelrhodopsin-2 driven by an EF1α-promotor and the wildtype mice with a CAMKII-promotor driven channelrhodopsin-2 in the entorhinal cortex at the coordinates described in **section 5.2.3.1**.

Experiment	Supplier Cat#	Viral construct	Volume (nL)	Titer (working dilution)	Internal code
Anterograde tracing	Custom see (Trouche et al., 2019)	AAV1-EF1a-DIO-FLPo-Myc	150-250	4.7x10e12	PPV325-1
Anterograde tracing	Addgene Cat# 59171	AAV2-Syn-ChrimsonR-tdT	150-250	1.9x10e12	DD031
Anterograde tracing	UNC Cat# AV6154B	AAV5-EF1a-fDIO-EYFP-WPRE	200	4.5x10e12	DD021-5
Functional connectivity	UNC Cat #AV3626	AAV2-EF1a-DIO-hChR2(H134R)-EYFP-WPRE	250	2.5x10e11	DD005-ChR2
Functional connectivity	Addgene Cat# 26969	AAV9-CAMKII-hChR2(H134R)-EYFP-WPRE-hGH	250	4.5x10e11	DD004-9_ChR2

Table 5.2.2 – Viruses used for anatomical and functional mapping experiments

5.2.3 Surgical procedures

5.2.3.1 Viral injection

Viral delivery was performed during a surgical procedure performed under isoflurane anaesthesia (induction at 4% and maintained at 0.5–2%) in O_2 (2 L/min) and peri-surgical analgesia using Vetergesic (0.1 mg/kg s.c.) systemically and combined with Marcaine (<8 mg/kg) locally. The mice were placed in a stereotactic frame and body temperature was maintained at ~37 ˚C. The virus was delivered using a glass micropipette (tip opening: ~15-20 μm) which was slowly inserted in the brain (~10 – 20 μm/s) at the following sites: CA1: AP -1.8, ML ±1.2, and DV -1.2 mm, CA3: AP -2, ML -2.3, and DV -1.8 mm, and entorhinal cortex: AP -4.85, ML -3.45, and DV -1.5 mm from bregma (ML/AP) or brain surface (DV). When the pipette reached its intended position, it was kept in position for at least 1 minute before viral infusion was started with a rate of 0.1 μL per minute. The pipette remained in position for at least 5 minutes after delivery to minimize viral backflow and slowly retracted at ~10 – 20 μm/s. The scalp was closed with 6-0 Ethicon Vicryl sutures and the mice were allowed to recover for at least one to three weeks depending on the experiment.

5.2.3.2 Microdrive and drive implantation

After a recovery period of at least one week, mice used for the electrophysiological connectivity mapping of superficial interneurons were implanted with 14 tetrode custom-built microdrives (see **section 2.2.2**) and implanted following the same procedure (see **section 2.2.3**). In contrast to Chapter 2, the implanted microdrives for the experiments in this Chapter were equipped with two fixed optic fibres (230 μm diameter, NA 0.37 Doric Lenses, Canada) positioned bilaterally above dorsal CA1 at AP -2.5 mm, ML ±1 mm from Bregma and DV -1 mm from the brain surface. Mice were allowed to recover for at least one week before habituation to the recording setup.

5.2.3.3 Recording procedure and optical stimulation protocol

Intracranial electrical signals, position tracking data, and tetrode positioning were acquired and performed as described in **section 2.2.6**. Every morning, stepwise tetrode positioning was followed by at least a 90-minute rest period before the recordings started. Once tetrodes were in

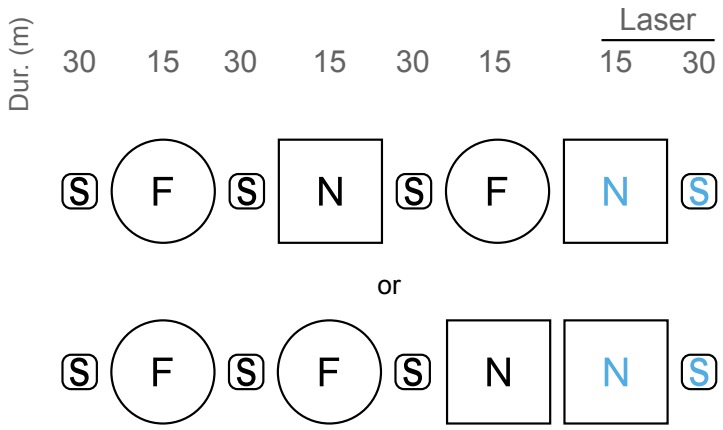


Figure 5.2.1 – Behavioural paradigm

Behaviour paradigm used for data acquisition: Consisting of sleep box sessions and awake exploration sessions. Blue sessions indicate laser sessions. Note that the novel and familiar environments are pseudorandomised. S: sleep box, F: familiar environment, N: novel environment.

position, the mice went through the same behavioural protocol every recording day. Mice went through 8 sessions (**Figure 5.2.1**). The first six sessions, performed without laser stimulation, comprised three sleep sessions interleaved with two exploration sessions in a familiar and novel environment. The last two sessions were a 15-minute exploration session and a 20 to 30-minute sleep session with 1 ms laser (230 μm diameter optic fibre passing through 400-600 μW with a wavelength of 473 nm) stimulation at 1 to 4-second intervals.

5.2.4 Histology

All mice were anaesthetized with pentobarbital either after completion of the electrophysiological recordings or 4 weeks after viral delivery and were transcardially perfused with saline followed by 4% PFA in PB (8-10ml/minute for 5 minutes; 8-10ml/minute for 15 minutes for implanted mice). Brains used for the tracing studies were processed following the sectioning and staining protocol described in Stedehouder, Brizee et al., 2018. In short, the brains were removed from the skull followed by post-fixation in 4% PFA for 2 hours. Subsequently stored in 10% sucrose solution (0.1 M PB) overnight at 4°C. The next day brains were embedded in gelatin (12% gelatin (Sigma-Aldrich)/10% sucrose), post-fixed (10% PFA/30% sucrose) for 2 h at room temperature, and then stored in 30% sucrose solution overnight at 4°C. Coronal sections were made on a freezing microtome in 40 µm and collected in 0.1 M PB. Heads of implanted mice were removed after perfusion and post-fixed in 4% PFA overnight before the implant was removed and brains

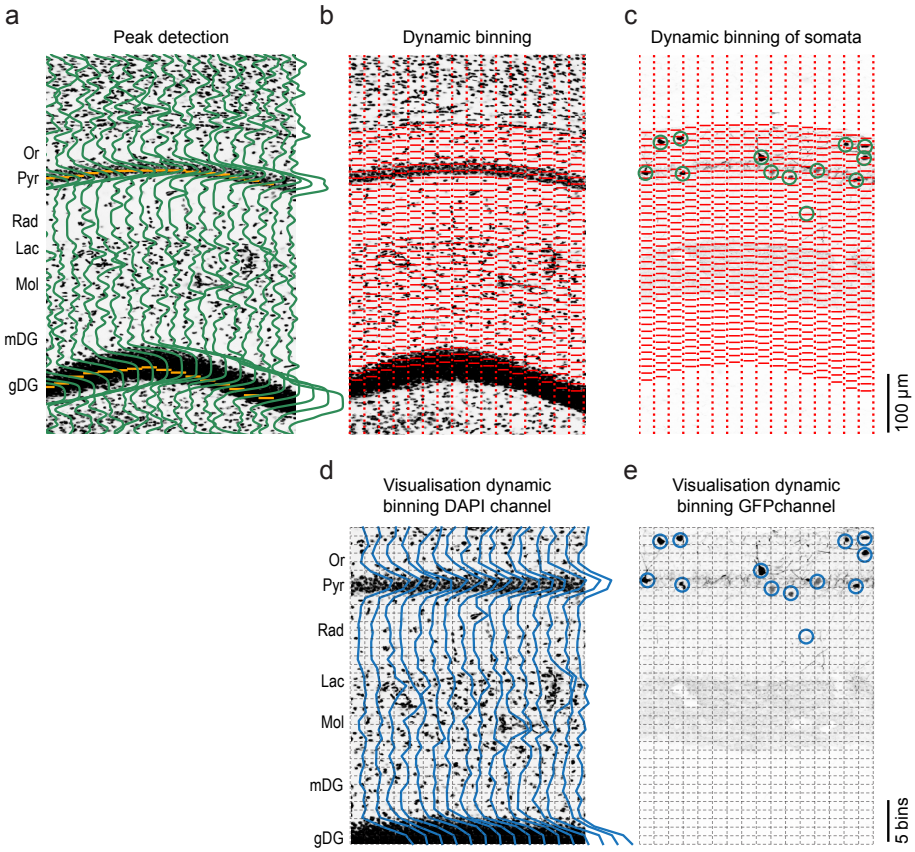


Figure 5.2.2 – Mapping individual hippocampal images into a common anatomical space

a) Representative image of dorsal CA1 showing in black DAPI staining cell nuclei. Green lines represent the mean fluorescence per analysed column, and the yellow ticks indicate the identified positions of the stratum pyramidale and granule layer of the dentate gyrus per analysed column. Layers are indicated on the left. **b**) Image from **a**) with a projection of the dynamic bin edges. Red vertical lines indicate the analysed columns and red horizontal ticks indicate the edges of the bins per column. Every column contained 7 bins from the dorsal border of the stratum oriens to the detected pyramidale and 30 bins from the pyramidale to the detected upper blade of the dentate gyrus' granule layer. The bin height is adjusted for every bin depending on the distance between the dorsal border of the stratum oriens and the pyramidale and the pyramidale to the granule layer, to align the layers and allow a direct comparison in the horizontal axis as well as across animals. **c**) Corresponding GFP channel of the image in **a**) with in red the bins indicated as in **b**). Green circles indicate identified soma locations. Somata are allocated to a bin for analysis, Scale bar 100 μm. **d**) Example image from **a**) showing the DAPI channel warped for illustration purposes, images are not warped for analysis. The blue lines represent the mean DAPI fluorescence intensity per bin across the columns. The grid shows the bin edges from **b-c**). Note that, in contrast to the peaks in **a**), the peaks are now aligned in the horizontal plane across the image. The dynamic alignment based on the fluorescence peaks in the stratum pyramidale and granule layer straightens the layers into a common anatomical space across images. **e**) Example image from **c**) showing the GFP channel warped for illustration purposes as also shown in **d**), images are not warped for analysis. The blue circles indicate soma location in warped anatomical space. The grid shows the bin edges from **b-c**). Or: oriens, Pyr: pyramidale, Rad: radiatum, Lac: lacunosum. Mol: moleculare, mDG: molecular layer of the dentate gyrus, gDG: granule layer of the dentate gyrus.

were taken out of the skull. Then, brains were treated as described above for the unimplanted mice, except section thickness, which was 50 µm rather than 40 µm. Sections were incubated in DAPI and mounted using Vectashield mounting medium.

5.2.5 Imaging

Image acquisition was performed using a Zeiss LSM 880 confocal microscope equipped with Plan-Apochromat 10x/0.45, 20x/0.8, 40x/1.4, and 63x/1.4 (oil immersion) objectives. DAPI and eYFP were imaged using excitation wavelengths 405 and 488 nm, respectively. Only coronal sections between -1.70 mm and –2.10 mm from bregma were included in the dataset. Both hippocampi were individually imaged per section across 5 CA3-injected and 4 EC-injected mice utilising a 20x objective (**Table 5.2.3**). To capture the full hippocampal volume available in the imaged section per hemisphere, 4x3 tile scans of ~1.6 mm, ~1.2 mm; 0.42 pixels per micron) were obtained across multiple optical planes (z-stack ~10 optical planes; 2.3-micron interval).

Mouse	Ipsi-lateral hemi-sphere (n sections)	Contra-lateral hem-isphere (n sections)	Mouse	Ipsi-lateral hemi-sphere (n sections)	Contra-lat-eral hemi-sphere (n sections)
CA3.1	7	6	EC.1	9	4
CA3.2	16	16	EC.2	18	16
CA3.3	18	16	EC.3	20	26
CA3.4	20	20	EC.4	14	12
CA3.5	16	10			

Table 5.2.3 – Overview of the mice and sections used for anterograde tracing experiment

5.2.6 Data analysis

5.2.6.1 Software

Data were analysed in Fiji v2.1.0/1.53f as well as Python 3.10 using the following packages: Numpy v1.24.3, Pandas 1.5.3, Scipy 1.10.1, Matplotlib v3.7.1, Seaborn v0.21.2, Imageio v2.31.1 and OpenCV-python 4.8.0.

5.2.6.2 Image analysis

First, images for the anterograde tracing experiment were loaded into Fiji and z-stacks were collapsed into a single maximum projection. Subsequently, a trained experimenter detected

and annotated YFP-positive neurons (neuron-like structures co-localising with the nuclear marker DAPI) using the Fiji pointer tool. Somata detected outside dorsal CA1 were excluded from the analysis. All coordinates were saved and used for further analysis in Python. Images were converted from .czi to .tiff files using Fiji and loaded into Python. First, the images were subdivided into 25 µm columns (**Figure 5.2.2a**,**b**). Within these columns, the stratum pyramidale and the granule cell layer (upper and lower blade) of the dentate were detected based on the mean fluorescence intensity of the DAPI channel. The raw fluorescence signal was filtered using the gaussian_filter1d function of scipy.ndimage and peaks detected in the filtered signal > 1.5 std with the signal.find_peaks function. If more than three peaks are detected in a column, the detected peaks are excluded, and the position of the cell layers is inferred based on the peak positions of the neighbouring columns (**Figure 5.2.2a**,**b**). Then, all columns of both the DAPI and the YFP channels (37 bins) were binned along the vertical axis. Distance from the dorsal edge of the stratum oriens to the pyramidale of CA1 and from the CA1 pyramidale to the granule layer (upper blade) of the dentate gyrus were binned for every image (Or-Pyr: 7 bins and Pyr-GL: 30 bins), morphing individual images in a shared anatomical space (**Figure 5.2.2a-d**). Depending on the analysis, either the number of detected cells or fluorescence intensity was computed across all generated bins within dorsal CA1. For soma counts, the normalised number of detected cells was computed by dividing the number of cells per bin through the mean fluorescent intensity of the DAPI channel of the same bin. To allow averaging across both hemispheres, data obtained from the right hemisphere were horizontally flipped to match the medial and lateral positions of the images of the left hemisphere.

Soma shape analysis

First, gaussian smoothing (using the GaussianBlur function from OpenCV package) and thresholding (using the threshold function in comination with THRESH_BINARY and THRESH_OTSU function) were applied to the YFP channel to reduce noise. Then, regions of interest (ROI; 22 μm in diameter) were drawn around the annotated soma location to quantify the soma shapes of detected neurons. Within this ROI the findContours function from the OpenCV package was used (combined with the cv.RETR_EXTERNAL, cv.CHAIN_APPROX_SIMPLE, functions) to

detect the somata. After the soma detection within the ROI, an ellipse is fitted onto the soma for further analysis. The minEnclosingCircle, contourArea, fitEllipse, and arcLength functions from OpenCV were used to compute the diameter, area, and ellipse angle. The circularity was computed as Circularity=4π×Area / Perimeter2

Neurite fluorescence

To prevent the fluorescence of somata from skewing the results of the neurite detection, ROIs from the soma shape analysis were subtracted from the image before fluorescence was quantified. Fluorescence was computed as a mean fluorescence value within the bins defined for the soma count and DAPI fluorescent signal analysis.

5.2.6.3 Electrophysiological data analysis

Unit detection, quality control, and layer assignment were performed as described in Chapters 2 and 3 (see **Methods sections 2.2** and **3.2**). Electrophysiological baseline characteristics were computed as described in Chapter 4 (see **section 4.2**).

Axon terminal stimulation modulation

Axon terminal stimulation response per cell was assessed by computing a laser-triggered average for all detected cells. All measures were averaged across both sleep and awake trials unless stated otherwise. For axon terminal stimulation response magnitude measures per cell, triggered averages for individual cells were z-scored across time and the mean z-score in a 0-20 ms (early excitatory component) and a 20-40 ms (inhibitory component) window from the laser onset was computed. To assess whether an individual neuron displayed a significant excitatory response, mean neuronal activity across 20 ms windows was randomly obtained from the laser-triggered pre-stimulation period (-800 to -50 ms). If the actual mean activity within the 0-20 ms or 20-40 ms post-stimulation window was <2.5th or >97.5th percentile of the random sampling distribution the neurons were considered significantly negative or positively correlated, respectively (Dudok et al., 2021).

Response delays

Response delays were computed as the mean response delay between the laser onset and the first detected spike across all individual stimulation trials and jitter was computed as the standard deviation of the response delay across stimulation trials. To assess information transfer, spike probability was computed as the proportion of stimulation trails in which the neuron responded with a spike within a 0 – 20 ms window of laser onset.

Phase dependent responses

Theta cycle detection was performed as described in Chapter 2. To examine the phase-dependent responses of individual neurons, the number of spikes in a 20 ms window after the laser onset was obtained for all neurons across all laser pulses. The laser pulses were sorted based on theta phase of occurrence and binned in 10-degree bins. The mean activity per cell per phase bin was computed, which was then averaged per layer group.

5.2.7 Statistics

Permutation testing and bootstrapped confidence intervals were obtained as described in Chapter 3 (see **section 3.2.3.8**). For all correlations, spearman's correlation coefficient was computed using Scipy's spearmanr function from the statistical functions module unless stated otherwise. Significance was assessed through permutation testing (see **section 4.2.2.7**).

5.3 Results

5.3.1 Cell type-specific, anterograde, transsynaptic tracing reveals differential targeting of dorsal CA1 GABAergic neurons by CA3 and entorhinal cortex

5.3.1.1 CA3 and entorhinal cortex target different numbers of interneurons across hippocampal layers in dorsal CA1

To examine whether CA3 and entorhinal cortex project to distinct interneuron populations, I performed interneuron-specific anterograde transsynaptic labelling in dorsal CA1 of Vgat-cre

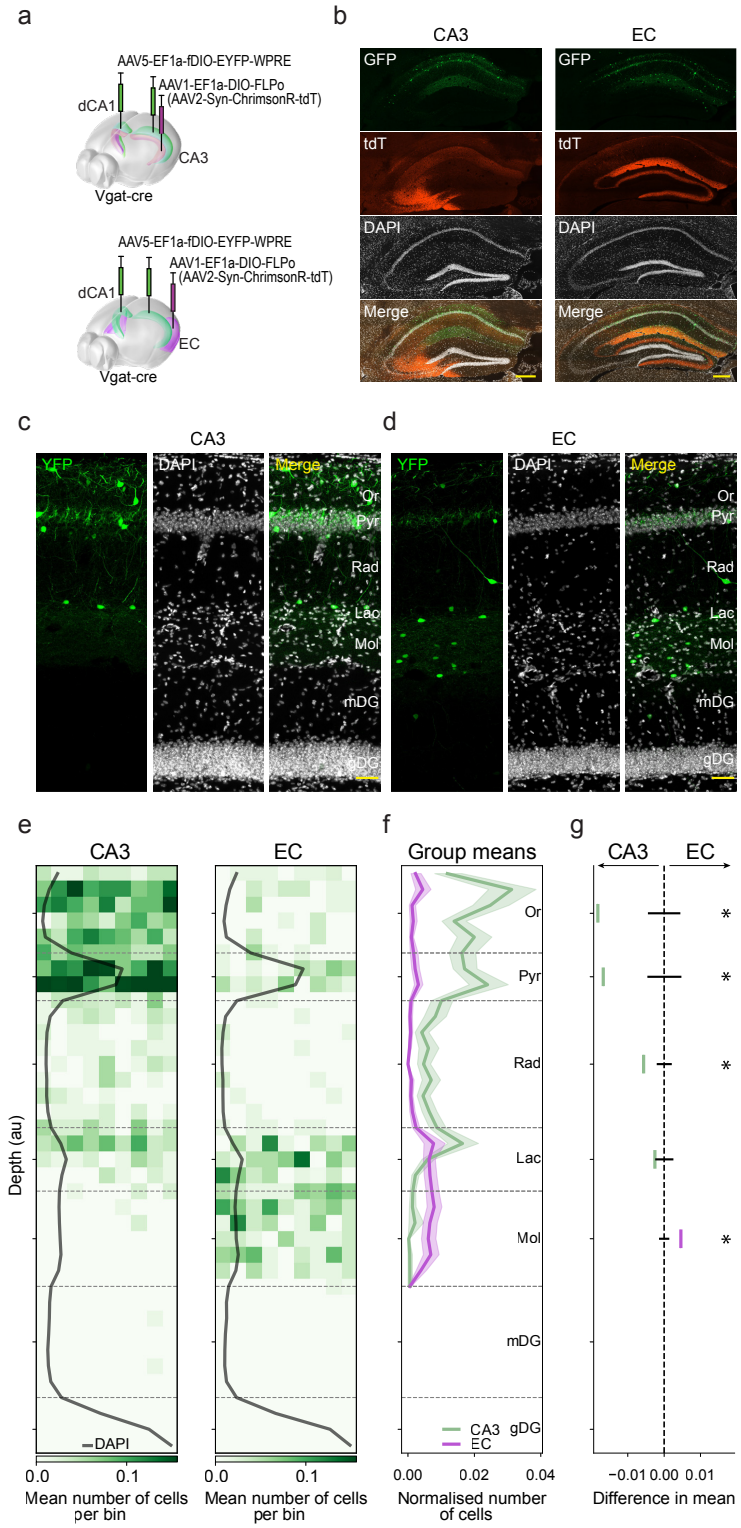


Figure 5.3.1 – CA3 and EC target different numbers of interneurons across distinct layers of dorsal CA1

a) Schematic of experimental design and timeline of anterograde transsynaptic tracing experiment. Vgat-cre mice are injected with an anterograde adeno-associated virus carrying a cre-dependent flippase in the left CA3 or EC. A second, FLPo-dependent YFP is bilaterally injected in dorsal CA1. **b**) Representative microscopy images of anterograde transsynaptic labelled YFP-expressing neurons (green) and the axonal projection patterns in dorsal CA1 from the starter region, which was co-injected with a tdT expressing virus (red), of mice injected with AAV1 construct »

»in CA3 (left) and EC (right). Only the first two subjected were co-injected with the AAV2-Syn-ChrimsonR-tdT to visualize the projections and injection sites. Note the visible injection site for the CA3-injected mouse in the CA3 region. DAPI staining (white) was used to identify the layers (indicated on the right). Scale bars 150 μm. **c**) Representative microscopy images of transsynaptic anterogradely labelled YFP-expressing neurons (green) in dorsal CA1 of a mouse injected with AAV1 construct in CA3, and DAPI staining (white) to identify the layers (indicated on the right). Scale bar 50 μm. **d**) Representative microscopy images of transsynaptic anterogradely labelled YFP-expressing neurons (green) in dorsal CA1 of a mouse injected with AAV1 construct in EC, and DAPI staining (white) to identify the layers (indicated on the right). Scale bar 50 μm. Note the differential distribution of somata across the layers of dorsal CA1 in comparison with **b**). **e**) Heatmaps showing the mean neuronal density of YFP-positive neurons for the CA3 (left; 5 mice) and EC (right; 4 mice) injection groups across both hemispheres for all mice projected into a common anatomical framework. The solid line indicated the mean DAPI fluorescence used to identify the layers of CA1. To morph individual images into a common framework the stratum pyramidale and granule layers of the dentate were used as landmarks. Somata were only counted for dorsal CA1. **f**) Normalised number of neurons for the CA3 (light green) and the EC (purple) injected groups. Solid lines indicate the means and shades area the 95%CI of the mean. Mean normalised number of neurons per layer $x10^{-2}$, 95%CI $x10^{-2}$: CA3 Or 2.03, 1.67-2.43; CA3 Pyr 1.91, 1.55 – 2.32; CA3 Rad 0.64, 0.48 – 0.84; CA3 Lac 0.83, 0.66 – 1.03; Mol 0.10, 0.04 – 0.17; EC Or 0.21, 0.14 – 0.31; EC Pyr 0.23, 0.15 – 0.34; EC Rad 0.08, 0.05 – 0.11; EC Lac 0.58, 0.43 – 0.73; EC Mol 0.56, 0.44 – 0.69. **g**) Plot showing the mean difference between the normalised number of YFP-positive neurons per layer between CA3 and EC injected groups. The vertical dash represents the difference of the mean between CA3 and EC-injected mice and the horizontal black line the 2.5th till the 97.5th percentile of the null distribution. Vertical dashes on the null line's left or right side indicate higher numbers in CA3 or EC, respectively. Stars indicate significant difference of the mean between the injection conditions. Difference of the mean, p-value per layer: Or -1.82, $<10^{-5}$; Pyr -1.67 $<10^{-5}$; Rad -0.56, $<10^{-5}$; Lac -0.25, 0.02; Mol 0.46, $<10^{-5}$. Significance threshold was set at p-val < 0.01 to correct for multiple comparisons.

mice to visualise the interneuron populations targeted by either CA3 or EC (**Figure 5.3.1a-d**) (Zingg et al., 2017, 2020). The anterograde tracer was confirmed to have been injected in the appropriate locations in CA3 and EC as evidenced by the axonal projection patterns visualized through co-injection in the starter region with a second virus encoding for tdTomato (**Figure 5.3.1b**). Additionally, no YFP-positive neurons were identified in CA3 or EC to confirm YFP-expression to be restricted to CA1 (data not shown). For CA3 and EC-injected mice, YFP-labelled neurons of both hemispheres were quantified and mapped into a common anatomical framework (see **Methods**; **Figure 5.3.1c-e**). CA3 primarily targets dCA1 interneurons with their soma located in strata oriens and pyramidale (35% and 36%, respectively), with decreasing proportions towards the hippocampal fissure (Rad 14%, Lac 13%, and Mol 1%; **Figure 5.3.1e, g-f**). Conversely, most dCA1 interneurons labelled through the EC were found in the moleculare (46%) with numbers declining towards the stratum pyramidale (Lac 26%, Rad 5%, Pyr 12%, and Or 10%; **Figure 5.3.1e, g-f**). Compared to EC, CA3 targeted more neurons in strata oriens, pyramidale, and

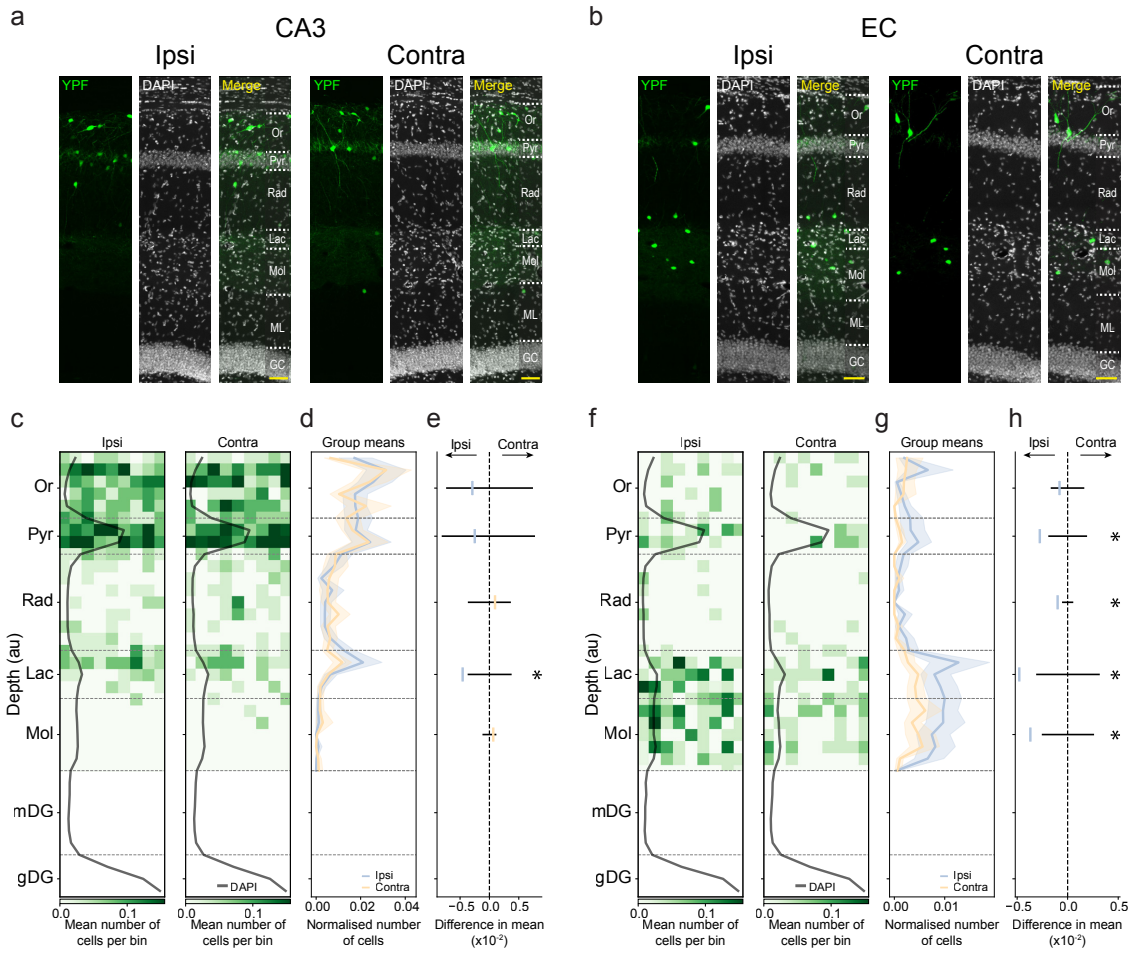


Figure 5.3.2 – Differential targeting pattern of interneurons by EC and CA3 in ipsi- and contralateral hemisphere

a) Representative microscopy images of transsynaptic anterogradely labelled YFP-expressing neurons (green) in dorsal CA1 of CA3-injected mice per hemisphere, and DAPI staining (white) to identify the layers (indicated on the right). Scale bar 50 μm. **b**) Representative microscopy images of transsynaptic anterogradely labelled YFP-expressing neurons (green) in dorsal CA1 of EC injected mice per hemisphere, and DAPI staining (white) to identify the layers (indicated on the right). Scale bar 50 μm. **c**) Heatmaps showing the mean neuronal density of YFP-positive neurons across mice for the CA3 injection group projected into a common anatomical framework for the ipsi- and contralateral hemispheres. The solid line indicated the mean DAPI fluorescence used to identify the layers of CA1. **d**) Normalised number of neurons for the ipsi- and contralateral hemispheres in the CA3-injected group. Solid lines indicate the means and shades area the 95%CI of the mean. Normalised number of neurons per layer, 95% CI: Left Or 2.18, 1.68 – 2.74, Left Pyr 2.03, 1.52 – 2.64; Left Rad 0.59, 0.43 – 0.82; Left Lac 1.06, 0.43 – 0.82; Left Mol 0.07, 0.03 – 0.10; Right Or 1.89, 1.36 – 2.42; Right Pyr 1.78, 1.25 – 2.40; Right Rad 0.69, 0.39 – 1.04; Right Lac 0.60, 0.43 – 0.78; Right Mol 0.13, 0.03 – 0.27. **e**) Plot showing the mean difference between the normalised number of YFP-positive neurons of the ipsi- and contralateral hemispheres. The vertical dash represents the difference of the mean between ipsi- and contralateral hemispheres and the horizontal black line the 95%CI of the null distribution. Vertical dashes on the null line's left or right side indicate higher numbers in ipsi- or contralateral hemisphere, respectively. Difference of the mean, p-value per layer: Or -0.29, 0.229; Pyr -0.25, 0.276; Rad 0.10, 0.311; Lac -0.46, 0.008; Mol 0.27, 0.206. **f**) Same as **c**) for EC injected mice. **g**) Same as **d**) for EC-injected mice. Normalised number of neurons per layer, 95% CI: Left Or0.25, 0.16 – 0.36, Left Pyr 0.37, 0.20 – 0.56; Left Rad 0.123, 0.08 – 0.18; Left Lac 0.82, 0.55 – 1.10; Left Mol 0.74, 0.54 – 0.97; Right Or 0.17, 0.06 – 0.32; Right Pyr 0.10, 0.06 – 0.13; Right Rad 0.03, 0.01 – 0.05; Right Lac 0.34, 0.25 – 0.43; Right Mol 0.37, 0.24 – 0.52. **h**) Same as **e**) for EC-injected mice. Difference of the mean, p-value per layer: Or -0.08, 0.187; Pyr -0.28, 0.001; Rad-0.10, $<10^{-5}$; Lac -0.48, 0.001; Mol -0.37, 0.003. Significance threshold was set at p-val < 0.01 to correct for multiple comparisons.

radiatum, while there was no difference in the stratum lacunosum (**Figure 5.3.1f-g**). Conversely, in stratum moleculare, more neurons were labelled through EC. Furthermore, examination of dCA1 ipsilateral and contralateral to transsynaptic tracer injection separately showed that CA3 targeted CA1 interneurons similarly across hemispheres (**Figure 5.3.2a, c-e**), while EC targeted preferentially ipsilateral interneurons compared to contralateral (**Figure 5.3.2b, f-h**). Together, these data show a gradual targeting of interneurons by CA3 and EC as a function of distance from their respective input layers, with CA3-targeted neurons gradually decreasing towards the superficial layers, EC targeting decreasing towards deeper layers, and overlapping targeting in stratum lacunosum.

5.3.1.2 Soma characteristics suggest targeting of distinct interneuron populations by CA3 and entorhinal cortex in stratum lacunosum

In the previous section, I show that CA3 and entorhinal cortex target different numbers of inhibitory neurons across distinct hippocampal layers while converging onto the stratum lacunosum. However, different strata house different interneuron types (Somogyi and Klausberger, 2005; Pelkey et al., 2017; Booker and Vida, 2018). Varying soma shapes and orientations have been described for different interneuron types (Booker and Vida, 2018). To gain insight into whether different populations of interneurons are targeted by EC or CA3, I computed orientations, circularities, and diameters of the somata of YFP-labelled neurons. This analysis revealed that somata features display a high inter-layer diversity (**Figure 5.3.3a-i**). In particular, across all detected neurons, soma diameter was found to be smallest in strata radiatum and lacunosum and largest in stratum pyramidale and moleculare (**Figure 5.3.3a-c**, **Table 5.3.1**). Additionally, higher angles in strata oriens, lacunosum, and moleculare indicate a greater presence of horizontally oriented neurons compared to pyramidale and radiatum (**Figure 5.3.3g-i**, **Table 5.3.1**). Furthermore, lower circularity in stratum lacunosum suggests more elongated rather than circular soma shapes compared to stratum radiatum (**Figure 5.3.3d-f**, **Table 5.3.1**). Input-specific analysis revealed that soma characteristics of CA3 or EC targeted neurons in the strata oriens and pyramidale did not differ, while in the superficial layers, neurons displayed input-dependent difference. In strata radiatum and lacunosum, neurons targeted by EC had a larger soma diameter and more vertical

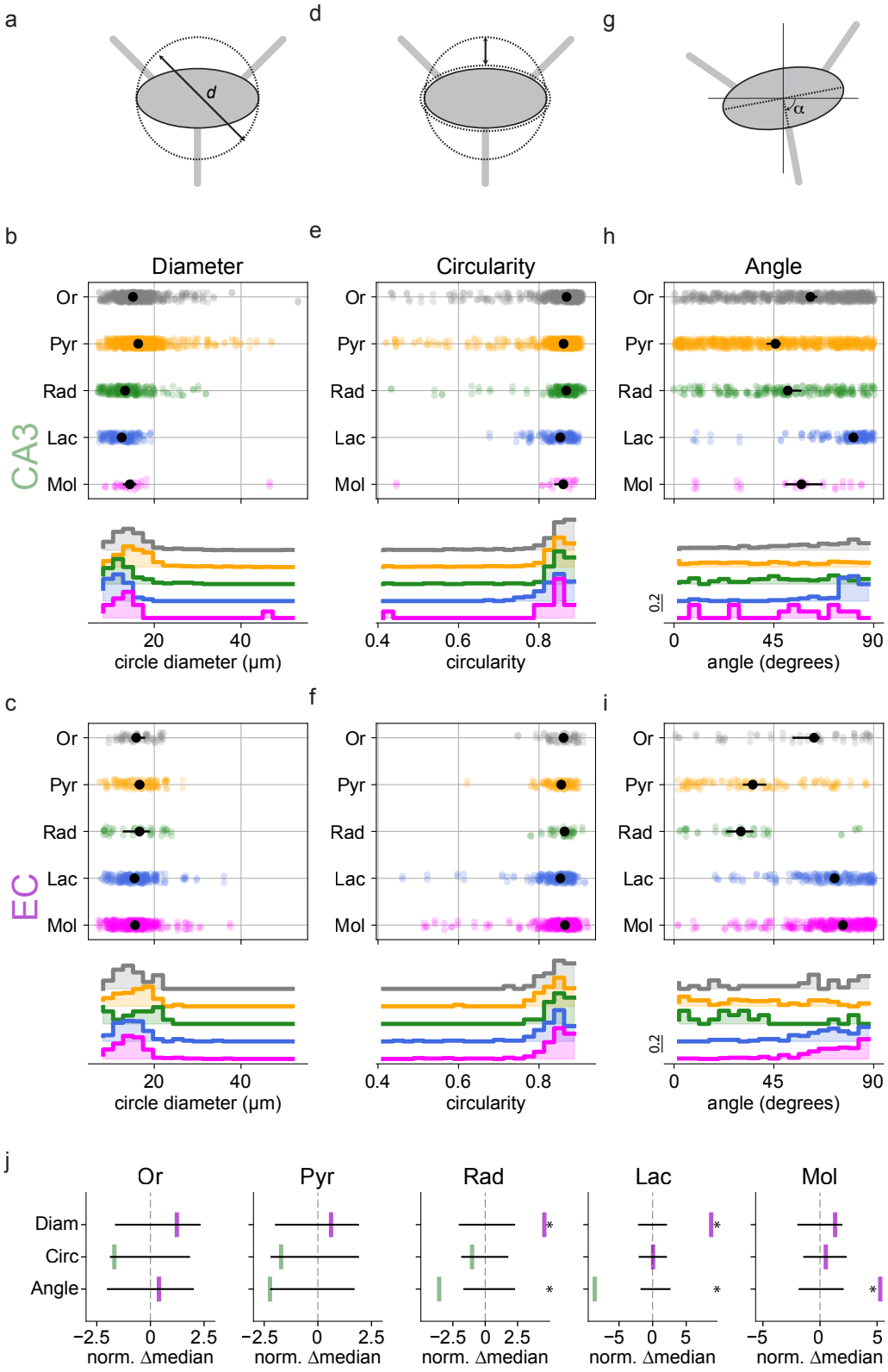


Figure 5.3.3 – Soma characteristics suggest targeting of distinct interneuron populations by CA3 and EC in stratum lacunosum

a) Schematic representing soma diameter **b**) Top: Strip plots showing the mean soma diameter for YFP-positive interneurons per CA1 layer anterogradely labelled through the CA3. Coloured data points represent neurons, the black dot the group median, and the whiskers 95% CI of the median. Bottom: histograms showing the soma angles per CA1 layer, Scale bar proportion of 0.2 of the »

» neurons per group. Median, 95% CI: Or 15.09, 14.68 – 15.40; Pyr 16.30, 16.04 – 16.67; Rad 13.29, 12.89 – 13.71; Lac 12.52, 11.82 – 13.13; Mol 14.38, 12.62 – 15.87. **c**) Same as in **b**) for the EC-injected group. Median, 95% CI: Or 15.85, 14.88 – 17.92; Pyr 16.62, 15.36 – 17.71; Rad 16.59, 12.76 – 18.98; Lac 15.46, 14.56 – 16.21; Mol 15.56, 14.91 – 15.81. **d**) Schematic representing soma circularity. **e**) Top: Strip plots showing the mean soma circularity for YFP-positive interneurons per CA1 layer anterogradely labelled through the CA3. Coloured data points represent neurons, the black dot the group median, and the whiskers 95% CI of the median. Bottom: histograms showing the soma angles per CA1 layer, Scale bar proportion of 0.2 of the neurons per group. Median $x10^{-2}$, 95% CI $x10^{-2}$: Or 86.84. 86.52 – 87.07; Pyr 86.10, 85.88 – 86.31; Rad 86.76, 86.54 – 87.11; Lac 85.27, 84.85 – 85.83; Mol 86.02, 83.77 – 86.75. **f**) Same as in **e**) for the EC-injected group. Median $x10^{-2}$, 95% CI $x10^{-2}$: Or 86.07, 85.62 – 86.60; Pyr 85.53, 84.47 – 86.14; Rad 86.35, 86.03 – 87.34; Lac 85.29, 84.77 – 85.57; Mol 86.43, 86.13 – 86.84. **g**) Schematic representing soma angle measurement. The angle (α) between the horizontal axis and the short axis of the fitted ellipse it taken as a measure of soma position. **h**) Top: Strip plots showing the mean soma angle for YFP-positive interneurons per CA1 layer anterogradely labelled through the CA3. Coloured data points represent neurons, the black dot the group median, and the whiskers 95% CI of the median. Bottom: histograms showing the soma angles per CA1 layer, Scale bar proportion of 0.2 of the neurons per group. Median, 95% CI: Or 61.48, 59.44 – 64.55; Pyr 49.69, 41.64 – 48.16; Rad 51.0, 49.04 - 57.44; Lac 80.83, 79.88 – 81.78; Mol 57.43, 49.97 – 66.99. **i**) Same as in **h**) for the EC-injected group. Median, 95% CI: Or 63.11, 53.37 – 65.73; Pyr 35.48, 31.00 – 41.54; Rad 30.10, 23.53 – 35.73; Lac 72.38, 70.62 – 73.66; Mol 76.13, 74.85 – 77.51. **j**) Plots showing the direct comparison of different soma characteristics between CA3 and EC-injected groups per layer. The vertical ticks indicate the difference between the group medians, with colour coding indicating the group with the larger median (CA3: green, EC: purple). The horizontal line indicates the 2.5th to 97.5th percentile of the null distribution. The median difference in diameter in μm, p-value: for Or 1.23, 0.110; Pyr 0.62, 0.281; Rad 4.57, $<10^{-5}$; Lac 8.72, $<10^{-5}$; Mol 1.32, 0.090. The median difference in circularity, p-value: for Or -1.68, 0.044; Pyr -1.71, 0.044; Rad -1.02, 0.155; Lac 0.07, 0.506; Mol 0.51, 0.263. The median difference in angle, p-value: for Or 0.39, 0.321; Pyr -2.23, 0.025; Rad -3.56, $<10^{-5}$; Lac -8.62, $<10^{-5}$; Mol 5.28, $<10^{-5}$. Stars indicate a significant difference. Significance threshold was set at p-val < 0.01 to correct for multiple comparisons. Or: oriens, Pyr: pyramidale, Rad: radiatum, Lac: lacunosum, Mol: moleculare. Scale bars represent proportion of 0.2 of the neurons per group.

.

	Mean	25th perc	75th perc	Mean differences				p-values			
Angle (degrees)											
				Pyr	**Rad**	**Lac**	**Mol**	**Pyr**	**Rad**	**Lac**	**Mol**
Or	56.5	36.5	78.4	-13.0	-7.9	15.3	14.2	$<10^{-5}$	$<10^{-5}$	$<10^{-5}$	$<10^{-5}$
Pyr	43.6	20.6	68.3		5.1	28.3	27.2		0.002	$<10^{-5}$	$<10^{-5}$
Rad	48.7	28.4	72.9			23.2	22.1			$<10^{-5}$	$<10^{-5}$
Lac	71.9	66.3	83.3				-1.1				0.159
Mol	70.8	64.3	84.1								
Circularity ($x10^{-3}$)											
	Mean	**25th per**	**75th perc**	**Pyr**	**Rad**	**Lac**	**Mol**	**Pyr**	**Rad**	**Lac**	**Mol**
Or	0.847	0.843	0.882	-8.179	3.337	-9.839	-1.482	0.010	0.234	0.006	0.359
Pyr	0.839	0.836	0.877		11.515	-1.661	6.697		0.007	0.337	0.052
Rad	0.851	0.845	0.878			-13.176	-4.819			0.001	0.150
Lac	0.837	0.823	0.872				8.357				0.019
Mol	0.846	0.84	0.877								
Diameter (micrometers)											
	Mean	**25th perc**	**75th perc**	**Pyr**	**Rad**	**Lac**	**Mol**	**Pyr**	**Rad**	**Lac**	**Mol**
Or	15.4	12.6	17.9	1.06	-2.41	-2.49	0.02	$<10^{-5}$	$<10^{-5}$	$<10^{-5}$	0.470
Pyr	16.4	13.6	19.0		-3.46	-3.55	-1.04		$<10^{-5}$	$<10^{-5}$	0.001
Rad	13.0	9.6	15.7			-0.08	2.42			0.418	$<10^{-5}$
Lac	12.9	10.1	16.1				2.50				$<10^{-5}$
Mol	15.4	13.1	17.3								

Table 5.3.1 – Comparative statistics of soma shapes between CA1 layers

The table shows the mean and the interquartile boundaries (25th – 75th percentile) per layer across all detected interneurons, the pair-wise mean differences between CA1 layers (column group minus row group), and the corresponding p-value on the right. The significance level was corrected for multiple testing per feature and was set at 0.005.

orientation (small angles) compared to those targeted by CA3 (**Figure 5.3.3j**), while circularity was not different. These differences indicate heterogeneity in soma shapes targeted by both input sources, which may suggest that CA3-and EC-originating axons target different interneuron populations in the superficial layers of dorsal CA1. Together, soma shape analysis revealed a large heterogeneity of soma characteristics across and within layers, with CA3 and EC targeting differentially shaped superficial interneurons.

5.3.1.3 GABAergic neurons targeted by CA3 and entorhinal cortex display differential neurite patterns in dorsal CA1

Historically, interneuron types in the hippocampus and cortex are defined by axonal targeting patterns (Somogyi and Klausberger, 2005). In addition to soma count, YFP expression in the local interneurons allows for examining neurite density across the radial axis of dorsal CA1 as a proxy for axonal projection patterns within the labelled population. To ensure somatic fluorescence did not interfere with this analysis, somata were removed from the YFP channel, followed by fluorescence intensity measurements mapped onto a normalised anatomical framework (see **Methods**). Across the superficial layers, EC-targeted neurons projected mostly to the moleculare and invaded the molecular layer of the dentate gyrus (**Figure 5.3.4b-e**). Notably, a band of fluorescence was visible within the pyramidale as well as the deepest part of the stratum oriens (**Figure 5.3.4b-d**). Conversely, CA3-targeted neurons projected strongest to stratum pyramidale followed by the oriens and moleculare, and to a lesser extent projected to the radiatum (**Figure 5.3.4a, c-d**). Neurite fluorescence differed across the deeper layers of CA1 and the molecular layer of the dentate gyrus for EC compared to CA3-injected mice (**Figure 5.3.4e**). The strongest fluorescence was found in strata oriens, pyramidale, and radiatum in CA3-injected mice, while there was no difference in the strata lacunosum and moleculare between CA3- and EC-injected mice (**Figure 5.3.4c-e**). In contrast, EC-injected mice's fluorescent signal was higher in the molecular layer of the dentate gyrus compared to CA3-injected (**Figure 5.3.4c-e**). With specific interneuron types displaying differential targeting patterns (Klausberger, 2009), these findings suggest different interneuron populations being targeted by CA3 and EC in dorsal CA1. Surprisingly, a comparison of neurite fluorescent intensity between the ipsi- and contralateral hemispheres in CA3-injected

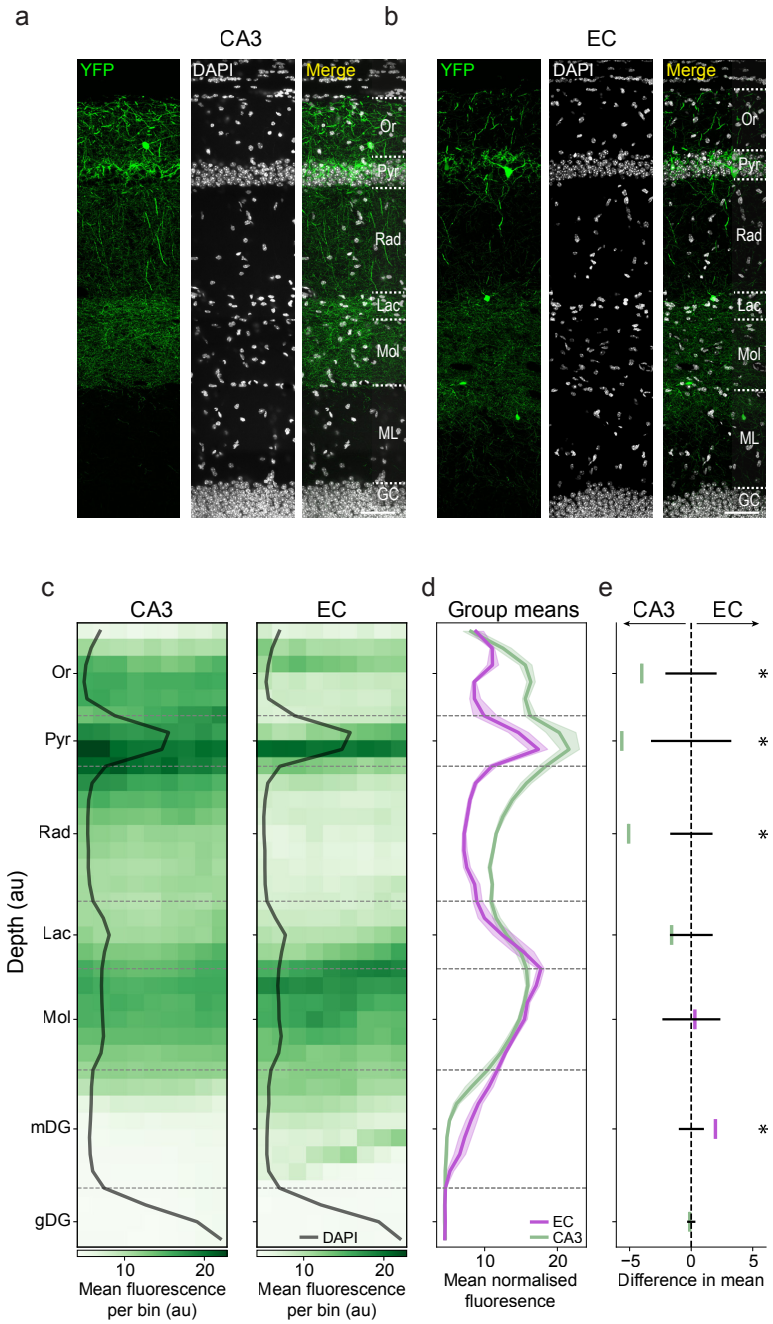


Figure 5.3.4 – EC and CA3-targeted interneurons show different axonal projection patterns within dCA1

a) Microscopy image showing YFP-positive neurons (green) in CA1 labelled through an anterograde transsynaptic labelling approach from CA3. DAPI staining (white) was used to identify CA1 layers. Layers indicated on the right, Scale bar 50 μm. Note the axonal and dendritic projections across different layers of CA1. **b**) Same as in **a**) for YFP-positive neurons labelled through EC. **c**) Heatmaps showing the mean neurite density of YFP-positive neurons for the CA3 (left) and EC (right) injection groups for both hemispheres across mice projected into a common anatomical framework. The solid line indicated the mean DAPI fluorescence used to identify the layers of CA1. **d**) Mean normalised fluorescence intensity of neurites originating from YFP-positive neurons in CA3 (light green) or EC (purple) injected mice. Solid lines indicate the means and shades area the 95%CI. Normalised fluorescence intensity per layer, 95% CI: CA3 Or 12.93, 11.68 – 14.30, CA3 Pyr 18.41, 16.18 – 20.88; CA3 Rad 12.78, 1.57 – 13.93; CA3 Lac 12.04, 11.05 – 13.10; CA3 Mol 13.61, 12.26 – 15.21; CA3 mDG 5.56, 5.19 – 5.95; CA3 gDG 4.47, 4.28 – 4.68; EC Or 8.92, 7.57 – 10.23; »

» EC Pyr 12.77, 10.69 – 14.98; EC Rad 7.70, 6.89 – 8.65; EC Lac 10.45, 9.04 – 11.91; EC Mol 13.91, 12.15 – 15.83; EC mDG 7.53, 6.59 – 8.52; EC gDG 4.35, 4.07 – 4.61. **e**) Plot showing the mean difference between the normalised neurite fluorescence intensity from YFP-positive neurons in CA3 or EC-injected mice. The vertical dash represents the difference in the mean between CA3 and EC groups and the horizontal black line the 95%CI of the null distribution. Vertical dashes on the null line's left or right side indicate higher fluorescent intensity in CA3 or EC, respectively. Difference of the mean, p-value per layer: Or -4.01, $<10^{-5}$; Pyr -5.64, $<10^{-5}$; Rad -5.08, $<10^{-5}$; Lac -1.59, 0.033; Mol -0.12, 0.408, mDG 1.97, $<10^{-5}$; gDG -0.12, 0.240. Significance threshold <0.007.

mice revealed higher average fluorescent intensity in the dentate gyrus on the contralateral side and a trend in the stratum moleculare (**Figure 5.3.5a, c-e**), despite similar soma counts between the hemispheres in stratum moleculare (**Figure 5.3.2e, f**). Conversely, the same analysis in EC-injected mice showed that, in line with higher soma counts (**Figure 5.3.2e, f**), neurite density was higher in the ipsilateral hemisphere (**Figure 5.3.5b, f-h**). Notably, the fluorescent bands in stratum oriens and pyramidale were most prominent on this ipsilateral site compared to the contralateral hemisphere. The differential targeting patterns between the ipsi- and contralateral hemispheres may indicate biased targeting in the respective hemispheres. Together, using fluorescent signals from CA3 or EC-targeted interneurons' neurites across the radial axis of dorsal CA1 revealed that CA3 and EC target, at least partially, different interneuron populations with distinct axonal distributions.

In summary, anterograde, transsynaptic tracing from CA3 and EC, reveals that these major afferents target, at least partially, different interneuron populations in dorsal CA1. Particularly, interneuron targeting is biased to the layers in which the afferent axons terminate, with most labelled neurons in strata oriens and radiatum for CA3-targeted populations and most in stratum moleculare for EC-targeted groups. Interestingly, both input sources target stratum lacunosum, but soma-shape analysis suggests that within this layer EC and CA3 may choose different postsynaptic partners. Lastly, the postsynaptic targets of CA3 and EC may engage differently with the local circuitry based on the axon-targeting patterns of the post-synaptic interneurons in dorsal CA1. Together, this anatomical assessment supports the idea that CA3 and EC may recruit differential interneuron subcircuits in dorsal CA1.

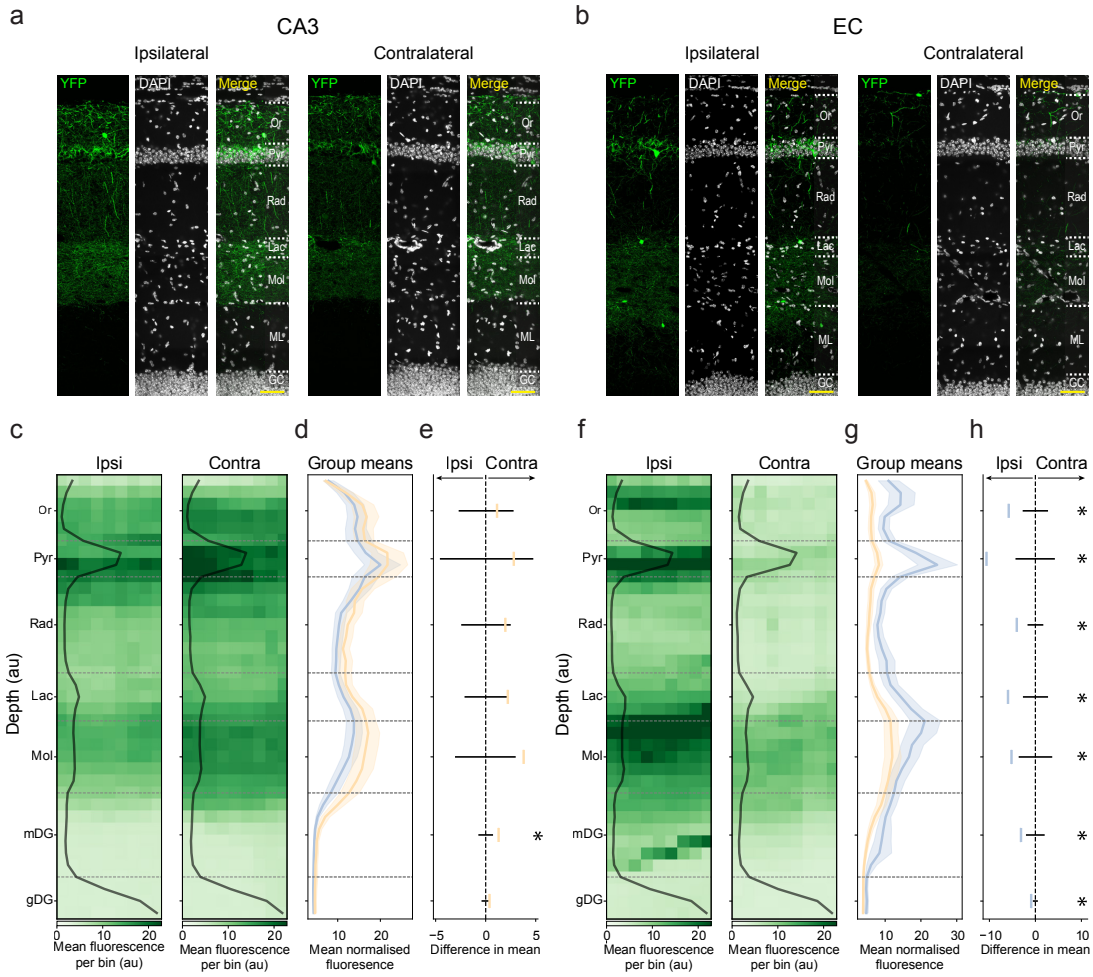


Figure 5.3.5 – Different neurite distribution in ipsi- vs contralaterally targeted interneurons

a) Microscopy images showing YFP-positive neurons (green) and their neurites in CA1 labelled through an anterograde transsynaptic labelling approach from CA3 for the ipsi- (left) and contralateral (right) hemispheres. DAPI staining (white) was used to identify CA1 layers. Layers indicated on the right, Scale bar 50 μm. Note the axonal and dendritic projections across different layers of CA1. **b**) Same as in **a**) for YFP-positive neurons labelled through EC. **c**) Heatmaps showing mean neurite density of YFP-positive neurons across mice for the CA3 injection group projected into a common anatomical framework for ipsi- (left) and contralateral (right) hemisphere. The solid line indicated the mean DAPI fluorescence used to identify the layers of CA1. **d**) Mean normalised fluorescence intensity of neurites originating from YFP-positive neurons in ipsi (light blue) or contralateral (yellow) hemisphere of CA3 injected mice. Solid lines indicate the means and shades area the 95%CI of the mean. Normalised number of neurons per layer, 95% CI: Left Or 12.40, 10.53 – 14.50; Left Pyr 17.09, 14.06 – 20.51; Left Rad 11.86, 10.36 – 13.46; Left Lac 11.00, 9.72 – 12.40; Left Mol 11.83, 10.11 – 13.58; Left mDG 4.49, 4.68 – 5.30; Left gDG 4.29, 4.16 – 4.43; Right Or 13.53, 11.56 – 15.39; Right Pyr 19.90, 16.81- 23.10; Right Rad 13.82, 11.98 – 15.86; Right Lac 13.21, 11.58 – 14.82; Right Mol 15.63, 13.33 – 18.26; Right mDG 6.25, 5.64 – 6.95; Right gDG 4.67, 4.28 – 5.11.**e**) Plot showing the mean difference between the normalised neurite fluorescence intensity from YFP-positive neurons in ipsi- (left) and contralateral (right) hemispheres of CA3 injected mice. The vertical dash represents the difference of the mean between the ipsi and contralateral hemispheres and the horizontal black line the 95%CI of the null distribution. Vertical dashes on the null line's left or right side indicate higher fluorescent intensity in the ipsi- or contralateral hemisphere, respectively. Stars indicate significant differences. Difference of the mean, p-value per layer: Or 1.13, 0.214; Pyr 2.81, 0.125; Rad 1.96, 0.065; Lac 2.21, 0.025; Mol 3.79, 0.008; mDG 1.29, $<10^{-5}$; gDG 0.38, 0.040. Significance threshold was set at p-val < 0.007 to correct for multiple comparisons. »

» **f**) Heatmaps showing the neurite density of YFP-positive neurons for the EC injection group projected into a common anatomical framework for ipsi- (left) and contralateral (right) hemisphere. The solid line indicated the mean DAPI fluorescence used to identify the layers of CA1. **g**) Mean normalised fluorescence intensity of neurites originating from YFP-positive neurons in ipsi (light blue) or contralateral (yellow) hemisphere of EC injected mice. Solid lines indicate the means and shades area the 95%CI of the mean. Normalised number of neurons per layer, 95% CI: Left Or 11.71, 9.24 – 14.12; Left Pyr 18.09, 14.57 – 21.98; Left Rad 9.72, 8.34 – 11.13; Left Lac 13.43, 11.15 – 15.70; Left Mol 16.51, 13.72 – 19.72; Left mDG 9.10, 7.39 – 11.13; Left gDG 4.81, 4.35 – 5.31; Right Or 5.92, 5.27 – 6.58; Right Pyr 7.46, 6.54 – 8.33; Right Rad 5.68, 5.12 – 6.30; Right Lac 7.47, 6.59 – 8.41; Right Mol 11.32, 9.48 – 13.22; Right mDG 5.97, 5.28 – 6.73; Right gDG 3.89, 3.67 – 4.11. **h**) Plot showing the mean difference between the normalised neurite fluorescence intensity from YFP-positive neurons in ipsi- (left) and contralateral (right) hemispheres of EC injected mice. The vertical dash represents the difference of the mean between the ipsi and contralateral hemispheres and the horizontal black line the 95%CI of the null distribution. Vertical dashes on the null line's left or right side indicate higher fluorescent intensity in the ipsi or contralateral hemisphere, respectively. Stars indicate significant differences. Difference of the mean, p-value per layer: Or -5.79, $<10^{-5}$; Pyr -10.63, $<10^{-5}$; Rad -4.04, $<10^{-5}$; Lac -5.95, $<10^{-5}$; Mol -5.19, 0.002; mDG -3.13, $<10^{-5}$; gDG -0.91, $<10^{-5}$.

5.3.2 Functional connectivity mapping

5.3.2.1 Comparable sampling and no effect of repeated afferent stimulation on dorsal CA1 circuitry in CA3 and EC-terminal stimulation groups

To map the functional connectivity between CA3 and EC, I performed region-specific optical terminal stimulation in dorsal CA1 while recording neurons from the stratum pyramidale to moleculare. Since CA3 and EC terminal stimulation effects were assessed in different mice, I first compared general spiking characteristics between the neurons to assess whether layer-based groups were comparable. This analysis revealed no differences in estimated recording depth, preferred theta phase, firing rate in theta, and waveform characteristics between CA3 and EC-injected groups in any layer (**Figure 5.3.6a-c**). However, slight differences in the sharp-wave ripple response scores were found between the lacunosum neurons recorded in the CA3 and EC-injected mice, while other groups did not show a statistical difference (**Figure 5.3.6a-c**). To test whether these differences are driven by unbalanced samples or by sampling from a distinct population, I compared the lacunosum neurons recorded across CA3 and EC-injected mice with the part of the dataset in which no terminal stimulation was performed (see **Chapter 4**). Nearly all neurons recorded from the stratum lacunosum in the CA3 and EC-injected groups fell within 2.5th and 97.5th percentiles of the lacunosum neuron ripple response score recorded across non-stimulated animals (23/23 (100%) neurons, 20/21 (95%) neurons, respectively; data not shown). This indicates that CA3 and EC lacunosum groups may represent subsamples but do not deviate

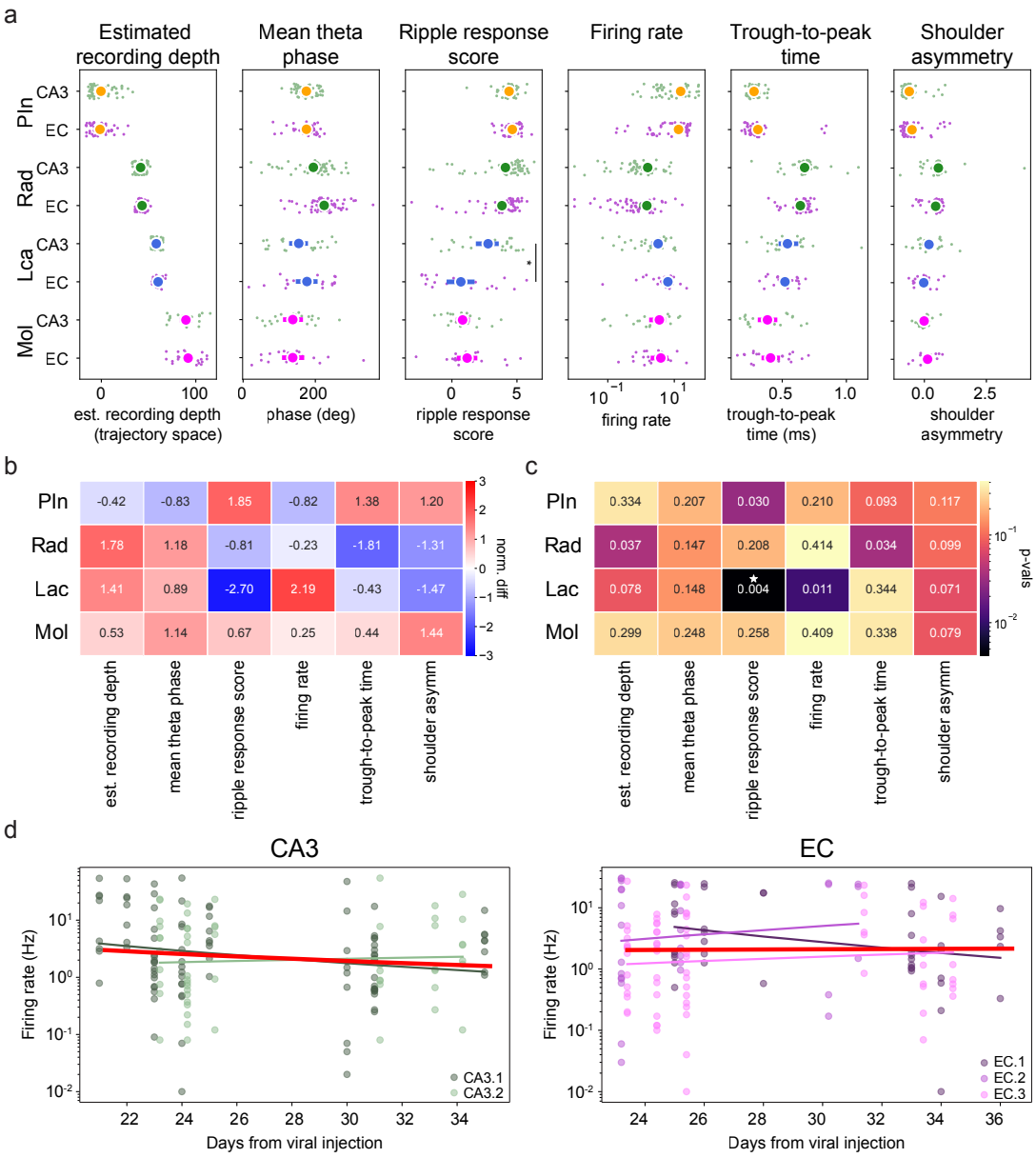


Figure 5.3.6 – Recorded interneuron populations are comparable between CA3 and EC stimulation groups and are not affected by repeated laser stimulation

a) Strip plots showing baseline electrophysiological characteristics for interneurons recorded in the CA3 and EC terminal stimulation groups. Data points represent individual neurons for the CA3 (light green) and EC (purple) stimulation groups. Larger coloured dots represent the group means and the whiskers the 99%CI of the mean, colours correspond to the recording layers (PIn: yellow, Rad: green, Lac: blue, Mol: magenta). Significant differences are indicated by a star. Normalised mean difference and p-values are shown in **b**) and **c**). **b**) Heatmap showing the z-scored mean differences between neuronal populations in the CA3 and EC terminal stimulation groups per layer and feature, corresponding to scatter plots in **a**). z-scoring was performed for the actual mean difference compared the control distribution. **c**) Heatmap showing the p-values corresponding to comparisons in **a**) per layer and feature. The p-value was obtained through permutation testing and Bonferroni corrected per recording group setting the significance threshold at 0.008, the star indicates significant differences. **d**) Firing rates of interneurons remain stable over recording days despite repeated laser stimulation and opsin expression. Scatter plots showing the firing rates of individual neurons across all recording layers (colour-coded per recorded animal) in the CA3 (greens) and EC stimulation groups (purples) as a function of the number of days from the viral injection. Green and purple show regressions per animal, the red line shows the regression lines at a group level (CA3 group: spearman's correlation coefficient -0.129, p-value 0.069; EC group: spearman's correlation coefficient 0.016, p-value 0.427)

from the general distribution. Secondly, recording days were treated as independent samples given that I aimed to record different neurons every recording day. However, the network as a whole received repeated laser stimulation over subsequent days. To ensure the network was not affected by laser stimulation, mean baseline firing rates were compared across days for the whole interneuron population. This analysis did not reveal a significant difference over time in either the CA3 or EC terminal stimulation groups (**Figure 5.3.6d**). Together, neurons recorded across CA3 and EC-injected mice were comparable and consecutive axon terminal stimulation did not alter the local CA1 network as measured by spiking activity over time.

5.3.2.2 Superficial interneurons are differently recruited by CA3 and entorhinal cortex along the radial axis of dorsal CA1

Next, I assessed the effect of CA3 and EC terminal stimulation on interneuron activity in dorsal CA1. For both CA3 and EC terminal stimulation, I found subsets of neurons responding to the optical stimulation by differentially increasing their firing rate in a layer-specific manner (**Figure 5.3.7**). In pyramidale, nearly 100% of interneurons responded with increased spiking activity to CA3 inputs, while 48% responded to EC (**Figure 5.3.7c**, **Figure 5.3.8a-c**). CA3 elicited excitatory responses in the superficial layers in radiatum and lacunosum neurons (61% and 78% of recorded neurons), but only 30% in the lacunosum. Conversely, EC stimulation led to increased spiking activity in more than half of the moleculare neurons (62% of the neurons), which decreased towards deeper layers (lac: 52%, rad: 28%; **Figure 5.3.7c**, **Figure 5.3.8a-c**). Additionally, I examined the post-stimulation firing rate change magnitude, revealing strong increases in strata pyramidale, radiatum, and lacunosum upon CA3 stimulation, while responses in stratum moleculare were minimal (Mean, 95%CI: Pyr 4.85, 4.28-5.35; Rad 1.73,1.18-2.27; Lac 2.39, 1.60-3.17; Mol 0.64, -0.04-0.1.32; **Figure 5.3.8b**). EC stimulation, on the other hand, resulted in lower firing rate increases across pyramidale, radiatum, and lacunosum, but stronger responses in moleculare (Mean, 95%CI: Pyr 1.05, 0.64-1.47; Rad 0.28, 0.13-0.44; Lac 0.96, 0.47-1.53; Mol: 1.94, 0.83-2.81; **Figure 5.3.8b**). Interestingly, however, inpection of the excitatory response dynamics at a smaller temporal scale revealed a bimodal response latency distribution in the CA3 terminal stimulation group (~4 and ~15 ms; **Figure 5.3.7c**, **Figure 5.3.8c**), which was absent in

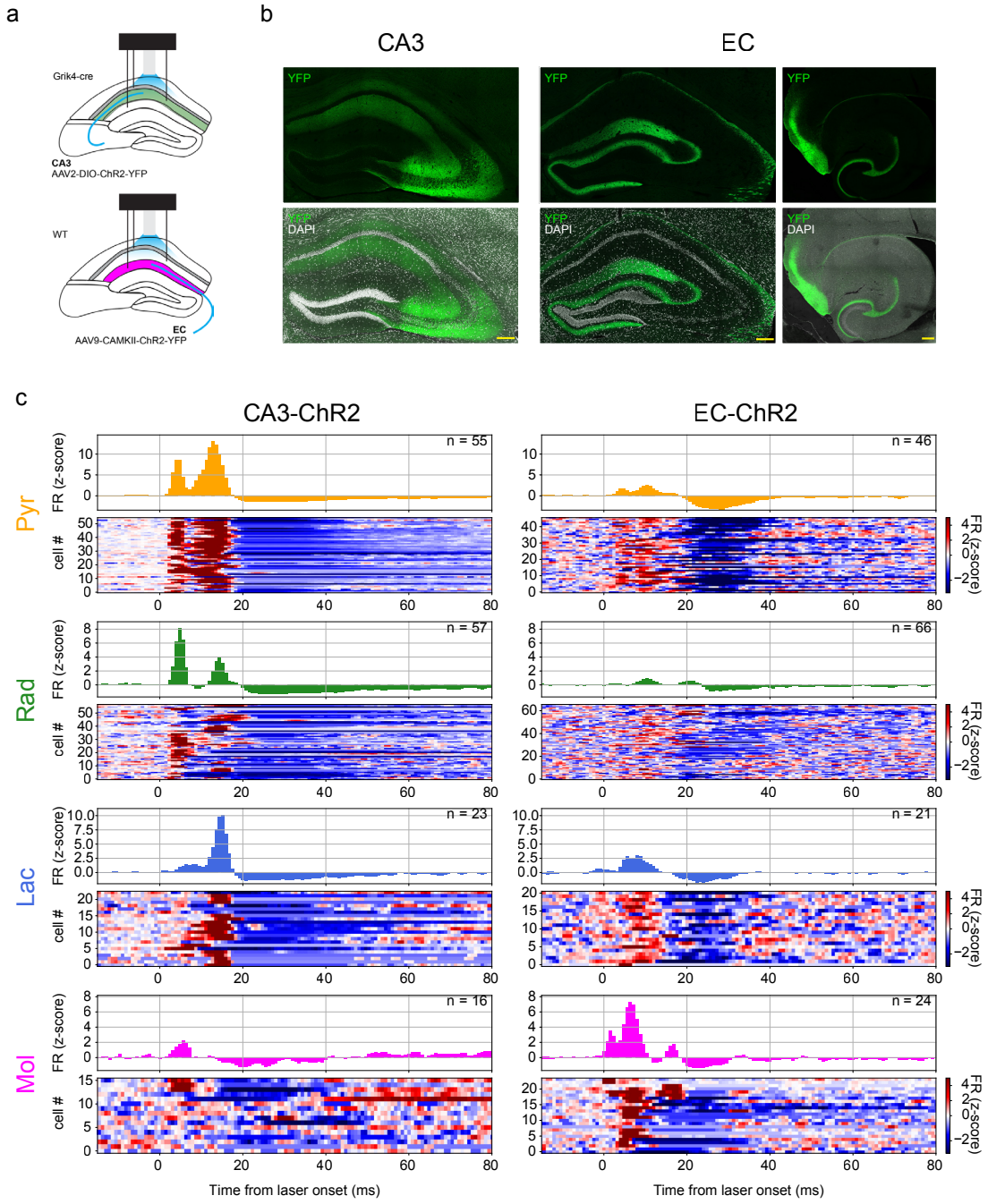


Figure 5.3.7 – Input-specific optical recruitment of superficial interneurons by CA3 and EC

a) Schematic of the optical stimulation experiment. Mice are injected with a viral vector expressing channelrhodopsin in CA3 (Grik4- cre mice with cre-dependent ChR2) or EC (wildype mice with a CAMKII promotor-driven ChR2). Optic fibres are positioned over dorsal CA1. **b**) Representative examples of the injection site and projection patterns in dorsal CA1 for CA3 and EC-injected mice. Left: Coronal section of hippocampus showing ChR2-YFP expressing neurons (green) in CA3 and their axonal projections in CA1, with DAPI staining (white). Note the projections in strata oriens and radiatum. Middle: Coronal section of the hippocampus showing axonal projections in dorsal CA1 originating from EC in dorsal CA1 (in green). Right: horizontal section of the EC, corresponding to the middle panel, showing ChR2-expressing neurons (green) and DAPI staining (white). Note the projections in the strata lacunosum and moleculare of CA1 as well as the middle molecular layer of the dentate gyrus, which is consistent with axonal projections from the medial EC. Scale bars, 200 μm. »

» **c**) Laser-triggered response patterns for interneurons across distinct recording layers in CA3 (left) and EC (right) terminal-stimulated mice. The top panels indicate the mean z-scored response across all recorded neurons, and colour-coding indicates the recording layer (Pyr: yellow, Rad: green, Lac: blue, Mol: magenta). The bottom panel shows z-scored mean responses per recorded neuron. Note the differential responses across layers and between stimulation conditions. Number of included neurons is indicated in the top right corner. Pyr: pyramidale, Rad: radiatum, Lac: lacunosum, Mol: moleculare, EC: entorhinal cortex, ChR2: Channelrhodopsin-2.

the EC stimulation group. Specifically, in the stratum pyramidale nearly all cells participated in both CA3 response windows, while in stratum radiatum neurons either responded to the first or the second, and nearly all neurons in lacunosum responded in the second window (Mean latency (ms), 95%CI: Pyr 3.84, 3.22-4.54; Rad 6.88, 5.26 – 8.62; Lac 10.36, 8.7-12.0; Mol 7.2, 3.6-10.7; **Figure 5.3.7c**, **Figure 5.3.8c**). Moleculare neurons responding to CA3 terminal stimulation showed a single peak falling between the peaks seen in the other layers. EC stimulation resulted in the fastest responses in stratum moleculare, with slightly slower responses across the other layers. Nevertheless, all mean peak response delays fell within 10 ms post-stimulation window (Mean latency (ms), 95%CI: Pyr 6.06, 4.65 – 7.58 ms; Rad 8.0, 5.53 – 10.47ms; Lac 7.05, 5.09 – 9.16 ms; Mol 4.30, 3.35 – 5.15 ms; **Figure 5.3.7c**, **Figure 5.3.8c**). Thus, CA3 and EC stimulation drive superficial interneurons differently across distinct layers.

Furthermore, nearly all recorded neurons displayed a strong, long-lasting, delayed spike rate reduction in both stimulation groups after ~20ms post-stimulation (**Figure 5.3.7c**, **Figure 5.3.8d-f**). CA3-terminal stimulation significantly reduced spiking activity in a 20-40 ms post-stimulation window in the majority of interneurons across pyramidale, radiatum, and lacunosum interneurons (Pyr 96%, Rad 90%, Lac 96%) and in half of the moleculare interneurons (Mol 50%). In some neurons, this spike reduction lasted up to ~200 ms from laser onset (**Figure 5.3.7c**, **Figure 5.3.8d**). EC terminal stimulation, on the other hand, resulted in a post-stimulation spike reduction in ~90% of the pyramidale neurons but inhibited fewer neurons in superficial layers of dorsal CA1 (Rad: 32%, Lac: 52%, Mol: 54%) and affected spiking up to ~100 ms after the laser for some neurons (**Figure 5.3.7c**, **Figure 5.3.8d**). The magnitude of the spike reduction was comparable across the strata pyramidale, radiatum, and lacunosum in the CA3 terminal stimulation group while having a limited inhibitory effect on the moleculare (Mean, 95%CI: Pyr -1.33, -1.53 – -1.14; Rad -1.21, -1.42 – -0.99; Lac -1.25, -1.48 – -1.04; Mol -0.42, -0.94 – 0.09; **Figure 5.3.7c**, **Figure 5.3.8e**).

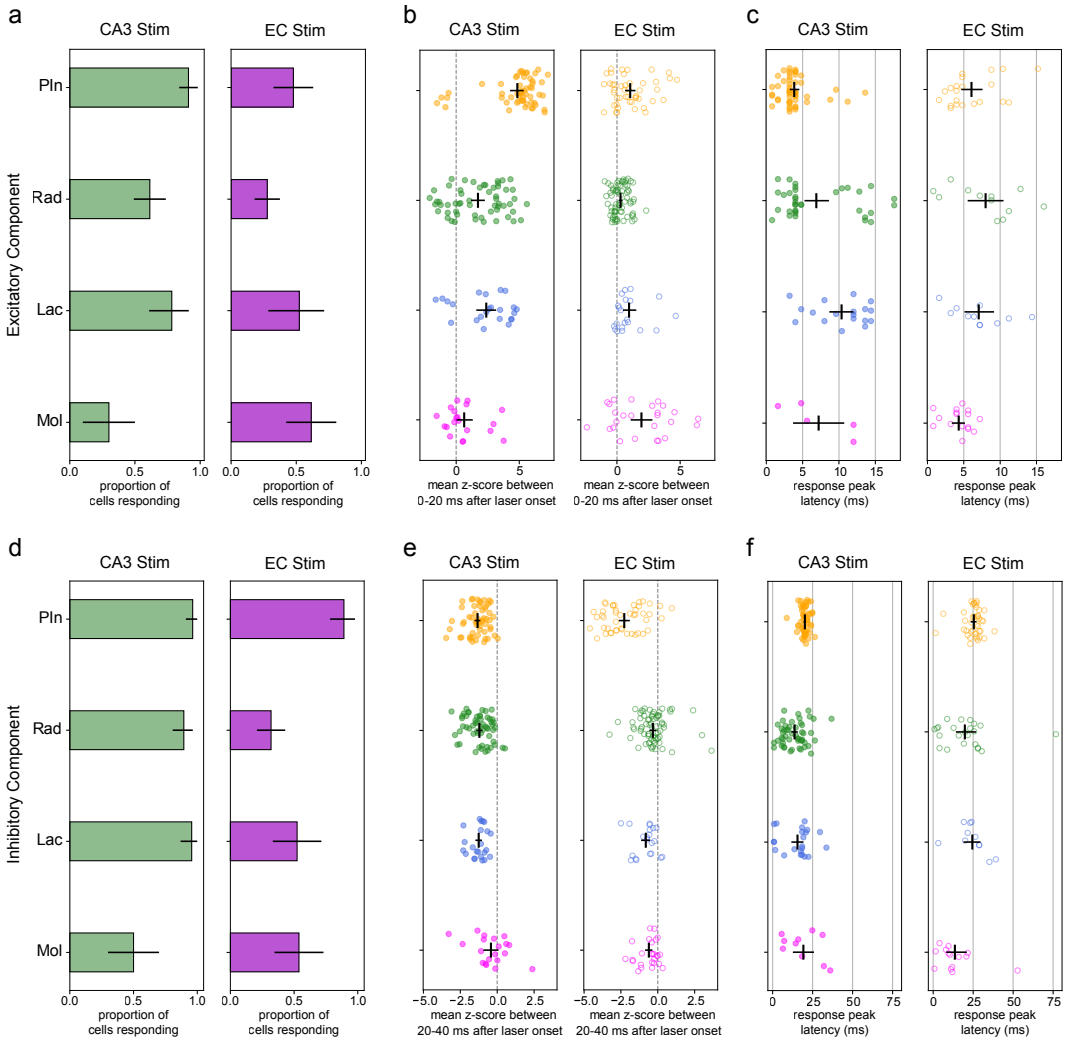


Figure 5.3.8 – CA3 and EC recruit superficial interneurons differently along the radial axis of dorsal CA1

a) Bar graphs showing the proportion of neurons significantly increasing their firing rates upon CA3 (light green) and EC (purple) terminal stimulation in a 20 ms post-stimulation window, whiskers indicate the 95% bootstrapped confidence interval. **b**) Scatter plots showing the mean z-score in the 20 ms post-stimulation window for all neurons in different recording layers in response to CA3 (right) and EC (left) terminal stimulation. Data points represent individual neurons, and colour-coding corresponds to neuron groups (PIn: yellow, Rad: green, Lac: blue, Mol: magenta). Vertical dash indicates the group mean and horizontal whiskers the 95% CI of the mean. Note the reversed patterns for CA3 compared to EC stimulation responses across layers (mean z-score in 0-20 post-stimulation window, 95%CI for CA3 terminal stimulation: Pyr 4.85, 4.28-5.35; Rad 1.73,1.18-2.27; Lac 2.39, 1.60-3.17; Mol 0.64, -0.04-0.1.32; EC terminal stimulation: mean z-score in 0-20 post-stimulation window, 95%CI: Pyr 1.05, 0.64-1.47; Rad 0.28, 0.13-0.44; Lac 0.96, 0.47-1.53; Mol: 1.94, 0.83-2.81). **c**) Scatter plots showing the mean response latency for significantly responding neurons in different recording layers in response to CA3 (right) and EC (left) terminal stimulation. Data points represent individual neurons, and colour-coding corresponds to neuron groups. Vertical dash indicates the group mean and horizontal whiskers the 95% CI of the mean. Note the bimodal response latencies in stratum radiatum in response to CA3 terminal stimulation, while not seen for EC terminal stimulation (response peak latency mean, 95%CI for CA3 terminal stimulation: Pyr 3.84, 3.22-4.54 ms; Rad 6.88, 5.26 – 8.62 ms; Lac 10.36, 8.7-12.0 ms; Mol 7.2, 3.6-10.7 ms; EC terminal stimulation: Pyr 6.06, 4.65 – 7.58 ms; Rad 8.0, 5.53 – 10.47ms; Lac 7.05, 5.09 – 9.16 ms; Mol 4.30, 3.35 – 5.15 ms). **d**) Same as **a**) for neurons showing a significant spike reduction in the 20-40 ms post-stimulation window. »

» Note that nearly all neurons display a significant spike rate reduction in response to the CA3 terminal stimulation while these effects are less pronounced for the EC terminal stimulation. **e**) Same as **b**) showing mean z-score in the 20-40 ms post-stimulation window. Note the homogenous response magnitude across the strata pyramidale, radiatum, and lacunosum to CA3 terminal stimulation, while particularly pyramidale neurons show the largest spike reduction magnitude after EC terminal stimulation (mean z-score in 20-40 ms post-stimulation window, 95%CI for CA3 terminal stimulation: Pyr -1.33, -1.53 – -1.14; Rad -1.21, -1.42 – -0.99; Lac -1.25, -1.48 – -1.04; Mol -0.42, -0.94 – 0.09; EC terminal stimulation: Pyr -2.27, -2.65 – -1.89; Rad -0.33, -0.57 – -0.09; Lac -0.81, -1.14 – -0.52; Mol -0.61, -0.88 – -0.36). **f**) Same as **c**) showing the time to maximal spike rate reduction for neurons showing a significant spike reduction in the 20-40 ms post-stimulation window. Response peak latency mean, 95%CI for CA3 terminal stimulation: Pyr 20.13, 19.35 – 20.86 ms; Rad 13.69, 11.66 – 15.75 ms; Lac 15.53, 11.67 – 19.27 ms; Mol 10.20, 12.64 – 25.84 ms; EC terminal stimulation: Pyr 25.43, 23.43 – 27.14 ms; Rad 19.83, 14.23 – 26.89 ms; Lac 24.51, 18.98 – 29.60ms; Mol 13.60, 8.17 – 21.03.

The EC terminal stimulation showed a strong spike reduction in the stratum pyramidale, while superficial neurons displayed a milder firing rate reduction (Mean, 95%CI: Pyr -2.27, -2.65 – -1.89; Rad -0.33, -0.57 – -0.09; Lac -0.81, -1.14 – -0.52; Mol -0.61, -0.88 – -0.36; **Figure 5.3.7c**, **Figure 5.3.8e**). The strongest spike reduction (minimum spike rate value in the laser-triggered average) was found at varying delays across different interneuron groups. In the CA3 terminal stimulation group, pyramidale interneurons reached the lowest spike rates at ~20 ms after the laser onset with little variation (**Figure 5.3.7c**, **Figure 5.3.8f**). Despite a larger variability, on average, stratum moleculare neurons displayed a spike reduction delay of ~19 ms. The strata radiatum and lacunosum, however, showed a faster inhibitory component compared to the pyramidale interneurons, with mean delays of ~14 and ~16 ms, respectively. Conversely, the delays detected in the EC terminal stimulation group displayed more variation within groups across the different layers (**Figure 5.3.7c**, **Figure 5.3.8f**). Despite not being significantly different from the strata radiatum (~20 ms) and lacunosum (~19 ms), the stratum moleculare showed a trend towards the shortest mean delays (~14 ms). The stratum pyramidale neurons, on the other hand, reached their lowest spike rates significantly later than the moleculare neurons, on average at ~25 ms. Together, these data indicate that the excitatory terminal stimulation results in input-specific recruitment of local inhibition and leads to layer-specific spike reduction.

In summary, similar to our anatomical study, these findings show that the CA3 inputs predominantly affect the neurons around the pyramidal layer, while minimally interacting with moleculare neurons. Conversely, EC stimulation mostly affected moleculare neurons while deeper positioned

neurons responded less. In addition, I found that both CA3 and EC terminal stimulation result in a prominent inhibitory response across nearly all neurons and layers. Overall, this suggests that, despite most neurons having dendrites across multiple layers, different inputs do not seem to target neurons equally across layers.

5.3.2.3 Spike characteristics show no difference in recruited interneuron types by CA3 and EC terminal stimulation

Distinct neuron types display differential morphologies as well as electrophysiological characteristics. The anatomical analysis in the previous section (see **Figure 5.3.3**) suggests differential targeting of superficial neurons by CA3 and EC based on soma morphology. To test this hypothesis at a functional level, I compared the neurons responding to laser stimulation across different baseline spike characteristics (**Figure 5.3.9**). Baseline firing rate characteristics showed a similar pattern across layers as earlier described (see **Chapter 4**). However, this analysis showed that baseline characteristics between CA3- or EC-responding neurons, recorded in distinct layers, did not differ in estimated recording depth, mean theta phase, ripple response score, firing rate in theta, trough-to-peak time, and shoulder asymmetry. Together, these data suggest that, within the same layers, interneurons recruited by CA3 and EC display similar spike characteristics.

5.3.2.4 Stimulation response timing and strength across different brain states

To examine whether hippocampal interneurons change their responsiveness to distinct inputs during various brain states, I compared individual neurons' spike probability and spike-timing across wake and sleep states (**Figure 5.3.10**). Spike probability upon CA3 stimulation was higher during sleep for pyramidale, radiatum, and lacunosum interneurons, which indicates that CA3-to-interneuron information transmission is stronger in sleep. Moleculare interneurons, however, showed a trend towards a higher spike probability in awake states (**Figure 5.3.10a**). Conversely, when the EC terminals were stimulated, spike probability was higher in awake states for pyramidale interneurons and a trend in lacunosum neurons, indicating that information transmission from EC to these interneurons is stronger in awake states (**Figure 5.3.10a**). Moleculare interneurons showed a trend towards higher spike probabilities in sleep, while stratum radiatum neurons were not

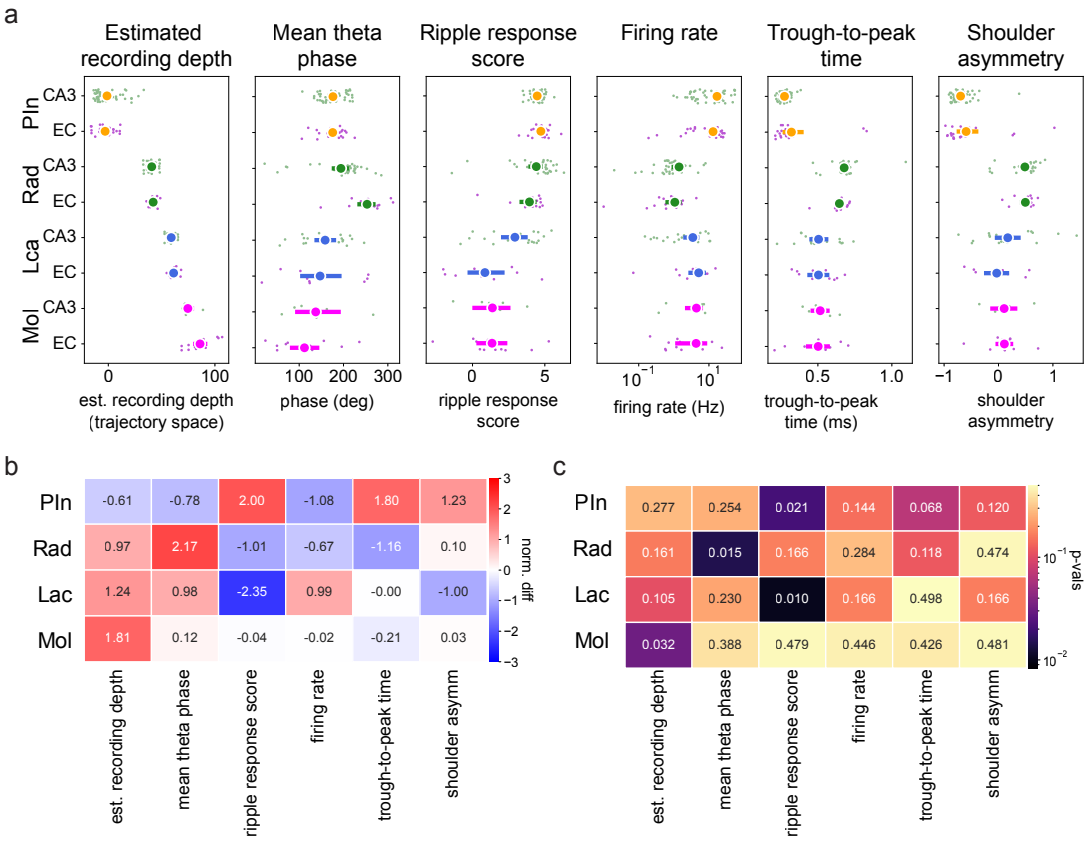


Figure 5.3.9 – Comparison of baseline spike characteristics shows no difference between interneurons recruited by CA3 or EC terminal stimulation

a) Strip plots showing baseline electrophysiological characteristics for interneurons significantly responding to CA3 or EC terminal stimulation. Data points represent individual neurons for the CA3 (light green) and EC (purple) stimulation groups. Larger coloured dots represent the group means and the whiskers the 99%CI of the mean, colours correspond to the recording layers (PIn: yellow, Rad: green, Lac: blue, Mol: magenta). **b**) Heatmap showing the z-scored mean differences between neuronal populations in the CA3 and EC terminal stimulation groups per layer and feature, corresponding to scatter plots in **a**).The z-scoring was obtained for the actual mean difference to the control distribution. **c**) Heatmap showing the p-values corresponding to comparisons in **a**) per layer and feature. p-value was obtained through permutation testing and Bonferroni corrected per recording group setting the significance threshold at 0.008, with no p-values passing this threshold.

affected (**Figure 5.3.10a**). Spike latency increased in sleep for stratum lacunosum and moleculare interneurons but not other groups upon EC stimulation. In contrast, spike latencies for moleculare interneurons were shorter in sleep compared to awake in response to CA3 terminal stimulation (**Figure 5.3.10b**). Lastly, I analysed spike jitter as the standard deviation of spike latency across trials. Spike jitter upon CA3 terminal stimulation did not differ significantly between awake and sleep states but showed a trend for stratum lacunosum and moleculare in awake states (**Figure 5.3.10c**). For EC terminal stimulation, pyramidale, radiatum, and moleculare neurons showed less variable spike latencies in awake states, while there was no difference for stratum lacunosum

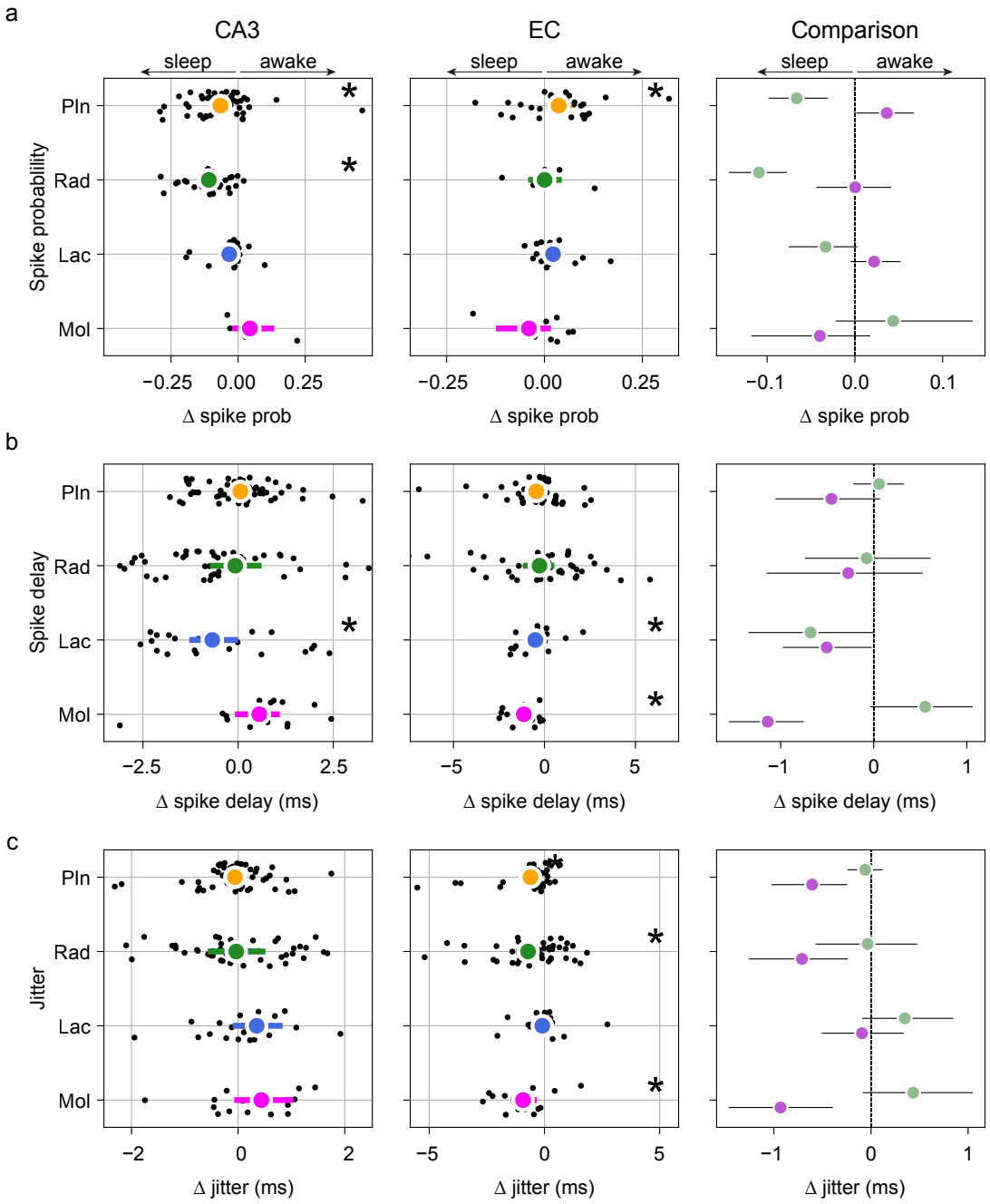


Figure 5.3.10 – Information transfer from CA3 and EC depends on brain state

a) Strip plots showing the spike probability in response to the laser in awake minus sleep for CA3 terminal stimulation (left) and EC terminal stimulation (middle). Black dots represent individual neurons grouped per recording layer. Coloured dots represent the group mean and the whiskers the 95% CI of the mean colour-coded based on recording layer. The right panel shows the group means of CA3 (light green) and EC (purple) terminal stimulation and the 95% CI. Negative group means indicate higher spike probability in sleep and positive values in awake, whiskers crossing the 0-line information indicate no significantly different spike probability between the two brain states (mean probability, 95% CI for CA3 terminal stimulation PIn -0.066, -0.098 – -0.031; Rad -0.109, -0.144 – -0.077; Lac-0.033, -0.076 – 0.003; Mol 0.044, -0.022 – 0.134; EC terminal stimulation PIn 0.036, 0.002 – 0.067; Rad 0.001, -0.044 – 0.042; Lac 0.022, -0.005 – 0.052; Mol -0.040, -0.118 – 0.018). **b**) Same as in **a**) for the laser to spike delay. (mean spike delay, 95% CI for CA3 terminal stimulation PIn 0.057, -0.218 – 0.327; Rad -0.077, -0.740 – 0.611; Lac-0.679, -1.344 – -0.007; Mol 0.554, -0.035 – 1.064; EC terminal stimulation PIn -0.454, -1.057 – 0.067; Rad -0.274, -1.151 – 0.527; Lac 0-0.505, 0.977 – -0.022; Mol -1.139, -1.558 – -0.753). »

» **c**) Same as in **a**) and **b**) for jitter in the spike delays (mean jitter, 95% CI for CA3 terminal stimulation PIn -0.061, -0.2418 – 0.119; Rad -0.035, -0.571 – 0.475; Lac0.348, -0.092 – 0.848; Mol 0.434, -0.085 – 1.047; EC terminal stimulation PIn -0.607, -1.025 – -0.245; -0.712, -1.257 – -0.239; Lac -0.093, -0.508 – 0.336; Mol -0.932, -1.465 – -0.393).

neurons (**Figure 5.3.10**). Together, this data indicates that network responses to distinct inputs differ across different brain states and implies that the circuit is more tuned towards EC inputs during awake states while more biased to CA3 inputs in sleep states.

5.3.2.5 Theta phase-dependent response to input-specific terminal stimulation

The previous section indicates that during different brain states the circuitry may be biased towards specific input streams. Neural circuit activity can also change at a sub-theta cycle scale in the hippocampus (Somogyi and Klausberger, 2005; Klausberger and Somogyi, 2008). Therefore, I tested whether CA3 or EC stimulation results in theta phase-dependent responses of hippocampal interneurons (**Figure 5.3.11**). To do so, I computed the mean spike rate in a 20 ms window for different theta phases at which the 1 ms laser stimulation occurred (see **Methods**). For the CA3 stimulation group, pyramidale interneurons increased their mean spike rate across the full cycle compared with the previous unstimulated cycle, with the strongest responses at descending and ascending phases (**Figure 5.3.11a, b**). Radiatum and lacunosum interneurons show a less pronounced spike rate increase across different theta phases. Radiatum neurons showed a non-uniformly distributed increase, with stronger responses toward the ascending phase. Although less strong, lacunosum neurons displayed, similar to pyramidale interneurons, spike rate increases at across nearly all phases except for the late descending phase (**Figure 5.3.11a, b**). Conversely, in line with earlier findings, moleculare neurons do not significantly increase their activity across the theta cycle. Interestingly, the largest activity gain appeared to occur in theta bins with the lowest based line activity, which was confirmed by correlation analysis. Strata pyramidale and radiatum neurons showed inversely correlated laser stimulation-driven spike rate differences to the baseline spike rates across theta (**Figure 5.3.11c**). Although not significant, stratum lacunosum interneurons showed a similar trend. Together, this data implies that CA3-to-interneuron information transmission varies at subtheta timescales.

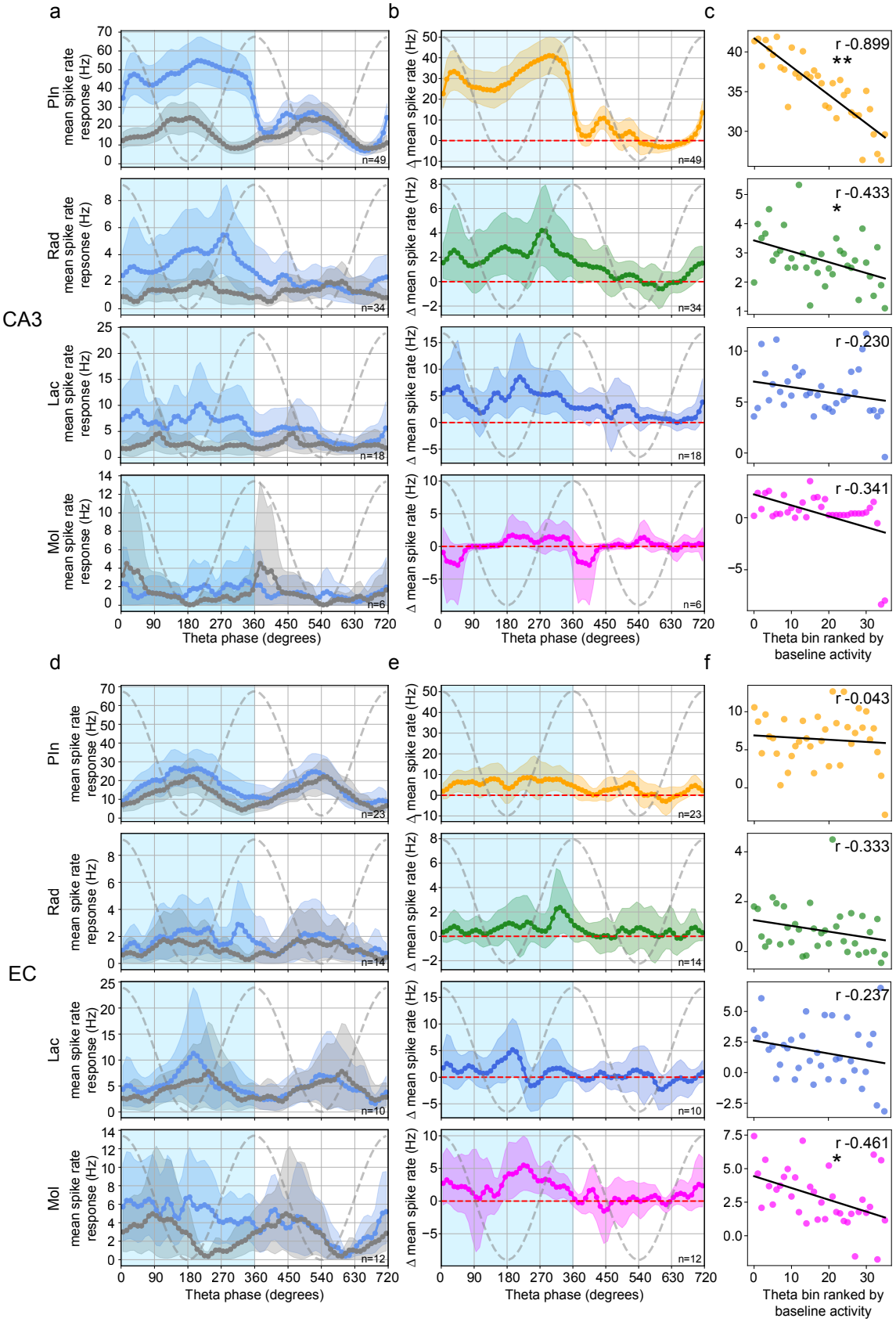


Figure 5.3.11 – Interneuron recruitment by CA3 and EC as a function of stimulation phase

a) Mean spike rate in a 20 ms post-stimulation window as a function of stimulation phase for light-responsive interneurons across different layers in the CA3 terminal stimulation group. »

» The blue line represents the stimulated theta cycle and the first subsequent cycle (cyclestim, cyclestim+1), and the shade indicates the 95% confidence interval. The grey line shows the rates for the theta cycle (cyclestim-1) before the stimulation cycle as a comparison, with the shade indicating the 95% confidence interval of the mean. This cycle was duplicated for illustration (cyclestim-1, cyclestim-1). The light blue shaded block highlights the stimulated cycle. **b**) Mean spike rate difference in the CA3 terminal stimulation group between the stimulated cycle + cyclestim+1 (cyclestim, cyclestim+1), and the cyclestim-1. The solid lines show the mean difference and the shaded areas the 95% confidence interval of the mean difference. The colour coding corresponds to the layer in which the neurons were recorded (PIn: yellow, Rad: green, Lac: blue, Mol: magenta). The light blue shaded block highlights the stimulated cycle. The red dashed line indicated the threshold for a significant difference. **c**) Scatter plot per interneuron group showing the mean spike rate difference per theta bin ranked by baseline activity per phase bin from the lowest to the highest activity bins. Spearman's correlation coefficients are indicated in the top right corner, stars indicate significance against a control distribution generated by 10000 bin label shuffles (p-values: PIn $<10^{-5}$, Rad 0.002, Lac 0.082, Mol 0.031). Per terminal stimulation group Bonferroni correction was applied setting the significance threshold at 0.012. **d, e, f**) Same as **a, b, c**) for the entorhinal cortex terminal stimulation group. The p-values: PIn 0.377, Rad 0.022, Lac 0.074, Mol 0.002. No star p-val>0.012, * 0.012> p-val > 0.001, ** 0.001> p-val. PIn: prymidale interneurons, Rad: radiatum, Lac: lacunosum, Mol: moleculare.

For EC terminal stimulation, response patterns were less overt. Pyramidale interneurons, although not significant, showed a trend to higher spike rates for stimulation at all phases of theta (**Figure 5.3.11d, e**). Radiatum and lacunosum neurons were not significantly increased but showed a similar trend in spike rate changes as for the CA3 terminal stimulation, with higher mean spike rates at the late ascending and around the trough of theta, respectively. In contrast to CA3 terminal stimulation, EC stimulation drove increased spiking in moleculare neurons with significantly higher spike rates when the laser stimulation arrived during the second half of the theta cycle (**Figure 5.3.11d, e**). EC terminal stimulation-induced spike rate gain was inversely correlated with baseline activity in stratum moleculare neurons while showing no significant correlation for stratum pyramidale, radiatum, and lacunosum neurons (**Figure 5.3.11d, f**). The gain in stratum lacunosum spike rates upon laser stimulation preceded the activity peak in the control cycles but both occurred during the theta trough/early ascending phase, implying a rate change mimicking the natural activity pattern. Together, this data shows that, similar to CA3, information transfer from EC to dorsal CA1 interneurons can vary depending on the local network state directed by theta oscillations.

In summary, functional connectivity assessment through input-specific optical terminal stimulation combined with electrophysiological interneuron recordings across the radial axis of dorsal CA1

revealed that interneurons are differently recruited by CA3 and EC. In particular, CA3 and EC preferentially recruited interneurons in their respective termination layers with different temporal dynamics. Beside an excitatory component, terminal stimulation of both input sources resulted in a strong inhibitory effect across all CA1 strata. Lastly, interneuron recruitment efficiency is differentially influenced by brain and network states for CA3 and EC inputs. Overall, this suggests that CA3 and EC recruit different microcircuits in dorsal CA1 under distinct network operations.

5.3.3 Discussion

Interneurons across the radial axis of CA1 display varying morphologies, with prominent differences in the extent and distribution of their dendrites and axons (Freund and Buzsáki, 1996; Somogyi and Klausberger, 2005; Pelkey et al., 2017; Booker and Vida, 2018). With dendrites of most types spanning multiple layers, one could expect that both CA3 and EC can target nearly all interneurons. However, through connectivity assessment at an anatomical and functional level, I found that CA3 and EC targeted interneurons differently across CA1's layers, which is in line with earlier reports (Kajiwara et al., 2008; Milstein et al., 2015) Anatomical assessment showed that somata of targeted neurons were predominantly found in the inputs' termination layers and comprised different subpopulations. Despite both inputs converging on to the stratum lacunosum, soma-shape analysis showed that CA3 and EC may target different subpopulations of lacunosum neurons. In contrast, functional connectivity mapping did not reveal within-layer differences between CA3 and EC-targeted interneurons. Lastly, I found that interneurons can be more or less likely to respond to input-specific optical stimulation depending on brain and network state. Together, these results indicate that CA3 and EC recruit different neuron populations in dorsal CA1, which implies engagement of different microcircuits.

Beside differential soma locations, GABAergic population targeted by CA3 and EC appeared to have different axonal projection patterns, further corroborating the idea that CA3 and EC recruit different GABAergic types and subcircuits. Surprisingly, high fluorescence intensity was found in the stratum moleculare for CA3-targeted interneuron populations, while the number of somata was lowest in this layer. This increased intensity is most likely due to neurons residing in the

stratum oriens and/or radiatum, which send their axons to the strata lacunosum and moleculare, rather than local moleculare neurons giving rise to these axonal projections (Klausberger, 2009). By recruiting these neurons CA3 may gain control over the information flow from EC to CA1 (Leão et al., 2012). In contrast, the fluorescence intensity in the EC-targeted population was lower in radiatum compared to the CA3-targeted group but showed a peak in the stratum pyramidale, suggesting that EC-targeted interneuron populations contain fewer neurons projecting to the radiatum, such as bistratified neurons or Schaffer collateral-associated neurons while including pyramidale targeting types, mostly consisting of basket cells (Freund and Buzsáki, 1996; Pelkey et al., 2017; Booker and Vida, 2018). Furthermore, one of the major differences between EC and CA3 targeted populations is the axonal invasion of the molecular layer of the dentate gyrus. The minimal detectible fluorescence in the dentate gyrus' molecular layer of CA3-injected mice indicates that molecular layer targeting types, such as neuroglia form and perforant path-associated neurons, are less likely to be targeted by CA3 compared to EC (Vida et al., 1998; Fuentealba et al., 2010). These different local axonal targeting patterns could imply an asymmetric control exerted by CA3 and EC over CA1 (**Figure 5.4.1**). In particular, the local inhibitory subcircuit recruited by CA3 targets EC input layers, while the EC-recruited neurons seem to avoid CA3 input layers and target layers associated with direct EC and CA1 input and output, respectively. Together, this indicates that CA3 and EC target distinct but overlapping interneuron populations in dorsal CA1 and, possibly, influence the local circuitry in an input-specific manner.

Inter-hemispheric hippocampal connectivity is not symmetric adding an additional level of complexity to interregional networks (Van Groen and Wyss, 1988; Li et al., 1994; Deller et al., 1996). The unilateral starter injection in CA3 and EC allowed assessment of their hemisphere-specific targeting of interneurons. Soma counts showed that EC-targeting was biased towards ipsilateral CA1 with significantly fewer labelled neurons on the contralateral side, possibly explained by less dense EC projections to contralateral CA1 (Deller et al., 1996; Van Groen et al., 2003). The remarkable fluorescent intensity difference in stratum pyramidale between hemispheres in EC-injected mice seems disproportioned for the soma count differences and may suggest differential targeting of interneuron. A recent study shows that axo-axonic cells

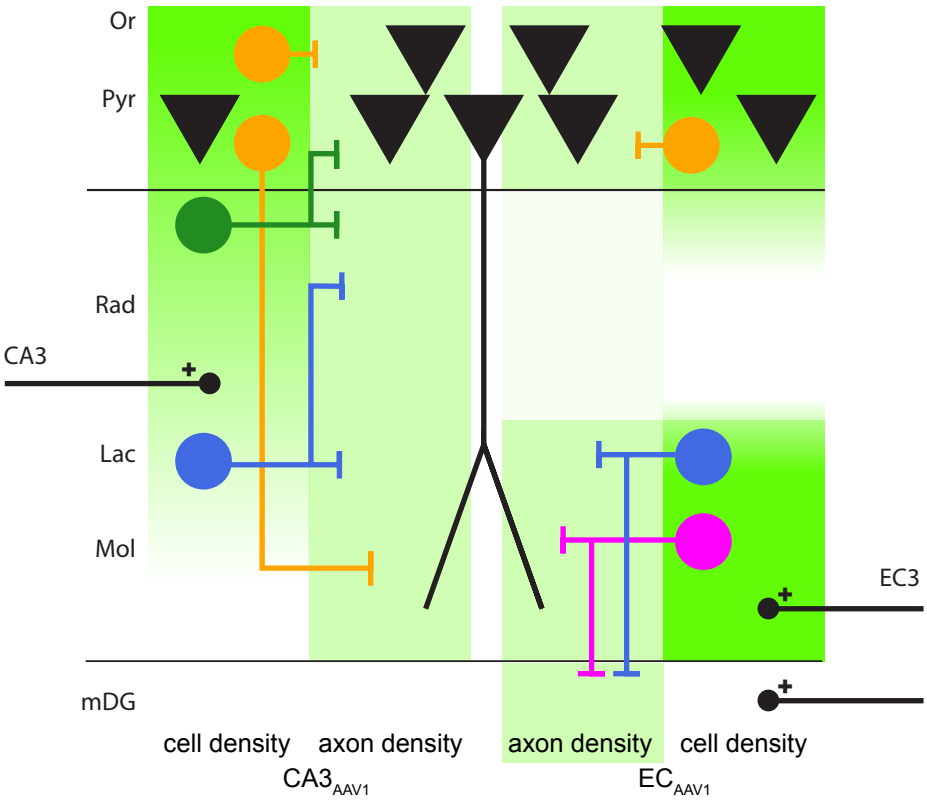


Figure 5.4.1 – CA3 and EC may have asymmetric inhibitory control over local CA1 network inputs

Schematic summarising the results of the anterograde transsynaptic tracing experiment in dorsal CA1. Outer columns indicate the cell density found across different layers for CA3 (left) and EC-starter injections (right), and colour intensity indicates the cell density with darker colours representing higher densities. The middle columns show the localisation of neurite fluorescence for CA3 (left) and EC (right) starter injections. Pyramidal neurons are indicated in black and interneurons corresponding to different layer groups in colour (Pyramidale interneurons: yellow, radiatum: green, lacunosum: blue, moleculare: magenta). Note that for the CA3-injected group somata mostly are found from oriens to lacunosum, while neurites are found across the whole radial axis of CA1. In contrast, for the EC-injected group, most neurons are found around the pyramidale, lacunosum, and moleculare, which corresponds to the neurite localisation. The asymmetric distribution of the axonal plexus of CA3-targeted interneurons may place EC input streams under control of CA3 activity, while EC-targeted interneurons mostly are confined to EC input and CA1 output layers.

(AAC; also known as chandelier cells), which specifically concentrate their axonal plexus to the stratum pyramidale, receive inputs from the ipsi- but not the contralateral entorhinal cortex (Raudales et al., 2024). Differential targeting of axo-axonic cells by EC highlights the asymmetric hemisphere targeting and may extend to more types. Furthermore, in the CA3-injected group, soma count differences between the ipsi- and contralateral hemispheres were restricted to the stratum moleculare, with higher cell density in this layer on the ipsilateral side. This bias could be explained by asymmetric targeting of CA3 projections, which are distributed across the stratum

oriens and radiatum in the ipsilateral hemisphere but are primarily found in stratum oriens on the contralateral side, making moleculare neurons less likely contralateral targets (Van Groen and Wyss, 1988; Li et al., 1994). Thus, these data indicate that both CA3 and EC may recruit different types in an input-specific and lateralised fashion.

Anatomical and functional connectivity mapping resulted in contradicting results on the identity of CA3 and EC-targeted interneurons. Morphological assessment of CA3 and EC-targeted somata suggested differential targeting of interneuron subpopulations within the strata lacunosum and moleculare. This contrasts with previous reports suggesting equal within-layer targeting (Kajiwara et al., 2008). In this study, however, neuron types have not been extensively examined. Additionally, functional connectivity mapping performed in this Chapter does not reveal a within-layer difference between CA3 and EC-responsive neurons. However, the sample size of responding neurons in this experiment is small and may interfere with finding subtle differences between the groups. Furthermore, due to the lack of morphological characteristics on the recorded neurons, it is unclear whether neurons across the full morphological range were included in the connectivity mapping experiments. Alternatively, similar spiking characteristics may be explained by the neurons' physical location in the local network, despite belonging to different types, due to layer-specific inhibitory or excitatory projections shaping their spiking patterns (Witter et al., 2000; Klausberger, 2009; Melzer et al., 2012; Booker and Vida, 2018; Tsoi et al., 2022). Overall, contrasting results do not allow definitive conclusions on whether superficial interneuron subgroups within the same layer are differentially targeted by CA3 and EC. Further anatomical and functional studies are required to elucidate the afferents targeting these cells at a layer-specific level.

CA3 and EC inputs target neurons in the stratum lacunosum – the interface between the superficial hippocampal layers as well as the axonal projections of CA3 and EC – perfectly positioning these interneurons to detect coincidental activity. In line with this idea, neuron peptide Y (NPY) and Cholecystokinin (CCK) have been shown to detect coincidental activity of CA3 and EC inputs (Milstein et al., 2015; Basu et al., 2016). While these studies were performed under *ex vivo* conditions, I found that both EC and CA3 terminal stimulation could drive lacunosum neurons *in*

vivo. Although my experiments were not performed in the same mouse, ~80% of the lacunosum neurons significantly increased their spike rate to CA3 and over half to EC terminal stimulation, which suggests that, at least a subpopulation, could integrate information from both input sources. By integrating multiple input streams and extending their axonal plexus across various layers of CA1 and the dentate gyrus (Klausberger, 2009), lacunosum interneurons are ideally positioned to dynamically scale inhibition based on CA3 and EC activity through regulating dendritic computations, synaptic plasticity, and pyramidal neuron output under specific conditions (Lovett-Barron et al., 2012, 2014; Grienberger et al., 2017; Bilash et al., 2023). Together, the convergence of CA3 and EC inputs onto stratum lacunosum may play an essential role in orchestrating information transmission to pyramidal neurons in a context-specific manner.

In the CA3 axon terminal stimulation group, CA1 interneurons displayed an unexpected bimodal response, with a second component showing a substantial delay beyond what would be expected from monosynaptic connections (English et al., 2017). Although this dual response cannot be dissected based on the current experiments, the delayed component likely reflects a second wave of activity originating from CA3 (Gunn et al., 2023). It can not be ruled out that this second wave of activity arose from unintended stimulation of CA3 pyramidal cell somata or commissural pathways, despite implanting the optic fibre directly over CA1. A recent *ex vivo* study showed highly comparable dynamics in CA1 field potentials driven by stimulation of the CA3's commissural system (Gunn et al., 2023). In addition, back-propagating action potentials through the Schaffer collaterals may have a similar effect (Allen et al., 2015). Alternatively, since Channelrhodopsin-2 was injected bilaterally, the second activity peak may originate from contralateral CA3, as similar delays were seen between contralateral CA3-to-CA1 activation in a recent all-optical study (Fan et al., 2023). Overall, the delayed second response peak upon CA3 stimulation likely reflects physiological network properties, but further experiments are necessary to identify how these responses come about.

During these different brain states, distinct network activity arises due to changing input and neuromodulation (Colgin, 2016; Wan et al., 2021; Zhang et al., 2021). Both network and brain states can influence excitability levels of hippocampal neurons (Lacaille and Schwartzkroin,

1988a; Chapman and Lacaille, 1999b; Buhler and Dunwiddie, 2002; Leão et al., 2012; Wyskiel and Andrade, 2016), possibly biasing the hippocampal circuit to specific input sources under particular circumstances (Bittner et al., 2015; Cohen et al., 2017; Palacios-Filardo et al., 2021; Zhang et al., 2021). Measuring information transfer to superficial interneurons, I found that the same stimulus results in brain state-specific responses. During sleep, most interneuron groups responded more strongly to CA3, while pyramidale and lacunosum neurons showed the opposite trend for EC terminal stimulation. Although recorded in different mice, these findings may suggest that interneurons facilitate differential information routing in different states. Additionally, local circuit connectivity combined with precisely timed subtheta scale inhibition is thought to regulate activity windows across the hippocampal network (Somogyi and Klausberger, 2005; Klausberger and Somogyi, 2008). In line with this hypothesis, I found that interneurons respond differentially to the same stimulus at subtheta timescales, with some displaying the largest spike rate change in the least preferred phases. This could indicate that either neuronal activity of interneurons is lower in these windows due to a lack of inputs or a stronger inhibitory control which restrains the laser-induced spike rate changes (Mizuseki and Buzsáki, 2013; Grienberger et al., 2017; Valero et al., 2022). These data suggest that information transfer from EC and CA3 onto hippocampal interneurons is theta-phase dependent. Overall, these findings indicate that hippocampal interneurons display context-specific responses to EC and CA3.

In summary, I found that hippocampal interneurons are differentially recruited by CA3 and EC through both anterograde tracing studies as well as functional connectivity mapping. In particular, CA3 and EC preferentially target neurons in their respective termination layers but converge on neurons in the stratum lacunosum. Moreover, I showed that CA3 and EC information transfer onto hippocampal interneurons was brain and network state-dependent, suggesting that EC and CA3 not only recruit interneurons differently in a spatial but also a temporal domain. This assessment of CA3 and EC interneuron targeting in an unbiased, CA1-wide manner has provided a unique opportunity to reveal layer-specific response patterns and forms a strong fundament to expand our knowledge on CA1 information routing by superficial interneurons.

Chapter 6. Interactions between superficial interneurons, pyramidal neurons, and the local network

6.1 Introduction

Throughout the brain, interneurons play an important role in orchestrating neural activity (Roux and Buzsáki, 2015). Ways through which interneurons influence their postsynaptic partners differ dramatically, ranging from direct blockage of spike generation in the axon initial segment and shunting of dendritic inputs to subtly shifting the input selection (Leão et al., 2012; Lovett-Barron et al., 2012; Royer et al., 2012; Palacios-Filardo et al., 2021; Bilash et al., 2023). Interneurons can be divided into three major groups based on their axonal targeting patterns: peri-somatic, dendrite, and interneuron targeting (Chamberland and Topolnik, 2012; Booker and Vida, 2018). Due to the differential positioning of their inhibitory synapses on the postsynaptic neuron, these groups can have different effects on the electrogenesis in their postsynaptic partners (Palmer et al., 2012a). While peri-somatic targeting interneurons play a role in rate control and assembly selection, dendrite-targeting neurons can influence the post-synaptic cell more subtly by directing dendritic integration, and interneuron targeting interneurons release distinct pyramidal neuron subdomains from its inhibition (Chamberland and Topolnik, 2012; Palmer et al., 2012a; Hu et al., 2014; Roux and Buzsáki, 2015). Together, combined with differential spike timing, these differential effects guide information processing through the local neural network.

In contrast to single-cell patch-clamp recordings, extra-cellular electrophysiological recording techniques do not permit registration of post-synaptic potentials, but communication between neurons can be captured through spike changes (English et al., 2017). In cortical regions,

interneuron-to-pyramidal neuron interactions can result in several changes in pyramidal neuron spike output. At a population level, removal or activation of distinct inhibitory neuron types can lead to a pyramidal neuron spike increase, decrease, or a change in spike timing, reflecting the inhibitory, disinhibitory, or integration-modulating effects interneurons can have on pyramidal neurons, respectively (Lovett-Barron et al., 2012; Royer et al., 2012; Rangel Guerrero et al., 2024). Direct inhibitory transmission from interneurons to putative excitatory neurons is detectible in extracellular recordings and has been used to infer network connectivity in large-scale extracellular recording datasets (Barthó et al., 2004; Stark et al., 2013; Petersen et al., 2021). While direct, putative monosynaptic, inhibition is detectible without opto- or chemogenetic interventions, disinhibition and spike timing changes are often revealed by manipulating particular interneuron subgroups in conjunction with large-scale recordings (Royer et al., 2012; Guo et al., 2021; Valero et al., 2022; Rangel Guerrero et al., 2024). Together, extracellular recording techniques, which are occasionally aided with interneuron-specific interventions, can reveal the effects of interneuron activity on single pyramidal neurons and population spiking.

Besides direct effects on the neural population, capturing the coactivity between several neuron types within the same local network can be informative when studying interneuron function. Recently, large-scale simultaneous recordings have been performed across different types of interneurons in dorsal CA1. These recordings showed that specific interneuron types display distinct co-activity patterns (Geiller et al., 2020). Furthermore, activity of interneurons in and around the stratum pyramidale has been shown to form distinct correlations with specific pyramidal neurons. Neuron class-specific circuit dissection of synaptically connected neurons revealed that pre-synaptic interneurons displayed reduced activity around their post-synaptic target's preferred place field compared to non-connected interneurons (Geiller et al., 2022). During learning, a subpopulation of interneurons has been shown to increase their co-activity with pyramidal neurons, while others weaken their connections (Dupret et al., 2013). These dynamic changes between interneurons and pyramidal neurons likely facilitate assembly formation and stabilisation. Furthermore, neural interactions can be influenced by network and behavioural states, resulting in dynamic interactions between pyramidal neurons and interneurons (Csicsvari

et al., 1998; Senzai et al., 2019; Guo et al., 2021) (see **Chapter 5**), which could provide windows of flexibility in these stable systems. Together, coactivity measures between interneurons and their local network reflect network dynamics and can inform interneuron function.

Coactivit analysis between interneurons and pyramidal neurons mostly focuses on interneuron populations found in and around the stratum pyramidale (Csicsvari et al., 1998; Royer et al., 2012; Dupret et al., 2013). In this Chapter, I leverage the superficial interneuron dataset to examine the effects of superficial interneurons on pyramidal neuron activity as well as their coactivity with other members of the local neural network. I found that superficial interneurons do not induce detectible spike reductions in pyramidal neurons, while this was the case for pyramidale interneurons. However, superficial interneuron activity was associated with changes in spike timing and spike phase of pyramidal neurons in a layer-specific manner. Lastly, superficial interneurons form state-dependent coactivity structures with the local network. Together, this Chapter provides insights into the coactivity and downstream effects of superficial interneurons in the context of their local network.

6.2 Methods

6.2.1 Mice, surgical procedure, and data acquisition

For this Chapter, the same dataset as presented in Chapter 3 was used, see the Methods section of Chapters 2 and 3 for a description of the included mice (**section 3.2.1**), surgical and habituation procedures (**sections 2.2.2 - 2.2.5**), electrophysiological and tracking data acquisition methods (**section 2.2.6**), and behavioural protocol (**section 3.2.2**). In short, 17 mice were intracranially recorded using 14-tetrode microdrives over a total of 65 recording days (maximum 8 days per mouse). Mice were allowed to explore either familiar or novel open fields interleaved with sleep sessions.

6.2.2 Data analysis

6.2.2.1 Software

Data were analysed in Python 3.10 using the following packages: Numpy v1.24.3, Pandas 1.5.3, Scipy 1.10.1, Matplotlib v3.7.1, Seaborn v0.21.2, and Networkx v3.3.

6.2.2.2 Data pre-processing and quality control

Signal pre-processing, spike sorting, and quality control were performed as described in Chapter 3.

6.2.2.3 Detecting Theta oscillations and sharp-wave ripples

Theta and sharp-wave ripple detection was performed as described in **sections 2.2.7.3** and **2.2.7.4**, and by Lopes-dos-Santos et al. 2023.

6.2.2.4 Computing correlation spike characteristics and co-activity

Spike triggered averages

To compute spike-triggered averages, first, an activity matrix was built with a 0.8 ms sample rate. For every neuron pair, a 400 ms window was centred around individual spikes of the triggering cell and averaged per pair.

Spike-triggered activity differences

To compute the spike-triggered activity difference of a neuron, the difference in mean rate between the pre-spike and post-spike window was taken as a percentage of the mean rate in the pre-window. Different window sizes were used (5, 10, 50, and 200ms), with the pre- and post -spike windows being of equal size.

Power spectrum density

Power spectrum density (PSD) was computed using the Fast Fourier Transform (FFT) function of the Numpy package (np.fft.fft), and the corresponding frequencies were obtained using the np.fft.fftfreq function based on the 1.25k Hz sampling rate. The PSD was obtained by taking the

positive values of the squared FFT results. The dominant frequency was defined as the frequency with the highest power.

Co-activity matrices

First event-based activity matrices were computed. These event-based matrices contained the number of spikes a given neuron fired within the boundaries of a theta-cycle or sharp-wave ripple for all neurons and theta-cycles per recording session. Event-pairwise Pearson's correlations were computed per recording day for the coactivity analysis between neurons. For the weighted graphs, correlation coefficients were pooled per group and averaged. To compare theta and sharp-wave ripple-based coactivity across events, the coactivity change was computed as the difference between the coefficients in SWR and theta (theta-SWR) as a percentage of the correlation coefficient in SWRs.

Interneuron activity-weighted pyramidal neuron spiking behaviour

To compute interneuron activity-weighted spiking behaviour of pyramidal neurons, event-based interneuron activity was obtained from the event-based activity matrices (see Co-activity matrices). Then the pyramidal neuron spike times within the same boundaries were computed. Per pyramidal neuron-interneuron pair, spike time differences and spike phases were computed for the pyramidal neuron, and weighted averages were generated based on the activity level of the interneuron. Only pyramidal neurons active in more than 100 theta cycles were included. Lastly, ISI and spike phase histograms were generated per pyramidal neuron-interneuron pair and averaged across mice and recording days.

6.2.3 Statistical testing

Permutation testing and bootstrapped confidence intervals were used for statistical testing and obtained as described in Chapter 3 (see **section 3.2.3.8**).

6.3 Results

6.3.1 Pyramidale interneurons but not superficial interneurons generate short-latency spike reduction in the pyramidal neuron population

To examine the interactions between superficial interneurons and pyramidal neurons, I first computed peri-spike triggered averages of pyramidal neuron activity using spikes from interneurons as reference (trigger) events, and quantified the median spike difference before and after interneuron spikes across the pyramidal neuron population (**Figure 6.3.1**). At short timescales, the spike-triggered average (STA) between pyramidal neurons and pyramidale interneurons showed a small spike reduction (1.8% reduction), while this was not the case for pyramidal neurons recorded in the contralateral hemisphere, which showed a spike increase (~2% increase) (**Figure 6.3.1**; **Table 6.3.1**). For superficial interneurons, no spike reduction was observed for short-latency windows. Instead, pyramidal neuron firing was higher in the 5 ms post-spike window compared to the pre-spike window of stratum lacunosum and moleculare interneurons (Lac 4.3%; Mol 3.7% increase) for ipsi- and contralaterally recorded populations (**Figure 6.3.1a-c**, **e-f**; **Table 6.3.1**). At longer time windows, only radiatum neuron-triggered pyramidal neuron activity showed a decrease for both ipsi- as well as contralaterally recorded pyramidal neurons (Ipsi 50ms 3.7%, 200ms 1.3%; Contra 50ms 2.6%, 200ms 1.2% reduction), while an increase or no change was found for lacunosum

		Ipsi			Contra		
Trigger	**Window (ms)**	**Difference (%)**	**97.5% CI**		**Difference (%)**	**97.5% CI**	
PIn	5	-1.768	-3.091	-0.502	2.051	0.747	3.09
	10	-1.055	-2.495	0.061	1.448	0.101	2.56
	50	0.219	-0.719	1.217	1.813	0.411	2.96
	200	-1.031	-1.418	-0.463	-0.516	-0.96	-0.087
Rad	5	1.137	-1.126	3.417	-0.161	-1.955	1.689
	10	0.638	-1.992	2.9	0.336	-0.926	1.999
	50	-3.733	-5.19	-2.297	-2.571	-3.574	-1.371
	200	-1.337	-2.097	-0.408	-1.153	-1.727	-0.48
Lac	5	4.299	2.482	6.11	3.943	2.014	6.156
	10	6.106	3.431	8.316	5.077	3.652	8.163
	50	2.27	1.046	3.933	2.646	1.358	4.469
	200	0.422	-0.376	1.042	0.467	-0.186	1.035
Mol	5	3.734	0.942	7.491	3.252	-0.461	6.347
	10	6.612	3.315	10.319	4.895	2.498	7.759
	50	4.227	1.685	7.198	3.271	1.074	5.195
	200	0.101	-0.718	0.755	-0.4	-1.19	0.319

Table 6.3.1 – Pyramidal neuron spike rate change in pre- and post-spike windows

Proportional difference in firing rate between pre- and post-spike window between ipsi- and contralateral pairs. Data corresponding to **Figure 6.3.1**.

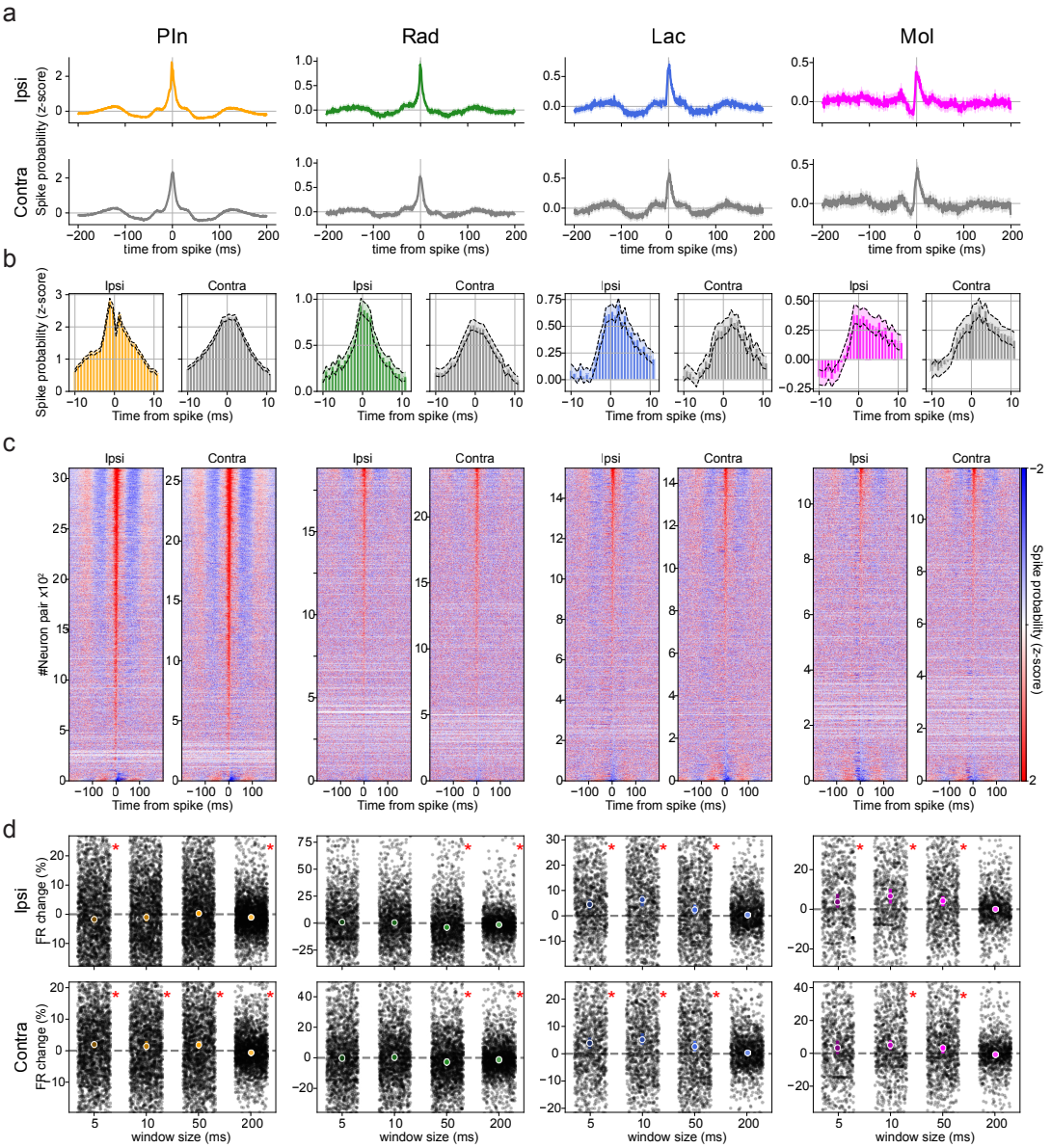


Figure 6.3.1 – Superficial interneurons do not induce detectible spike reduction in pyramidal neuron population

a) Mean spike-triggered averages of pyramidal neuron activity triggered by interneuron spikes for ipsi- (colour) and contralaterally (grey) recorded pyramidal neurons. Shaded area represents the 95% CI. Colour coding indicates interneuron groups (interneurons in the stratum pyramidale: yellow, radiatum: green, lacunosum: blue, moleculare: magenta) **b**) Same as in **a**) depicted for a shorter time window for visualisation purpose. **c**) Same as in **a**) depicting all interneuron-pyramidal neuron pairs (rows) sorted based on the mean activity around 0 ms for ipsi- (left) and contralaterally (right) recorded pyramidal neurons triggered by interneurons from different groups. **d**) Mean difference between spiking activity pre- and post-interneuron spike for different time windows ranging from 5-50 ms for ipsi- (top row) and contralateral (bottom row) pairs. Individual data point indicate pyramidal neuron-interneuron pairs. Significance depicted by red astricts for statistics see **Table 6.3.1**. For illustration purposes, only the 95% of the population is depicted.

and moleculare triggered averages (Lac Ipsi 50ms 2.3%, Contra 50ms 2.6%; Mol Ipsi 50ms 4.2%, Contra 50ms 3.3%; **Figure 6.3.11a-c**, **e-f**; **Table 6.3.1**). Furthermore, the STAs revealed spike coherence in the theta-band frequency between pyramidal neurons and pyramidale, radiatum, and lacunosum interneuron, while less prominent for moleculare interneurons (power spectrum density analysis for ipsilateral population peak frequency (Hz), power: PIn 8.0Hz, $21x10^3$; Rad 7.8Hz, $12x10^2$; Lac 7.3Hz, $14x10^2$; Mol 6.8Hz, $2x10^2$; **Figure 6.3.1a, c**). Similarly, STAs between interneurons and contralateral pyramidal neurons showed comparable dynamics (Contralateral population frequency (Hz), power: PIn 8.0Hz, $23x10^3$; Rad 7.8Hz, $9x10^2$; Lac 7.8Hz, $11x10^2$; Mol 7.0Hz, $3x10^2$: **Figure 6.3.1a, c**). Together, these results show that superficial interneurons do not induce detectible short-latency spike reductions in the overall pyramidal neuron population, while spike coherence indicates well-times spiking relationships.

6.3.2 Pyramidal neuron spiking patterns are influenced by superficial interneurons

Beside rate control, interneurons can influence pyramidal neuron spike timing (Royer et al., 2012; Rangel Guerrero et al., 2024). To test whether superficial interneuron population can induce such effect, I examined the relation between superficial interneuron activity on pyramidal neuron inter-spike intervals and spike phases in theta cycles during awake exploration(see **Methods**; **Figure 6.3.2**). The theta cycle-specific inter-spike intervals were weighted against the activity level of individual interneurons on a cycle-by-cycle basis and compared to equally weighted cycles. This analysis revealed that pyramidal neuron inter-spike interval probabilities changed in a layer- and interval-specific manner (**Figure 6.3.2a**,**b**). Pyramidal neurons showed a lower proportion of ISIs in the burst range (2 – 7 ms) in theta cycles biased to high stratum radiatum interneuron activity (**Figure 6.3.2c**; **Table 6.3.3**). A similar trend was found for pyramidale interneurons but not for stratum lacunosum and moleculare interneurons. In contrast, for ISIs in a mid-gamma range (11 – 20 ms), pyramidal neurons showed a mild decrease when stratum lacunosum neurons were active, while this was not seen for the other interneuron groups. Pyramidal neurons displayed a reduction of ISIs in a slow-gamma range (22 – 33 ms) when stratum moleculare interneurons were active and a trend towards an increase for high activity cycles of stratum pyramidale and

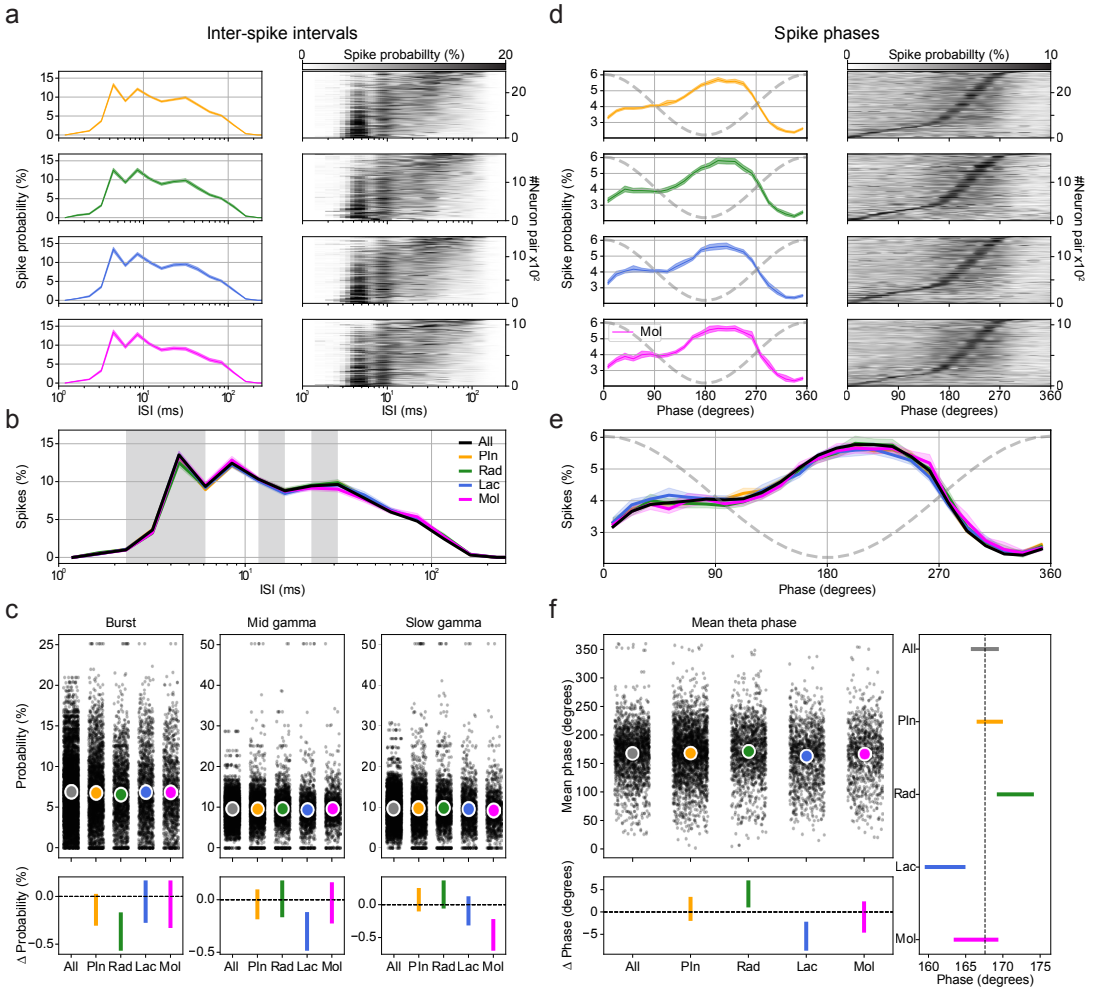


Figure 6.3.2 – Cycle-by-cycle superficial interneuron activity is associated with pyramidal neuron spike timing changes

a) Left: Averaged inter-spike interval histograms of pyramidal neuron supra-theta ISIs weighted by interneuron-specific activity for different interneuron groups. Shaded area represents the 95% CI. Colour coding indicates interneuron groups (interneurons in the stratum pyramidale: yellow, radiatum: green, lacunosum: blue, moleculare: magenta). Right: inter-spike interval histograms for pyramidal neuron-interneuron pairs (rows represent individual pairs). **b**) Averaged inter-spike interval histograms of pyramidal neuron supra-theta ISIs weighted by interneuron-specific activity for different interneuron groups from **a**) superimposed. Grey shaded area indicate the interval ranges corresponding to burst, mid-gamma, and slow-gamma, from left to right. **c**) Top: Mean Inter-spike interval probability in burst, mid-gamma, and slow-gamma interval ranges. Data points represent individual pyramidal neuron-interneuron pairs. The coloured dot indicates the group mean, with colour coding corresponding to **a**). For 95%CI see **Table 6.3.3**. Bottom: bootstrapped difference between all pairs across all cycles (cycles equally weighted) compared to interneuron activity-weighted groups. Bars indicate the 95%CI difference. **d**) Left: Averaged spike-phase histograms of pyramidal neurons weighted by interneuron-specific activity for different interneuron groups. Shaded area represents the 95% CI. Colour coding is similar to **a**). Right: spike-phase histograms for pyramidal neuron-interneuron pairs (rows represent individual pairs). **e**) Averaged spike-phase histograms of pyramidals weighted by interneuron-specific activity for different interneuron groups from **a**) superimposed. Dotted line represents theta phase. **f**) Left top and bottom: Same as in **c**) for spike phase. Right: 95% CI per group corresponding to the scatter plots (top left panel).

Group	Subgroup	Mean	95% CI		Mean Diff	p-value
Pyramidal neuron ISI						
ISI range (ms)		**Probability (%)**				
2 – 7	Pyr	6.9	6.8	7.0		
	Pin	6.7	6.6	6.9	0.142	0.048
	Rad	6.5	6.3	6.7	0.367	0
	Lac	6.8	6.6	7.1	0.054	0.315
	Mol	6.8	6.5	7.1	0.08	0.264
11 – 20	Pyr	9.6	9.5	9.6		
	Pin	9.5	9.4	9.7	0.041	0.29
	Rad	9.6	9.3	9.8	-0.01	0.449
	Lac	9.3	9.0	9.5	0.298	0
	Mol	9.5	9.3	9.8	0.029	0.388
22 – 33	Pyr	9.5	9.5	9.6		
	Pin	9.6	9.4	9.8	-0.078	0.192
	Rad	9.7	9.4	10.0	-0.155	0.076
	Lac	9.4	9.2	9.7	0.094	0.199
	Mol	9.1	8.8	9.4	0.458	0
Pyramidal neuron theta spike phase						
		Phase (degrees)				
	Pyr	168	166	169		
	Pin	168	167	170	-0.7	0.306
	Rad	172	169	174	-4.0	0.006
	Lac	162	160	165	5.4	0.001
	Mol	166	163	170	1.1	0.274

Table 6.3.2 – Pyramidal neurons spike timing changes in response to interneuron activity

Table shows mean spike probability in defined windows and mean spike phase for neurons in different recording layers, and the difference to the control cycles. Data related to **Figure 6.3.2**

radiation interneurons. Furthermore, pyramidal neurons showed a spike phase shift associated with superficial interneuron-specific high-activity cycles (**Figure 6.3.2d, e**). In cycles with high radiatum interneuron activity, pyramidal neurons displayed a phase delay, while they advanced in cycles with high stratum lacunosum activity (**Figure 6.3.2f**; **Table 6.3.3**). For stratum pyramidale and moleculare interneurons, such a shift was not observed. Together, these results suggest that superficial interneuron activity is associated with changes in spike timing of pyramidal neurons.

6.3.3 Co-activation between superficial interneurons and the neural local network is state-dependent

To gain insights into the activity patterns of interneurons in relation to the local neural network, I tested co-activity between co-recorded neuron pairs in awake exploration and sleep states. To sample comparable brain states across animals, I used network-relevant time bins (theta cycles and sharp-wave ripples; see **Methods**; **Figure 6.3.3**). In theta cycles, the mean correlation coefficients

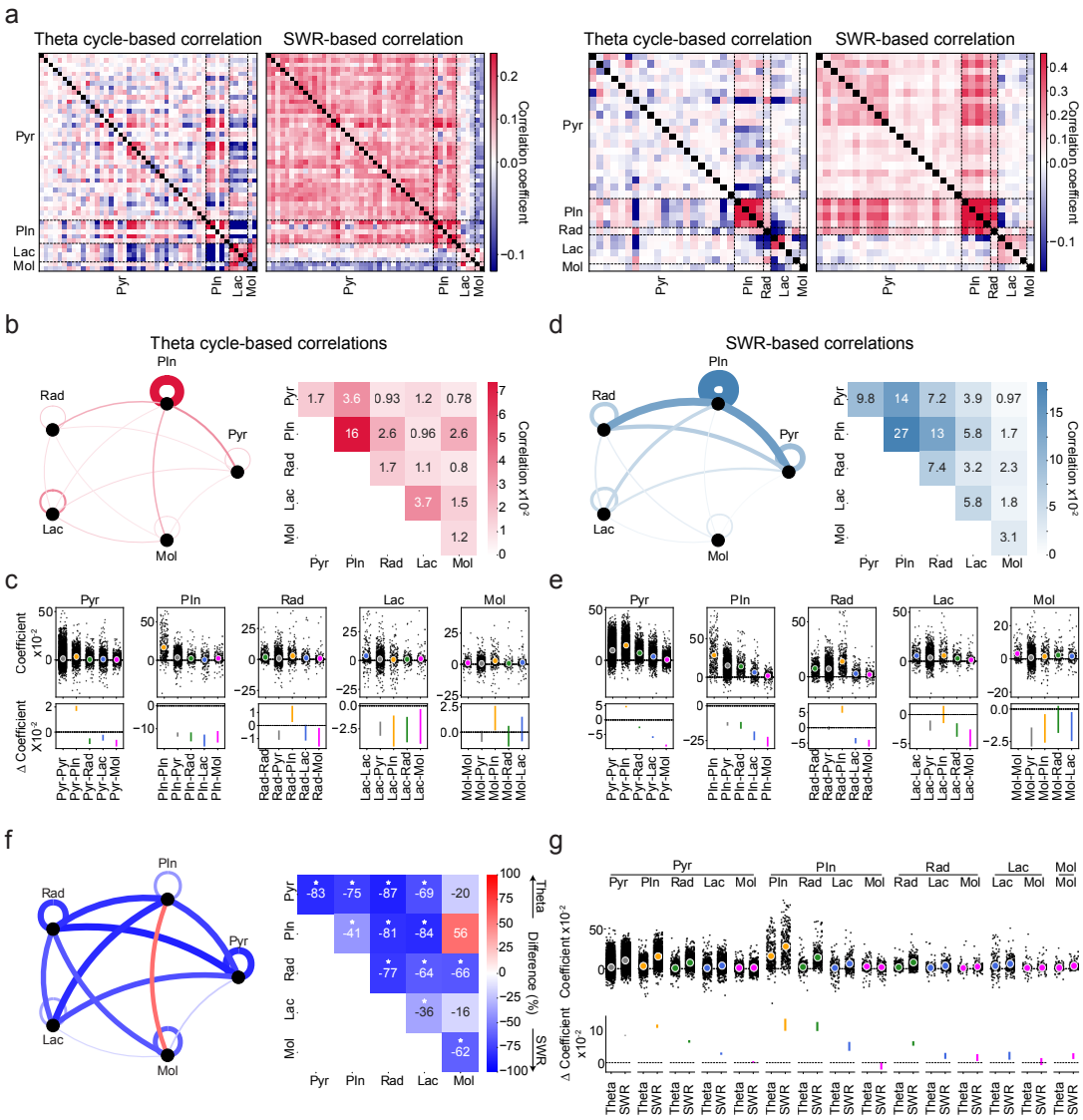


Figure 6.3.3 – Superficial interneurons display layer- and state-specific coactivity structures

a) Two examples of event-related co-activity matrices recorded from two different mice, including pyramidal neurons and different interneuron groups. Note the state-dependent differences in both examples. **b**) Left: weighted graphs depicting the mean correlation coefficient between groups. Thickness of the edge and colour correspond to correlation strength. Right: heatmap showing the mean correlation coefficient between groups from the weighted graph. **c**) Top: difference in correlation coefficient between within-layer pairs and between-layer pairs. Datapoints represent individual neuron pairs and the coloured dots indicate the group mean, colour indicates the corresponding neuron group (pyramidal neurons: grey, interneurons in the stratum pyramidale: yellow, radiatum: green, lacunosum: blue, moleculare: magenta). For the means and 95%CI see **Table 6.3.3**. Bottom: bootstrapped difference between within-layer correlation and between-layer correlations. Bars indicate 95%CI of the mean difference. **d**) Same as in **b**) for sharp-wave ripple-based correlations. **e**) Same as in **c**) for sharp-wave ripple-based correlations corresponding to **d**). For the means and 95%CI see **Table 6.3.4**. **f**) Left: weighted graph showing the difference between correlation coefficient in theta-based and sharp-wave ripple-based coactivity ((theta-SWR)/SWR). The colour and thickness of the edges correspond to the change magnitude. Right: heatmap showing the difference between the correlation coefficient between theta-based and sharp-wave ripple-based coactivity from the weighted graph. **g**) Top: difference in correlation coefficient in theta- and sharp-wave ripple-based correlation coefficients per neuron group. Datapoints represent individual neuron pairs and the coloured dots indicate the group mean. For the means and 95%CI see **Table 6.3.5**. Bottom: bootstrapped difference between theta- and sharp-wave ripple-based correlation. Bars indicate the 95%CI of the mean difference.

Mean and difference in correlation coefficients per layer in theta cycles						
Layer	**Layer**	**Mean**	**95% CI**		**Mean Diff**	**p-value**
Pyr	Pyr	1.664	1.602	1.729		
Pyr	Pin	3.552	3.357	3.749	-1.888	$<10^{-5}$
Pyr	Rad	0.931	0.774	1.101	0.733	$<10^{-5}$
Pyr	Lac	1.204	0.989	1.426	0.46	$<10^{-5}$
Pyr	Mol	0.777	0.612	0.939	0.887	$<10^{-5}$
Pin	Pin	16.097	14.381	17.722		
Pin	Pyr	3.552	3.348	3.761	12.545	$<10^{-5}$
Pin	Rad	2.565	1.996	3.139	13.532	$<10^{-5}$
Pin	Lac	0.956	-0.284	2.165	15.142	$<10^{-5}$
Pin	Mol	2.601	1.611	3.506	13.496	$<10^{-5}$
Rad	Rad	1.667	1.392	1.982		
Rad	Pyr	0.931	0.773	1.105	0.736	$<10^{-5}$
Rad	Pin	2.565	2.018	3.156	-0.898	0.002
Rad	Lac	1.131	0.596	1.71	0.536	0.037
Rad	Mol	0.799	0.102	1.699	0.868	0.006
Lac	Lac	3.713	2.504	4.895		
Lac	Pyr	1.204	0.973	1.436	2.509	$<10^{-5}$
Lac	Pin	0.956	-0.272	2.096	2.757	0.001
Lac	Rad	1.131	0.585	1.773	2.582	$<10^{-5}$
Lac	Mol	1.511	0.441	2.663	2.202	0.009
Mol	Mol	1.201	0.554	1.811		
Mol	Pyr	0.777	0.615	0.949	0.424	0.075
Mol	Pin	2.601	1.678	3.481	-1.4	0.014
Mol	Rad	0.799	0.049	1.633	0.402	0.222
Mol	Lac	1.511	0.384	2.591	-0.31	0.305

Table 6.3.3 – Correlation coefficients between neuron groups in theta oscillations

Data related to **Figure 6.3.3**

Mean and difference in correlation coefficients per layer in sharp-wave ripples						
Layer	**Layer**	**Mean**	**95% CI**		**Mean Diff**	**p-value**
Pyr	Pyr	9.801	9.72	9.876		
Pyr	Pin	14.392	14.082	14.679	-4.592	$<10^{-5}$
Pyr	Rad	6.246	7.014	498	2.554	$<10^{-5}$
Pyr	Lac	3.895	3.623	4.183	5.906	$<10^{-5}$
Pyr	Mol	0.974	0.783	1.225	8.827	$<10^{-5}$
Pin	Pin	27.395	25.479	29.487		
Pin	Pyr	14.392	14.071	14.717	13.003	$<10^{-5}$
Pin	Rad	13.364	12.294	14.375	14.031	$<10^{-5}$
Pin	Lac	5.818	4.631	6.944	21.577	$<10^{-5}$
Pin	Mol	1.665	0.814	2.451	25.73	$<10^{-5}$
Rad	Rad	7.39	6.917	7.853		
Rad	Pyr	7.246	6.989	7.5	0.144	0.299
Rad	Pin	13.364	12.377	14.518	-5.974	$<10^{-5}$
Rad	Lac	3.151	2.565	3.791	4.239	$<10^{-5}$
Rad	Mol	2.349	1.595	3.139	5.041	$<10^{-5}$
Lac	Lac	5.781	4.834	6.596		
Lac	Pyr	3.895	3.587	4.189	1.886	$<10^{-5}$
Lac	Pin	5.818	4.553	7.062	-0.037	0.487
Lac	Rad	3.151	2.504	3.809	2.63	$<10^{-5}$
Lac	Mol	1.792	0.88	2.718	3.989	$<10^{-5}$
Mol	Mol	3.141	2.464	3.874		
Mol	Pyr	0.974	0.742	1.198	2.167	$<10^{-5}$
Mol	Pin	1.665	0.849	2.438	1.477	0.003
Mol	Rad	2.349	1.543	3.112	0.792	0.068
Mol	Lac	1.792	0.908	2.751	1.349	0.008

Table 6.3.4 – Correlation coefficients between neuron groups in sharp-wave ripples

Data related to **Figure 6.3.3**

Difference between theta cycles and SWR correlation coefficients			
Layer	**Layer**	**Mean Diff**	**p-value**
Pyr	Pyr	-8.145	$<10^{-5}$
Pyr	Pin	-10.867	$<10^{-5}$
Pyr	Rad	-6.328	$<10^{-5}$
Pyr	Lac	-2.691	$<10^{-5}$
Pyr	Mol	-0.192	0.076
Pin	Pin	-11.298	$<10^{-5}$
Pin	Rad	-10.799	$<10^{-5}$
Pin	Lac	-4.863	$<10^{-5}$
Pin	Mol	0.949	0.04
Rad	Rad	-5.723	$<10^{-5}$
Rad	Lac	-2.02	$<10^{-5}$
Rad	Mol	-1.502	0.001
Lac	Lac	-2.068	$<10^{-5}$
Lac	Mol	-0.301	0.293
Mol	Mol	-1.957	$<10^{-5}$

Table 6.3.5 – Differences in correlation coefficients between network states across layers

Data related to **Figure 6.3.3**

between pairs recorded in the same layer (within-layer) were higher than between-layer pairs for pyramidale and lacunosum interneurons (**Figure 6.3.3b**; **Table 6.3.3**). In contrast, pyramidal neurons, radiatum and moleculare interneurons displayed higher correlations with interneurons in the stratum pyramidale than neurons in the same layer, and lower or equal correlations with neurons of other layers (**Figure 6.3.3b, c**). Although these differences were layer-specific, no apparent structure emerged as a function of depth (**Figure 6.3.3b**; **Table 6.3.3**). In sharp-wave ripples, the coactivity structure revealed a different pattern (**Figure 6.3.3d, e**; **Table 6.3.4**). Pyramidal neurons displayed higher coactivity with pyramidale interneurons compared to within-layer coactivation and lower with these superficial interneuron groups. Notably, the coactivation strength decreased as a function of depth with higher mean coactivity between pyramidal neurons and stratum pyramidale interneurons and the lowest with neurons in the moleculare. Across the interneuron groups, a similar pattern was seen, with most groups displaying the highest correlations with within-layer partners and decreasing coactivity values for partners in more superficial layers (**Figure 6.3.3d, e**; **Table 6.3.4**). Furthermore, when I compared the correlation coefficients between theta and SWR, I found that all within-layer groups showed an increased coactivity in SWR compared to theta cycles (**Figure 6.3.3f, g**; **Table 6.3.5**). Nearly all between-layer coactivity increased in SWR, except for the coactivity between stratum moleculare interneurons

and those from other layers, with a trend toward increased activity between stratum pyramidale and moleculare interneurons in theta cycles. Together, this data reveals state- and layer-dependent coactivity structures between superficial interneurons and the local neural network.

Discussion

In this Chapter, I performed cross-correlation and coactivity analysis to examine the interactions between superficial interneurons and the local network. I found that, at least in this dataset, superficial interneurons do not result in short-latency spike reductions at population level. However, superficial interneuron activity showed an interneuron group-specific effect on pyramidal neuron spike timing and spike phase in theta cycles. Furthermore, the coactivity analysis revealed that superficial interneurons display state-dependent and layer-specific coactivity structures with the local CA1 network. Together, these observations shed light on the interactive features of superficial interneurons in dorsal CA1.

Direct inhibitory effects of interneurons on pyramidal neurons have been detected in extracellularly recorded spiking activity (Barthó et al., 2004). For pyramidale interneurons, I observed a similar effect at a population level, while this was not observed for contralaterally recorded pyramidal neurons or between superficial interneurons and pyramidal neurons. However, the algorithm used to extract spikes from the recorded signal can not discriminate coinciding spikes from multiple sources, due to which an artificial spike reduction in the pyramidal neuron population can not be ruled out (Barthó et al., 2004). Furthermore, a pyramidal neuron spike increase was seen in most post-interneuron spike windows in both ipsi- and contralateral populations. Since most interneurons do not cross the midline (Pelkey et al., 2017; Booker and Vida, 2018), and given the highly similar responses observed in both ipsi- and contralateral populations, it is unlikely that the spike-triggered increases are directly caused by interneuron spikes. Instead, these increases likely reflect precisely timed network activity. The lack of spike reduction in pyramidal neurons in response to superficial interneuron spiking can be caused by methodological as well as biophysical properties. First, to find direct inhibitory connections in extracellular recordings, these connections need to be strong and active during the recordings to be revealed (English et al., 2017). Due to

superficial interneurons mostly targeting pyramidal neuron dendrites, their effect may remain local in the dendrite and only cause subtle changes in pyramidal neuron outputs (Somogyi and Klausberger, 2005; Palmer et al., 2012a). Secondly, mono-synaptic connectivity between neurons rapidly decays as a function of distance (English et al., 2017; Huang et al., 2024). Since neurons analysed here are scattered across the hippocampus, the likelihood of finding mono-synaptically connected pairs is low. Therefore, population-based analysis may mask individual inhibitory responses. Lastly, the analysis was performed under physiological conditions. Interneuron type-specific silencing through opto- or chemogenetic approaches may be required to reveal causal relationships between superficial interneurons and pyramidal neurons (Royer et al., 2012; Turi et al., 2019; Rangel Guerrero et al., 2024). Together, the lack of inhibitory effects on pyramidal neurons in response to superficial interneuron activity suggests that superficial interneuron activation may subtly influence pyramidal neuron spike counts, which makes detection of inhibitory interneuron-to-pyramidal neuron effects challenging in extracellular recordings.

Interneurons have been shown to affect spike timing, bursting states, and spike phase of pyramidal neurons (Royer et al., 2012; Rangel Guerrero et al., 2024). I found that superficial interneuron activity is associated with differential spiking patterns of pyramidal neurons in the bursting, slow, and mid-gamma range in a layer-specific manner when cycles were weighted to the activity levels of specific interneuron groups. Pyramidal neurons showed a reduced burst probability when stratum radiatum interneurons were active consistent with previous findings on SST- and CCK-positive interneurons (Royer et al., 2012; Rangel Guerrero et al., 2024). Stratum lacunosum activity was linked to fewer pyramidal neuron ISIs in the mid-gamma range, potentially driven by neurogliaform neurons (Sakalar et al., 2022). Although speculative, moleculare interneuron activity reduced slow-gamma intervals in pyramidal neurons, possibly through targeting slow-gamma-supporting interneurons in the strata pyramidale and radiatum (Chamberland and Topolnik, 2012). It is important to note, however, that the inter-spike intervals analysed here may reflect pyramidal neuron coupling to gamma-oscillations but do not provide proof that superficial interneuron activity affects these well-established rhythms, and should be interpreted with caution in this context. Furthermore, the inter-spike interval probability changes induced by all

groups were small (~0.5% change), and while significant, it is unclear whether these changes are biologically relevant. Experiments targeting and manipulating specific interneuron populations are required to elucidate the causal relationship between superficial interneurons and pyramidal neurons. Together, it remains unclear how and which superficial interneuron types are involved in spike timing changes in pyramidal neurons, these observations, albeit small, may provide new insights into the interactions between superficial interneurons and the spike timing regulation of pyramidal neurons.

Besides spike timing changes in the time domain, I found interneuron activity-related changes in pyramidal spike phase during theta cycles. In high-activity cycles of stratum radiatum interneurons, pyramidal neurons displayed a phase delay, while increased lacunosum interneuron activity was associated with a phase advance. Interestingly, stratum radiatum and lacunosum interneurons preferentially spike after and before the theta trough, respectively (see **Chapter 4**). By selecting cycles in which these interneurons are most active, pyramidal neuron activity may biased to a similar phase due to a common drive. However, if a common input would explain this spiking behaviour, one would expect a similar effect in high-activity cycles of the peak-preferring moleculare interneuron, which was not observed. Alternatively, these spike phase changes may be the result of cycle-specific selection of distinct types of pyramidal neurons with distinct spiking characteristics (Valero et al., 2015; Soltesz and Losonczy, 2018). Deep pyramidal neurons (pyramidal neurons closest to stratum oriens) receive more peri-somatic inputs from PV-positive interneurons, while superficial pyramidal neurons are preferentially innervated by CCK-positive peri-somatic targeting interneurons (Valero et al., 2015). While PV-positive interneurons are mostly found around the stratum pyramidale, CCK-positive basket cells are also found in the lacunosum (Booker and Vida, 2018). Furthermore, deep pyramidal neurons preferentially spike just before the theta through, while superficial pyramidal neurons spike after (Lopes-dos-Santos et al., 2023). The differential inhibition of deep and superficial pyramidal neurons by interneurons in distinct layers may explain the phase shift in the pyramidal neuron population. In this model, high radiatum neurons inhibit deep pyramidal neurons and bias the pyramidal population activity to the later spiking superficial pyramidal neurons and lacunosum-located CCK-positive basket cells

bias the population activity to the earlier spiking deep pyramidal neurons (Klausberger, 2005). However, additional experiments are required to test causal relationships between superficial interneuron firing and pyramidal neuron spike timing. Together, pyramidal neuron spike phase changes in relation to superficial interneuron activity could reflect differential targeting of distinct pyramidal populations by superficial interneurons.

Coactivity analysis is often performed for pyramidal neurons in the hippocampus, but such analysis is less frequently employed for interneurons, which is likely due to the challenges around interneuron-type identification in large-scale electrophysiological recordings (Ascoli et al., 2008; Roux et al., 2014). Recently, a large-scale study co-recorded interneurons across multiple layers of dorsal hippocampus CA1 utilising calcium-imaging techniques combined with *post hoc* molecular identification of distinct interneuron types (Geiller et al., 2020) and showed that distinct interneuron types display different coactivity with other members of the local network. However, expression of the calcium indicator was interneuron-specific and did not permit coregistration of pyramidal neurons. Based on the current dataset, I examined the coactivity between superficial interneurons and other local network members, including pyramidal neurons, which revealed layer-specific and state-dependent coactivity structures. During theta cycles, stratum radiatum and moleculare neurons showed stronger correlations with pyramidale neurons than within-layer partners, while during sleep-related sharp-wave ripples, coactivity increased within layers and decreased with more superficial partners. These changes in co-activity can arise from different factors, such as a differential input correlation and neuron-specific internal fluctuations (Doiron et al., 2016), and indicate that a structurally fixed architecture can rapidly reorganise under different network- and behavioural states. Furthermore, superficial interneurons showed distinct coactivity structures. Particularly, stratum lacunosum neurons exhibited, similar to pyramidale interneurons, the highest correlations with within-layer partners rather than pyramidale interneurons as seen for radiatum and moleculare groups. Although highly speculative, this may indicate that lacunosum neurons form an independent processing unit. Together, these observations emphasise the dynamic cooperation between pyramidal neurons and interneurons across different CA1 layers, which may form flexible subdomains differentially recruited under different network demands.

Overall, different types of coacitivity analysis provide important insights into the possible function of interneurons. I leveraged simultaneous recording of superficial interneurons and pyramidal neurons to examine the relationships between neuron populations across nearly all layers in dorsal CA1. Although subtle, I found that superficial interneurons may be involved in pyramidal neuron spike timing modulation. Furthermore, flexible coactivity structures across different states likely support information routing in a state-dependent manner. These observations illustrate the potential of large-scale datasets focused on superficial interneurons to unravel their function. Together, these findings provide new insights into the state- and layer-specific roles of superficial interneurons in regulating pyramidal neuron activity and contributing to the local network dynamics in CA1.

Chapter 7. Stratum Lacunosum is a distinct layer in dorsal CA1

7.1 Introduction

The hippocampus consists of multiple regions, each of which is subdivided into layers. The early neuroanatomists Ramon y Cajal and Schaffer described six layers in dorsal CA1: the alveus, oriens, pyramidale, radiatum, lacunosum, and moleculare (Schaffer, 1892; Ramón y Cajal, 1904). However, in recent literature, the strata lacunosum and moleculare have predominantly been combined into a single layer: the lacunosum-moleculare (Witter et al., 2000; van Strien et al., 2009; Szirmai et al., 2012; Strange et al., 2014; Booker et al., 2016). It has even been argued that the historical descriptions were incorrect in segregating the strata lacunosum and moleculare (Szirmai et al., 2012). Although no formal definition of a 'layer' appears to exist, generally layers in the brain are defined by differences in cell density, soma shape (often used as a proxy for cell type), the presence of distinct fibre tracts, and differential molecular expression patterns (Schaffer, 1892; Ramón y Cajal, 1904; Förster et al., 2006; Szirmai et al., 2012). In addition to these anatomical characteristics, electrophysiological recordings have opened novel ways to assess layers and have shown that layers can feature distinct functional signatures (Senzai et al., 2019; Lopes-dos-Santos et al., 2023). In this Chapter, building on previous observations, I reopen the debate on the distinctiveness of the stratum lacunosum and propose that it is a distinct entity based on unique connectivity patterns, electrophysiological characteristics, and neuronal spiking properties.

In the late 19th and early 20th century, neuroanatomists Ramón y Cajal and Schaffer described the lamination of the CA1 region to consist of 6 layers, among which the stratum lacunosum

and moleculare (Schaffer, 1892; Ramón y Cajal, 1904). The lacunosum was characterised by multiple types of horizontally oriented fibres, some of which myelinated, and the presence of morphologically distinct 'short axons' neurons (Schaffer, 1892; Ramón y Cajal, 1904; Merchan et al., 2016). One type of fibres were thick axonal projections originating from CA3 pyramidal neurons (Ramón y Cajal, 1904; fig 787, 788, and 790), now widely known as Schaffer collaterals. Additionally, Cajal mentioned thin fibres branching from the alvear tracts passing through the pyramidal layer ascending to and ramifying in the stratum lacunosum. Lastly, somata of short axon neurons – now more commonly known as interneurons – in the stratum lacunosum were described by Cajal as triangular and multipolar with axons horizontally aligning to the layer. Although modern nomenclature disagrees with some aspects of these descriptions, others have withstood the test of time. In contrast to Cajal and Schaffer's descriptions, it is agreed that Schaffer collaterals are unmyelinated fibres, which terminate in the stratum radiatum rather than the lacunosum/moleculare (Li et al., 1994; Szirmai et al., 2012). However, in agreement with Cajal's descriptions, the existence of thin fibres travelling from the alveus to the lacunosum and moleculare has been reported more recently (Deller et al., 1996; Takács et al., 2012; Bell et al., 2021), as well as specific GABAergic neurons primarily found at the radiatum and lacunosum-moleculare border (Lacaille and Schwartzkroin, 1988a, 1988b; Deller et al., 1996; Vida et al., 1998; Wyskiel and Andrade, 2016; Pelkey et al., 2017; Booker and Vida, 2018; Bell et al., 2021). Furthermore, both scientists mention myelinated fibres in the stratum lacunosum, a finding corroborated by recent studies which show a sharp increase of myelination from radiatum to strata lacunosum/moleculare (Kitamura et al., 2014; Stedehouder and Kushner, 2017). Moreover, the study by Kitamura and colleagues, suggests that the myelinated fibres passing through the stratum lacunosum originate from entorhinal cortex projection neurons (Kitamura et al., 2014). Together, the description of Schaffer collaterals passing through the stratum lacunosum may misalign with modern nomenclature, Cajal and Schaffer's additional observations appear valid and should perhaps not be discarded as outdated.

The distinction may have been lost to history, but over the last decades, evidence has accumulated suggesting that stratum lacunosum could be a separate layer. First, as described by Cajal,

GABAergic interneurons with distinct morphological and electrophysiological properties have been recognised in this region, mostly referred to as the radiatum/lacunosum-moleculare border (Lacaille and Schwartzkroin, 1988a, 1988b; Vida et al., 1998; Chapman and Lacaille, 1999a, 1999b; Bertrand and Lacaille, 2001; Gangarossa et al., 2012; Wyskiel and Andrade, 2016) (see also **Chapters 3** and **4**). Secondly, noncanonical input sources have been described selectively targeting the lacunosum or its neurons (Gangarossa et al., 2012; Melzer et al., 2012; Kitamura et al., 2014; Teixeira et al., 2018; Tsoi et al., 2022). Thirdly, electron microscopy studies show differential distribution of synapse types on the pyramidal neuron dendrites in stratum lacunosum compared to radiatum and moleculare (Pokorný and Yamamoto, 1981). In addition, excitatory synapses on pyramidal neuron dendrites have been found to be less dense and display a higher turnover in stratum lacunosum compared to the adjacent layers (Bulovaite et al., 2022). Lastly, neurons in the lacunosum are uniquely positioned to sense inputs arriving in both the strata radiatum, lacunosum, and moleculare (Lacaille and Schwartzkroin, 1988a; Kajiwara et al., 2008; Milstein et al., 2015)(see also **Chapter 5**) allowing them to perform logical comparative operations within the hippocampal network (Milstein et al., 2015). Thus, although not commonly acknowledged in literature, stratum lacunosum meets multiple anatomical criteria to be considered an independent layer.

These distinct anatomical and molecular features of the stratum lacunosum hint that it may represent a unique domain in CA1, but a functional characterisation is lacking. In this Chapter, I assess the electrophysiological differences between the stratum lacunosum and the strata radiatum and moleculare at both a network and a single-cell level. I provide evidence supporting the distinctiveness of the lacunosum, based on its theta-nested gamma profile, differential inputs, and neurons with specific spike characteristics. I particularly focus on individual findings or combinations of characteristics unique to the stratum lacunosum, which cannot be explained by simply being an average of the strata radiatum and moleculare. Overall, these findings support the uniqueness of the stratum lacunosum and underscore that it should be treated as a separate layer.

7.2 Methods

7.2.1 Literature review

A PubMed search was performed using the following search terms: “CA1” AND “Hippocampus” and “CA1” AND “Lacunosum”. All available entries published up to 19 April 2024 with an online abstract were included. The entry information was saved using the ‘abstract (text)’ option in the ‘save citations to file’ tool in PubMed. Using custom Python code, all abstracts were automatically scanned for words indicating that the authors reported the stratum lacunosum as an independent or a merged with the moleculare (see table). Abstracts were categorized in lacunosum-only (containing ‘Lacunosum’ and not ‘Lacunosum-Moleculare’ search words), lacunosum-moleculare (containing ‘Lacunosum-Moleculare’), or ‘rest’ (not containing any of the search words). In addition, publication years were extracted from the entry information retrieved from PubMed.

Lacunosum-Moleculare	Lacunosum
‘lacunosum-moleculare’, ‘lacunosum/moleculare’, ‘lacunosum moleculare’, ‘lacunosum\nmoleculare’, ‘lacunosum \nmoleculare’, ‘lacunosum-\nmoleculare’, ‘lacunosum\nmol’, ‘lacunosum \nmol’, ‘lacunosum mol’, ‘lm’	‘ lacunosum ‘, ‘lacunosum’

Table 7.2.1 – Terms used for PubMed search

7.2.2 Data collection

No new experimental data has been collected for this Chapter. See the corresponding Chapters for methods (**Table 7.2.2**).

Section	Chapter	Section
7.3.1	2	Layer-specific gamma profiles
7.3.2	3 & 4	Layer-specific spike characteristics
7.3.3	5	Layer-specific interneuron recruitment by CA3 and EC

Table 7.2.2 – Chapters from which data originates

7.2.3 Data analysis

Computing gamma power

To compare gamma power across different tetrodes in the dataset, supra-theta wavelet

spectrograms were generated as previously described (Lopes-dos-Santos et al., 2023). For each tetrode, the mean amplitude for various supra-theta frequencies was computed as function of the theta oscillation phase using a pyramidale layer tetrode, resulting in the so-called theta-gamma profile. From each tetrodes' theta-gamma profile, I obtained the mean power within three specific windows: (1) slow-gamma, between 25-45 Hz and 140 - 220 degrees; (2) mid-gamma, between 60-90 Hz and 15-90 degrees; and (3) fast-gamma, between 100-130 Hz and 160-200 degrees. To get the relative difference between the tetrodes within the same recording day, values across all tetrodes and gamma frequencies were normalised to the highest value, with the highest value being set to 1.

7.2.4 Statistical testing

Permutation testing and bootstrapped confidence intervals were obtained as described in Chapter 3 (see **section 3.2.3.8**).

7.3 Results

7.3.1 The majority of studies mention stratum lacunosum as a joined layer with moleculare

Historical descriptions mentioned stratum lacunosum and moleculare separately, while it seemed that recent reports mostly grouped these layers. To objectively examine this change, I conducted a PubMed search and compared the number of abstracts mentioning the stratum lacunosum separately with those that combined them (**Figure 7.3.1**). First, I performed a general search for hippocampus-related search terms ('CA1' AND 'Hippocampus'), resulting in 26 861 articles. ~15% (3950) of the found articles mentioned the stratum lacunosum (0.1%) or lacunosum-moleculare (14.6%) in the abstract (**Figure 7.3.1a, b**). Interestingly, from the mid-1980s to 2000s the number of entries on the hippocampus dramatically increased, while this was not the case for entries including the search terms related to the strata lacunosum and moleculare (**Figure 7.3.1a, b**). This discrepancy implies that over the last four decades, studies have been biased toward the deep layers such as the strata oriens and pyramidale. To better examine the relationship between the use of lacunosum and lacunosum-moleculare, I specifically focussed on the stratum

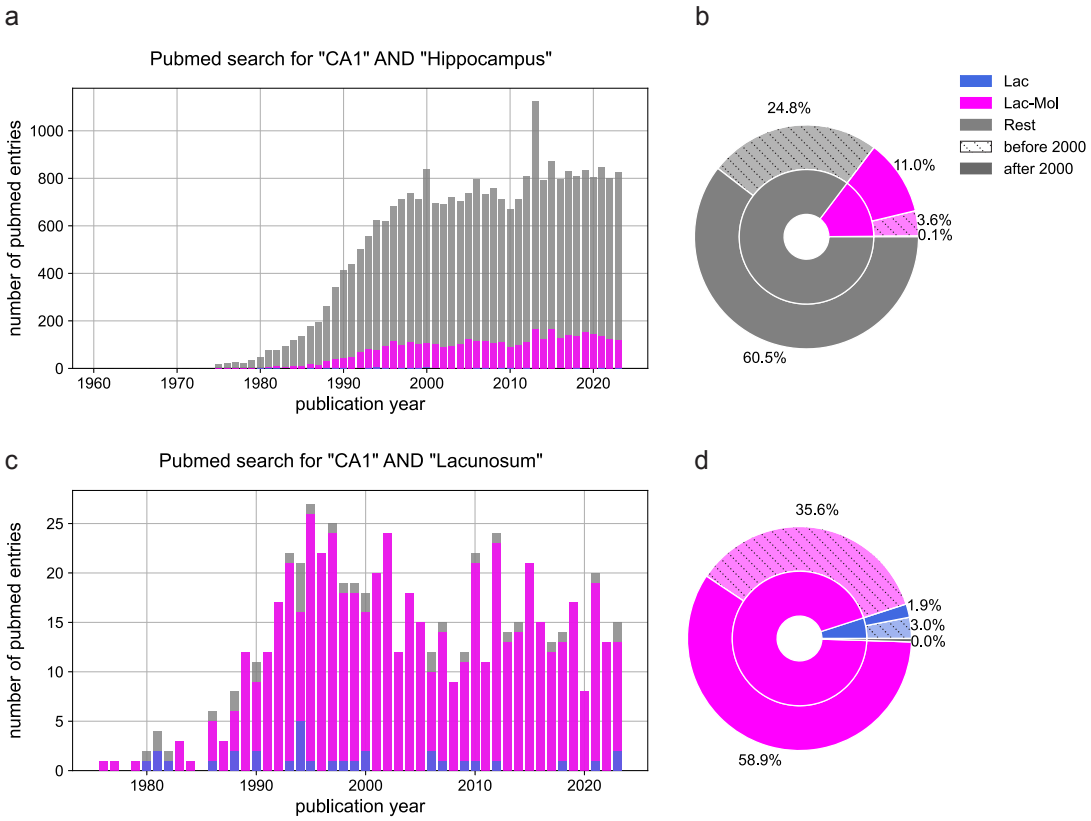


Figure 7.3.1 – The vast majority of papers published between 1960 and present group the strata lacunosum and moleculare

a) Bar graph showing PubMed entries retrieved when searching for "CA1" and "Hippocampus" per year since 1960. Grey bars indicate all papers, the papers mentioning the 'stratum lacunosum-moleculare' in magenta and those referring to the stratum lacunosum and moleculare separately in blue. **b**) Inner circle: Pie chart showing the number of entries over all years as shown in **a**). Entries referring to stratum 'lacunosum-moleculare' are in magenta and those referring to the stratum lacunosum and moleculare separately are in blue, grey represents the remaining entries. Outer circle: Shows the segregation between entries published before (lighter patterned areas) versus after (solid darker shades) 2000. **c**) Bar graph showing PubMed entries retrieved when searching for "CA1" and "Lacunosum" per year since 1960. Grey bars indicate all papers, the papers mentioning the 'stratum lacunosum-moleculare' in magenta and those referring to the stratum lacunosum and moleculare separately in blue. **d**) Inner circle: Pie chart showing the number of entries over all years as shown in **c**). Entries referring to stratum 'lacunosum-moleculare' are in magenta and those referring to the stratum lacunosum and moleculare separately are in blue, grey represents the remaining entries. Outer circle: Shows the segregation between entries published before (lighter patterned areas) versus after (solid darker shades) 2000. Note that despite more entries found after 2000 for stratum lacunosum-moleculare, fewer entries are found for those referring to these layers separately.

lacunosum using 'CA1' AND 'Lacunosum' as search terms. This resulted in 623 articles since the 1970s (**Figure 7.3.1c, d**). Strikingly, only ~5% (31/623) of the abstracts examined mentioned the stratum lacunosum separate rather than merged with the moleculare. Furthermore, most articles mentioning stratum lacunosum separately were published before the year 2000 (3.0% (19/623) versus 1.9% (12/623) out of all articles). When considering the total number of articles published

in the period before versus after, this difference becomes even clearer with 7.9% (19/241) of the articles before 2000 considering the stratum lacunosum as a separate layer and only 3.1% (12/382) after the year 2000 (**Figure 7.3.1c, d**). Together, these results indicate that the number of articles mentioning stratum lacunosum as a separate layer relative to the number of studies examining the hippocampus has declined over time.

7.3.2 Lacunosum exhibits a unique gamma profile

In Chapter 2, I showed that stratum lacunosum tetrodes displayed a theta-nested fast-gamma oscillation not visible in the radiatum and moleculare tetrodes (**Figure 2.3.3**), suggesting that this oscillation may be specific for the lacunosum. To test this hypothesis, I computed the power of three distinct gamma oscillations along the radial axis of dorsal CA1 (slow-gamma: 25-45 Hz between 140 - 220 degrees in theta, mid-gamma: 60-90 Hz between 15-90 degrees in theta, and fast-gamma: 100-130 Hz between 160-200 degrees in theta; **Figure 7.3.2a**) across all ~750 tetrodes in the dataset (see **Chapters 3** to **5**). In line with the findings in Chapter 2 and previous literature (Colgin et al., 2009; Schomburg et al., 2014; Lopes-dos-Santos et al., 2023), I found that radiatum tetrodes and moleculare tetrodes were dominated by slow and mid-gamma oscillations, respectively (**Figure 7.3.2a-c**). The mean normalised power of slow-gamma was significantly higher in radiatum tetrodes compared to both lacunosum and moleculare, with no significant difference between lacunosum and moleculare (Mean 95%CI: Rad 8.95, 7.86 – 10.0; Lac 3.75, 3.20 – 4.31; Mol 3.35, 2.90 – 3.77; **Figure 7.3.2c**). For mid-gamma, the mean normalised power was significantly higher in moleculare tetrodes compared to radiatum and lacunosum, and radiatum was significantly higher than lacunosum (Mean 95%CI: Rad 47.16, 42.60 – 51.53; Lac 34.60, 32.19 – 37.10; Mol 74.84, 70.89 – 78.68). Lastly, the detected fast-gamma was highest in the lacunosum tetrodes, while radiatum and moleculare were not significantly different (Mean 95%CI: Rad 5.71, 95%CI 4.85 – 6.68; Lac 9.18, 8.20 – 10.09; Mol 4.83, 4.32 – 5.35). This data shows that slow, mid, and fast gamma dominate different layers in dorsal CA1, with slow, mid, and fast-gamma being strongest in radiatum, molecule, and lacunosum, respectively. Together, this shows that the lacunosum features a unique gamma profile less prominent in radiatum and moleculare.

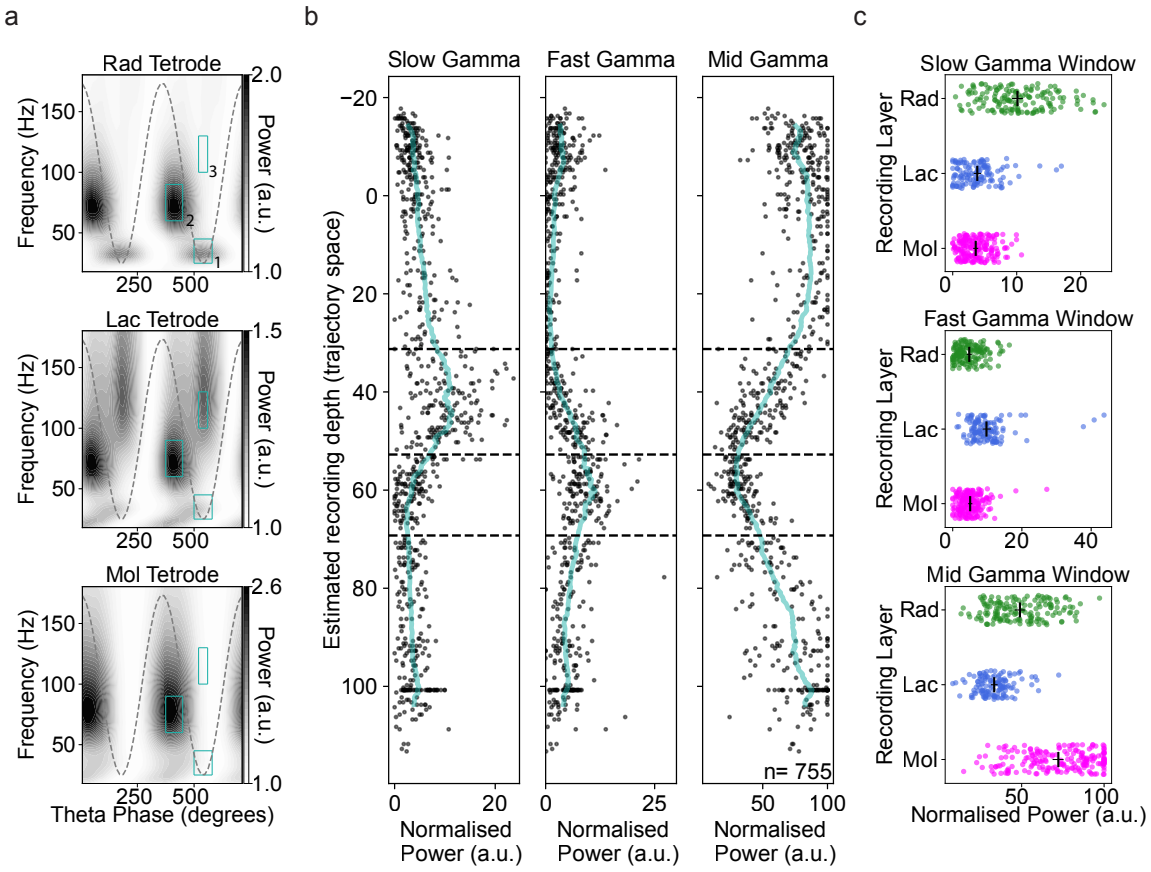


Figure 7.3.2 – Distinct theta-nested gamma profile in stratum lacunosum

a) Representative examples of supra-theta theta triggered spectrograms for tetrodes in the stratum radiatum (Rad), lacunosum (Lac), or moleculare (Mol). Blue squares indicate the gamma windows used in further analysis: 1) slow-gamma: 25-45 Hz between 140 - 220 degrees in theta, 2) mid-gamma: 60-90 Hz between 15-90 degrees in theta, and 3) fast-gamma: 100-130 Hz between 160-200 degrees in theta. **b**) Scatter plots showing normalised gamma power for the slow gamma, fast gamma, and mid gamma windows plotted as a function of the recording tetrode's estimated recording depth. Data points represent individual tetrodes, blue line a running mean. Note that the slow gamma power is highest in the stratum radiatum tetrodes; the fast gamma power is highest for tetrodes in the stratum lacunosum; and mid gamma is high in strata pyramidale and moleculare while being lowest in stratum lacunosum. **c**) Strip plots showing normalised gamma power for the slow gamma, fast gamma, and mid gamma windows per recording layer (Rad: green, Lac: blue, Mol: magenta). The Vertical ticks represent the group mean and the vertical whiskers the 95% CI of the mean. Slow gamma window: radiatum mean 8.95, 95%CI 7.86 – 10.0; lacunosum mean 3.75, 95%CI 3.20 – 4.31 moleculare mean 3.35, 95%CI 2.90 – 3.77; rad vs lac p-val<10^{-5}; rad vs mol p-val<10^{-5}; lac vs mol p-val = 0.135. Fast gamma: radiatum mean 5.71, 95%CI 4.85 – 6.68; lacunosum mean 9.18, 95%CI 8.20 – 10.09; moleculare mean 4.83, 95%CI 4.32 – 5.35; rad vs lac p-val<10^{-5}; rad vs mol p-val<10^{-5}; rad vs mol p-val = 0.05. Mid gamma: radiatum mean 47.16, 95%CI 42.60 – 51.53; lacunosum mean 34.60, 95%CI 32.19 – 37.10; moleculare mean 74.84, 95%CI 70.89 – 78.68; rad vs lac p-val<10^{-5}; rad vs mol p-val<10^{-5}; lac vs mol p-val<10^{-5}.

7.3.3 Lacunosum houses unique interneurons based on spike-waveform and firing patterns

In Chapters 3 and 4, I have shown that distinct waveforms and spike characteristics were observed in the stratum lacunosum compared to other layers of dorsal CA1. In this section, I tested whether stratum lacunosum neurons from a unique group or are merely a transition group from stratum radiatum to moleculare. To differentiate between these options, I compared the mean of the stratum lacunosum group to the combined means of radiatum and moleculare groups (Rad+Mol) across several spike characteristics presented in Chapter 4 (**Figure 7.3.3a**). Stratum lacunosum neurons showed a significant difference for seven out of nine characteristics when compared to the rad+mol group (**Figure 7.3.3b**; **Table 7.3.1**). Lacunosum neurons had a higher spike probability in theta cycles (mean proportion, 95%CI: Lac 0.411, 0.359 - 0.461, Rad+Mol 0.201, 0.173 - 0.231) and burst less compared to the other two layers (mean burst index, 95%CI: Lac 0.032, 0.025 - 0.039, Rad+Mol 0.073, 0.065 - 0.083). In addition, lacunosum neurons have the highest firing rates during awake exploration (mean rate (Hz), 95%CI: Lac 6.738, 5.569 - 8.015, Rad+Mol 3.371, 2.729 - 4.076), are more active in awake states than during sleep (mean proportional difference, 95%CI: Lac 0.190, 0.129 - 0.250, Rad+Mol -0.051, -0.104 - -0.004), and activate less or decrease their firing rate during sharp wave ripples (mean rate (Hz), 95%CI: Lac 1.489, 1.022 - 1.965, Rad+Mol 2.821, 2.567 - 3.065). Lacunosum have the highest number of cells that reduce their firing rate at higher traveling speed (mean correlation, 95%CI: Lac 0.079, -0.042 - 0.201, Rad+Mol 0.324, 0.260 - 0.385), and, lastly, lacunosum cell couple stronger to pyramidal layer theta compared to the rad+mol group (mean vector length, 95%CI: Lac 0.296, 0.273 - 0.318, Rad+Mol 0.263, 0.248 - 0.280). Conversely, spike probability in ripples (mean proportion, 95%CI: Lac 0.18, 0.15 - 0.21, Rad+Mol 0.18, 0.16 - 0.20) and the mean preferred phase in theta did not significantly differ between lacunosum and the two flanking layers (mean, 95%CI in degrees: Lac 179, 160 - 164, Rad+Mol 196, 186 - 205) (**Figure 7.3.3b**). Thus, these findings suggest that stratum lacunosum neurons displayed distinct behaviour and do not form an intermediate ‘transition’ group between the strata radiatum and moleculare.

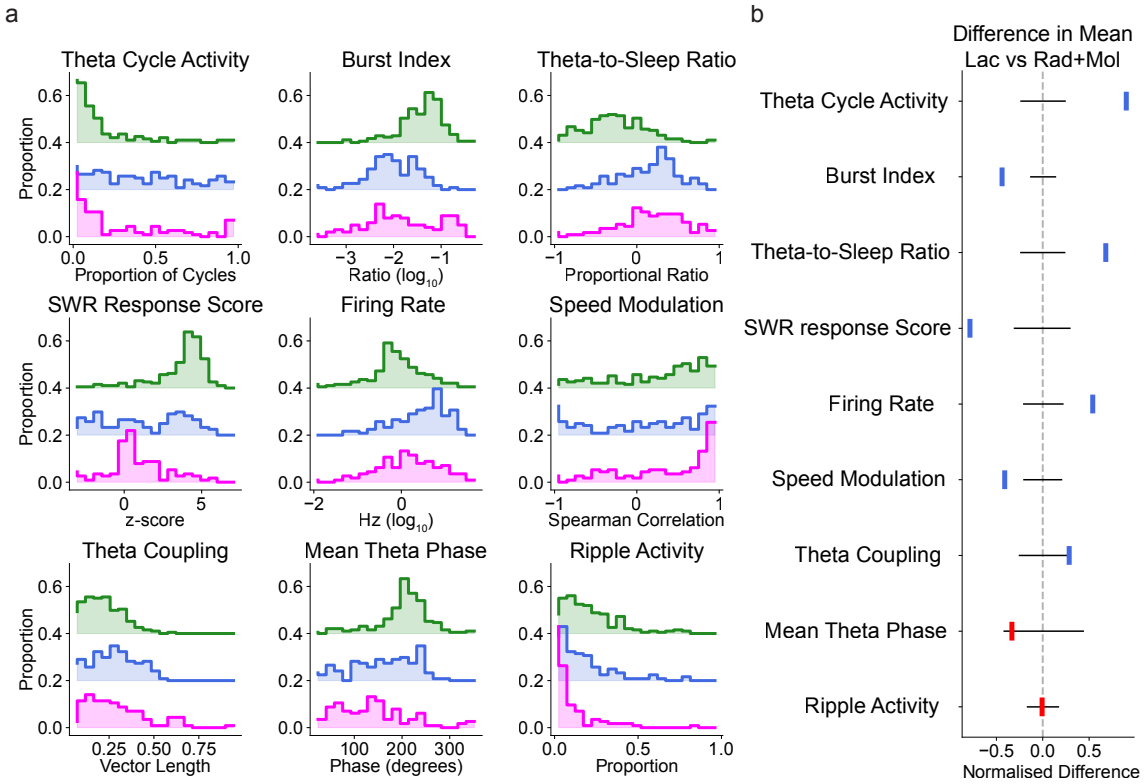


Figure 7.3.3 – Distinct spike characteristics in stratum lacunosum compared to strata radiatum and moleculare

a) Histograms showing the distributions for different spike characteristics (introduced in Chapter 4) for strata radiatum (green), lacunosum (blue), and moleculare (magenta). Note that the centre of mass of most of the stratum lacunosum distributions lay laterally to those of the strata radiatum and moleculare. **b**) Assessment of the mean differences between stratum lacunosum versus strata radiatum and moleculare grouped (rad+mol) for the spike characteristics presented in **a**). The vertical ticks indicate the true normalised difference (z-score of the null distribution) of the mean between the lacunosum and rad+mol population. The horizontal black line shows the 2.5-97.5th percentile range of the null distribution derived from 10.000 label shuffles. The colour of the vertical ticks indicated whether the tick falls within (red) or outside (blue) the 2.5-97.5th percentile range of the null distribution.

	Radiatum+Moleculare			Lacunosum					
Feature Name	**Mean**	**95%CI**		**Mean**	**95%CI**		**Mean diff**	**Normalised mean diff**	**p-value**
Theta Cycle Activity	0.201	0.173	0.231	0.411	0.359	0.461	0.211	0.897	$<10^{-5}$
Burst Index	0.073	0.065	0.083	0.032	0.025	0.039	-0.042	-0.384	$<10^{-5}$
Theta-to-Sleep Ratio	-0.051	-0.104	-0.004	0.19	0.129	0.25	0.241	0.654	$<10^{-5}$
SWR response Score	2.821	2.567	3.065	1.489	1.022	1.965	-1.333	-0.771	$<10^{-5}$
Firing Rate	3.371	2.729	4.076	6.738	5.569	8.015	3.367	0.534	$<10^{-5}$
Speed Modulation	0.324	0.26	0.385	0.079	-0.042	0.201	-0.244	-0.404	$<10^{-5}$
Theta Coupling	0.263	0.248	0.28	0.296	0.273	0.318	0.032	0.289	$<10^{-5}$
Mean Theta Phase	3.417	3.261	3.576	3.118	2.837	3.408	-0.299	-0.334	0.059
Ripple Activity	0.181	0.162	0.199	0.183	0.153	0.214	0.002	0.009	0.454

Table 7.3.1 – Means and differences between Lacunosum and Raditam+Moleculare interneurons across spike characteristics

Data corresponding to **Figure 7.3.3**

7.3.4 Lacunosum neurons are differentially targeted by CA3 and EC inputs compared to radiatum and moleculare neurons

Stratum lacunosum features unique network patterns and neuronal spike characteristics. Given that stratum lacunosum neurons live at the interface between CA3 and EC inputs, these features may arise from differential excitatory drive. To test the connectivity patterns between CA3 or EC, and CA1 interneurons, I performed trans-synaptic tracing experiments as well as physiology-based connectivity mapping (see **Chapter 5**). Anterograde transsynaptic labelling of CA1 interneurons showed that CA3 and EC converge onto stratum lacunosum neurons, while stratum radiatum and moleculare neurons are preferentially targeted by the afferent associated with the respective layers (**Figure 5.3.1**). These *ex vivo* anatomy results were further corroborated by *in vivo* examination of interneuron responses to afferent-specific terminal activation. This revealed that, in line with the anatomical assessment, stratum lacunosum neurons responded to both CA3 and EC stimulation, while radiatum and moleculare neurons primarily responded to CA3 and EC terminal stimulation, respectively (**Figure 5.3.7-5.3.8**). Taken together, these observations indicate that neurons in stratum lacunosum read from both CA3 and EC inputs, which reveals a unique connectivity pattern for neurons in stratum lacunosum compared to the other two adjecent superficial layers.

7.4 Discussion

Early descriptions of the hippocampus' laminar organisation defined the stratum lacunosum as an independent layer (Schaffer, 1892; Ramón y Cajal, 1904). However, modern literature has abandoned the distinction between stratum lacunosum and moleculare (Szirmai et al., 2012). The comparable appearance, when using nuclear staining, and similar input patterns have likely led to the merge of these layers into the stratum lacunosum-moleculare (Szirmai et al., 2012; Booker et al., 2016), see **section 7.3.1**). Whether this anatomical merge was justified from a physiological perspective remained unclear. Here, I utilise the superficial interneuron tetrode dataset (**Chapters 3** to **5**) obtained through layer-specific tetrode targeting in freely moving mice to examine whether stratum lacunosum displays unique electrophysiological features. I found that stratum lacunosum is characterised by distinct theta-nested network patterns, neuronal firing characteristics including

layer- as well as neuron cluster-specific features, and different recruitment of interneurons by major afferents. Together these findings suggest that stratum lacunosum is a distinct entity and should be treated as such to gain a better understanding of hippocampal network functioning.

Generally, it is challenging to capture changes in nomenclature over long time periods. In **section 7.3.1**, I aimed to evaluate the usage of the stratum lacunosum as an independent layer by performing a quantitative PubMed search, which revealed that only a minority of articles refer to the stratum lacunosum in isolation and that the relative number of studies declined even further over the years. However, this quantitative study only examined the abstracts rather than the full articles, which may have led to the exclusion of articles mentioning the stratum lacunosum as a separate layer in the main text or illustrations. Nevertheless, this approach allowed for a high throughput large-scale quantitative study that reflects general practice in the hippocampal field of research. Together, these observations underscore the idea that stratum lacunosum has mostly been considered part of a single layer combined with the stratum moleculare: the stratum lacunosum-moleculare.

Recent work from our laboratory has shown that distinct layer-specific theta-nested gamma oscillations can be found along the radial axis of dorsal CA1 (Lopes-dos-Santos et al., 2023). Interestingly, a new type of fast-gamma was described, which I showed to be primarily present in stratum lacunosum tetrodes (see **Chapter 2**), rather than in 'distal radiatum' as previously assumed (Lopes-dos-Santos et al., 2023). Although the layer-specific superficial interneuron tetrode dataset includes individual, simultaneously recorded interneurons a causal relationship between fast-gamma generation and lacunosum interneuron activity has not been tested here. Therefore, the cellular basis of the fast oscillation in stratum lacunosum remains unclear. Nevertheless, based on earlier literature, I can speculate on what underlies this oscillation. First, fast oscillations are mostly thought to be locally generated by recurrent interactions between inhibitory-excitatory and inhibitory-inhibitory neurons as seen in the stratum pyramidale (Bartos et al., 2007; Buzsáki and Wang, 2012). Given that nearly all neurons across the superficial layers are GABAergic and pyramidal neurons do not send axons to these layers (Amaral et al., 1991;

Freund and Buzsáki, 1996), it is unlikely that the fast-gamma found in the stratum radiatum arises from a local inhibitory-excitatory network motif (Buzsáki and Wang, 2012). Conversely, the presence of interneuron-specific interneurons across the superficial layers makes a local, recurrent interneuron motif a suitable candidate (Chamberland and Topolnik, 2012). Alternatively, this oscillation may arise from a mixed network consisting of external excitatory inputs driving local inhibitory neurons (Buzsáki et al., 2012). Such a feed-forward motif could generate fast and local gamma oscillation by targeting a subset of interneurons specifically projecting to pyramidal neuron dendrites in the stratum lacunosum (Booker et al., 2016). Lastly, the superficial fast-gamma oscillation may be generated by an interregional inhibition-inhibition network. Entorhinal cortex-originating GABAergic projections have been shown to target superficial layers in CA1 (Melzer et al., 2012; Basu et al., 2016). While these long-range inputs are not restricted to the stratum lacunosum, the interneurons they target accumulate in and around this layer, possibly resulting in fast entrainment of lacunosum interneurons. The precise targeting of interneurons by extrahippocampal inputs may provide an alternative to local circuit motifs on how superficial fast-gamma arises. Overall, identification of this lacunosum-specific fast-gamma indicates that this layer may house a unique circuit compared to the strata radiatum and moleculare.

Stratum lacunosum displays distinct spike characteristics compared to stratum radiatum and moleculare. Interestingly, the most striking differences between stratum lacunosum neurons compared to the radiatum/moleculare group were found for features that capture spiking participation in theta cycles and sharp-wave ripples. The spike probability and rate in theta cycles were higher for lacunosum neurons compared to the other two groups, while stratum lacunosum uniquely houses neurons inhibited during ripples. It is unclear why specifically lacunosum neurons participate strongly in theta cycles and spike less in ripples compared to the other superficial interneurons. One reason could be that lacunosum neurons have distinct neuron-intrinsic properties. Lacunosum neurons have been shown to strongly respond to neuromodulators, such as serotonin and acetylcholine, resulting in membrane depolarisation and subthreshold theta-frequency oscillatory patterns, respectively (Chapman and Lacaille, 1999b, 1999b; Wyskiel and Andrade, 2016). In addition, cholinergic inputs accumulate around the lacunosum as compared

to the stratum radiatum and moleculare (Storm-Mathisen, 1970; Aznavour et al., 2002), likely targeting lacunosum neurons. The release of these neuromodulators, which are most abundantly present during awake states (Zhang et al., 2021), combined with their impact on lacunosum neurons may explain why particularly lacunosum neurons show strong participation in theta cycles during awake exploration. In addition to neuron-intrinsic properties, spiking behaviour can be influenced by afferent activity. In line with earlier reports, I found that lacunosum neurons are targeted by inputs from both CA3 and EC, while radiatum and moleculare neurons are mostly targeted by a single afferent. The higher firing rates in lacunosum compared to radiatum and moleculare interneurons may arise from a powerful excitatory drive lacunosum interneurons receive from these dual inputs (Milstein et al., 2015). Furthermore, lacunosum interneurons are preferential targets of specific sets of excitatory projection neurons in the entorhinal cortex layers 2 and 5, providing an alternative drive to other superficial interneurons that may not have access to (Kitamura et al., 2014; Tsoi et al., 2022). These intra- and extrahippocampal projections particularly targeting the stratum lacunosum could result in higher firing rates of stratum lacunosum interneurons. Taken together, the presence of layer-specific neuronal spike characteristics underscores the uniqueness of the stratum lacunosum at a neuronal level and may be driven by neuron-intrinsic properties and/or distinct input patterns.

Overall, I propose that stratum lacunosum is a distinct entity and should not be grouped with the stratum moleculare. The first descriptions of the stratum lacunosum already pointed out some distinctive characteristics, and more evidence has been accumulating suggesting that stratum lacunosum not only displays unique anatomical but also electrophysiological features. Here, I showed that stratum lacunosum houses unique network patterns, cell types, and projection patterns. Alongside the existing evidence, these observations underscore that stratum lacunosum is an independent layer which likely features unique network operations. Identification of this layer opens new avenues to study hippocampal functioning and information gating to CA1 pyramidal neurons.

Chapter 8. General Discussion

8.1 Overview

Inhibitory neurons are crucial for hippocampal function, and understanding the complex network dynamics of dorsal CA1 requires deeper insights into interneuron function. However, most reports on the function of hippocampal inhibition have focused on fast-spiking interneurons or the molecularly well-defined PV- and SST-positive families. In CA1, most of these interneuron types are found in the deep layers: the strata oriens and pyramidale. In this Thesis, I aimed to record and investigate superficial interneurons in dorsal CA1 of the mouse hippocampus and expand our insights on their function. To do so, I first validated a layer-specific tetrode-targeting approach, which allowed me to estimate the recording depth of detected units utilising layer-specific LFP signatures (**Chapter 2**), and revealed a unique stratum lacunosum-specific LFP signature, distinguishing the lacunosum from its flanking layers. Then, using this depth estimation tool, I recorded over 600 interneurons across different hippocampal layers alongside over 1500 pyramidal neurons in freely moving mice at temporal resolution of single spikes. Spike waveform analysis showed that superficial interneurons display different waveform shapes, which spatially cluster along the radial axis of dorsal CA1, and that general interneuron classification rules are not sufficient for superficial interneurons (**Chapter 3**). Additionally, spike characteristics analysis showed that superficial interneurons display layer-specific differences in spike rate and timing, as well as differential engagement in awake theta oscillations and sharp-wave ripples during sleep. Notably, interneurons in the stratum lacunosum exhibited unique activity patterns in local network events compared to neurons in the other strata (**Chapter 4**). Furthermore, I tested whether superficial interneurons are differentially recruited by CA1's major input sources – CA3 and entorhinal cortex – and found that these afferents preferentially target neurons with somata in their respective termination layer, while both converging on the stratum lacunosum (**Chapter 5**).

I showed that superficial interneurons display differential co-activity patterns between different layers and cell types, which may reflect distinct subcircuits (**Chapter 6**). Lastly, supported by previous literature and data from this Thesis, I propose that the stratum lacunosum, normally grouped with the stratum moleculare, forms an anatomically and electrophysiologically unique layer (**Chapter 7**). Overall, these results provide a promising tetrode depth estimation technique, novel insights on the spatial and temporal structure of inhibitory activity, and revealed that the stratum lacunosum has a unique electrophysiological profile.

8.2 Spatial structure of inhibition along the radial axis of dorsal CA1

The hippocampus is a structurally well-organised brain region (Freund and Buzsáki, 1996; van Strien et al., 2009). In CA1, dendrites of pyramidal neurons are perfectly aligned, its major input sources occupy non-overlapping spaces, and interneuron-originating axonal projections target distinct cellular subdomains along the dendritic tree. This precise organisation suggests that the position of these circuit elements is relevant to their function (Somogyi and Klausberger, 2005). While the relationship between soma location and electrophysiological differences, such as distinct spiking characteristics and interregional connectivity, has been well established for spatially segregated pyramidal neurons (Royer et al., 2012; Valero et al., 2015; Sharif et al., 2021; Harvey et al., 2023), the importance of interneuron soma position remains controversial (Klausberger, 2005; Varga et al., 2014; Geiller et al., 2020). While Varga and colleagues found interneuron differences correlated to soma location within the PV-positive family in the hippocampus (Varga et al., 2014), Klausberger et al. and Geiller et al. did not find such within-type, soma location-dependent relationship across CCK-positive interneurons and other canonical types, respectively (Klausberger, 2005; Geiller et al., 2020). Although I could not identify molecularly defined interneuron types due to the nature of the methods used, in Chapters 3, 4, and 5, I provided evidence for a spatial organisation of interneuron activity and recruitment. Recorded interneurons displayed distinct waveform shapes as a function of depth as well as varying spike timing and engagement in local network events. These results suggest that soma location may influence interneuron spiking activity more than previously appreciated.

Soma and dendrite location is an important determinant for which inputs a neuron can receive and for the relative influence these inputs may have (Stuart and Spruston, 2015). Therefore, soma location may play a role in the emergence of a spatial structure of CA1 inhibitory activity. The layer-specific targeting by distinct CA1 afferents results in spatially well-controlled positioning of synapses as a function of distance from the soma in the radial axis, which influences the input-output function of the excitatory input to the interneurons (Kitamura et al., 2014; Milstein et al., 2015) (see also **Chapter 5**). Similarly, inhibitory control is spatially well organised, with local and remote long-ranging interneurons targeting CA1 and its interneurons in a layer- and interneuron-specific manner (Somogyi and Klausberger, 2005; Chamberland and Topolnik, 2012; Melzer et al., 2012). Together, the interplay between interneuron soma locations and the layer-specific axonal projections forms a basis for distinct anatomical circuit submodules (Elfant et al., 2007; Basu et al., 2013).

Furthermore, the importance of afferent connectivity is reflected by the gradual advancement of preferential spike phase of superficial interneurons as a function of depth, across layers but also within layers (preliminary analysis on data from **Chapter 4**; data not shown). This gradual phase advancement seems to mirror the well-described phase shift of extracellular recorded theta oscillations (Buzsáki, 2002), and aligns with a recent study which recorded pyramidal neuron dendrite inputs as a function of distance from the soma (Liao et al., 2024). This study showed that inputs move as a 'theta wave' from the stratum moleculare to the pyramidale. In addition, in sharp-wave ripples, this gradual activity pattern changes in a layer-based activity pattern (**Chapter 4**), which corresponds to the relative change in input behaviour (Buzsáki, 2015; Liao et al., 2024). The layer-specific activation of superficial interneurons during distinct network events, each with varying afferent input, highlights the importance of soma location and afferent connectivity in driving CA1 interneuron activity. Together, the soma location is a relevant determinant of CA1 interneuron anatomical circuit embedding and their spatially determined activity patterns.

In addition to soma location potentially explaining the structure of inhibitory activity along CA1's radial axis, the unequal distribution of interneuron types provides an alternative explanation.

Shaped by type-specific combinations of cell signalling-related proteins, distinct interneurons exhibit varying spike timing characteristics and differential engagement in local network activity (Somogyi and Klausberger, 2005; Földy et al., 2016; Harris et al., 2018). Additionally, canonical interneuron types have been shown to occupy different spaces along CA1's radial axis (Somogyi and Klausberger, 2005; Klausberger and Somogyi, 2008; Pelkey et al., 2017; Booker and Vida, 2018). The interneuron type-specific spiking characteristics and the skewed distribution of interneurons along CA1's radial axis could underly the layer-specific spiking differences I found. Unfortunately, due to the nature of the tetrode recording method, *post hoc* identification of the recorded interneurons was not possible. However, if spike waveform is predictive of interneuron type (Földy et al., 2016; Petersen et al., 2021; Ye et al., 2023), the clustering of spike waveforms in space provides evidence that unequally distributed interneuron populations may, at least partially, be responsible for the layer-based spiking differences found (see **Chapter 3**). This finding is further supported by the soma shape analysis in an independent cohort (see **Chapter 5**). Together, the varying distribution of distinct interneuron types can underly spatial structuring of inhibition.

In summary, given that interneuron types and synaptic inputs are organised in the spatial domain, it is likely that soma location, as a determinant for presynaptic partners, as well as interneuron type-specific intrinsic characteristics underly the inhibitory activity structure in dorsal CA1. The differential layer-specific engagement in network events indicates that this spatial structure may have functional implications. Overall, the spatial structure of inhibitory activity along dorsal CA1's radial axis provides novel starting points in unravelling the function of inhibition in the hippocampal network.

8.3 Temporal structure of inhibition along the radial axis of dorsal CA1

Hippocampal activity can rapidly adapt to continuously meet ongoing behavioural demands and facilitate different network operations (Lopes-dos-Santos et al., 2018). The temporal structure of inhibition in the hippocampus can be examined at scales ranging from single spikes to intervals related to oscillatory patterns, and behavioural timescales (Klausberger and Somogyi, 2008; Dupret

et al., 2013; Turi et al., 2019; Geiller et al., 2020; Dudok et al., 2021a). Despite being essential to our current understanding of superficial interneurons to date, previous reports have painted a static image of interneuron activity in hippocampal network events. When spike characteristics of superficial interneurons are reviewed, authors often focus on simplified models and, therefore, reduce complex temporal spiking dynamics in theta oscillations and sharp-wave ripples to mean spike rates and phases (Klausberger and Somogyi, 2008; Topolnik and Tamboli, 2022; Tzilivaki et al., 2023). Furthermore, neuronal interactions are state-dependent (Csicsvari et al., 1998; Senzai et al., 2019; Luo et al., 2020), but little is known about how superficial interneurons are affected by these changes *in vivo*. Thus, while simplification of this highly intricate network can be beneficial to our general understanding of complex networks, the temporal dynamics of superficial interneurons may contain clues critical to understanding the dynamics of inhibition.

At short timescales, hippocampal interneurons have been shown to prefer different phases in relation to oscillations and time their spikes differently in relation to sharp-wave ripples (Lapray et al., 2012; Katona et al., 2014; Rangel Guerrero et al., 2024). Despite the use of a different recording technique, I find similar short-time-scale patterns across different interneuron populations, which resemble spiking patterns described for canonical interneuron types (Klausberger and Somogyi, 2008). It has been suggested that this well-timed activity is required to constrain pyramidal neuron activity (Klausberger, 2005). Indeed, removal of global or interneuron type-specific inhibition can shift the preferred phase of pyramidal neurons in theta oscillations (Royer et al., 2012; Valero et al., 2022; Rangel Guerrero et al., 2024). However, this view, based on averaged interneuron activity across all recorded cycles, assumes that the interneuron activity is homogeneous in time, but accumulating evidence suggests this may not be the case. First, elaborate LFP analysis suggests that dorsal CA1 features distinct theta-nested gamma oscillations on a cycle-to-cycle basis (Lopes-dos-Santos et al., 2018), assumed to arise from fluctuations in CA3 and EC inputs (Colgin et al., 2009; Lasztóczi and Klausberger, 2014; Schomburg et al., 2014). The connectivity analysis in this Thesis showed that interneurons are differently recruited by CA3 and EC inputs (**Chapter 5**) and, if CA3 and EC inputs dominate different theta cycles, interneurons may exhibit theta-cycle specific activity. Second, cross-layer spike analysis showed

that superficial interneurons, except for a subpopulation of lacunosum interneurons, display low spike probability across theta cycles and sharp-wave ripples, and varying inter-spike intervals. These observations indicate that superficial interneuron activity is less homogeneous in time than previously assumed (**Chapter 4**). Third, theta cycle-specific co-activity analysis showed that superficial interneurons, particularly those in stratum lacunosum, exhibit stronger within-layer correlations than between-layer correlations (**Chapter 6**). Similarly, in sharp-wave ripples, within-layer correlations were higher than between-layer correlations, representing a layer-based coactivity pattern. These asymmetric correlations indicate that superficial interneuron activity changes are not homogeneous across layers over time, suggesting that layer-based interneuron populations participate differently in individual network events. Together, these observations emphasize that interneuron activity is highly dynamic across time, a feature that seems often overlooked in reviews and models.

Beside short timescales, interneurons have been shown to vary spiking patterns between behavioural states (Lapray et al., 2012; Katona et al., 2014; Senzai et al., 2019; Geiller et al., 2020; Dudok et al., 2021a; Szabo et al., 2022), which add another layer of network complexity in the temporal domain and support distinct network demands under varying behavioural and environmental conditions (Topolnik and Tamboli, 2022). Similar to earlier findings (Katona et al., 2014, 2014; Szabo et al., 2022; Rangel Guerrero et al., 2024), I found that most superficial interneurons change their spike patterns in awake versus sleep states. These changes appeared to be layer-dependent, with higher firing rates and regularity in awake versus sleep states for lacunosum and moleculare neurons, but not for radiatum neurons (**Chapter 4**). Since dendritic targeting interneurons and interneuron-specific interneurons preferentially target specific neuronal subdomains and interneuron types, respectively (Somogyi and Klausberger, 2005; Chamberland and Topolnik, 2012), such relative shifts in inhibitory activity of specific subpopulations could result in information rerouting through dorsal CA1. This hypothesis is further supported by the theta and sharp-wave ripple-specific correlation analysis which revealed state-dependent changes in superficial interneuron coactivity, suggesting state-specific network configurations **(Chapter 6**). Together, similar to pyramidal neurons and pyramidale interneurons, superficial interneurons display state-dependent, behavioural time-scale activity patterns.

These network- and state-dependent activity changes likely result from differing synaptic inputs and/or intrinsic excitability of the interneurons. Although excitability measures are not directly accessible through the recording methods used, I deduced state-dependent information transmission strength from responses to input-specific stimulation (Barthó et al., 2004; English et al., 2017). These experiments revealed that during awake exploration layer-specific superficial interneuron response probability to CA3 and EC inputs can fluctuate within subtheta timescales (**Chapter 5**). The rapid theta phase-dependent changes are likely due to theta-associated periods of increased excitatory or inhibitory drive (Somogyi and Klausberger, 2005; Mizuseki et al., 2009; Grienberger et al., 2017; Valero et al., 2022). Furthermore, spike transmission comparison between brain states, showed that superficial interneuron subpopulations display state-dependent sensitivity to CA3 and EC inputs (**Chapter 5**), a phenomenon previously described for local pyramidal neuron to interneuron transmission (Csicsvari et al., 1998; English et al., 2017). Besides varying synaptic strength, these slower state-dependent differences can reflect interneuron type-specific excitability changes, which can be due to varying levels of neuromodulatory molecules, such as acetylcholine (Chapman and Lacaille, 1999b; Wyskiel and Andrade, 2016; Zhang et al., 2021). Together, these observations underscore that superficial interneurons are under tight but dynamic control.

In summary, superficial interneuron activity is highly dynamic in the temporal domain. Simplification of the CA1 circuitry, as is often seen in models and reviews, omits important clues to unravel the function of superficial interneurons. Superficial interneurons engage differently with local network events at a single-spike resolution and alter their spiking patterns across different brain states. Furthermore, superficial interneuron responsiveness to CA1's major afferents can be reconfigured in a network- and brain-state-dependent manner. Overall, both the short and behavioural timescale layer-specific fluctuations in interneuron activity may permit the local CA1 circuitry to flexibly switch information routing to meet ever-changing environmental demands.

8.4 Functional implications of laminarly organised and state-dependent inhibitory activity

Interneurons are widely implicated in all kinds of regulatory functions in the neuronal network (Topolnik and Tamboli, 2022). Superficial interneurons exhibit layer-specific electrophysiological features, suggesting that these location-dependent differences may have functional implications for local network operations. Indeed, in the barrel cortex, SST-positive interneurons display behaviourally relevant bidirectional spiking activity depending on the cortical layer they reside in (Muñoz et al., 2017). The authors proposed that these laminar differences result from the interneurons' spatial positions, which determine their afferent connectivity rules. Combined with their distinct efferent targeting, this differential activity results in a precisely targeted pattern of inhibition and disinhibition along the dendrites of pyramidal neurons. In addition, in the visual cortex, interneurons have been shown to couple in a layer-specific manner to gamma-band oscillations, which may indicate differential involvement in distinct network operations (Senzai et al., 2019). In the current work, I found significant layer-specific differences in the spike timing in theta cycles and sharp-wave ripples, which suggests that CA1 interneurons may form functional submodules organised in a laminar fashion. Thus, similar to the cortex, inhibitory neuron activity in dorsal CA1 is organised in a laminar structure and may play a role in distinct network operations.

Laminarly organised interneuron activity may reflect layer-specific feedforward submodules in the CA1 circuitry. Such layer-specific submodules would allow independent feedforward regulation of spatially segregated excitatory inputs by recruiting pyramidal neuron dendrite-targeting interneurons of which the axonal projections overlap with the inputs' termination zone (Buzsáki, 1984; Somogyi and Klausberger, 2005)(see also **Chapter 5.3.1**). While most interneuron dendrites span multiple layers, both the anatomical and functional connectivity assessment in Chapter 5 showed that CA3 and EC preferentially target and reliably activate interneurons in their corresponding target layers. CA3 terminal stimulation robustly recruited stratum radiatum and pyramidale interneurons, while EC terminal stimulation generated reliable activation of moleculare interneurons, both followed by a network-wide inhibitory component suggestive of

feedforward inhibition (Buzsáki, 1984). In addition, the axonal patterns of input-specific labelled interneurons were shown to strongly overlap with the input source's termination zone (see **Figure 5.4.1**). These observations support the idea that neurons in stratum radiatum and lacunosum/moleculare may form independent submodules with layer-specific input sources. Furthermore, physiological spike timing in theta oscillations further supports a layer-based feedforward motif, with stratum radiatum interneurons preferentially spiking around the trough, which is just after the proposed spike timing of CA3 pyramidal neurons, while moleculare interneurons preferentially spike at the descending phase of theta, the period coinciding with the highest entorhinal cortex activity (Colgin et al., 2009; Mizuseki et al., 2009; Schomburg et al., 2014). Lastly, independent functioning of layer-specific submodules is further corroborated by the relatively low coactivity levels between superficial layers compared to the within-layer coactivity (**Chapter 6**). Together, the layer-specific activation patterns may represent, at least partially, input-specific feedforward submodules regulating temporal and spatially distinct inputs.

Distinct excitatory inputs activate in a spatially and temporally segregated manner (Colgin et al., 2009; Mizuseki et al., 2009; Schomburg et al., 2014), and while recruiting independent interneuron populations, these excitatory afferents all converge on to the pyramidal neurons (Kajiwara et al., 2008). Although layer-specific feedforward submodules could coordinate the incoming inputs on specific subdomains, a higher-order inhibitory structure may be required to orchestrate overall excitatory activity on the pyramidal neuron. Lacunosum interneurons, living at the interface between CA3 and EC inputs, are ideally situated to monitor overall excitatory drive. By sensing both CA3 and EC inputs, lacunosum interneurons could function as multi-signal integrators or comparators and possibly provide such higher-order inhibition (Milstein et al., 2015; Magó et al., 2021). Anatomical and functional connectivity mapping showed that CA3 and EC converge on the stratum lacunosum (Kajiwara et al., 2008) (see **Chapter 5**). Indeed, neurogliaform and CCK-positive interneurons in stratum lacunosum have been shown to integrate or respond to both CA3 and EC inputs (Chapman and Lacaille, 1999b; Milstein et al., 2015), and some interneuron-specific interneurons, exhibit appropriate dendritic morphologies to perform a similar function (Chamberland and Topolnik, 2012). This favourable morphology combined with cell-intrinsic

properties, such as differential expression of neuromodulatory receptors as well as precise axonal patterning, would allow lacunosum interneurons to selectively add inhibition to distinct pyramidal subdomains, or in case of interneuron-specific interneurons, release such subdomains from inhibition (Chapman and Lacaille, 1999b; Wyskiel and Andrade, 2016; Palacios-Filardo et al., 2021; Bilash et al., 2023). Through domain-specific 'add-on' inhibition or disinhibition of specific interneuron types, these integrating interneurons could regulate input selection and plasticity in CA1 (Gulyás et al., 1999; Elfant et al., 2007; Bilash et al., 2023), which would position them as master conductors of the CA1 circuitry. Together, interneurons in stratum lacunosum are ideally situated to play a key role in multi-signal integration in the dorsal CA1 circuitry by monitoring CA3, EC, and state-dependent signals.

Overall, the spatial, temporal, and state-dependent activity patterns of superficial interneurons transform the structurally static CA1 circuitry into a highly flexible system, which is essential to navigating daily life and meeting continuously varying environmental demands (Topolnik and Tamboli, 2022; Tzilivaki et al., 2023). The state-dependent activity patterns as well as alterations in information transfer during different states support the idea that superficial interneurons can reroute inputs under various short and long-term network conditions (see **Chapters 4** and **5**). As nearly all neurons have been shown to preferentially target distinct postsynaptic domains and partners (Somogyi and Klausberger, 2005; Chamberland and Topolnik, 2012), recruitment by specific inputs or neuromodulators can flexibly switch information flow through neuronal submodules on a moment-to-moment basis. Together, the spatial structure of inhibition combined with network- and state-dependent activity patterns support dynamic CA1 information processing specifically tailored to ongoing demands.

8.5 Future directions

The current work shows that superficial interneurons display dynamic properties of the intact mouse brain and supports the idea that distinct groups perform different functions in the local dorsal CA1 network. However, to unravel the function of superficial interneurons and how they affect their post-synaptic partners *in vivo* more research is required.

One of the major advantages of layer-specific tetrode targeting performed in this Thesis is the opportunity to co-register interneurons across nearly all layers alongside pyramidal neurons, or other regions, depending on the tetrode layout (McHugh et al., 2024). Due to time limitations, I have not been able to explore the interactions between superficial interneurons and pyramidal neurons to the full extent. Future studies should focus on a more in-depth analysis of superficial interneuron to pyramidal neuron interactions. For example, neurogliaform cells have recently been shown to decouple pyramidal neurons from entorhinal cortex inputs (Sakalar et al., 2022). The current dataset is well-suited to investigate such effect for all interneurons along the radial axis of dorsal CA1. Additionally, the flexibility of the current dataset, which includes sleep and exploration sessions, as well as different behavioural states (novel vs familiar environments), permits more extensive data mining on interneuron to pyramidal neuron interactions under different behavioural conditions. Lastly, the 'gating' properties of superficial interneurons could be further investigated by optogenetic or chemogenetic manipulations of superficial interneurons and/or long-range inputs (Melzer et al., 2012; Kitamura et al., 2014; Turi et al., 2019; Guo et al., 2021; Tsoi et al., 2022; Bilash et al., 2023; Rangel Guerrero et al., 2024). For example, through a combination of the optogenetic activation of excitatory inputs, as performed in **Chapter 5**, and simultaneous chemo- or optogenetic interference with interneuron activity (Zutshi et al., 2022), the effects of superficial interneuron activity on the input-output function of pyramidal neurons could be assessed *in vivo*(Milstein et al., 2015; Furutachi et al., 2024). Together, future studies should focus on in-depth investigation of causal relationships between superficial interneuron and pyramidal neuron activity.

In this Thesis, I have only discussed recordings in mice during awake exploration and sleep sessions and have not leveraged the different contexts to which the mice were exposed (see **Figure 3.2.1**). In line with previous reports (Geiller et al., 2020; Guo et al., 2021), preliminary analysis suggested that superficial interneurons not only display brain state-specific spiking characteristics but also exhibit context-dependent (i.e. novel versus familiar) spike rate differences (data not shown). These preliminary findings underscore the need for further exploration of superficial interneuron activity under different behavioural conditions. For example, further analysis could

focus on firing rate differences of distinct superficial interneuron groups in novel versus familiar environments as well as the coactivity structures as presented in **Chapter 6**. Furthermore, the continuous, 15-minute recordings during exploration in the novel environment permit a more granular analysis when parsing these novel-exploration epochs into smaller time bins, which may capture changes reflecting learning as the mice get acquainted with the environment over time (Geiller et al., 2020). Particularly, diverging spiking behaviour between interneuron groups across environments could provide clues on how superficial interneurons may reorganise information processing during contextual changes favouring either recall or encoding (Geiller et al., 2020; Tamboli et al., 2024). Thus, leveraging all behavioural dimensions this dataset has to offer could provide further insights into the role of superficial interneurons in information encoding and retrieval.

While exploiting the existing data is an accessible step to exploring the role of superficial interneurons in learning and memory, tasks specifically designed to test learning and memory performance could complement the current dataset. Particularly, temporally segmented or spatial learning tasks provide several advantages in investigating hippocampal dynamics during encoding and retrieval epochs (Jadhav et al., 2012; Dupret et al., 2013; Zhang et al., 2021). First, the power to reveal subtle differences in neural spiking behaviour across these relatively sparse superficial interneuron populations increases if mice perform multiple trials per session or recording day. Secondly, these memory-guided tasks have the advantage that they provide behavioural readouts of learning and allow linking neural spiking activity to performance. For example, to test whether superficial interneuron activity during learning scales with memory performance (Guo et al., 2021). Lastly, tasks parsed into discrete memory-guided decision points and return trajectories, such as out and inbound trajectories in a radial-arm or w-maze spatial navigation task (Jadhav et al., 2012; Gillespie et al., 2021), would allow a more granular analysis of learning and memory-related superficial neuron spike patterns. If superficial interneurons play differential roles in memory formation and retrieval, changes in spike timing and coactivity patterns likely occur across different task phases (i.e. out versus inbound trajectories). Additionally, such tasks would provide data for within-session behavioural control analyses interleaved with memory-guided

behaviour (e.g. running speed across task phases). Together, bespoke spatial memory tasks could complement the current dataset and provide further insight into the function of superficial interneurons in learning and memory.

Furthermore, sharp-wave ripples are distinct network events occurring during slow-wave sleep and awake immobility epochs (Jadhav et al., 2012; Yamamoto and Tonegawa, 2017). It has been suggested that awake ripples may serve a differential purpose from sharp-wave ripples during sleep (Roumis and Frank, 2015). While sleep ripples are associated with long-term memory consolidation (van de Ven et al., 2016), the spatially more accurate awake ripples may favour rapid information processing, online evidence accumulation, and behavioural planning (Jadhav et al., 2012; Gillespie et al., 2021). Additionally, the driving mechanisms between awake and sleep ripples may be different, with the entorhinal cortex playing a more prominent role in the generation of awake ripple bursts, while CA3 is required regardless of brain state (Yamamoto and Tonegawa, 2017). Based on these differential state-dependent ripple-driving mechanisms, combined with the distinct superficial interneuron-afferent connectivity (**Chapter 5**) and state-dependent spiking characteristics (**Chapter 4**), it is possible that superficial interneurons differentially participate in awake versus sleep ripples and might even facilitate divergent information processing across these ripple types. While lacunosum and moleculare interneuron firing rates have been shown to decrease or remain stable in CA3 input-dominated sleep ripples (**Chapter 4**; Buzsáki, 2015; Yamamoto and Tonegawa, 2017; Sakalar et al., 2022) the differential afferents-to-superficial interneurons connectivity predicts that these superficial interneurons may participate in EC-driven awake ripple bursts (**Chapter 5**). However, the nature of the task used in this Thesis, with mice exposed to exploration-promoting environments, is less suitable for testing this prediction than tasks naturally reinforcing immobility epochs (Jadhav et al., 2012; Vöröslakos et al., 2025). Hence, future studies could focus on superficial interneuron recordings in a task permitting parallel examination of sleep and awake ripples. Ripple-related activity patterns, such as firing rate-related metrics and ripple-to-ripple co-activity across CA1 layers (see **Chapters 4** and **6**), could be employed to perform within-neuron analysis of superficial interneuron state-dependent ripple engagement. Together, state-dependent ripple types may recruit superficial interneurons

differently, but complementary studies employing awake as well as sleep ripple-promoting tasks are required to elucidate superficial interneuron participation across ripple types.

Based on anatomical and functional studies, I concluded that interneuron in lacunosum must be able to integrate information from both CA3 and EC. However, all experiments presented here have been performed in independent mice. To further investigate such integration, it would be necessary to perform combined terminal stimulation *in vivo*. The expression of differentially activated opsins in CA3 and EC could permit direct comparison between afferent effects on the same interneuron (Hooks, 2018). Furthermore, the use of specific stimulation protocols would allow examination of temporal summation rules as have been seen *ex vivo* (Milstein et al., 2015; Basu et al., 2016). Thus, combined input-specific activation is necessary to further unravel interneuron-specific integration rules *in vivo*.

Besides CA3 and EC, the nucleus reunions of the thalamus is a major excitatory source of axon terminals to dorsal CA1 (Wouterlood et al., 1990; Dolleman-van der Weel et al., 2017). The connection between the thalamus and CA1 – which is perhaps even less well studied than superficial interneurons – may be an important input source of superficial interneurons, particularly those in the strata lacunosum and moleculare (Dolleman-Van Der Weel et al., 1997). Anatomical and functional connectivity studies, as performed in **Chapter 5** for CA3 and EC, could unravel cortical and subcortical connectivity rules of superficial interneurons. Additionally, an important question would be whether these excitatory projections target the same different interneuron populations as has been shown for thalamic projections to the neocortex (Anastasiades et al., 2021). Thus, future studies considering subcortical inputs to dorsal CA1 interneurons may be important to fully grasp interneuron function.

As discussed in **section 1.4** of the introduction, most interneurons are categorised based on morphological and/or molecular markers (Somogyi and Klausberger, 2005; Pelkey et al., 2017; Booker and Vida, 2018). However, electrophysiological recordings often have no access to these features without additional interventions, such as opto-tagging. The development of interneuron-

type identification markers would greatly benefit future studies of superficial interneurons (Roux et al., 2014). Exploration of targetable and interneuron type-specific genes is invaluable to aid opto- and chemogenetic targeting strategies (Taniguchi et al., 2011), and the growing number of large-scale transcriptomic datasets could guide the search to appropriate targets (Harris et al., 2018; Bugeon et al., 2022). Based on type-specific expression patterns, cre-mouse lines could be developed to build ground truth electrophysiological identification libraries (Roux et al., 2014; Petersen et al., 2021). Although, to my knowledge, no elaborate identification library covering superficial interneurons is publicly available, such projects are currently being undertaken (Abad Pérez et al., 2024). These identification tools, combined with the depth estimation tool discussed in this Thesis, will accelerate future superficial interneuron research in freely moving rodents.

Overall, this work has laid a foundation for the study of superficial interneurons of dorsal CA1 in freely behaving mice. Future directions could follow the more elaborate exploration of local circuit interactions among superficial interneurons and between interneurons and pyramidal neurons. Furthermore, open questions remain on which major excitatory inputs drive distinct populations of superficial interneurons and what role the thalamic projections may play. Lastly, and perhaps most importantly, interneuron type- and input-specific manipulations are essential to examine the role of superficial interneurons in modulating the input/output function between CA1 afferents and pyramidal neurons. Together, the work and suggestions presented here may aid essential future studies aiming to elucidate the function of superficial interneurons in the local CA1 circuitry.

8.6 Concluding remarks

The heterogeneity among interneurons in dorsal CA1 is vast and the functional parameter space is overwhelming considering differential axonal targeting patterns, receptor expression, afferent connectivity, and distinct synaptic facilitation and/or depression rules (Somogyi and Klausberger, 2005; Kajiwara et al., 2008; Bugeon et al., 2022; Chamberland et al., 2023). To understand the complex interactions between interneurons and their networks, models of interneuron function are simplified and, in particular, the highly heterogeneous group of dendrite-targeting interneurons

is often underrepresented (Topolnik and Tamboli, 2022). Therefore, I aimed to examine the understudied population of superficial interneurons in dorsal CA1. Although I have not (yet) found a satisfactory answer to my initial question about how superficial interneurons 'gate' information, this work has moved the frontiers of our knowledge on superficial interneurons.

In this Thesis, I have tackled one of the hurdles holding back superficial interneuron research *in vivo*: the accessibility of these interneurons with electrophysiological recording techniques. By combining advantages across different recording platforms, namely depth estimation based on silicon probes and maximal spatial recording coverage with tetrodes, the accessibility of superficial interneurons has improved greatly. The depth estimation tool (**Chapter 2**) has allowed me to study large quantities of superficial interneurons in isolation as well as in combination with co-recorded neurons and has revealed a spatial and temporal structure in inhibitory activity and interneuron groups in dorsal CA1 (**Chapters 3** and **4**). Furthermore, I was able to refine known temporal structures by illuminating the cycle-to-cycle and ripple-to-ripple differences as well as state-dependent changes (**Chapters 4** and **5**), and reveal cross-layer coactivity structures in the CA1 circuitry (**Chapter 6**). Finally, these analyses uncovered a more granular structure across the superficial layers of dorsal CA1, and collectively suggest that stratum lacunosum is an independent electrophysiological domain, featuring distinct network and neuronal signatures (**Chapter 7**). Together, this work underscores the heterogeneity of superficial interneurons along the radial axis of dorsal CA1 and opens new avenues to hippocampal interneurons in a more refined context.

Overall, the work in this Thesis emphasizes the heterogeneity of CA1 interneurons and the intricacies of the network they live in, despite often referred to as (anatomically) simple compared to the neocortex. Hopefully, the findings presented here will inspire new questions and more elaborate research on superficial interneurons, and together push the frontiers of our knowledge forward to, ultimately, unravel their function and implications in health and brain diseases.

References

Abad Pérez P, Garcia Hernandez R, Gallardo A, Picco M, Machold R, Brotons-Mas J, Rudy B, Buzsáki G, Valero M (2024) Automatic Classification of the Hippocampal Neuronal Diversity from Large-Scale Extracellular Recordings. Federation of European Neuroscience Societies Forum; 25-29 June, 2024; Vienna, Austria

Acsády L, Görcs TJ, Freund TF (1996) Different populations of vasoactive intestinal polypeptide-immunoreactive interneurons are specialized to control pyramidal cells or interneurons in the hippocampus. Neuroscience 73:317–334.

Aime M, Calcini N, Borsa M, Campelo T, Rusterholz T, Sattin A, Fellin T, Adamantidis A (2022) Paradoxical somatodendritic decoupling supports cortical plasticity during REM sleep. Science 376:724–730.

Allen BD, Singer AC, Boyden ES (2015) Principles of designing interpretable optogenetic behavior experiments. Learn Mem 22:232–238.

Altimus CM, Marlin BJ, Charalambakis NE, Colón-Rodríguez A, Glover EJ, Izbicki P, Johnson A, Lourenco MV, Makinson RA, McQuail J, Obeso I, Padilla-Coreano N, Wells MF (2020) The Next 50 Years of Neuroscience. J Neurosci 40:101–106.

Amaral DG, Dolorfo C, Alvarez-Royo P (1991) Organization of CA1 projections to the subiculum: A PHA-L analysis in the rat. Hippocampus 1:415–435.

Anastasiades PG, Collins DP, Carter AG (2021) Mediodorsal and Ventromedial Thalamus Engage Distinct L1 Circuits in the Prefrontal Cortex. Neuron 109:314-330.e4.

Armstrong C, Soltesz I (2012) Basket cell dichotomy in microcircuit function. The Journal of Physiology 590:683–694.

Ascoli GA et al. (2008) Petilla terminology: nomenclature of features of GABAergic interneurons of the cerebral cortex. Nature Reviews Neuroscience 9:557–568.

Aznavour N, Mechawar N, Descarries L (2002) Comparative analysis of cholinergic innervation in the dorsal hippocampus of adult mouse and rat: A quantitative immunocytochemical study. Hippocampus 12:206–217.

Barthó P, Hirase H, Monconduit L, Zugaro M, Harris KD, Buzsáki G (2004) Characterization of Neocortical Principal Cells and Interneurons by Network Interactions and Extracellular Features. Journal of Neurophysiology 92:600–608.

Bartos M, Vida I, Jonas P (2007) Synaptic mechanisms of synchronized gamma oscillations in inhibitory interneuron networks. Nat Rev Neurosci 8:45–56.

Basu J, Srinivas KV, Cheung SK, Taniguchi H, Huang ZJ, Siegelbaum SA (2013) A Cortico-Hippocampal Learning Rule Shapes Inhibitory Microcircuit Activity to Enhance Hippocampal Information Flow. Neuron 79:1208–1221.

Basu J, Zaremba JD, Cheung SK, Hitti FL, Zemelman BV, Losonczy A, Siegelbaum SA (2016) Gating of hippocampal activity, plasticity, and memory by entorhinal cortex long-range inhibition. Science 351:aaa5694.

Bell KA, Delong R, Goswamee P, McQuiston AR (2021) The Entorhinal Cortical Alvear Pathway Differentially Excites Pyramidal Cells and Interneuron Subtypes in Hippocampal CA1. Cerebral Cortex 31:2382–2401.

Bertrand S, Lacaille J (2001) Unitary synaptic currents between lacunosum-moleculare interneurones and pyramidal cells in rat hippocampus. The Journal of Physiology 532:369–384.

Bezaire MJ, Soltesz I (2013) Quantitative assessment of CA1 local circuits: Knowledge base for interneuron-pyramidal cell connectivity: Quantitative Assessment Of Ca1 Local Circuits. Hippocampus 23:751–785.

Bilash OM, Chavlis S, Johnson CD, Poirazi P, Basu J (2023) Lateral entorhinal cortex inputs modulate hippocampal dendritic excitability by recruiting a local disinhibitory microcircuit. Cell Reports 42:111962.
Bittner KC, Grienberger C, Vaidya SP, Milstein AD, Macklin JJ, Suh J, Tonegawa S, Magee JC (2015) Conjunctive input processing drives feature selectivity in hippocampal CA1 neurons. Nat Neurosci 18:1133–1142.
Bloss EB, Cembrowski MS, Karsh B, Colonell J, Fetter RD, Spruston N (2016) Structured Dendritic Inhibition Supports Branch-Selective Integration in CA1 Pyramidal Cells. Neuron 89:1016–1030.
Booker SA, Althof D, Gross A, Loreth D, Müller J, Unger A, Fakler B, Varro A, Watanabe M, Gassmann M, Bettler B, Shigemoto R, Vida I, Kulik Á (2016) KCTD12 Auxiliary Proteins Modulate Kinetics of GABA B Receptor-Mediated Inhibition in Cholecystokinin-Containing Interneurons. Cereb Cortex:bhw090.
Booker SA, Vida I (2018) Morphological diversity and connectivity of hippocampal interneurons. Cell Tissue Res 373:619–641.
Bowery NG, Smart TG (2006) GABA and glycine as neurotransmitters: a brief history. British J Pharmacology 147
Bragin A, Jando G, Nadasdy Z, Hetke J, Wise K, Buzsaki G (1995) Gamma (40-100 Hz) oscillation in the hippocampus of the behaving rat. J Neurosci 15:47–60.
Bugeon S, Duffield J, Dipoppa M, Ritoux A, Prankerd I, Nicoloutsopoulos D, Orme D, Shinn M, Peng H, Forrest H, Viduolyte A, Reddy CB, Isogai Y, Carandini M, Harris KD (2022) A transcriptomic axis predicts state modulation of cortical interneurons. Nature 607:330–338.
Buhler AV, Dunwiddie TV (2002) α7 Nicotinic Acetylcholine Receptors on GABAergic Interneurons Evoke Dendritic and Somatic Inhibition of Hippocampal Neurons. Journal of Neurophysiology 87:548–557.
Bulovaite E, Qiu Z, Kratschke M, Zgraj A, Fricker DG, Tuck EJ, Gokhale R, Koniaris B, Jami SA, Merino-Serrais P, Husi E, Mendive-Tapia L, Vendrell M, O'Dell TJ, DeFelipe J, Komiyama NH, Holtmaat A, Fransén E, Grant SGN (2022) A brain atlas of synapse protein lifetime across the mouse lifespan. Neuron 110:4057-4073.e8.
Buzsáki G (1984) Feed-forward inhibition in the hippocampal formation. Progress in Neurobiology 22:131–153.
Buzsáki G (1986) Hippocampal sharp waves: Their origin and significance. Brain Research 398:242–252.
Buzsáki G (2002) Theta Oscillations in the Hippocampus. Neuron 33:325–340.
Buzsáki G (2015) Hippocampal sharp wave-ripple: A cognitive biomarker for episodic memory and planning. Hippocampus 25:1073–1188.
Buzsáki G, Anastassiou CA, Koch C (2012) The origin of extracellular fields and currents — EEG, ECoG, LFP and spikes. Nat Rev Neurosci 13:407–420.
Buzsáki G, Czopf J, Kondákor I, Kellényi L (1986) Laminar distribution of hippocampal rhythmic slow activity (RSA) in the behaving rat: Current-source density analysis, effects of urethane and atropine. Brain Research 365:125–137.
Buzsáki G, Wang X-J (2012) Mechanisms of Gamma Oscillations. Annu Rev Neurosci 35:203–225.
Campagnola L et al. (2022) Local connectivity and synaptic dynamics in mouse and human neocortex. Science 375:eabj5861.
Capogna M (2011) Neurogliaform cells and other interneurons of stratum lacunosum-moleculare gate entorhinal-hippocampal dialogue: GABA A,slow in the hippocampus. The Journal of Physiology 589:1875–1883.
Cardin JA (2019) Functional flexibility in cortical circuits. Current Opinion in Neurobiology 58:175–180.
Cardin JA, Carlén M, Meletis K, Knoblich U, Zhang F, Deisseroth K, Tsai L-H, Moore CI (2009) Driving fast-spiking cells induces gamma rhythm and controls sensory responses. Nature 459:663–667.
Carr MF, Frank LM (2012) A single microcircuit with multiple functions: state dependent information processing in the hippocampus. Current Opinion in Neurobiology 22:704–708.
Chamberland S, Grant G, Machold R, Nebet ER, Tian G, Stich J, Hanani M, Kullander K, Tsien RW (2024) Functional specialization of hippocampal somatostatin-expressing interneurons. Proc Natl Acad Sci USA 121:e2306382121.
Chamberland S, Nebet ER, Valero M, Hanani M, Egger R, Larsen SB, Eyring KW, Buzsáki G, Tsien RW (2023) Brief synaptic inhibition persistently interrupts firing of fast-spiking interneurons. Neuron:S089662732300065X.
Chamberland S, Topolnik L (2012) Inhibitory control of hippocampal inhibitory neurons. Front Neurosci 6

Chapman CA, Lacaille J-C (1999a) Intrinsic Theta-Frequency Membrane Potential Oscillations in Hippocampal CA1 Interneurons of Stratum Lacunosum-Moleculare. Journal of Neurophysiology 81:1296–1307.
Chapman CA, Lacaille J-C (1999b) Cholinergic Induction of Theta-Frequency Oscillations in Hippocampal Inhibitory Interneurons and Pacing of Pyramidal Cell Firing. J Neurosci 19:8637–8645.
Chen G, Zhang Y, Li X, Zhao X, Ye Q, Lin Y, Tao HW, Rasch MJ, Zhang X (2017) Distinct Inhibitory Circuits Orchestrate Cortical beta and gamma Band Oscillations. Neuron 96:1403-1418.e6.
Cohen JD, Bolstad M, Lee AK (2017) Experience-dependent shaping of hippocampal CA1 intracellular activity in novel and familiar environments. eLife 6:e23040.
Colgin LL (2015) Do slow and fast gamma rhythms correspond to distinct functional states in the hippocampal network? Brain Research 1621:309–315.
Colgin LL (2016) Rhythms of the hippocampal network. Nat Rev Neurosci 17:239–249.
Colgin LL, Denninger T, Fyhn M, Hafting T, Bonnevie T, Jensen O, Moser M-B, Moser EI (2009) Frequency of gamma oscillations routes flow of information in the hippocampus. Nature 462:353–357.
Csicsvari J, Hirase H, Czurko A, Buzsáki G (1998) Reliability and State Dependence of Pyramidal Cell–Interneuron Synapses in the Hippocampus. Neuron 21:179–189.
Csicsvari J, Hirase H, Czurkó A, Mamiya A, Buzsáki G (1999) Oscillatory Coupling of Hippocampal Pyramidal Cells and Interneurons in the Behaving Rat. J Neurosci 19:274–287.
David A, Pierre L (2006) Hippocampal Neuroanatomy. In: The Hippocampus Book (Andersen P, Morris R, Amaral D, Bliss T, O'Keefe J, eds), pp 0. Oxford University Press.
Deller T, Adelmann G, Nitsch R, Frotscher M (1996) The alvear pathway of the rat hippocampus. Cell and Tissue Research 286:293–303.
Doiron B, Litwin-Kumar A, Rosenbaum R, Ocker GK, Josić K (2016) The mechanics of state-dependent neural correlations. Nat Neurosci 19:383–393.
Dolleman-Van Der Weel MJ, Lopes Da Silva FH, Witter MP (1997) Nucleus Reuniens Thalami Modulates Activity in Hippocampal Field CA1 through Excitatory and Inhibitory Mechanisms. J Neurosci 17:5640–5650.
Dolleman-van der Weel MJ, Lopes da Silva FH, Witter MP (2017) Interaction of nucleus reuniens and entorhinal cortex projections in hippocampal field CA1 of the rat. Brain Struct Funct 222:2421–2438.
Dudok B, Klein PM, Hwaun E, Lee BR, Yao Z, Fong O, Bowler JC, Terada S, Sparks FT, Szabo GG, Farrell JS, Berg J, Daigle TL, Tasic B, Dimidschstein J, Fishell G, Losonczy A, Zeng H, Soltesz I (2021a) Alternating sources of perisomatic inhibition during behavior. Neuron 109:997-1012.e9.
Dudok B, Szoboszlay M, Paul A, Klein PM, Liao Z, Hwaun E, Szabo GG, Geiller T, Vancura B, Wang B-S, McKenzie S, Homidan J, Klaver LMF, English DF, Huang ZJ, Buzsáki G, Losonczy A, Soltesz I (2021b) Recruitment and inhibitory action of hippocampal axo-axonic cells during behavior. Neuron 109:3838-3850.e8.
Dupret D, O'Neill J, Csicsvari J (2013) Dynamic Reconfiguration of Hippocampal Interneuron Circuits during Spatial Learning. Neuron 78:166–180.
Elfant D, Pál BZ, Emptage N, Capogna M (2007) Specific inhibitory synapses shift the balance from feedforward to feedback inhibition of hippocampal CA1 pyramidal cells: Synaptic inhibition between hippocampal interneurons. European Journal of Neuroscience 27:104–113.
English DF, McKenzie S, Evans T, Kim K, Yoon E, Buzsáki G (2017) Pyramidal Cell-Interneuron Circuit Architecture and Dynamics in Hippocampal Networks. Neuron 96:505-520.e7.
Evangelista R, Cano G, Cooper C, Schmitz D, Maier N, Kempter R (2020) Generation of Sharp Wave-Ripple Events by Disinhibition. J Neurosci 40:7811–7836.
Fan LZ, Kim DK, Jennings JH, Tian H, Wang PY, Ramakrishnan C, Randles S, Sun Y, Thadhani E, Kim YS, Quirin S, Giocomo L, Cohen AE, Deisseroth K (2023) All-optical physiology resolves a synaptic basis for behavioral timescale plasticity. Cell 186:543-559.e19.
Fernandez-Ruiz A, Sirota A, Lopes-dos-Santos V, Dupret D (2023) Over and above frequency: Gamma oscillations as units of neural circuit operations. Neuron 111:936–953.
Ferrante M, Migliore M, Ascoli GA (2009) Feed-forward inhibition as a buffer of the neuronal input-output relation. Proc Natl Acad Sci USA 106:18004–18009.
Fishell G, Kepecs A (2020) Interneuron Types as Attractors and Controllers. Annu Rev Neurosci 43:1–30.
Florey E (1954) An Inhibitory and an Excitatory Factor of Mammalian Central Nervous System, and Their Action on A Single Sensory Neuron. Archives Internationales de Physiologie 62:33–53.
Földy C, Darmanis S, Aoto J, Malenka RC, Quake SR, Südhof TC (2016) Single-cell RNAseq reveals cell adhesion molecule profiles in electrophysiologically defined neurons. Proc Natl Acad Sci USA 113

Förster E, Zhao S, Frotscher M (2006) Laminating the hippocampus. Nat Rev Neurosci 7:259–268.
Francavilla R, Villette V, Luo X, Chamberland S, Muñoz-Pino E, Camiré O, Wagner K, Kis V, Somogyi P, Topolnik L (2018) Connectivity and network state-dependent recruitment of long-range VIP-GABAergic neurons in the mouse hippocampus. Nat Commun 9:5043.
Freund T f., Buzsáki G (1996) Interneurons of the hippocampus. Hippocampus 6:347–470.
Fuentealba P, Begum R, Capogna M, Jinno S, Márton LF, Csicsvari J, Thomson A, Somogyi P, Klausberger T (2008) Ivy Cells: A Population of Nitric-Oxide-Producing, Slow-Spiking GABAergic Neurons and Their Involvement in Hippocampal Network Activity. Neuron 57:917–929.
Fuentealba P, Klausberger T, Karayannis T, Suen WY, Huck J, Tomioka R, Rockland K, Capogna M, Studer M, Morales M, Somogyi P (2010) Expression of COUP-TFII Nuclear Receptor in Restricted GABAergic Neuronal Populations in the Adult Rat Hippocampus. Journal of Neuroscience 30:1595–1609.
Furutachi S, Franklin AD, Aldea AM, Mrsic-Flogel TD, Hofer SB (2024) Cooperative thalamocortical circuit mechanism for sensory prediction errors. Nature 633:398–406.
Gan J, Weng S, Pernía-Andrade AJ, Csicsvari J, Jonas P (2017) Phase-Locked Inhibition, but Not Excitation, Underlies Hippocampal Ripple Oscillations in Awake Mice In Vivo. Neuron 93:308–314.
Gangarossa G, Longueville S, De Bundel D, Perroy J, Hervé D, Girault J, Valjent E (2012) Characterization of dopamine D1 and D2 receptor-expressing neurons in the mouse hippocampus. Hippocampus 22:2199–2207.
Geiller T, Sadeh S, Rolotti SV, Blockus H, Vancura B, Negrean A, Murray AJ, Rózsa B, Polleux F, Clopath C, Losonczy A (2022) Local circuit amplification of spatial selectivity in the hippocampus. Nature 601:105–109.
Geiller T, Vancura B, Terada S, Troullinou E, Chavlis S, Tsagkatakis G, Tsakalides P, Ócsai K, Poirazi P, Rózsa BJ, Losonczy A (2020) Large-Scale 3D Two-Photon Imaging of Molecularly Identified CA1 Interneuron Dynamics in Behaving Mice. Neuron 108:968-983.e9.
Gillespie AK, Astudillo Maya DA, Denovellis EL, Liu DF, Kastner DB, Coulter ME, Roumis DK, Eden UT, Frank LM (2021) Hippocampal replay reflects specific past experiences rather than a plan for subsequent choice. Neuron 109:3149-3163.e6.
Grienberger C, Milstein AD, Bittner KC, Romani S, Magee JC (2017) Inhibitory suppression of heterogeneously tuned excitation enhances spatial coding in CA1 place cells. Nat Neurosci 20:417–426.
Guardamagna M, Eichler R, Pedrosa R, Aarts A, Meyer AF, Battaglia FP (2022) The Hybrid Drive: a chronic implant device combining tetrode arrays with silicon probes for layer-resolved ensemble electrophysiology in freely moving mice. J Neural Eng 19:036030.
Guet-McCreight A, Skinner FK, Topolnik L (2020) Common Principles in Functional Organization of VIP/Calretinin Cell-Driven Disinhibitory Circuits Across Cortical Areas. Front Neural Circuits 14:32.
Gulyás AI, Hájos N, Freund TF (1996) Interneurons Containing Calretinin Are Specialized to Control Other Interneurons in the Rat Hippocampus. J Neurosci 16:3397–3411.
Gulyás AI, Megı´as M, Emri Z, Freund TF (1999) Total Number and Ratio of Excitatory and Inhibitory Synapses Converging onto Single Interneurons of Different Types in the CA1 Area of the Rat Hippocampus. J Neurosci 19:10082–10097.
Gunn B, Pruess B, Gall C, Lynch G (2023) Input / Output Relationships for the Primary Hippocampal Circuit.
Guo J, Oliveros HC, Oh SJ, Liang B, Li Y, Kavalali ET, Lin D-T, Xu W (2021) Stratum Lacunosum-moleculare Interneurons of the Hippocampus Coordinate Memory Encoding and Retrieval. Neuroscience.
Hájos N, Mody I (1997) Synaptic Communication among Hippocampal Interneurons: Properties of Spontaneous IPSCs in Morphologically Identified Cells. J Neurosci 17:8427–8442.
Harris KD, Hochgerner H, Skene NG, Magno L, Katona L, Bengtsson Gonzales C, Somogyi P, Kessaris N, Linnarsson S, Hjerling-Leffler J (2018) Classes and continua of hippocampal CA1 inhibitory neurons revealed by single-cell transcriptomics Jonas P, ed. PLoS Biol 16:e2006387.
Harvey RE, Robinson HL, Liu C, Oliva A, Fernandez-Ruiz A (2023) Hippocampo-cortical circuits for selective memory encoding, routing, and replay. Neuron:S0896627323003008.
Hasselmo ME, Bodelón C, Wyble BP (2002) A Proposed Function for Hippocampal Theta Rhythm: Separate Phases of Encoding and Retrieval Enhance Reversal of Prior Learning. Neural Computation 14:793–817.
Henze DA, Borhegyi Z, Csicsvari J, Mamiya A, Harris KD, Buzsáki G (2000) Intracellular Features Predicted by Extracellular Recordings in the Hippocampus In Vivo. Journal of Neurophysiology 84:390–400.
Hijazi S, Smit AB, Van Kesteren RE (2023) Fast-spiking parvalbumin-positive interneurons in brain

physiology and Alzheimer's disease. Mol Psychiatry 28:4954–4967.
Hill DN, Mehta SB, Kleinfeld D (2011) Quality Metrics to Accompany Spike Sorting of Extracellular Signals. Journal of Neuroscience 31:8699–8705.
Hippenmeyer S, Vrieseling E, Sigrist M, Portmann T, Laengle C, Ladle DR, Arber S (2005) A Developmental Switch in the Response of DRG Neurons to ETS Transcription Factor Signaling Sanes JR, ed. PLoS Biol 3:e159.
Hodgkin A, Huxley A (1990) A quantitative description of membrane current and its application to conduction and excitation in nerve. Bulletin of Mathematical Biology 52:25–71.
Holt GR, Softky WR, Koch C, Douglas RJ (1996) Comparison of discharge variability in vitro and in vivo in cat visual cortex neurons. Journal of Neurophysiology 75:1806–1814.
Hooks BM (2018) Dual-Channel Photostimulation for Independent Excitation of Two Populations. CP Neuroscience 85:e52.
Hu H, Gan J, Jonas P (2014) Fast-spiking, parvalbumin + GABAergic interneurons: From cellular design to microcircuit function. Science 345:1255263.
Huang Y-C, Chen H-C, Lin Y-T, Lin S-T, Zheng Q, Abdelfattah AS, Lavis LD, Schreiter ER, Lin B-J, Chen T-W (2024) Dynamic assemblies of parvalbumin interneurons in brain oscillations. Neuron 112:2600-2613.e5.
Jadhav SP, Kemere C, German PW, Frank LM (2012) Awake Hippocampal Sharp-Wave Ripples Support Spatial Memory. Science 336:1454–1458.
Jadi M, Polsky A, Schiller J, Mel BW (2012) Location-Dependent Effects of Inhibition on Local Spiking in Pyramidal Neuron Dendrites Gutkin BS, ed. PLoS Comput Biol 8:e1002550.
Jiang X, Shen S, Cadwell CR, Berens P, Sinz F, Ecker AS, Patel S, Tolias AS (2015) Principles of connectivity among morphologically defined cell types in adult neocortex. Science 350:aac9462.
Jinno S, Klausberger T, Marton LF, Dalezios Y, Roberts JDB, Fuentealba P, Bushong EA, Henze D, Buzsaki G, Somogyi P (2007) Neuronal Diversity in GABAergic Long-Range Projections from the Hippocampus. Journal of Neuroscience 27:8790–8804.
Jonas P, Buzsáki G (2007) Neural inhibition. Scholarpedia 2:3286.
Kajiwara R, Wouterlood FG, Sah A, Boekel AJ, Baks-te Bulte LTG, Witter MP (2008) Convergence of entorhinal and CA3 inputs onto pyramidal neurons and interneurons in hippocampal area CA1—An anatomical study in the rat. Hippocampus 18:266–280.
Katona L, Lapray D, Viney TJ, Oulhaj A, Borhegyi Z, Micklem BR, Klausberger T, Somogyi P (2014) Sleep and Movement Differentiates Actions of Two Types of Somatostatin-Expressing GABAergic Interneuron in Rat Hippocampus. Neuron 82:872–886.
Kepecs A, Fishell G (2014) Interneuron cell types are fit to function. Nature 505:318–326.
Kitamura T, Pignatelli M, Suh J, Kohara K, Yoshiki A, Abe K, Tonegawa S (2014) Island Cells Control Temporal Association Memory. Science 343:896–901.
Klausberger T (2005) Complementary Roles of Cholecystokinin- and Parvalbumin-Expressing GABAergic Neurons in Hippocampal Network Oscillations. Journal of Neuroscience 25:9782–9793.
Klausberger T (2009) GABAergic interneurons targeting dendrites of pyramidal cells in the CA1 area of the hippocampus. European Journal of Neuroscience 30:947–957.
Klausberger T, Magill PJ, Márton LF, Roberts JDB, Cobden PM, Buzsáki G, Somogyi P (2003) Brain-state- and cell-type-specific firing of hippocampal interneurons in vivo. Nature 421:844–848.
Klausberger T, Márton LF, Baude A, Roberts JDB, Magill PJ, Somogyi P (2004) Spike timing of dendrite-targeting bistratified cells during hippocampal network oscillations in vivo. Nat Neurosci 7:41–47.
Klausberger T, Somogyi P (2008) Neuronal Diversity and Temporal Dynamics: The Unity of Hippocampal Circuit Operations. Science 321:53–57.
Konopka G, Friedrich T, Davis-Turak J, Winden K, Oldham MC, Gao F, Chen L, Wang G-Z, Luo R, Preuss TM, Geschwind DH (2012) Human-Specific Transcriptional Networks in the Brain. Neuron 75:601–617.
Krienen FM et al. (2020) Innovations present in the primate interneuron repertoire. Nature 586:262–269.
Kriener B, Hu H, Vervaeke K (2022) Parvalbumin interneuron dendrites enhance gamma oscillations. Cell Reports 39:110948.
Kullmann DM (2011) Interneuron networks in the hippocampus. Current Opinion in Neurobiology 21:709–716.
Lacaille J, Schwartzkroin P (1988a) Stratum lacunosum-moleculare interneurons of hippocampal CA1 region. I. Intracellular response characteristics, synaptic responses, and morphology. J Neurosci 8:1400–1410.

Lacaille J, Schwartzkroin P (1988b) Stratum lacunosum-moleculare interneurons of hippocampal CA1 region. II. Intrasomatic and intradendritic recordings of local circuit synaptic interactions. J Neurosci 8:1411–1424.
Lapray D, Lasztoczi B, Lagler M, Viney TJ, Katona L, Valenti O, Hartwich K, Borhegyi Z, Somogyi P, Klausberger T (2012) Behavior-dependent specialization of identified hippocampal interneurons. Nat Neurosci 15:1265–1271.
Larkum ME, Wu J, Duverdin SA, Gidon A (2022) The Guide to Dendritic Spikes of the Mammalian Cortex In Vitro and In Vivo. Neuroscience 489:15–33.
Lasztóczi B, Klausberger T (2014) Layer-Specific GABAergic Control of Distinct Gamma Oscillations in the CA1 Hippocampus. Neuron 81:1126–1139.
Leão RN, Mikulovic S, Leão KE, Munguba H, Gezelius H, Enjin A, Patra K, Eriksson A, Loew LM, Tort ABL, Kullander K (2012) OLM interneurons differentially modulate CA3 and entorhinal inputs to hippocampal CA1 neurons. Nat Neurosci 15:1524–1530.
Lee S-H, Marchionni I, Bezaire M, Varga C, Danielson N, Lovett-Barron M, Losonczy A, Soltesz I (2014) Parvalbumin-Positive Basket Cells Differentiate among Hippocampal Pyramidal Cells. Neuron 82:1129–1144.
Levenstein D, Gornet J, Huszár R, Girardeau G, Grosmark A, Peyrache A, Senzai Y, Watson BO, Mizuseki K, Rinzel J, Buzsáki G (2021) Distinct ground state and activated state modes of firing in forebrain neurons.
Lewandowska MK, Bakkum DJ, Rompani SB, Hierlemann A (2015) Recording Large Extracellular Spikes in Microchannels along Many Axonal Sites from Individual Neurons Martinoia S, ed. PLoS ONE 10:e0118514.
Lewicki MS (1998) A review of methods for spike sorting: the detection and classification of neural action potentials. Network (Bristol) 9:R53–R78.
Li X-G, Somogyi P, Ylinen A, Buzsáki G (1994) The hippocampal CA3 network: An in vivo intracellular labeling study: THE HIPPOCAMPAL CA3 NETWORK. J Comp Neurol 339:181–208.
Liao Z, Gonzalez KC, Li DM, Yang CM, Holder D, McClain NE, Zhang G, Evans SW, Chavarha M, Simko J, Makinson CD, Lin MZ, Losonczy A, Negrean A (2024) Functional architecture of intracellular oscillations in hippocampal dendrites. Nat Commun 15:6295.
Loomba S, Straehle J, Gangadharan V, Heike N, Khalifa A, Motta A, Ju N, Sievers M, Gempt J, Meyer HS, Helmstaedter M (2022) Connectomic comparison of mouse and human cortex. Science 377:eabo0924.
Lopes-dos-Santos V, Brizee D, Dupret D (2023) Spatio-temporal organization of network activity patterns in the hippocampus. bioRxiv 2023.10.17.562689.
Lopes-dos-Santos V, van de Ven GM, Morley A, Trouche S, Campo-Urriza N, Dupret D (2018) Parsing Hippocampal Theta Oscillations by Nested Spectral Components during Spatial Exploration and Memory-Guided Behavior. Neuron 100:940-952.e7.
Lovett-Barron M, Kaifosh P, Kheirbek MA, Danielson N, Zaremba JD, Reardon TR, Turi GF, Hen R, Zemelman BV, Losonczy A (2014) Dendritic Inhibition in the Hippocampus Supports Fear Learning. Science 343:857–863.
Lovett-Barron M, Turi GF, Kaifosh P, Lee PH, Bolze F, Sun X-H, Nicoud J-F, Zemelman BV, Sternson SM, Losonczy A (2012) Regulation of neuronal input transformations by tunable dendritic inhibition. Nat Neurosci 15:423–430.
Luo X, Guet-McCreight A, Villette V, Francavilla R, Marino B, Chamberland S, Skinner FK, Topolnik L (2020) Synaptic Mechanisms Underlying the Network State-Dependent Recruitment of VIP-Expressing Interneurons in the CA1 Hippocampus. Cerebral Cortex 30:3667–3685.
Maccaferri G, Lacaille J-C (2003) Interneuron Diversity series: Hippocampal interneuron classifications – making things as simple as possible, not simpler. Trends in Neurosciences 26:564–571.
Magland J, Jun JJ, Lovero E, Morley AJ, Hurwitz CL, Buccino AP, Garcia S, Barnett AH (2020) SpikeForest, reproducible web-facing ground-truth validation of automated neural spike sorters Meister M, Calabrese RL, Meister M, eds. eLife 9:e55167.
Magloire V, Mercier MS, Kullmann DM, Pavlov I (2019) GABAergic Interneurons in Seizures: Investigating Causality With Optogenetics. Neuroscientist 25:344–358.
Magó Á, Kis N, Lükő B, Makara JK (2021) Distinct dendritic Ca2+ spike forms produce opposing input-output transformations in rat CA3 pyramidal cells. eLife 10:e74493.
Marín O (2012) Interneuron dysfunction in psychiatric disorders. Nat Rev Neurosci 13:107–120.
Markram H, Toledo-Rodriguez M, Wang Y, Gupta A, Silberberg G, Wu C (2004) Interneurons of the neocortical inhibitory system. Nat Rev Neurosci 5:793–807.

Masurkar AV, Srinivas KV, Brann DH, Warren R, Lowes DC, Siegelbaum SA (2017) Medial and Lateral Entorhinal Cortex Differentially Excite Deep versus Superficial CA1 Pyramidal Neurons. Cell Reports 18:148–160.
Mátyás F, Freund TF, Gulyás AI (2004) Convergence of excitatory and inhibitory inputs onto CCK-containing basket cells in the CA1 area of the rat hippocampus. Eur J of Neuroscience 19:1243–1256.
McHugh SB, Lopes-dos-Santos V, Castelli M, Gava GP, Thompson SE, Tam SKE, Hartwich K, Perry B, Toth R, Denison T, Sharott A, Dupret D (2024) Offline hippocampal reactivation during dentate spikes supports flexible memory. Neuron:S0896627324006469.
McKenzie S (2018) Inhibition shapes the organization of hippocampal representations. Hippocampus 28:659–671.
McKenzie S, Huszár R, English DF, Kim K, Christensen F, Yoon E, Buzsáki G (2021) Preexisting hippocampal network dynamics constrain optogenetically induced place fields. Neuron 109:1040-1054.e7.
Melzer S, Michael M, Caputi A, Eliava M, Fuchs EC, Whittington MA, Monyer H (2012) Long-Range–Projecting GABAergic Neurons Modulate Inhibition in Hippocampus and Entorhinal Cortex. Science 335:1506–1510.
Merchan MA, DeFelipe J, de Castro F (2016) Cajal and de Castro's Neurohistological Methods. Oxford University Press.
Milstein AD, Bloss EB, Apostolides PF, Vaidya SP, Dilly GA, Zemelman BV, Magee JC (2015) Inhibitory Gating of Input Comparison in the CA1 Microcircuit. Neuron 87:1274–1289.
Mizuseki K, Buzsáki G (2013) Preconfigured, Skewed Distribution of Firing Rates in the Hippocampus and Entorhinal Cortex. Cell Reports 4:1010–1021.
Mizuseki K, Miyawaki H (2017) Hippocampal information processing across sleep/wake cycles. Neuroscience Research 118:30–47.
Mizuseki K, Sirota A, Pastalkova E, Buzsáki G (2009) Theta Oscillations Provide Temporal Windows for Local Circuit Computation in the Entorhinal-Hippocampal Loop. Neuron 64:267–280.
Moore JJ, Ravassard PM, Ho D, Acharya L, Kees AL, Vuong C, Mehta MR (2017) Dynamics of cortical dendritic membrane potential and spikes in freely behaving rats. Science 355:eaaj1497.
Morrison DJ, Rashid AJ, Yiu AP, Yan C, Frankland PW, Josselyn SA (2016) Parvalbumin interneurons constrain the size of the lateral amygdala engram. Neurobiology of Learning and Memory 135:91–99.
Muñoz W, Tremblay R, Levenstein D, Rudy B (2017) Layer-specific modulation of neocortical dendritic inhibition during active wakefulness. Science 355:954–959.
Noguchi A, Huszár R, Morikawa S, Buzsáki G, Ikegaya Y (2022) Inhibition allocates spikes during hippocampal ripples. Nat Commun 13:1280.
Nuñez A, Buño W (2021) The Theta Rhythm of the Hippocampus: From Neuronal and Circuit Mechanisms to Behavior. Front Cell Neurosci 15:649262.
Pachitariu M, Sridhar S, Pennington J, Stringer C (2024) Spike sorting with Kilosort4. Nat Methods 21:914–921.
Pachitariu M, Steinmetz NA, Kadir SN, Carandini M, Harris KD (2016) Fast and accurate spike sorting of high-channel count probes with KiloSort. In: Advances in Neural Information Processing Systems (Lee D, Sugiyama M, Luxburg U, Guyon I, Garnett R, eds). Curran Associates, Inc.
Palacios-Filardo J, Udakis M, Brown GA, Tehan BG, Congreve MS, Nathan PJ, Brown AJH, Mellor JR (2021) Acetylcholine prioritises direct synaptic inputs from entorhinal cortex to CA1 by differential modulation of feedforward inhibitory circuits. Nat Commun 12:5475.
Palmer L, Murayama M, Larkum M (2012a) Inhibitory Regulation of Dendritic Activity in vivo. Front Neural Circuits 6
Palmer LM, Schulz JM, Murphy SC, Ledergerber D, Murayama M, Larkum ME (2012b) The Cellular Basis of GABA B -Mediated Interhemispheric Inhibition. Science 335:989–993.
Pawelzik H, Hughes DI, Thomson AM (2002) Physiological and morphological diversity of immunocytochemically defined parvalbumin- and cholecystokinin-positive interneurones in CA1 of the adult rat hippocampus. J Comp Neurol 443:346–367.
Paxinos G, Franklin K (2019) Paxinos and Franklin's the Mouse Brain in Stereotaxic Coordinates, 5. Edition. London San Diego Cambridge; MA Kidlington, Oxford: Elsevier, Academic Press.
Pelkey KA, Chittajallu R, Craig MT, Tricoire L, Wester JC, McBain CJ (2017) Hippocampal GABAergic Inhibitory Interneurons. Physiological Reviews 97:1619–1747.
Petersen PC, Siegle JH, Steinmetz NA, Mahallati S, Buzsáki G (2021) CellExplorer: A framework for visualizing and characterizing single neurons. Neuron 109:3594-3608.e2.
Pinson A, Xing L, Namba T, Kalebic N, Peters J, Oegema CE, Traikov S, Reppe K, Riesenberg S, Maricic

T, Derihaci R, Wimberger P, Pääbo S, Huttner WB (2022) Human TKTL1 implies greater neurogenesis in frontal neocortex of modern humans than Neanderthals. Science 377:eabl6422.
Pokorný J, Yamamoto T (1981) Postnatal ontogenesis of hippocampal CA1 area in rats. II. Development of ultrastructure in stratum lacunosum and moleculare. Brain Research Bulletin 7:121–130.
Price CJ (2005) Neurogliaform Neurons Form a Novel Inhibitory Network in the Hippocampal CA1 Area. Journal of Neuroscience 25:6775–6786.
Ramón y Cajal 1899-1904 Santiago (1904) Textura del sistema nervioso del hombre y de los vertebrados : estudios sobre el plan estructural y composición histológica de los centros nerviosos adicionados de consideraciones fisiológicas fundadas en los nuevos descubrimientos. Volumen III.
Rangel Guerrero DK, Balueva K, Barayeu U, Baracskay P, Gridchyn I, Nardin M, Roth CN, Wulff P, Csicsvari J (2024) Hippocampal cholecystokinin-expressing interneurons regulate temporal coding and contextual learning. Neuron:S0896627324001971.
Raudales R, Kim G, Kelly SM, Hatfield J, Guan W, Zhao S, Paul A, Qian Y, Li B, Huang ZJ (2024) Specific and comprehensive genetic targeting reveals brain-wide distribution and synaptic input patterns of GABAergic axo-axonic interneurons. eLife 13:RP93481.
Righes Marafiga J, Vendramin Pasquetti M, Calcagnotto ME (2021) GABAergic interneurons in epilepsy: More than a simple change in inhibition. Epilepsy & Behavior 121:106935.
Roberts E, Frankel S (1950) γ-aminobutyric acid in brain: its formation from glutamic acid. Journal of Biological Chemistry 187:55–63.
Roumis DK, Frank LM (2015) Hippocampal sharp-wave ripples in waking and sleeping states. Current Opinion in Neurobiology 35:6–12.
Roux L, Buzsáki G (2015) Tasks for inhibitory interneurons in intact brain circuits. Neuropharmacology 88:10–23.
Roux L, Stark E, Sjulson L, Buzsáki G (2014) In vivo optogenetic identification and manipulation of GABAergic interneuron subtypes. Current Opinion in Neurobiology 26:88–95.
Roy DS, Kitamura T, Okuyama T, Ogawa SK, Sun C, Obata Y, Yoshiki A, Tonegawa S (2017) Distinct Neural Circuits for the Formation and Retrieval of Episodic Memories. Cell 170:1000-1012.e19.
Royer S, Zemelman BV, Losonczy A, Kim J, Chance F, Magee JC, Buzsáki G (2012) Control of timing, rate and bursts of hippocampal place cells by dendritic and somatic inhibition. Nat Neurosci 15:769–775.
Ruden JB, Dugan LL, Konradi C (2021) Parvalbumin interneuron vulnerability and brain disorders. Neuropsychopharmacol 46:279–287.
Sakalar E, Klausberger T, Lasztóczi B (2022) Neurogliaform cells dynamically decouple neuronal synchrony between brain areas. Science 377:324–328.
Scala F, Kobak D, Bernabucci M, Bernaerts Y, Cadwell CR, Castro JR, Hartmanis L, Jiang X, Laturnus S, Miranda E, Mulherkar S, Tan ZH, Yao Z, Zeng H, Sandberg R, Berens P, Tolias AS (2021) Phenotypic variation of transcriptomic cell types in mouse motor cortex. Nature 598:144–150.
Schaffer K (1892) Beitrag zur Histologie der Ammonshornformation. Archiv für mikroskopische Anatomie 39:611–632.
Schomburg EW, Fernández-Ruiz A, Mizuseki K, Berényi A, Anastassiou CA, Koch C, Buzsáki G (2014) Theta Phase Segregation of Input-Specific Gamma Patterns in Entorhinal-Hippocampal Networks. Neuron 84:470–485.
Sebastian ER, Esparza J, M. De La Prida L (2024) Quantifying the distribution of feature values over data represented in arbitrary dimensional spaces Curto C, ed. PLoS Comput Biol 20:e1011768.
Senzai Y, Fernandez-Ruiz A, Buzsáki G (2019) Layer-Specific Physiological Features and Interlaminar Interactions in the Primary Visual Cortex of the Mouse. Neuron 101:500-513.e5.
Sharif F, Tayebi B, Buzsáki G, Royer S, Fernandez-Ruiz A (2021) Subcircuits of Deep and Superficial CA1 Place Cells Support Efficient Spatial Coding across Heterogeneous Environments. Neuron 109:363-376.e6.
Shin JN, Doron G, Larkum ME (2021) Memories off the top of your head. Science 374:538–539.
Siwani S, França ASC, Mikulovic S, Reis A, Hilscher MM, Edwards SJ, Leão RN, Tort ABL, Kullander K (2018) OLMα2 Cells Bidirectionally Modulate Learning. Neuron 99:404-412.e3.
Smart TG, Stephenson FA (2019) A half century of γ-aminobutyric acid. Brain and Neuroscience Advances 3:239821281985824.
Sohal VS, Zhang F, Yizhar O, Deisseroth K (2009) Parvalbumin neurons and gamma rhythms enhance cortical circuit performance. Nature 459:698–702.
Soltesz I, Losonczy A (2018) CA1 pyramidal cell diversity enabling parallel information processing in the hippocampus. Nat Neurosci 21:484–493.

Someck S, Levi A, Sloin HE, Spivak L, Gattegno R, Stark E (2023) Positive and biphasic extracellular waveforms correspond to return currents and axonal spikes. Neuroscience.
Somogyi J, Baude A, Omori Y, Shimizu H, Mestikawy SE, Fukaya M, Shigemoto R, Watanabe M, Somogyi P (2004) GABAergic basket cells expressing cholecystokinin contain vesicular glutamate transporter type 3 (VGLUT3) in their synaptic terminals in hippocampus and isocortex of the rat. Eur J Neurosci 19:552–569.
Somogyi P, Klausberger T (2005) Defined types of cortical interneurone structure space and spike timing in the hippocampus: Interneurones structure space and spike timing in the hippocampus. The Journal of Physiology 562:9–26.
Somogyi P, Nunzi MG, Gorio A, Smith AD (1983) A new type of specific interneuron in the monkey hippocampus forming synapses exclusively with the axon initial segments of pyramidal cells. Brain Research 259:137–142.
Spruston N (2008) Pyramidal neurons: dendritic structure and synaptic integration. Nat Rev Neurosci 9:206–221.
Stark E, Eichler R, Roux L, Fujisawa S, Rotstein HG, Buzsáki G (2013) Inhibition-Induced Theta Resonance in Cortical Circuits. Neuron 80:1263–1276.
Stedehouder J, Brizee D, Shpak G, Kushner SA (2018) Activity-Dependent Myelination of Parvalbumin Interneurons Mediated by Axonal Morphological Plasticity. J Neurosci 38:3631–3642.
Stedehouder J, Kushner SA (2017) Myelination of parvalbumin interneurons: a parsimonious locus of pathophysiological convergence in schizophrenia. Mol Psychiatry 22:4–12.
Steinmetz NA, Koch C, Harris KD, Carandini M (2018) Challenges and opportunities for large-scale electrophysiology with Neuropixels probes. Current Opinion in Neurobiology 50:92–100.
Storm-Mathisen J (1970) Quantitative histochemistry of acetylcholinesterase in rat hippocampal region correlated to histochemical staining. Journal of Neurochemistry 17:739–750.
Strange BA, Witter MP, Lein ES, Moser EI (2014) Functional organization of the hippocampal longitudinal axis. Nat Rev Neurosci 15:655–669.
Stuart GJ, Spruston N (2015) Dendritic integration: 60 years of progress. Nat Neurosci 18:1713–1721.
Sun SH, Almasi A, Yunzab M, Zehra S, Hicks DG, Kameneva T, Ibbotson MR, Meffin H (2021) Analysis of extracellular spike waveforms and associated receptive fields of neurons in cat primary visual cortex. J Physiol 599:2211–2238.
Szabo GG, Farrell JS, Dudok B, Hou W-H, Ortiz AL, Varga C, Moolchand P, Gulsever CI, Gschwind T, Dimidschstein J, Capogna M, Soltesz I (2022) Ripple-selective GABAergic projection cells in the hippocampus. Neuron 110:1959-1977.e9.
Szirmai I, Buzsáki G, Kamondi A (2012) 120 years of hippocampal Schaffer collaterals. Hippocampus 22:1508–1516.
Takács VT, Klausberger T, Somogyi P, Freund TF, Gulyás AI (2012) Extrinsic and local glutamatergic inputs of the rat hippocampal CA1 area differentially innervate pyramidal cells and interneurons. Hippocampus 22:1379–1391.
Tamboli S, Singh S, Topolnik D, El Amine Barkat M, Radhakrishnan R, Guet-McCreight A, Topolnik L (2024) Mouse hippocampal CA1 VIP interneurons detect novelty in the environment and support recognition memory. Cell Reports 43:114115.
Taniguchi H, He M, Wu P, Kim S, Paik R, Sugino K, Kvitsani D, Fu Y, Lu J, Lin Y, Miyoshi G, Shima Y, Fishell G, Nelson SB, Huang ZJ (2011) A Resource of Cre Driver Lines for Genetic Targeting of GABAergic Neurons in Cerebral Cortex. Neuron 71:995–1013.
Teixeira CM, Rosen ZB, Suri D, Sun Q, Hersh M, Sargin D, Dincheva I, Morgan AA, Spivack S, Krok AC, Hirschfeld-Stoler T, Lambe EK, Siegelbaum SA, Ansorge MS (2018) Hippocampal 5-HT Input Regulates Memory Formation and Schaffer Collateral Excitation. Neuron 98:992-1004.e4.
Topolnik L, Tamboli S (2022) The role of inhibitory circuits in hippocampal memory processing. Nat Rev Neurosci 23:476–492.
Trouche S, Koren V, Doig NM, Ellender TJ, El-Gaby M, Lopes-dos-Santos V, Reeve HM, Perestenko PV, Garas FN, Magill PJ, Sharott A, Dupret D (2019) A Hippocampus-Accumbens Tripartite Neuronal Motif Guides Appetitive Memory in Space. Cell 176:1393-1406.e16.
Tsoi SY, Öncül M, Svahn E, Robertson M, Bogdanowicz Z, McClure C, Sürmeli G (2022) Telencephalic outputs from the medial entorhinal cortex are copied directly to the hippocampus Giocomo L, Colgin LL, Allen K, eds. eLife 11:e73162.
Tukker JJ, Fuentealba P, Hartwich K, Somogyi P, Klausberger T (2007) Cell Type-Specific Tuning of Hippocampal Interneuron Firing during Gamma Oscillations In Vivo. Journal of Neuroscience 27:8184–8189.

Tukker JJ, Lasztóczi B, Katona L, Roberts JDB, Pissadaki EK, Dalezios Y, Márton L, Zhang L, Klausberger T, Somogyi P (2013) Distinct Dendritic Arborization and In Vivo Firing Patterns of Parvalbumin-Expressing Basket Cells in the Hippocampal Area CA3. J Neurosci 33:6809–6825.
Turi GF, Li W-K, Chavlis S, Pandi I, O'Hare J, Priestley JB, Grosmark AD, Liao Z, Ladow M, Zhang JF, Zemelman BV, Poirazi P, Losonczy A (2019) Vasoactive Intestinal Polypeptide-Expressing Interneurons in the Hippocampus Support Goal-Oriented Spatial Learning. Neuron 101:1150-1165.e8.
Tyan L, Chamberland S, Magnin E, Camiré O, Francavilla R, David LS, Deisseroth K, Topolnik L (2014) Dendritic Inhibition Provided by Interneuron-Specific Cells Controls the Firing Rate and Timing of the Hippocampal Feedback Inhibitory Circuitry. J Neurosci 34:4534–4547.
Tzilivaki A, Tukker JJ, Maier N, Poirazi P, Sammons RP, Schmitz D (2023) Hippocampal GABAergic interneurons and memory. Neuron:S0896627323004750.
Ulyanova AV, Koch PF, Cottone C, Grovola MR, Browne KD, Weber MT, Russo RJ, Gagnon KG, Chen HI, Johnson VE, Cullen DK, Wolf JA (2018) Electrophysiological Signature Reveals Laminar Structure of the Porcine Hippocampus.
Urbán N, Guillemot F (2014) Neurogenesis in the embryonic and adult brain: same regulators, different roles. Front Cell Neurosci 8
Urban-Ciecko J, Barth AL (2016) Somatostatin-expressing neurons in cortical networks. Nat Rev Neurosci 17:401–409.
Valero M, Cid E, Averkin RG, Aguilar J, Sanchez-Aguilera A, Viney TJ, Gomez-Dominguez D, Bellistri E, de la Prida LM (2015) Determinants of different deep and superficial CA1 pyramidal cell dynamics during sharp-wave ripples. Nat Neurosci 18:1281–1290.
Valero M, Navas-Olive A, de la Prida LM, Buzsáki G (2022) Inhibitory conductance controls place field dynamics in the hippocampus. Cell Reports 40:111232.
van de Ven GM, Trouche S, McNamara CG, Allen K, Dupret D (2016) Hippocampal Offline Reactivation Consolidates Recently Formed Cell Assembly Patterns during Sharp Wave-Ripples. Neuron 92:968–974.
Van Groen T, Miettinen P, Kadish I (2003) The entorhinal cortex of the mouse: Organization of the projection to the hippocampal formation. Hippocampus 13:133–149.
Van Groen T, Wyss M (1988) Species differences in hippocampal commissural connections: Studies in rat, guinea pig, rabbit, and cat. J of Comparative Neurology 267:322–334.
van Strien NM, Cappaert NLM, Witter MP (2009) The anatomy of memory: an interactive overview of the parahippocampal–hippocampal network. Nat Rev Neurosci 10:272–282.
Varga C, Golshani P, Soltesz I (2012) Frequency-invariant temporal ordering of interneuronal discharges during hippocampal oscillations in awake mice. Proc Natl Acad Sci USA 109
Varga C, Oijala M, Lish J, Szabo GG, Bezaire M, Marchionni I, Golshani P, Soltesz I (2014) Functional fission of parvalbumin interneuron classes during fast network events. eLife 3:e04006.
Vida I, Halasy K, Szinyei C, Somogyi P, Buhl EH (1998) Unitary IPSPs evoked by interneurons at the stratum radiatum-stratum lacunosum-moleculare border in the CA1 area of the rat hippocampus in vitro. The Journal of Physiology 506:755–773.
Viney TJ, Lasztoczi B, Katona L, Crump MG, Tukker JJ, Klausberger T, Somogyi P (2013) Network state-dependent inhibition of identified hippocampal CA3 axo-axonic cells in vivo. Nat Neurosci 16:1802–1811.
Wan J, Peng W, Li X, Qian T, Song K, Zeng J, Deng F, Hao S, Feng J, Zhang P, Zhang Y, Zou J, Pan S, Shin M, Venton BJ, Zhu JJ, Jing M, Xu M, Li Y (2021) A genetically encoded sensor for measuring serotonin dynamics. Nat Neurosci 24:746–752.
Wehrl HF, Bezrukov I, Wiehr S, Lehnhoff M, Fuchs K, Mannheim JG, Quintanilla-Martinez L, Kohlhofer U, Kneilling M, Pichler BJ, Sauter AW (2015) Assessment of murine brain tissue shrinkage caused by different histological fixatives using magnetic resonance and computed tomography imaging. Histol Histopathol 30:601–613.
Weir K, Blanquie O, Kilb W, Luhmann HJ, Sinning A (2015) Comparison of spike parameters from optically identified GABAergic and glutamatergic neurons in sparse cortical cultures. Front Cell Neurosci 8
Windolf C, Paulk AC, Kfir Y, Trautmann E, Garcia S, Meszéna D, Muñoz W, Hardstone R, Caprara I, Jamali M, Boussard J, Williams ZM, Cash SS, Paninski L, Varol E (2023) Robust Online Multiband Drift Estimation in Electrophysiology Data. bioRxiv:2022.12.04.519043.
Witter MP, Wouterlood FG, Naber PA, Van Haeften T (2000) Anatomical Organization of the Parahippocampal-Hippocampal Network. Annals of the New York Academy of Sciences 911:1–24.
Wouterlood FG, Saldana E, Witter MP (1990) Projection from the nucleus reuniens thalami to the hip-

pocampal region: Light and electron microscopic tracing study in the rat with the anterograde tracer-Phaseolus vulgaris-leucoagglutinin. J Comp Neurol 296:179–203.
Wyskiel DR, Andrade R (2016) Serotonin excites hippocampal CA1 GABAergic interneurons at the stratum radiatum-stratum lacunosum moleculare border: Serotonin Excites Interneurons at the SR-SLM Border. Hippocampus 26:1107–1114.
Yamamoto J, Tonegawa S (2017) Direct Medial Entorhinal Cortex Input to Hippocampal CA1 Is Crucial for Extended Quiet Awake Replay. Neuron 96:217-227.e4.
Ye Z et al. (2023) Ultra-high density electrodes improve detection, yield, and cell type identification in neuronal recordings.
Zhang Y et al. (2023) Fast and sensitive GCaMP calcium indicators for imaging neural populations. Nature 615:884–891.
Zhang Y, Cao L, Varga V, Jing M, Karadas M, Li Y, Buzsáki G (2021) Cholinergic suppression of hippocampal sharp-wave ripples impairs working memory. Proc Natl Acad Sci USA 118:e2016432118.
Zingg B, Chou X, Zhang Z, Mesik L, Liang F, Tao HW, Zhang LI (2017) AAV-Mediated Anterograde Transsynaptic Tagging: Mapping Corticocollicular Input-Defined Neural Pathways for Defense Behaviors. Neuron 93:33–47.
Zingg B, Peng B, Huang J, Tao HW, Zhang LI (2020) Synaptic Specificity and Application of Anterograde Transsynaptic AAV for Probing Neural Circuitry. J Neurosci 40:3250–3267.
Zutshi I, Valero M, Fernández-Ruiz A, Buzsáki G (2022) Extrinsic control and intrinsic computation in the hippocampal CA1 circuit. Neuron 110:658-673.e5.